Evolution of phases and microstructure in rapidly solidified metallic multilayer films

- A correlative microscopy study -

Dissertation

zur Erlangung des Grades
des Doktors der Ingenieurwissenschaften
der Naturwissenschaftlich-Technischen Fakultät III
Chemie, Pharmazie, Bio- und Werkstoffwissenschaften
der Universität des Saarlandes



von

Karl Peter Leibenguth

Saarbrücken, den 21. April 2013

Tag des Kolloquiums:	31.10.2013
Dekan:	Univ.-Prof.Dr. Volkhard Helms
Berichterstatter:	Univ.-Prof.Dr. Frank Mücklich
	Univ.-Prof.Dr. Ralf Busch
	Univ.-Prof.Dr. Martin Heilmaier
Vorsitz:	Univ.-Prof.Dr. Guido Kickelbick
Akad. Mitarbeiter:	Dr. Michael Marx

Dedicated to my family and friends.

[The critical scientific method of trial and error:]
It is the method to draw up bold hypotheses and subject them to the severest criticism, to find out where we were wrong.

Karl Popper

Abstract

During the last decade, Laser Interference Metallurgy (LIMET) was employed on a variety of metallic surfaces to deliberately modify their physical properties in a spatially ordered and periodic manner. Its application to multilayered metallic thin films was envisioned to enable the synthesis of bioinspired composite materials. Further research was needed to understand the processes governing phase selection and formation.

The present thesis is focused on elucidating the relation between LIMET and the theoretical framework of pulsed-laser induced rapid solidification, partitionless transformations from the melt and super lateral grain growth. As model materials, the thermodynamically well-known binary systems Ni/Al, Ti/Al and Ni/Ti were chosen. Depending on substrate material and local stoichiometry, different metastable and ordered equilibrium phases were formed and frozen-in to room temperature. By means of correlative microscopy, localised structural and compositional data on the sub-μm and nm scales were obtained to derive an explanation for the heat-induced mechanisms at the multilayer interfaces. Here, a combination of selected area diffraction in a transmission electron microscope and atom probe tomography was successfully employed. It was accompanied by finite-element thermal simulations. In contrast to former studies, here, the contributions from released energies of mixing were accounted for, thus yielding an improved approximation to the real heat-affected zone.

Kurzfassung

Im vergangenen Jahrzehnt wurde Laser Interferenz Metallurgie (LIMET) zur gezielten Modifikation metallischer Oberflächen genutzt, um die physikalischen Eigenschaften in einer räumlich-periodischen Anordnung zu verändern. Ihre Anwendung auf metallische Multilagen-Dünnschichten wurde als Zugang zur Herstellung bioinspirierter Komposite erachtet. Die Mechanismen von Phasenselektion und -bildung blieben jedoch unklar.

Die vorliegende Studie ordnet LIMET in das theoretische Rahmenwerk laserinduzierter schneller Erstarrung, partitionsloser Phasenumwandlungen und des superlateralen Kornwachstums ein. Als Modell wurden die thermodynamisch gut erforschten Zweistoffsysteme Ni/Al, Ti/Al und Ni/Ti ausgewählt. Abhängig vom Substrat und der lokalen Stöchiometrie wurden metastabile und geordnete Gleichgewichtsphasen gebildet und bis Raumtemperatur eingefroren. Anhand korrelativer Mikroskopie wurden lokalisiert strukturelle und chemische Informationen auf sub-μm- und nm-Skala gewonnen, die zur Aufklärung der wärmeinduzierten Prozesse an den Grenzflächen der Multischicht dienten. Hierzu wurde Feinbereichsbeugung im Transmissionselektronenmikroskop mit Atomsondentomographie erfolgreich kombiniert. Dies wurde ergänzt durch Finite-Elemente-basierte thermische Simulationen, welche die energetischen Beiträge des Durchmischens der Komponenten berücksichtigten, so dass eine getreue Abbildung der real vorliegenden Wärmeeinflusszone gewonnen wurde.

Contents

Abstract v

Kurzfassung vi

List of symbols x

I. Introduction 1

1. Introduction 2

1.1. Background and motivation 2

1.2. State of the art – Laser rapid solidification 5

1.3. Objectives and organisation of the thesis 13

II. Theoretical part 16

2. Laser-matter interaction 17

2.1. Absorption of light in metals 18

2.2. Laser as a heat source and heat transfer in matter 22

3. Rapid solidification and phase formation 27

3.1. Nucleation and growth 29

3.1.1. Nucleation 29

3.1.2. Growth 32
3.2. Interfacial kinetics and metastable thermodynamics 38
3.2.1. Interfacial kinetics 39
3.2.2. Thermodynamic considerations and metastability 46
3.2.3. Microstructure and phase selection 51

4. Materials selection **58**
4.1. Substrate materials 59
4.2. Metallic multilayer systems 60
4.2.1. Nickel-Aluminium System (Ni/Al) 62
4.2.2. Titanium-Aluminium System (Ti/Al) 63
4.2.3. Nickel-Titanium System (Ni/Ti) 64

III. Experimental part **66**

5. Experiments and methods **67**
5.1. Design of experiment 67
5.2. Specimen preparation, Laser processing and characterisation 70
5.2.1. Ion beam Physical Vapor Deposition 70
5.2.2. Laser interference metallurgy 72
5.2.3. Scanning electron and focused ion beam microscopy 76
5.2.4. Transmission electron microscopy 78
5.2.5. Atom probe tomography 79
5.3. Finite element thermal simulations 84

6. Results **90**
6.1. FEM thermal simulations 90
6.1.1. Influence of substrate, periodicity and fluence – Ni/Al 92
6.1.2. Influence of multilayer material combination 101

6.2. Microstructural characterisation and structure determination 106
6.2.1. As-deposited multilayers 106
6.2.2. LIMET-processed multilayers 111
6.3. Localised chemical analysis by APT 151
6.4. Correlative summary of the results 174

7. Discussion **181**
7.1. Solidification and phase formation 181
7.1.1. Region (II) – Solid-state amorphisation 185
7.1.2. Region (III) – Rapid solidification 196
7.2. Consequences on designing LIMET processing 214

IV. Conclusions and outlook **219**

8. Conclusions and outlook **220**

V. Appendices **A**

Material data on selected phases **B**

Multilayer thickness analysis **E**

List of symbols

Interaction of laser radiation with matter

ν	Frequency
$\vec{S}$	Poynting-vector
$\langle\cdot\rangle_{\Delta t}$	Time-average of a harmonic function
t	Time
Δt	Time interval
i	Imaginary unit
ω	Angular frequency
c	Vacuum light speed
ϵ_0	Vacuum dielectric constant
$\vec{E}$	Electric field vector with magnitude $\vec{E}_0$
$\vec{B}$	Magnetic induction vector with magnitude $\vec{B}_0$
$\vec{r}$	Position vector with cartesian components $(x, y, z)^\top$
$\vec{k}$	Wave vector with cartesian components $(k_x, k_y, k_z)^\top$
I	Intensity, energy flux per unit area

$\vec{F}$	Force
$n^2(\omega)$	Dispersion function of refraction
σ_e	Scalar electric conductivity
γ_e	Electronic damping constant
N	Number of atoms
V	Volume
q_e	Electron charge
m_e	Electron mass
ϵ_r	Complex scalar relative permitivity, with real $\epsilon_{r,re}$ and imaginary part $\epsilon_{r,im}$
n	Complex index on refraction, with real n_{re} and imaginary part n_{im}
β	Absorption coefficient
e	Euler´s constant
δ	Skin depth
ω_p	Plasma frequency
λ	Wavelength
i, j, k, l, m	Indices
n_j	Complex scalar refractive index of medium j
R	Reflectivity with reflected intensity I_{ref}
A	Absorbance with absorbed intensity I_{abs}

T	Transmittance with absorbed intensity I_{trn}
I_0	Irradiating electromagnetic intensity
τ_p	Laser pulse duration
τ_e	Electronic relaxation time interval
τ_{e-ph}	Electron-phonon relaxation time interval
$Q(\vec{r}, t)$	Heat source term
$\vec{\nabla}$	Nabla-operator with cartesian components $(\partial/\partial x, \partial/\partial y, \partial/\partial z)^\top$
$U(\vec{r}, t)$	Term of energy addition and loss contributions
$I(\vec{r}, t)$	Spatial and temporal intensity distribution
U_{rad}	Radiation loss term
U_{conv}	Convection loss term
A	Surface area
σ	Stefan-Boltzmann constant
ϵ	Surface emissivity
T	Temperature
T_{amb}	Ambient temperature
α_{conv}	Convection heat transfer coefficient
ΔT	Temperature difference
$A(z)$	Attenuation factor
$P(t)$	Gaussian temporal laser pulse shape

t_p	Time instant of the laser pulse
ς	Variance of the temporal shape
$\underline{\underline{D_{th}}}$	Tensor of thermal diffusivity
D_{th}	Scalar thermal diffusivity
$\underline{\underline{\lambda_{th}}}$	Tensor of thermal conductivity
λ_{th}	Scalar thermal conductivity
ρ	Mass density
c_P	Specific heat capacity at constant pressure
C	Heat capacity per unit volume
l_{th}	Thermal diffusion length
ν_m	Volume fraction of medium m
e_{th}	Thermal effusivity

Rapid solidification and phase formation

T_m^j	Melting temperature of phase j at thermodynamic equilibrium
$G_{(\cdot)}$	Gibbs´ free energy of phase $(\cdot)$
$G_{V,(\cdot)}$	Gibbs´ free energy per unit volume of phase $(\cdot)$
$\gamma_{(s)-(l)}$	Excess energy at (s)-(l) interface, interfacial energy
N_A	Avogadro´s constant
ΔH_m	Latent heat of melting

$\Delta H_{m,V}$	Latent heat of melting per unit volume
ΔS_m	Entropy of melting
$\Delta S_{m,V}$	Entropy of melting per unit volume
R	Ideal gas constant
T_i	Interfacial temperature
ΔT_i	Interfacial undercooling
ΔG	Difference in free energy between two phases
ΔG_V	Released free energy difference per unit volume
ΔG_r	Change in free energy due to nucleation
ΔG_{ex}	Excess free energy barrier for homogeneous (hom) or heterogeneous (het) nucleation
ΔG_{hom}	Change in free energy due to homogeneous nucleation
ΔG_{het}	Change in free energy due to heterogeneous nucleation
r	Nucleus radius
r_{crit}	Critical radius of a stable nucleus
$s(\theta)$	Nucleant factor
θ	Wetting angle
ΔT_{th}	Thermal undercooling
$\nabla T_{i,(\cdot)}$	Thermal gradient at the (s)-(l) interface in phase $(\cdot)$
$\lambda_{th,(\cdot)}$	Thermal conductivity of phase $(\cdot)$

v_i	Interfacial growth rate, solidification velocity
ΔT_r	Curvature undercooling (Gibbs-Thomson effect)
Γ	Gibbs-Thomson coefficient
X_0	Alloy composition in mole fractions
$X_{(\cdot)}$	Composition of phase $(\cdot)$ in mole fractions
k_{eq}	Equilibrium partition coefficient
$D_{(l)}$	Solute diffusivity in (l) phase
$\nabla c_{(l)}$	Concentration gradient in (l) at the solidification front
$c_{(l)}$	Concentration of phase $(\cdot)$
T_{liq}	Liquidus temperature
T_{sol}	Solidus temperature
T_e	Liquidus temperature distribution in (l) due to constitutional undercooling
$T_{(l)}$	Temperature distribution in (l)
$\nabla T_{e,crit}$	Critical interfacial temperature gradient for planar solidification
ΔT_c	Constitutional undercooling
l_D	Diffusion distance
τ	Time interval for monolayer solidification
ΔG^*	Energy barrier for thermal activation
$j_{(\cdot)\rightarrow(\cdot)}$	Rate of atomic flux between two phases

a_0	Interatomic distance
A	Interfacial accommodation factor for atoms
ν	Frequency of atomic vibration
v_0	Kinetic prefactor
v_D	Diffusive speed
c_j	Geometrical factor, j=(1,2)
η_S	Shear viscosity
k_B	Boltzmann´s constant
l_{crit}	Dendrite radius, cell spacing, spacing between eutectic lamellae
β_{Pe}	Péclet number
v_S	Sound velocity
k_v	Kinetic partition coefficient
$X^{neq}_{(\cdot),i}$	Non-equilibrium composition of phase $(\cdot)$ at the (s)-(l) interface
ΔT_{kin}	Kinetic undercooling
ΔT_{drag}	Undercooling due to solute drag
ΔT_{trap}	Undercooling due to solute trapping
ΔT_{fract}	Fractional contributions to interfacial undercooling due to kinetics
ΔG_{alloy}	Driving force for alloy solidification
$\Delta\mu^j$	Difference between the chemical potentials of a component j=(A, B)
A	Solvent component

B	Solute component
G_{alloy}	Alloy free energy
G^j	Free energy of component j
ΔG_{mix}	change in free energy due to mixing two components
$X^j_{(\cdot)}$	Chemical composition of component j in phase $(\cdot)$ in mole fractions
$\mu^j_{(\cdot)}$	Chemical potential of component j in phase $(\cdot)$
$\Delta\mu^j$	Difference in chemical potential of component j between two phases
T_N	Nucleation temperature
X_N	Chemical composition of the first stable nuclei in mole fractions
ΔH_{mix}	Enthalpy of mixing
ΔS_{mix}	Entropy of mixing
Ω	Binding energy parameter
$\Delta G_{alloy,max}$	Maximum thermodynamic driving force for alloy formation
ΔT_i^{total}	Total interfacial undercooling
T_0	Temperature for equal liquidus and solidus lines
$v_{e,crit}$	Critical interfacial velocity for planar solidification
v_a	Velocity limit of absolute stability
T_{liq}^{neq}	Non-equilibrium liquidus temperature
T_{sol}^{neq}	Non-equilibrium solidus temperature
∇T_a	Temperature gradient limit of absolute stability

v_{trap}	Velocity limit for solute trapping
∇T_a	Critical interfacial temperature gradient for absolute stability
$\dot{T}$	Cooling rate
r_{at}	Atomic radius
$r_{at,s}$	Atomic radius, smaller component
$r_{at,l}$	Atomic radius, larger component
d_{melt}	Melt depth
P	Irradiation power
$\tau_{(l)}$	Melt lifetime
l_{mono}	Diffusion length in (l) during τ
T_{soft}	Glass softening temperature
T_b	Equilibrium boiling temperature
α_{th}	Thermal expansion coefficient
M_S	Martensite start temperature

Experiments and methods

t_{tot}	Total film thickness
t_i	Individual thickness layer i
Λ	Bilayer thickness
T_{max}	Maximum temperature at the interference maximum location

P_{fwd}	Forward power
P_{ref}	Reflected power
ν	HF-frequency
p_{base}	Base pressure PVD chamber
f_{Ar}	Ar flow
p_{Ar}	Ar pressure, process gas pressure
U_{beam}	Ion-beam voltage
j_{beam}	Ion-beam current
U_{acc}	Accelerator voltage
j_{acc}	Accelerator current
$\vec{E}_{sum}(\vec{r},t)$	Algebraic superposition of electric fields $\vec{E}_j(\vec{r},t)$
c_j	Weighting cofficient
I_{sum}	Interference pattern intensity distribution
$\vec{E}_{line}(\vec{r},t)$	Electric field distribution line-like pattern
$I_{line}(\vec{r},t)$	Intensity distribution line-like pattern
ϕ	Phase difference
I_{max}	Intensity at interference maximum
I_{min}	Intensity at interference minimum
d	Periodicity
F	Fluence

F_{max}	Maximum fluence
η	Efficiency of the optical setup
P	Irradiation power
f	Pulse repetition rate
A	Irradiated surface area
α	Half-angle of two-beam divergence
r_{tip}	Tip radius APT specimen
U_{DC}	Electric potential at APT specimen
E_{tip}	Average electric field at APT specimen
U_{pulse}	Magnitude voltage pulse
k	Geometric factor
v	Final velocity of the extracted ions
M	Imaging magnification
s	Distance APT specimen tip – detector
κ	Image compression factor
m	Ionic mass
n	Ionisation state
t_{TOF}	Ion travel time
E_P	Energy laser pulse
$m/\Delta m$	Mass resolution

$T(\vec{r}, t)$	Spatial and temporal temperature distribution
t_0	Time instant of simulation start
t_{sim}	Simulation duration
Q_m	Latent heat of melting
Q_b	Latent heat of boiling
U_{trans}	Heat contribution of phase transitions
$\Delta T_{0,trans}$	Temperature interval of phase transition

Results and discussion

l_{top}	Lateral expansion along x axis of point A
l_{bot}	Lateral expansion along x axis of point B
t_{dep}	Depth expansion along z axis of point B
∇T_{lat}	Lateral thermal gradient at A-B boundary
∇T_{dep}	Depth thermal gradient at A-B boundary
∇T	Effective thermal gradient at A-B boundary
α	Heat flow angle
$f_{(l)}$	Volume fraction of molten low-T_m component
$d_{\{hkl\}}$	Interplanar distance of plane set $\{hkl\}$
n	Substrate normal direction as indicated in D
Z	Atomic number

$X^i(z)$	Composition profile of component i in normal direction z
$\nabla X^i(z)$	Gradient of composition profile $X^i(z)$
G_a	Free energy of an amorphous phase
G_{IP}	Free energy of an intermetallic phase
ΔG_{ac}	Driving force for the nucleation of the intermetallic phase
ΔG_a	Driving force for the nucleation of the amorphous phase
ΔG_{pc}	Free energy of polymorphous crystallisation
κ_X	Curvature of G_a-X^i
G_N	Free energy for polymorphous nucleation of the intermetallic phase
γ_{pc}	Interfacial energy of the polymorphous crystallisation front
χ	Constant
$\nabla X^i_{crit}(z)$	Critical gradient of composition profile $X^i(z)$
$\dot{T}_i$	Interfacial cooling rate
G_f	Free energy of phase formation
E_L	Energy delivered to an individual interference maximum line
E_{mix}	Energy released due to elemental mixing at an individual interference maximum line
E_{tot}	Total energy present at an individual interference maximum line
F	Nominal fluence
F_{act}	Actual fluence

$\Delta F/F$	Relative increase of fluence through released ΔG_{mix}
v_{iso}	Isotherm velocity
η	Ordering parameter
m	Twin habit plane
s_j	Twin variant

Abbreviations

MEMS	Microelectromechanical System
(s)	Solid state
(l)	Liquid state
a	Amorphous
sc	Single Crystalline
pc	Polycrystalline
LIMET	Laser Interference Metallurgy
TEM	Transmission Electron Microscopy
APT	Atom Probe Tomography
FEM	Finite Element Method
cw	Continuous Wave
TCR	Transient Conductance and Reflectance Technique
STEM	Scanning Transmission Electron Microscopy

EDX	Energy Dispersive X-ray Spectroscopy
AES	Auger Electron Spectroscopy
RBS	Rutherford Backscattering Spectrometry
SLG	Super Lateral Growth
TEM_{00}	Fundamental transverse mode of a Gaussian beam
CALPHAD	CALculation of PHAse Diagrams
fcc	Face-centred cubic structure
fct	Face-centred tetragonal structure
bcc	Body-centred cubic structure
bct	Body-centred tetragonal structure
SHS	Self-propagating exothermic solid state reactions
I-PVD	Ion Beam Physical Vapor Deposition
HF	High-frequency
DC	Direct Current
WLI	White-Light Interferometry
XRD	X-Ray Diffraction
GIXRD	Grazing Incidence X-Ray Diffraction
SEM	Scanning Electron Microscopy
FIB	Focused Ion Beam
E-CVD	Electron induced-Chemical Vapor Deposition

I-CVD	Ion induced-Chemical Vapor Deposition
SE	Secondary Electrons
SAD	Selected Area Diffraction
SADP	Selected Area Diffraction Pattern
BF	Bright-Field imaging
C-DF	Centered Dark-Field imaging
CCD	Charge coupled device
ICDD	International Center for Diffraction Data
FIM	Field-Ion Microscopy
TOF-MS	Time-Of-Flight Mass-Spectroscopy
LEAP	Local Electrode Atom Probe
UHV	Ultra-High Vacuum
MCP	Multichannel Plate
CSR	Charge-state-ratio
FWHM	Full width at half maximum
FWTM	Full width at tenth of maximum
ROI	Region of interest
Iso-surface	Iso-concentration surface
Proxigram	Proximity histogram

Acknowledgements

My research would not have been possible without my supervisor Prof. Dr.-Ing. Frank Mücklich (Chair of Functional Materials, Saarland University), who gave me the opportunity to freely select and pursue scientific questions and challenges. Thank you very much for the confidence you have placed in me over the last decade at your chair and the new institute. I have gained experience and insight into several aspects of science and research, giving lectures, working with industry and beyond that. I also would like to express my gratitude to my second supervisor Prof. Dr. rer.nat. Ralf Busch (Chair of Metallic Materials, Saarland University) for the fruitful discussions on thermodynamics and phase transitions and for accepting this thesis for revision. I would also like to thank the European Union for funding my work in project AME-Lab (C/4-EFRE-13/2009/Br).

During the course of this thesis, several chairs and institutes at Saarland University and neighbouring universities were of particular importance, especially regarding the preparation of thin-film specimens. The PVD equipment at the Chair of Microfluidics and Micromechanics as well as those at the Chair of Nanostructural Research and Nanotechnology were kindly made avaliable by Prof. Dr.-Ing Helmut Seidel and Prof. Dr. rer.nat. Uwe Hartmann. A most deserved mention is made to Dr.-Ing. Abdallah Ababneh and Dipl.-Ing. Henning Völlm for sharing their experience in deposition techniques and their helpful advice. The TEM images were taken at the Chair of Technical Physics of Prof. Dr. rer.nat Rainer Birringer. An infinite

thank you goes to Dipl.-Phys. Jörg Schmauch for his uncomplicated attitude and his calmness when dealing with microscope (and user) errors.

This thesis is a product of the years of interaction with, and contributions by, a large number of colleagues at the Chair of Funcional Materials. I wish to sincerely thank all of you, who advised, supported, commented and encouraged me in academic and peronal ways. You made this a place I like to work in. Unfortunately, I cannot account for everyone, but I would like to thank some of you individually.

The last year of the thesis would have been impossible to tackle without the help of student research assistants like Ines Blatter, B.Sc. Andreas Hegetschweiler, Cand.-Ing. Leander Reinert, M.Sc. Benjamin Kelkel, B.Sc. Thomas Kreuter and B.Sc. Nils Harste. Thank you very much! In those years before, a number of students contributed to this thesis with their own scientific work under my supervision. Dr.-Ing. Anna Manzoni, Dr.-Ing. Eric Detemple, Dipl.-Ing. Coralie Frey, Dipl.-Ing. Mark Wobrock, M.Sc. Marcos Soldera and B.Sc. Daniel Henry. You all have left a mark on this work and I wish you all the best for your lives and carreers. In similar manner, I would like to thank Dipl.-Ing. Stefan Schommer for his effort in setting up the framework for the thermal simulations. Also, I would like to thank technician Wolfgang (Higgs) Ott for his support concerning PVD and CAD design.

An outstanding attribute of this chair is its multiculturalism, which broadened my horizon with respect to foreign cultures, manners and languages. Dr.-Ing. Flavio Soldera plays a vital role in bringing together people of from different countries and continents for which I am especially grateful. In this context I would like to mention Nicolas Souza for his competent revision (and abridgement) of the manuscript. Gracias por todo! For enduring my bad jokes and puns and being good company in the lab I

would like to extend my thanks to Dipl.-Ing. Andreas Rosenkranz, Dipl.-Phys. Björn Lechtaler, Dipl.-Ing. Benjamin Bax and Dipl.-Ing. Dominik Britz. Also part of this group is Dipl.-Ing. Sebastian Slawik, who especially deserves my thanks for his support concerning XRD both in laboratory and in lecture. A substantial amount of the experimental work relied on FIB was supported by the expertise and speed of Dipl.-Ing. Christoph Pauly. Besides this, I want to thank him for the severe criticism he introduces to our discussions about experiments and results. M.Sc. Isabella Schramm deserves my sincerest gratitude for her effort in atom probe tomography and for all the discussions and the exchange of ideas we had on the thesis and beyond.

At the beginning of my undergraduate studies I was lucky to meet three fellow students, who over the years became my closest colleagues and friends. Dr.-Ing. Carsten Gachot, Dr.-Ing. Christian Selzner and Dr.-Ing. Karsten Woll, I owe a great deal to all of you. Thank you for the past twelve years and those to come!

To my family I would wholeheratedly like to thank you for the understanding, the support, and the warmth I am glad to receive and hope to return.

Part I.

Introduction

1. Introduction

1.1. Background and motivation

Materials research during the 20th century is primarily characterised by the evolution from the use and production of materials based on empirical knowledge to a more enlightened or guided approach relying on a profound understanding of the governing physical mechanisms of the global behaviour. Especially the role of the microstructure (present phases, chemical distributions, boundaries and defects) on the resulting material properties represents a key issue both in basic research and in actual production. Besides the rather obvious effects on the material behaviour exerted by phase-specific properties and their anisotropy, textures and phase composition, there are several other contributing factors, whose impact was studied intensively in the last decades. Mainly, these are *size* and *size distribution* of the individual grains forming the material and the controlled formation of *metastable phases* with desirable properties. A further influence is introduced by the design of *architectured microstructures*: a designed spatial arrangement and volume ratio of the present phases allows for new concepts of composite materials.

Size effects on material properties were summarised by Arzt in his widely recognised comprehensive overview on this topic [1]. Their implications can be attributed to an interaction of length scales that are characteristic of the microstructure, e.g. grain and precipitate sizes, average distances between the latter, and a dimensional constraint of the physical mechanism underlying the property under investigation. Arzt discussed

this in the context of well-known hardening mechanisms like Hall-Petch and Orowan, both related to the characteristic dimensions of the dislocations responsible for plastic behaviour. Together with Gleiter´s proposition during the 1980s regarding the prospective outstanding capabilities of *nanostructured materials*, the manufacture and scientific assessment of dimensionally constrained microstructures and the associated defect types and densities experienced rapid development [2][3][4]. During this time, thin film systems received special attention due their increasingly broad application field as protective coatings or structural and functional elements in miniaturised *microelectromechanical systems* (MEMS) [5]. Moreover, *multilayered films* with bilayer periods on the nm scale were found to exhibit enhanced yield strengths due to dislocation pinning effected by the close proximity of interfaces [6][7].

Also in the 1980s, Spaepen reviewed both the development of processing techniques leading to the formation of *metastable phases* and the theoretical background in thermodynamics and kinetics needed to explain the resulting nucleation processes, phase transformations and microstructural morphology. His summary mainly aimed at highlighting the possibilities of controlling the outcome of the processing by employing production methods which allow for manipulating suitable processing parameters [8]. Since metastable phases are mostly formed by increasing the free energy of educt materials through heating and subsequent energy removal via quenching, the parameters to control are *heating* and *cooling rates* as well as *solidification velocities*. Besides other techniques like melt-spinning or splat-quenching covering cooling rates of 10^6 to $10^8\,\mathrm{K/s}$, it was particularly the use of newly developed Q-switched ultra-short pulsed laser radiation which significantly enhanced the range of accessible rates. With these reaching the order of $10^{12}\,\mathrm{K/s}$, an effective reduction of atomic mobility during solidification can be achieved leading to e.g. solid solutions with unusually high solute content or configurationally frozen phases by suppressing further transformations. In consequence, not only amorphous metals could successfully be produced; the whole field of research dealing

with nucleation and growth processes during solidification benefited from the emerging systematic experimental assessments yielding satisfying theories both on slowly moving (s)-(l) fronts as well as rapid solidification conditions.

According to Brechet´s recent concise review on *architectured materials*, the ability to control phase composition and morphology as inferred by Spaepen´s summary, represents only one facet in the design of novel materials [9]. The envisioned deliberate production of engineered materials with adapted properties for structural applications as well as specific functions at the same time affords additional considerations. These encompass the use of dedicated *design strategies*, which account for appropriate material combinations, optimised geometries with respect to the microstructure and the overall system as well as an adjusted spatial distribution of phases while ensuring high mutual cohesion. Most notably, the increased interest in *biological composite materials* led to the derivation of new models for composite materials. Especially nacre, antler and bone were seen as promising archetypes due to their unique combination of high elasticity and high fracture toughness not usually encountered in technical materials [10][11][12][13]. Key to this successful integration is the ordered spatial distribution of a brittle, hard ceramic phase in a ductile, crack-stopping collagen matrix on length scales on the order of 1 nm to 10 μm [14][15][16].

The cunning combination of these three disciplines could lead to a promising processing route, useful in the guided development of metallic thin film microstructures, tailored to the requirements of mechanically and/or tribologically loaded surfaces both in macroscopic and miniaturised applications. *Laser Interference Metallurgy* (LIMET), as a possible means to μm scale periodic surface modifications with long-range order over several mm^2, was found to combine the needed features in one technique [17][18]. It simultaneously allows for control of processing parameters, large cooling rates and a simple geometric approach to create spatially ordered microstructural arrangements

on a length scale relevant to trigger mechanically active dimensional constraints. Prior to this thesis, the feasibility of this approach was principally evaluated by structuring Ni/Al multilayer specimens in order to generate hard intermetallic grains embedded with good cohesion into the ductile multilayer matrix and subsequently measuring the local and global mechanical response [19][17][18]. In a first approximation, the overall elastic behaviour fitted fairly well to the predictions of a bio-inspired composite model introduced by Jäger and Fratzl [20][21][22][15][23][24]. It describes the lowest hierarchy level of bone and calculates a scalability of the effective elastic modulus as inversely proportional to the square of the structure periodicity.

This thesis returns to a more basic treatment of the underlying models regarding microstructure formation and phase selection in the context of rapid solidification. Its aim is to derive design guidelines and limits appropriate for the successful employment of LIMET on metallic multilayer thin films based on thermodynamic and kinetic considerations. Furthermore, through the combined use of high resolution and complementary characterisation techniques like *transmission electron microscopy* (TEM) and *atom probe tomography* (APT) with FEM-based thermal simulations, the processes associated with microstructure and phase formation during LIMET shall be elucidated.

1.2. State of the art – Laser rapid solidification

The widespread use of continuous-wave (cw) and pulsed laser radiation in materials processing applications like topographic surface structuring or component welding led to an increased interest in the accompanying microstructural modifications. Especially in the case of laser welding by moving cw lasers it becomes evident, that the solidification conditions in the heat-affected zone dictate the performance and durability of the bonding under load. As the previous discussion infers, the microstructure formed there and in the adjacent regions strongly affects the resulting mechanical properties. This rep-

resented a strong incentive for experimental and theoretical investigations concerning laser-induced rapid solidification processes and their implications on the formation of phases and morphologies [25]. In association with research conducted on other processing techniques capable of fast heat extraction, a range of cooling rates spanning several orders of magnitude (from 10^6 to 10^{12} K/s) could systematically be assessed with respect to the governing thermodynamic and kinetic mechanisms. Ultimately, adequate theories for *microstructure* and *phase selection* valid in different solidification velocity regimes could be derived and will be summarised in the third chapter of this thesis.

A significant boost to this field was experienced in the early 1980s with the advent of reliable Q-switched pulsed laser systems permitting pulse durations on the ns and ps scale. Mehrabian, Poate and Baeri discuss in their instructive reviews the early development of this technology and the Materials Research Society Symposium Proceedings of the years 1983 to 1986 collected a large set of related basic investigations [25][26][27]. The first systematic studies were concentrated on relatively simple, dilute material combinations with different tuned tendencies for solubility of the constituent elements. Thus, an assortment of model systems with differing and simple phase diagram shapes could be accessed. Particularly the surfaces of Si samples, in the form of amorphous (a) or single crystalline (sc) pure material and ion-implanted dilute alloys, were ideal for laser annealing [1] experiments. In order to learn more about the dynamics of these fast melting and solidification processes, Peercy and Thompson devised the so called *transient conductance and reflectance technique* (TCR). Employing this, actual *solidification front velocities* can be observed which effected a refined theoretical derivation and subsequent experimental verification of the kinetic models for rapid solidification. In the case of Si, melting and resolidification took place within 100 ns yielding melt depths of 100 nm and

[1] Poate relatively early pointed out, that this term, despite its widespread use, is rather misleading when considering the given probability of transitions between (s) and (l) state to occur. Hence, *laser resolidification* is the better fitting choice [26].

solidification front velocities of 1 to 30 m/s [26][27]. Depending on the pulse duration, the solidification of an atomic monolayer thus takes place in time intervals critical for atomic diffusion in the (l) phase. Employing ps or even shorter pulses, the melt can be quenched below its configurational freezing temperature effecting the formation of amorphous states. For ns pulses, a monolayer solidifies in an interval of 10 to 100 ps which corresponds to the time needed for an atom to diffuse in (l) phase over an interatomic distance [27].

Consequentially, the solidification front can travel at speeds higher than the rate of solute rejection at its location, leading to a burying of large amounts of comparatively immobile solute atoms in the fast expanding (s) phase. Hence, the formation of a random solid solution with solute contents substantially exceeding those predicted by the corresponding equilibrium phase diagram can be expected [28]. This *solute trapping* behaviour was experimentally confirmed by laser annealing performed on sc-Si whose surface prior to the treatment had been either ion-implanted, e.g. with As or Bi, or coated with thin metallic layers like Ni [29][27][30][31][32]. The spatial distribution of the solute element content was subsequently analysed using STEM-EDX, AES or RBS in a quantitative manner. Using these concentration profiles, the understanding of the kinetics at planar (s)-(l) interfaces could be increased, culminating with the development of the interface attachment theory for solute trapping by Aziz and coworkers and several derivate treatments [33][34][30]. For front speeds reaching or exceeding (l) diffusion velocity, these concordantly predict a (l)-(s) transition without changing the chemical composition. This process is called *partitionless solidification* and represents a remarkable characteristic of rapid solidification [35][36][37].

Besides these considerations on an atomistic level, macroscopic models for the heat flow at the solidification front were formulated, since the crystal growth rate strongly depends on the balance between heat removal from the moving (s)-(l) front through

the local temperature gradient and the added heats of mixing or phase formation released there. From the standpoint of thermodynamic driving force for phase transitions, solidification requires the temperature at the growing interface to be lower than the equilibrium transformation temperature for the given chemical composition. In the vicinity of a moving (s)-(l) interface, the magnitude of the *kinetic undercooling* effective there is connected to the solidification velocity, according to findings of Spaepen and Turnbull [38][27].

In a parallel development, several research groups tackled the same set of problems associated to the laser treatment of *metallic* and *intermetallic* surfaces both in bulk and thin film specimens. Most notably the initial work of von Allmen et al. and Spaepen and coworkers shall be introduced here, since it partially prepared the ground for the LIMET approach pursued in this thesis. Bearing in mind the aforementioned discussion on possible kinetic hindrances, it is comprehensible that their principal interest was centred around the *glass forming ability* of metals and alloys. Using a multilayer approach with bilayer thicknesses on the order of 3 nm, model thin film specimens on Ni-, Ti- and Co-basis were prepared [39][40][41][42]. A more complete intermixing of the constituent metallic elements during melting and resolidification was thus intended as well as to willingly select the compositional region of interest in the corresponding phase diagram.

Especially in conjunction with the T_0 *concept* of partitionless solidification, the kinetics and thermodynamics of metallic metastable phase formation, both amorphous and crystalline, could be addressed [35][36][37]. Due to the comparatively enhanced quench rates of laser processes, the composition range capable of glass formation could be increased in certain metal combinations. Spaepen´s work on Ni/Nb and Nb/Si multilayers on different substrate materials gave first insights into the interplay between the formation of amorphous and intermetallic phases and its relation to selected composition and kinetic limitations [42][43]. Moreover, by altering the underlying substrate material

according to its thermal conductivity, Spaepen introduced a further means to systematically altering heat flow vectors and quench rates. Based on heat-flow considerations they were estimated to be on the order of 100 m/s or even above for metals, which was confirmed in experiment by employing the aforementioned TCR technique [44].
The majority of the laser treatments discussed so far was performed using beam diameters on the order of several mm, which is significantly larger than the microstructural features present and the total thickness in the case of thin films. By means of beam focusing, projection masks or interference setups, the irradiated width can be reduced to length scales on the order of several tens of μm and below. This effects an altered orientation of the associated *heat flow vector*. For the examples discussed above, the heat was extracted parallel to the depth direction making this a one-dimensional problem. A narrower irradiation gives rise to an additional, increasingly dominating lateral flow component which necessitates a two-dimensional treatment. Since growth occurs along the thermal gradient, it is obvious that the resulting microstructure is directly affected by these different heat flow conditions. During the mid 1990s, the first observations of *super lateral growth* (SLG) phenomena in 50 to 100 nm thick amorphous (a) and polycrystalline (pc) Si films on bulk single crystalline (sc) Si and SiO_2 substrates were made by the groups of Im, Grigoropoulos and Aichmayr [45][46][47][48][49][50].

In their experiments, the confined laser irradiation effected a complete melting of the film to the substrate and a melting front moving laterally within the thin film plane. As soon as the melting process abated, heterogeneous crystallisation set in and the unmolten thin film directly in contact with the (s)-(l) front acted as a nucleation seed. The ensuing resolidification front also travels laterally but in opposite direction leaving a microstructure closely resembling the one encountered in conventional chill casting. There, mainly elongated crystals are observed, with their long axis aligned parallel to thermal gradient. In SLG, the resulting in-plane grain size was observed to reach the order of 1 to 10 μm, significantly exceeding the film´s total thickness. Similar observations were

made in monolithic metallic thin films of comparable and slightly larger thicknesses by the groups of Kline and Leonard as well as Mücklich [51][52][53][54][55][56][57]. While the first group employed a projection mask technique on Cu and Au, Mücklich´s researchers used LIMET on Au, Pt, Ti, Cu and W to not only create these enlarged grains but to also willingly distribute them in a spatially ordered manner with periodicities on the order of the attained grain size. The latter represents one of the remarkable features of LIMET, since this technique combines a local irradiation spatially confined to length scales comparable to those of microstructure characteristics with a tailored geometrical arrangement of the heat-affected zones on the same dimensional order.

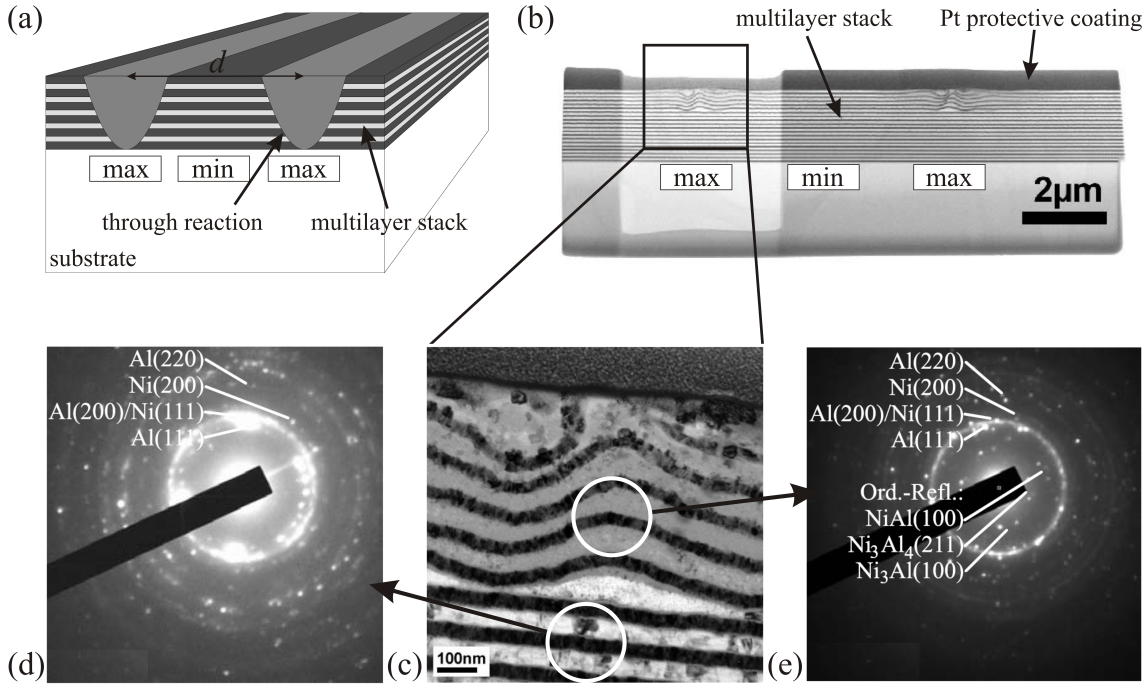


Figure 1.1.: Schematic representation of two adjacent interference maxima (*max*) embedded into a minimum region (*min*). The heat-affected zone (grey) is suitable for a *through reaction* (a). Corresponding TEM foil extracted perpendicular to the periodic line pattern (b) with close-up image of the modified surface layers (c). The structural situation within unaffected (d) and processed multilayer (e) is shown in according SADs (modified from [19]).

Joining Spaepen´s multilayer approach with LIMET could be the desired combination of techniques capable of producing thin film composite materials with architectured phase composition and microstructure. Daniel´s thesis evaluated this notion with a first approximation in Ni/Al multilayers with 50 nm bilayer periodicity and was accompanied by Lasagni´s investigations in Fe/Al and Cu/Al systems [58][19][59][17][18][60]. In order to achieve the envisioned composite thin film, it is necessary that the laser interference treatment produces spatially distinct heat-affected zones that reach down to the multilayer-substrate interface. A schematic representation of this desired *through reaction* is depicted in figure 1.1(a). This complete separation of the compliant multilayer matrix from the intended intermetallic stiff phase meets a prerequisite for a meaningful application of the mechanical composite models [20][23]. The microstructure modification in Ni/Al was characterised by TEM analysis of site-specifically prepared foils containing both heat-affected zones and adjacent multilayers [19].
Obviously, for the LIMET conditions selected in that thesis, the heat-affected zone did not extend to the substrate. Together with FEM thermal simulations, a close-up examination of maximum sites (see figure 1.1(c)) and the determination of the local crystal structure ((d) and (e)) led Daniel to the observation that the laser processing effected melting of the topmost layers, high speed deformation of the initially flat thin film stack and diffusion (see contrast change in the layers in figure 1.1(c)) rather than the formation of a substantial volume fraction of intermetallic phases. The existence of the latter, namely Ni_3Al_4, NiAl and Ni_3Al, was attributed to cooling rates on the order of 10^{10} K/s as approximated by FEM. TEM dark-field imaging visualised those phases embedded into the deformed layers as mostly equiaxed grains with sizes less or approximately equal to the thickness of the unreacted Al and Ni, hence between 20 and 30 nm.

Using nanoindentation and the wafer-bow technique local and global mechanical properties were analysed in order to verify the modulation in elastic modulus and hardness as well as the composite´s overall stiffness [5][61][62][63]. As displayed in figure 1.2(a),

nanoindentation revealed an increase in both reduced elastic modulus and the indentation hardness in heat-affected zones by 30 and 60 %, respectively, when compared to the untreated matrix.

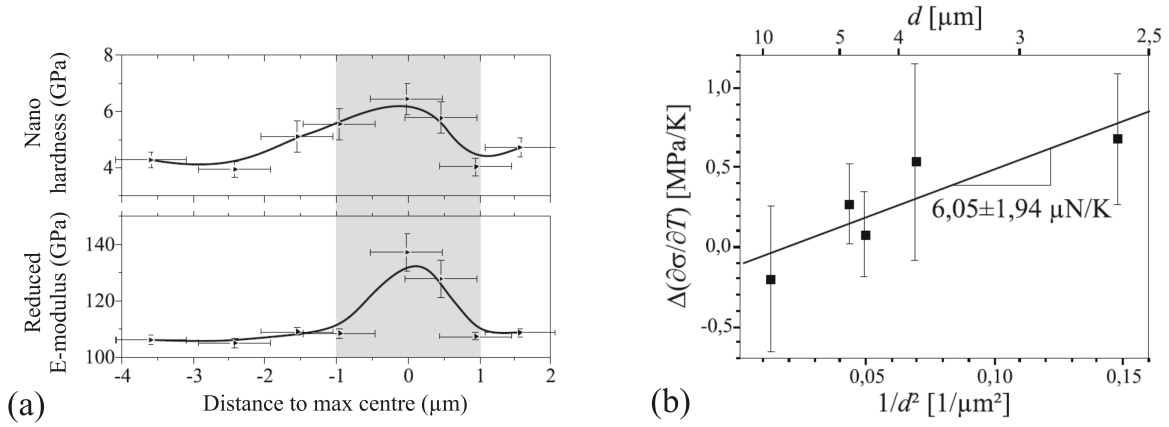


Figure 1.2.: Local variation of indentation hardness and reduced elastic modulus between adjacent min and max positions (a). Wafer-bow results of the global elastic behaviour of large-area LIMET treated Ni/Al multilayers plotted as a function of $1/d^2$ with linear regression following Jäger´s bone model (taken from [19]).

Performing wafer-bow measurements on entirely LIMET-structured samples with individual periodicities d between 2.5 and 10 μm, it was attempted to substantiate the presence of a scaling law [19]. Plotting the results of the global thin film stiffness as a function of $1/d^2$, as shown in figure 1.2(b), and assuming a linear relation, Daniel concluded that a composite behaviour along the lines of Jäger´s prediction for natural bone [20] was confirmed for LIMET-processed metallic thin films [19]. Seen in conjunction with the microstructure present, the measured local mechanical effects were to be attributed mostly to the high speed deformation introducing compressive residual stresses and an anisotropic grain growth close to the multilayer surface, especially taking place in Al layers [19].

In hindsight, the appraisal of the global behaviour remains controversial considering that the interpretation of the linear fit to the wafer-bow data in figure 1.2(b) was rather optimistic[2]. In turn, the locally achieved spatially varying modulation of the elasticity and the hardness (figure 1.2(a)) seems to be a promising achievement for potential applications. Yet, even their conclusive interpretation is difficult in light of the commonly known boundary conditions for nanoindentation experiments. Especially the lacking through reaction poses a problem, since the stress field induced by the indenter tip is evidently not confined to a single grain. It interacts with a combination of different phases and interdiffusion zones atop unaffected multilayer structures, thus generating a convoluted signal [63].

1.3. Objectives and organisation of the thesis

Considering these results it is clear, that the former thesis was mostly concerned with elaborating the potentials of LIMET regarding an application-oriented property modification. However, its scope did not address more basic theoretical issues necessary to evolve this processing technique into a reliable tool for the manufacture of architectured materials. The thesis presented here aims at achieving this by focusing on the following topics:

1. Identifying the ideal conditions to achieve a heat-affected zone spanning the whole thickness of the multilayer and finally effecting a *homogeneous through-reaction* of the constituent elements. To this end, the parameters governing the processing need to be varied systematically both experimentally and in thermal simulations. Thus, the combination of periodicity d and fluence F as well as material selection

[2]During his discussion, Daniel ascribed this to the problem with the idealised assumption of a phase being infinitely stiff in comparison to its matrix which can obviously not be fulfilled for metallic materials.

concerning both the multilayer and the underlying substrate are in focus [42][27].

2. Identifying the *physical processes* determining the microstructural modification achieved by the localised laser heat treatment in metals. In order to achieve this, the correlative use of characterisation techniques allowing for high resolution chemical, structural and microstructural analysis on the nm-μm length scale in question here is necessary.

3. Comparing the relation between the LIMET-induced heat-affected zones as measured in microstructural characterisation and their FEM-estimated dimensions. Up to now, this has been only rarely systematically and conclusively analysed. As the theses of Lasagni and Daniel describe [19][60], their simulations of the microscopic spatial and temporal temperature distribution did not include free energies of mixing or heats of formation which are released during the intermixing process while melting or the solidification of phases. Overcoming this flaw would generate *more realistic simulation data* allowing for reliable à priori knowledge on the attained dimensional modification.

4. Joining the obtained data on microstructural modification concerning dimensions, morphology, local chemistry and present phases with well-established theories on non-equilibrium processes. A deeper coverage of the extensive research on the kinetic and thermodynamic implications of resolidification seems a logical vantage point for further development. As described in the previous section 1.2, current literature already offers a considerably large body of information dealing with laser-induced rapid solidification processes. It thus is intended to identify parameters governing microstructure and phase selection, like *solidification velocity*, and their relation to the processing parameters accessible by LIMET and specimen design.

To tackle the first set of issues, the material basis of the multilayer-substrate system is enhanced. The choice of the substrate material with respect to its thermal diffusivity

holds the key to investigate the heat propagation in its duration as well as in its lateral and depth expansion. Still, the substrate has to fit to the needs of MEMS, reason for which fused silica (a-SiO_2), silicon nitride (a-Si_xN_y) and sc-Si are chosen [64]. They encompass two orders of magnitude of thermal conductivity, thus enabling a systematic scrutinisation. Also, the combination of multilayer constituents is revised. Here, besides the technical applicability, the constituents´ individual melting points and thermal diffusivities as well as their binary equilibrium phase diagrams play a role. Strictly, the latter are not applicable to explain phase formation in the case of ns-pulsed laser heating of thin films, which both represent situations of strong non-equilibrium. Nevertheless, they and their associated free energy characteristics may prove useful as a guideline in the interpretation of the resulting microstructure and phase composition. To this end, Ni/Al, Ti/Al and Ni/Ti were selected as multilayer systems to be studied, each representing a well-investigated binary system with a wide range of technical uses. Special interest is laid on the Ni/Al system, since it forms the main basis for comparison with the results from former theses.

The second set of questions is strongly related to the ability to perform site-specific and unequivocal analyses with respect to the attained structural, microstructural and compositional modification. Those in turn need to be compared to the results of the FEM thermal simulations. Special attention is given to the complementary use of TEM and, for the first time in context with LIMET, APT[3]. In the end, it is only the thorough correlation of the results of both the microstructural investigation and the thermal simulation that holds the clue to the successful explanation of the local processes induced by laser irradiation. Therefore, a *correlative microscopy approach* is pursued in this thesis.

[3]First results of this approach performed on Ti/Al multilayers have already been published by the author in [65].

Part II.

Theoretical part

2. Laser-matter interaction

The use of laser radiation to manipulate the surface properties of materials is motivated by its unique characteristics and by the multitude of processes which can be activated by its interaction with matter. Said properties can be summarised as monochromacity, tunability, high degree of spatial and temporal coherence, high directionality and high energy density. The latter are complex in nature and depend on the relation between processing parameters - like laser intensity and pulse duration - and material-related threshold values as well as characteristic time and length scales of the process involved. These include absorption leading to heating, melting, evaporation and plasma formation. Material transport in the form of diffusion or convection can be induced, enabling modifications to the chemical composition necessary for alloying and induction of phase transitions among others [66][67][68].

Since lasers have been used in technical applications for decades, the focus of the present theoretical chapter is not placed on a detailed description of the generation of laser radiation[1]. However, the role of a laser as a source of heat shall be elucidated, as well as the associated boundary conditions. Special attention will be given to the interaction of laser radiation with metals, main material class of this thesis, and to the behaviour of thin films, whose reduction in one length scale results in differences with respect to bulk properties.

[1]The reader may consult the following references as introductory treatises to this area: [69][70][71].

2.1. Absorption of light in metals

The energy transported by an electromagnetic wave is equally distributed among its electric and magnetic components. It can be calculated by introducing the *Poynting vector* which represents the instantaneous energy flux per unit area and unit time. Since the frequency ν of optically relevant electromagnetic fields is on the order of 10^9 to 10^{18} Hz, a direct measurement of the instantaneous magnitude of the Poynting vector is not possible. Nevertheless, its time-average[2] is experimentally accessible:

$$\langle \vec{S} \rangle_{\Delta t} = \frac{c^2 \epsilon_0}{2} |\vec{E}_0 \times \vec{B}_0| \tag{2.1}$$

with $\vec{E}_0$ and $\vec{B}_0$ as magnitudes of the electric and magnetic field components. As indicated by the vector product, the energy of the electromagnetic wave in vacuum propagates in a direction $\vec{k}$ perpendicular to the plane formed by $\vec{E}$ and $\vec{B}$. Equation 2.1 gives the net energy flux per unit area, which is also called *intensity* I[70]:

$$I \equiv \langle \vec{S} \rangle_{\Delta t} = \frac{c^2 \epsilon_0}{2} |\vec{E}_0|^2 \tag{2.2}$$

In the presence of matter, both components of the electromagnetic field are altered according to the electric and magnetic properties of the material. This means that electric dipoles, magnetic moments, polarisation charges and induced currents can be caused by interaction [72][73].

As the last paragraphs of the section above infer, the interaction of light and matter is related to the ability of matter to create polarisation under an electric field and to produce a net magnetic moment per volume under a magnetic induction. Looking at a single electron being the smallest buliding block of matter, the force $\vec{F}$ exerted by an electromagnetic field is calculated according to the *Lorentz force*. Since the electrical

[2]The time-average of a harmonic function in a time interval Δt is given by

$$\langle f(t) \rangle_{\Delta t} = \int_{t+\Delta t/2}^{t+\Delta t/2} f(t) dt = \langle \exp[i\omega t] \rangle_{\Delta t} = \mathrm{sinc}\,(\omega \Delta t/2) \exp[i\omega t]$$

.

field magnitude surpasses that of the magnetic field by several orders of magnitude, the latter field component can be neglected. Using a plane wave solution it is clear, that the electric field stimulates the electron to enforced harmonic oscillations having the same frequency. This corresponds to the electron absorbing the energy of the wave. Hence, the atomic response to the interaction with an electromagnetic wave, is over a large part of the spectrum determined by its electrons. In the case of dielectrics where electrons are bound to the atoms, *Lorentz theory* describes the optical behaviour [70][74][68]. A part of the electrons in metals are free or only loosely bound, which is accounted for in *Drude theory*. As a first approximation to the response of metals, only the contribution of the conduction electrons is considered [75][70][74]. Without going into a detailed derivation on how electric conduction currents are considered, the dispersion relation of metals is formulated to

$$n^2(\omega) = 1 + \frac{\sigma_e/\epsilon_0}{i\omega\left(1 + i\omega\frac{1}{\gamma_e}\right)} = 1 + \frac{\sigma_e/\epsilon_0}{i\omega\left(1 + i\omega\frac{Nq_e^2}{Vm_e\sigma_e}\right)} \tag{2.3}$$

including angular frequency of the electromagnetic wave ω, the average frequency of thrusts between conduction electrons γ_e, electric conductivity σ_e and vacuum dielectric constant ϵ_0 [74][70]. Actually, the complex index of refraction n is a complex and anisotropic value, since it is linked to relative permittivity ϵ_r representing the polarisability of a medium via

$$\epsilon_r = \epsilon_{r,re} - i\epsilon_{r,im} \tag{2.4}$$

written in scalar form which transforms to

$$n^2 = \epsilon_r = (n_{re} - in_{im})^2 \tag{2.5}$$

where the imaginary part n_{im} represents the attenuation of an electromagnetic wave when propagating in matter due to the energy dissipation in atomic oscillators. Take for example a linearly polarised electromagnetic wave propagating in the z direction with its electric field vector parallel to x:

$$\vec{E} = E_{0,x}\exp\left[i\omega\left(t - \frac{n_{re}z}{c}\right)\right]\exp\left[-\frac{\omega n_{im}z}{c}\right] \tag{2.6}$$

The first exponential function in equation 2.6 has a complex argument, thus representing an oscillating wave propagating in the z direction with velocity c/n_{re}. On the contrary, the argument of the second one is real resulting in an exponential decay. Calculating the intensity of this wave according to equation 2.2 yields

$$I \propto \left(\exp\left[-\frac{\omega n_{im} z}{c}\right]\right)^2 = \exp\left[-\frac{2\omega n_{im} z}{c}\right] = \exp\left[-\beta z\right] \tag{2.7}$$

with the absorption coefficient β as known from *Lambert-Beer´s law* [72][70]. To get a feeling for the optical behaviour of metals, it is instructive to perform a case-by-case analysis of equation 2.3 with respect to the frequency ω of the perturbing wave:

1. Small ω (i.e. $\omega \ll \gamma_e$ and $\omega \ll \sigma_e/\epsilon_0$): In this case, the real and imaginary parts of n become equal with $n_{re} = n_{im} = \sqrt{\sigma_e/2\epsilon_0\omega}$. Introducing this into our example of an attenuated electromagnetic wave in equation 2.6 we can see, that an imaginary part this large yields a strong attenuation of the wave in metals. Again looking at equation 2.7, we can calculate the depth δ at which the intensity of the wave is only $1/e$ of its original value:

$$\delta = \sqrt{\frac{2\epsilon_0 c^2}{\sigma_e \omega}} \tag{2.8}$$

   Per definition, this corresponds to the *penetration depth* of electromagnetic waves in metals[3], also called *skin depth*. For UV radiation δ is on the order of sub-nm, while for IR several nm can be reached [70].

2. Very large ω (i.e. $\omega \gg \gamma_e$): Here, the electrons are forced to perform a large number of oscillations in between two thrusts. Therefore, the damping effect γ_e can be neglected, making $n^2(\omega)$ a real value with

$$n^2(\omega) = 1 - \frac{N}{V}\frac{q_e^2}{m_e \epsilon_0 \omega^2} = 1 - \left(\frac{\omega_p}{\omega}\right)^2 < 1 \tag{2.9}$$

   with number of atoms N within a volume V. $\omega_p = \sqrt{N q_e^2 / V m_e \epsilon_0}$ represents the *plasma frequency* as a characteristic threshold for metals which is situated

[3]Hence, the inverse of β from equation 2.7 is the *penetration depth*.

approximately in the UV and X-ray regions of the spectrum. For values of ω above ω_p, the aforementioned relation for $n^2(\omega)$ remains valid, which means that the metal is transparent to the wave and the absorption is low; otherwise, the refractive index remains a complex value and the wave is attenuated [74][70].

Summarising these theoretical considerations, it can generally be stated that the interaction of light, including the monochromatic laser light used in this thesis in particular, strongly depends on the electronic structure of the processed material. The grade of absorption, and consequenty the generation of heat, depends on the convenient choice of the frequency ω, or (via $\omega = 2\pi c/\lambda$) the wavelength λ, of the applied laser light according to the material properties. Since metals are of foremost interest here, ϵ_r, σ_e and ω_p are of importance.

The presented treatment implicitly assumed that the electromagnetic wave under investigation was travelling in an infinitely-stretched and homogeneous medium. In reality electromagnetic waves propagate through different media j, each with a complex refractive index n_j. At every medium *interface*, light can be *reflected* (ref), *absorbed* (abs) and *transmitted* (trn). While propagation in a medium is governed by the refractive index, the optical behaviour at the interfaces is given by the length over which the optical properties change from one medium to another. If this change happens over a distance of several wavelengths of the used radiation, the amount of reflection is generally low. In the present case of a wave approaching the interface between air and metal, the properties change abruptly in under a wavelength promoting the aforementioned interface effects [74][70]. Our main interest in using laser light lies in delivering energy to a material in order to heat it up.

Particularly the *reflectivity* R of a surface needs to be discussed, since it reduces the *absorbance* A and *transmittance* T. This can be readily understood by formulating

energy conservation at an interface irradiated by light with intensity I_0:

$$1 = \frac{I_{ref}}{I_0} + \frac{I_{abs}}{I_0} + \frac{I_{trn}}{I_0} = R + A + T \tag{2.10}$$

which reduces to

$$1 = R + A \tag{2.11}$$

when the material thickness is significantly larger than the optical penetration depth as calculated by equations 2.7 or 2.8. Since the latter holds for the present case where also the laser beam impinges almost parallel to the surface normal, we will continue using relation 2.11 [69].

2.2. Laser as a heat source and heat transfer in matter

Up to this point, light has been considered as continuous wave. Laser light sources, however, produce pulsed radiation: even in continuous wave (cw) lasers, where the time between two pulses is very short [69]. Hence, the interaction cannot be viewed as being static, but rather a transient process. Whether a laser can be used as a heat source, strongly depends on the duration τ_p of a pulse and the characteristic time scale of the prevailing thermalisation mechanisms in the material. Since metals absorb via their conduction electrons, their interaction with each other and with lattice vibrations, quantised as *phonons*, governs the heat generation and transfer. In the first case of absorbtion, the time between two collisions $\tau_e = 1/\gamma_e$ is on the order of 10^{-14} s to 10^{-12} s, while in the second case a relaxation time τ_{e-ph} of 10^{-12} s to 10^{-10} s can be estimated. If the excitation duration, here τ_p, is smaller than the relaxation time, we speak of a *non-thermally activated* or *photochemical process*. Otherwise, a *thermally activated* process can be induced. A combination of both types is referred to as *photophysical* [76][67]. In the present case, we are dealing with thermally activated processes due to the use of a laser with τ_p =10·10^{-9} s.

The localised thermal processing of thin metallic multilayers with such a laser radiation requires the use of comparatively low or medium intensities (see section 5.2.2) in order to hinder the vaporisation of the coating. In this intensity range, the laser can be treated as a heat soure located directly at the sample surface and all the light energy absorbed by the medium assumed transformed to heat. According to the Poynting vector as defined in equation 2.2, the term describing a heat source is

$$\begin{aligned} Q(\vec{r},t) &= -\nabla\langle\vec{S}(\vec{r},t)\rangle_{\Delta t} + U(\vec{r},t) \\ &= -\nabla I(\vec{r},t) - U_{rad} - U_{conv} + U_{trans} \end{aligned} \tag{2.12}$$

with $U(\vec{r},t)$ accounting for heat variation due to processes which accompany the laser treatment or are even induced by it [67]. Besides reflection, whose effects on the term $I(\vec{r},t)$ will be discussed later on, energy loss can take place at the surface via emission of radiation U_{rad} and convection U_{conv} in the surrounding gaseous medium. The first contribution is described using the *Stefan-Boltzmann law* of radiation

$$U_{rad} = A\epsilon\sigma\left(T^4 - T_{amb}^4\right) \tag{2.13}$$

with σ the Stefan-Boltzmann constant, A the surface area of the sample, T_{amb} the ambient temperature and ϵ the surface emissivity (≈ 1 for black surfaces) [77]. The convection loss, due to the thermal conduction of the fluid together with its particle motion, presents a more labourous calculation [78]. Here, *Newton´s empirical cooling law* is introduced

$$U_{conv} = \alpha_{conv} A\Delta T \tag{2.14}$$

where α_{conv} represents the heat transfer coefficient, which is independent of the material´s properties. It must be experimentally determined for each condition since it mostly depends on the geometry of the material-fluid system (especially its roughness), the surface temperature distribution and the thin laminar fluid film next to it [77]. These effects can be omitted to some degree when using pulsed laser radiation [79]. The

ns-pulsed laser used in this thesis produces a linearly polarised, monochromatic electromagnetic wave in approximate normal incidence (z direction) on the material´s surface. The function describing the absorbed intensity $I(\vec{r},t)$ can be formulated as

$$I(\vec{r},t) = I(x,y,z=0,t)\,(1-R)\,A(z)P(t) \tag{2.15}$$

where the reflectivity R accounts for the lateral intensity distribution at the surface as in equation 2.11, $I(x,y,z=0,t)$[4], the factor $A(z)$ represents the depth attenuation according to Lambert-Beer´s law in equation 2.7

$$A(z) = \exp\left[-\beta z\right] \tag{2.16}$$

and $P(t)$ introduces the effect of a finite pulse duration τ_p

$$P(t) = \frac{1}{\varsigma\sqrt{2\pi}}\exp\left[\frac{-(t-t_p)^2}{2\varsigma^2}\right]. \tag{2.17}$$

The laser pulse is assumed Gaussian over time, impinging on the surface at time t_p with a variance of $\varsigma = \tau_p/2\sqrt{2\ln(2)}$ [67][79][80].

In the absence of (s)-(l) phase transitions in a solid, the heat transfer away from the irradiated region is governed by *heat conduction*. The present case of pulsed heating is a transient excitation and requires the introduction of *thermal diffusivity* $\underline{\underline{D_{th}}}$ in the description of this non-stationary phenomenon[5] [81][82]. Considering a single, homogeneous and isotropic material, the thermal diffusivity is defined as scalar

$$\underline{\underline{D_{th}}} = \frac{\underline{\underline{\lambda_{th}}}}{\rho c_P} \cong \frac{\lambda_{th}}{\rho c_P} = D_{th} \tag{2.18}$$

with a density ρ, and the specific heat capacity c_P at constant pressure. Thus, D_{th} is the ratio of propagating to stored heat, through and inside a volume, respectively [82]. For

[4]If the interaction of only one beam is of interest, a gaussian shape perpendicular to the propagation direction z is selected, which holds for TEM_{00} rays [69].

[5]The thermal conductivity $\underline{\underline{\lambda_{th}}}$ is used, counterintuitively, only when the temperature is constant over time and the heat capacity per unit volume $C = \rho c_P$ holds for static problems, where the temperature is independent of position and time.

a Gaussian thermal energy distribution both in space and time, the $1/e$ spatial decay of the temperature distribution is described by the *thermal diffusion length*

$$l_{th} = 2\sqrt{D_{th}\tau_p} \tag{2.19}$$

This characteristic length plays a role in determining which directional component of the heat flow dominates in a homogeneous material. l_{th} is compared with other characteristic dimensions: the optical penetration depth $1/\beta$ and the dimensions of the laser-irradiated area, for depth and lateral propagations, respectively [67]. Multilayered materials, in contrast, must be treated as composites: conglomerates of different materials and thermal properties. In this case, the thermal waves transporting the heat undergo reflection and transmission at each interface analogous to electromagnetic waves (see section 2.1). The *equivalent thermal behaviour* of a homogeneous material can be calculated for a multilayer using convenient rules of mixture and serial/parallel circuit models, which will be shown in the following assuming a diphase multilayer with volume fractions ν_1 and ν_2. According to equation 2.18 ρc_P must be replaced by an effective heat capacity per unit volume

$$(\rho c_P)_{eff} = \nu_1\rho_1 c_{P,1} + \nu_2\rho_2 c_{P,2} = \nu_1\frac{\lambda_{th,1}}{D_{th,1}} + \nu_1\frac{\lambda_{th,1}}{D_{th,1}} \tag{2.20}$$

following a simple rule of mixture. The thermal conductivities parallel (lateral) and perpendicular (depth) to the layer´s surface follow the composite models of *Voigt* and *Reuss*[6], respectively:

$$\lambda_{th,lat} = \nu_1\lambda_{th,1} + \nu_2\lambda_{th,2} \tag{2.21}$$

$$\frac{1}{\lambda_{th,dep}} = \frac{\nu_1}{\lambda_{th,1}} + \frac{\nu_2}{\lambda_{th,2}} \tag{2.22}$$

[6]The analogy to mechanical models holds, when the elastic moduli in both models are replaced by *thermal effusivity* $e_{th} = \lambda_{th}/\sqrt{D_{th}}$ representing a material´s ability to exchange heat with its environment [81].

Consequently, equation 2.18 is modified to account for those orientational dependencies [81][83][82]:

$$D_{th,lat} = \frac{\nu_1\lambda_{th,1} + \nu_2\lambda_{th,2}}{\nu_1\frac{\lambda_{th,1}}{D_{th,1}} + \nu_1\frac{\lambda_{th,1}}{D_{th,1}}} \tag{2.23}$$

$$\frac{1}{D_{th,dep}} = \frac{\nu_1^2}{D_{th,1}} + \frac{\nu_2^2}{D_{th,2}} + \nu_1\nu_2\left(\frac{\lambda_{th,2}}{\lambda_{th,1}D_{th,2}} + \frac{\lambda_{th,1}}{\lambda_{th,1}D_{th,1}}\right) \tag{2.24}$$

Concluding these theoretical considerations, a statement as to the experimental reality is necessary. All material properties related to optical and thermal response, are strictly a function of the temperature. Thus, the material under laser processing will alter its behaviour during the treatment due to temperature change. This can only be accounted for when experimental data on individual thermal dependencies is given in literature (see section 5.3). Changes also arise, when the dimensions of the material are significantly reduced, e.g. thin films. In this case, l_{th} needs to be compared with the mean free path of free electrons and phonons in confined media [67].

3. Rapid solidification and phase formation

As discussed in the previous chapter, melting induced by pulsed laser irradiation gives rise to resolidification and phase formation on short time scales. The theoretical framework necessary to understand and describe the resulting microstructure goes well beyond classical textbook knowledge on conventional solidification theories, as will be shown in this chapter. Especially the complex interplay between compositional and thermal distributions at the liquid-solid interface as well as the kinetic and thermodynamic implications associated with high processing velocities effect strong deviations from equilibrium. This can only be explained by enhancing the common theories which came about during the 1960s and the following three decades. Throughout this development, two different processing approaches to rapid solidification were introduced, which differ in the thermal conditions imposed on the melt: *atomisation*, where the liquid phase is significantly undercooled prior to solid nucleation; and *substrate quenching*, where a high amount of heat extraction from the melt plays a decisive role [84].

Although the cooling rates associated with those processing routes (10^4 to 10^7 K/s) exceed the 10^2 K/s of conventional chill casting by several orders of magnitude, Jacobson et al. emphasise in their review on this topic, that a distinction based on the cooling rate alone is not reasonable [84][37]. Instead, deviations from commonly encountered microstructure formations and morphologies are in focus, achievable by large solid-liquid interface velocities associated with high cooling rates together with suppressed nucle-

ation at lower ones. Generally, the developed processing techniques allow for a certain degree of control over heat introduction and its subsequent removal as well as local stoichimetry. These factors, in turn, together govern the resulting formation and morphology of microstructure and phases [84][68]. Hence, research led not only to a more systematic and profound understanding of the mechanisms of phase selection, nucleation and grain growth as a function of the solidification velocity, it had a strong impact on the study of metastable phases, be they amorphous or crystalline [85][36][86][87]. To some extent, 2011´s Nobel prize in chemistry awarded to Daniel Shechtman (Technion, Haifa) for his discovery of quasicrystals in rapidly solidified Al alloys can be seen as recognition for the outstanding efforts in this field [88][89].

Since the research field of rapid solidification spans all relevant material classes and a multitude of individual processing techniques, the aim of the present chapter is solely to give a comprehensive summarisation of its aspects associated with pulsed laser-based techniques and processing of metallic bulk and thin film systems. Laser-induced resolidification during surface alloying, melt quenching or welding can be attributed to the substrate quenching techniques and is particularly of interest due its cooling rates exceeding $10^9\,\mathrm{K/s}$. The scope of this topic is covered in the following journal reviews [25][90][35][84][91] and basic textbooks on materials science [37][92][93] as well as on laser processing [68], which served as basis for the oncoming sections.

3.1. Nucleation and growth

The concept of solidification and the associated processes of nucleation and growth are recapitulated in various textbooks on physical metallurgy. As foundation for the following discussion, the descriptions given in [93] and [92] were consulted and briefly summarised here. This section aims at highlighting the generally known aspects of solidification under comparatively low transformation rates. On the contrary, the following section 3.2 introduces the alterations necessary when considering rapid solidification processes.
Since solidifying corresponds to the advance of the solid (s) into the liquid (l) phase, one needs to understand the atomistic processes associated with the movement of the interface. Those mechanisms hold for all processes in physical metallurgy which are based on nucleation and growth. Assuming a thermodynamic equilibrium at the melting temperature T_m, where the free energy of both phases is the same ($G_{(s)} = G_{(l)}$), the disturbance introduced by the presence of the interface creates an excess free energy $\gamma_{(s)-(l)}$ at the location of the (s)-(l) interface.
The type of interface a system presents depends on its possibilities to minimise this excess energy. As a rule of thumb, a criterion was derived based on the ratio between the latent heat of melting ΔH_m and T_m, which equals the *entropy of melting* ΔS_m. Jackson et al. argued that systems whose ratio is larger than $4R$ are likely to exhibit flat interfaces. This is the case for most single-component semiconductors and intermetallic compounds. Metals and their alloys on the contrary fall short of this critical value with $\Delta H_m/T_m \approx R$, thus leading to rough interfaces, where potentially all interface sites may serve as sites for crystallisation events [94][34].

3.1.1. Nucleation

During the nucleation of a new phase, an interface is created which then migrates into the parent phase during its growth. The growth of (s) can be subdivided into two limiting cases. If the chemical composition of the phases is the same, the growth of the

new phase is limited only by the ability of the atoms to cross the interface. Should the rate of these jumps be low, an *interface-controlled* process occurs: atoms impinging the (s)-(l) interfaces encounter a limited number of potential accommodation sites and only find a place in the advancing (s) through *ledge growth* as is typical for sharp interfaces. Conversely, if the jumps over the interface are fast and easy, growth is limited only by the necessity to transport atoms via long-range diffusion to the newly formed phase. This *diffusion-controlled* process has a higher accommodation possibility for incoming atoms, as is known from rough interfaces. Such a *continuous growth* solidification leads to differing product compositions. In order to get a mathematical grip on the propagation of the advancing (s)-(l) front, a *rate theory* is applied as will be discussed in more detail in section 3.2.1.

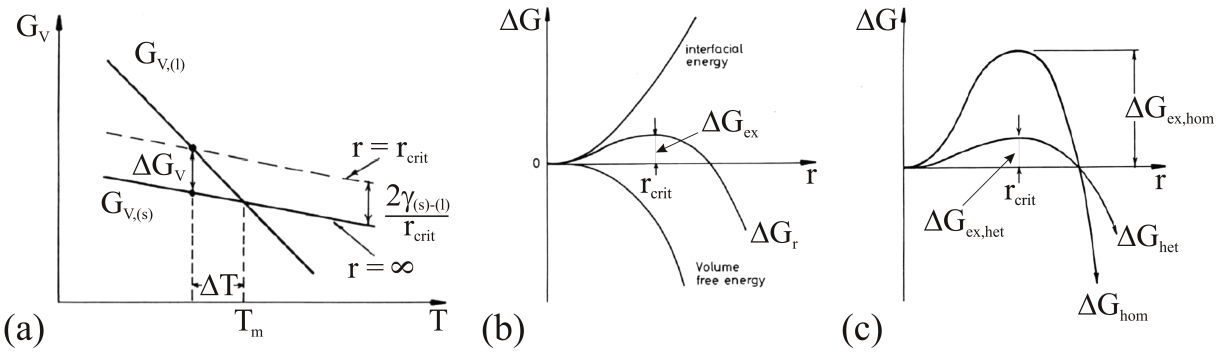


Figure 3.1.: Change in volume free energy (a) in dependence on temperature in (s) and (l) and change in free energy (b) during homogeneous nucleation of a sphere with radius r. (c) schematically shows the energetic difference between homogeneous and heterogeneous nucleation (all modified from [93]).

Soldidification initiates with the formation of stable (s) nuclei in the (l) phase through a statistical process where atoms in (l) join together to form sufficiently large clusters or embryos. To this end, sufficient undercooling ΔT_i is needed at the (s)-(l) interface of (l) with respect to T_m in the case of pure metals or the liquidus temperature T_{liq} in the

case of alloys (see figure 3.1(a)). From a free energy standpoint, nucleation can be seen as a competition between the released free energy ΔG_V per unit volume of (s) formation in thermodynamic equilibrium[1]

$$\Delta G_V = G_{V,(l)} - G_{V,(s)} = \frac{\Delta H_{m,V} \Delta T_i}{T_m} \tag{3.1}$$

and the energy consumed by the creation of a new interface $\gamma_{(s)-(l)}$:

$$\Delta G_r = \left[-\frac{4}{3}\pi r^3 \Delta G_V + 4\pi r^2 \gamma_{(s)-(l)} \right] \cdot s(\theta) \tag{3.2}$$

where ΔG_r is the change in free energy due to nucleation of a sphere with radius r, as depicted in figure 3.1(b). Factor $s(\theta)$ accounts for the influence of nucleating agents like nucleants or mold walls by lowering the energy barrier set up by the excess free energy ΔG_{ex} of (s) clusters (c.f. figure 3.1(c)):

$$\Delta G_{ex} = \frac{16\pi\gamma^3_{(s)-(l)}}{3\Delta G_V} = \left(\frac{16\pi\gamma^3_{(s)-(l)} T_m^2}{3\Delta H^2_{m,V}} \right) \cdot \frac{s(\theta)}{(\Delta T_i)^2} \tag{3.3}$$

where

$$s(\theta) = \frac{1}{4} \left(2 + \cos(\theta)\right) \left(1 - \cos(\theta)\right)^2 . \tag{3.4}$$

and $0 < s(\theta) \leq 1$. Angle θ stems from the wetting behaviour between (l) and (s) expressed in terms of the balance of their interfacial tensions. In absence of nucleants, $s(\theta) = 1$ and *homogeneous nucleation* is attained. All other values of $s(\theta)$ yield a reduction in the nucleation energy barrier, which is associated with *heterogeneous nucleation*. The critical radius r_{crit} of a stable nucleus is the same for both situations (see figure 3.1(c)) and calculates to

$$r_{crit} = \frac{2\gamma_{(s)-(l)}}{\Delta G_V} = \frac{2\gamma_{(s)-(l)} T_m}{\Delta H_{m,V} \Delta T_i}. \tag{3.5}$$

which corresponds to a free energy increase due to capillarity described by the *Gibbs-Thomson effect*. Obviously, good wetting behaviour (low values of wetting angle θ)

[1] The underlying assumption concerning the entropy of melting $\Delta S_{m,V} = H_{m,V}/T_m$ strictly holds for $T = T_m$, but is also employed as an approximation for temperatures other than T_m [68].

goes hand in hand with improved nucleation[2]. This effect can be exploited deliberately in order to influence the phase selection during solidification. As studies of Herlach and coworkers revealed, bringing an external *nucleation seed* in contact with the melt helps to circumvent spontaneous nucleation by offering energetically more attractive heterogeneus nucleation sites. Clearly, the seed material needs to be chosen such that it resembles closely the structure of the intended solidification product [95][96]. Moreover, r_{crit} is affected only by the amount of melt undercooling. Since this effect has a significant influence on the formation of the microstructure resulting from rapid solidification, its implications on free energy are discussed in section 3.2.

3.1.2. Growth

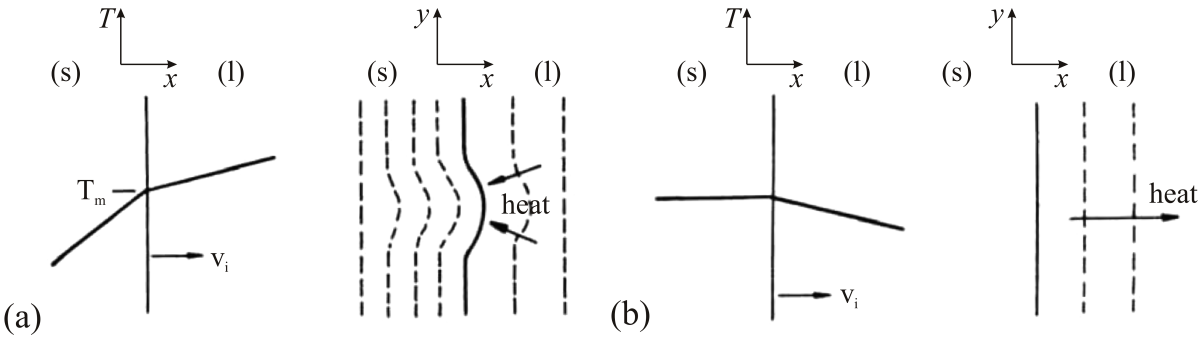


Figure 3.2.: Schematic situation at a (s)-(l) interface when (a) heat is extracted into (s) and (b) heat is conducted into a supercooled liquid: temperature distribution (left) and associated isotherms (right) (modified from [93]).

So far, growth has only been adressed with respect to different modes in which atoms accommodate into (s)-(l) interfaces. A description of the crystal growth process itself affords a closer look at the thermal and compositional situation directly at and around the moving interface. It is clear that alloy solidification needs a treatment that deals

[2]If θ=0 °, the above mentioned wetting model is invalid.

with both parameters, while a pure solid depends solely on the thermal distribution. For the sake of simplicity, we first deal with this case assuming a planar boundary between (s) and (l). Equation 3.1 gives the driving force for solidification in thermodynamic equilibrium. Therein, the necessary condition for solidification is evidently related to the interfacial undercooling ΔT_i, which here is created only by the contribution of the thermal conditions in the melt (*thermal undercooling* ΔT_{th}).

As described in the introduction to this chapter, there are two different processing approaches for rapid solidification: atomisation and substrate quenching. The main difference lies in the direction of the thermal gradient perpendicular to the interface, and thus the heat flow, across the phase boundary. Figures 3.2 (a) and (b) directly compare the respective interfacial situations. In (a), the thermal gradient in (l) at the interface is positive ($\nabla T_{i,(l)} > 0$) leading to a heat flux from the superheated (l) to (s) as encountered in substrate quenching. (b) on the contrary depicts a negative gradient ($\nabla T_{i,(l)} < 0$), and thus a heat flow into the undercooled (l) characteristic for atomisation methods. The *interfacial growth rate* v_i then follows for both cases by calculating the balance of heat flows at the interface:

$$\lambda_{th,(s)} \cdot \nabla T_{i,(s)} = \lambda_{th,(l)} \cdot \nabla T_{i,(l)} + v_i \cdot \Delta H_{m,V} \tag{3.6}$$

where the heat flow ($\lambda_{th,(\cdot)} \cdot \nabla T_{i,(\cdot)}$) in (s) and (l) as well as the latent heat of melting per unit volume $\Delta H_{m,V}$ released during the solidification at the interface are taken into account[3]. Hence, the solidification rate v_i of a single component system is governed by the conduction of heat away from the (s)-(l) interface, resembling a competition between the release of latent heat and the rate of external heat extraction [25].

The different algebraic signs of $\nabla T_{i,(l)}$ in the aforementioned cases have direct consequences on the ability of the interface to maintain a planar front during propagation. All effects related to this behaviour are summarised under the term *interfacial stability*.

[3]Please be aware of the role of the algebraic sign of velocity v_i. Since our discussion deals with solidification, v_i is positive taking into account the coordinate system introduced in figure 3.2 (a). Negative values represent the case of melting [68].

In the event of heat extraction into (s), a planar interface can be sustained. Otherwise, interfacial stability is jeopardised since heat loss from (s) protrusions into the (l) locally increases the undercooling, thus yielding a preferential growth of this feature ahead of the interface. Finally, a microstructure consisting of *thermal dendrites* can be achieved, if there is a sufficiently large curvature of the unstable interface, making the Gibbs-Thomson effect no longer negligible. By this, a further contribution to ΔT_i is introduced

$$\Delta T_r = \frac{2\gamma_{(s)-(l)} T_m}{r \Delta H_{m,V}} = \frac{2\Gamma}{r} \tag{3.7}$$

where r represents the curvature radius of the destabilised interface and Γ the Gibbs-Thomson coefficient. Thus, this effect leads to a reduction of the melting temperature by *curvature undercooling* $\Delta T_r = T_m - T_i$. Due to the fact that the occurrence of interfacial instabilites is more pronounced in growth under rapid solidification conditions, a more in-depth treatment of the contributing factors will be given in section 3.2.

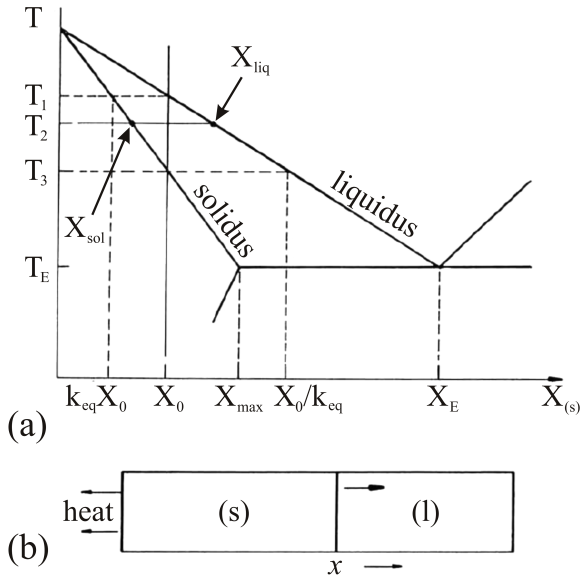


Figure 3.3.: Hypothetical binary phase diagram with linearised phase boundaries (a) and assumed idealised situation (b) for unidirectional planar solidification of an alloy with composition X_0 (modified from [93]).

Introducing even the slightest amount of a different type of atoms in the melt subjects the solidification process to the influence of chemical composition. The behaviour of a solidifying alloy is often discussed considering a simplifyed binary eutectic system, whose phase diagram exhibits linearised phase boundaries (see figure 3.3 (a)). Strictly, this simplification applies only to dilute alloys [37]. Following this approach, we take a look at a hypothetical alloy with a composition of X_0 (given in mole fractions of the solute atoms[4]). The ratio between the composition of the newly formed (s) and the (l), as given by the solidus and liquidus lines at X_0

$$k_{eq} = \frac{X_{(s)}}{X_{(l)}} \tag{3.8}$$

represents the *equilibrium partition coefficient*. A thermal condition at the interface, $\nabla T_{i,(l)} > 0$ shall be assumed (c.f. figure 3.3 (b)). Furthermore, three limiting cases can be distinguished depending on the spatial distribution of the composition $X_{(s)}$ of the newly formed (s). They differ in their thermodynamic stability leading to different possibilities of atomic exchange between (l) and (s):

1. Unhindered mixing in both phases, with a homogeneous (s) composition X_0. This can be achieved through very slow cooling, i.e. thermodynamic equilibrium.

2. No diffusion (s) but perfect mixing in (l) leads to a compositional distribution along the path travelled by the (s)-(l) interface. It is described by the *Scheil equations* which hold for local equilibrium.

3. No diffusion in (s) and only diffusional exchange in (l) is also able to create a homogeneous (s) composition X_0 over large parts of the distance travelled by the front under steady state growth conditions (depicted in figure 3.3 (c)).

Our discussion here shall be restricted to the third case, because it describes best the mechanisms present during rapid solidification. The conditions for atomic transport re-

[4]Unless stated otherwise, all concentrations given in the following represent the solute content in order to ensure a more clearly arranged notation.

quired for this case are achieved when the temperature drop occurs fast, thus impeding (s) diffusion. As for the (l) phase, no permanent convectional matter transport takes place, leaving solute atom diffusion as the only option. Therefore, solute atoms which are not built into (s) can only be transported away from the advancing solidification front by (l) diffusion. Consequently, the (l) directly ahead of the interface contains a growing amount of solute atoms leading to an increasing (s) content starting from $k_{eq}X_0$. As soon as the solidus temperature for X_0 is reached at the interface (T_3 in figure 3.3 (a)), the steady state is achieved with constant solidification rate v_i. The newly formed (s) then reaches a constant composition X_0, while the (l) adjacent to the front presents a concentration profile with a steep gradient from X_0/k_{eq} to X_0. During steady state growth, the concentration profile ahead of the moving front is maintained.

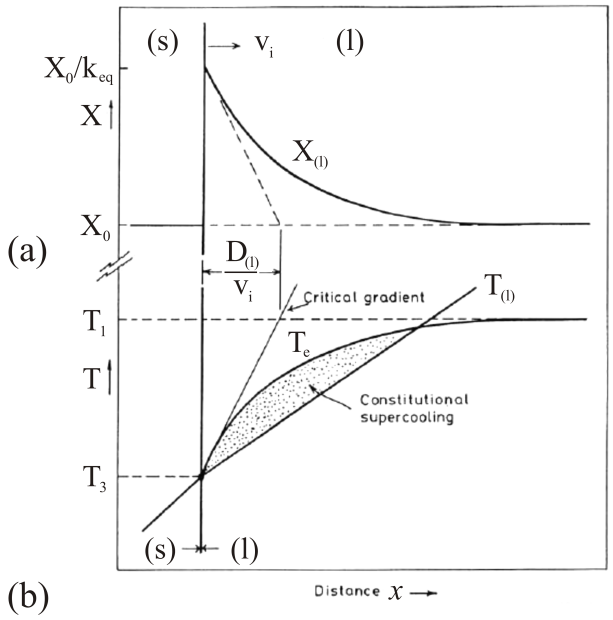


Figure 3.4.: Constitutional undercooling at a planar solidification front: composition profile during steady-state growth (a) and temperature profile $T_{(l)}$ (b) for heat extraction into (s) along with equilibrium liquidus temperature characteristic T_e (modified from [93]).

Analogous to the treatment of pure metal solidification, a flow balance at the interface can be formulated for the case of alloys. The following expression focuses on solute atom exchange across the front instead of heat flow:

$$-D_{(l)} \cdot \nabla c_{(l)} = v_i \cdot \left(c_{(l)} - c_{(s)}\right) \tag{3.9}$$

$D_{(l)}$ represents the diffusivity of the solute atoms at the given temperature and concentration gradient $\nabla c_{(l)}$ in (l). Equation 3.9 expresses the balance between the down-hill solute diffusion away from the front due to $\nabla c_{(l)}$ and the rate of solute rejection during solidification. The solution to this diffusion equation for the assumed planar growth, corresponding to unidirectional solidification (here in x direction), yields

$$X_{(l)} = X_0 \left(1 + \frac{1 - k_{eq}}{k_{eq}} \cdot \exp\left[-\frac{x}{(D_{(l)}/v_i)}\right]\right) \tag{3.10}$$

describing the (l) concentration profile moving with the solidification front. The denominator of the exponential function´s argument gives the width of the profile, which is reduced if convection is present in (l). There is another implication from the analogy between equations 3.6 and 3.9 and thus between pure metal and alloy solidification. The transfer of solute atoms into (l) in the second case corresponds in the first case to conducting latent heat $\Delta H_{m,V}$ in the same direction. By this, the thermal gradient $\nabla T_{i,(l)}$ at the interface is influenced locally, leading to interfacial instabilities which were already discussed. Figure 3.4 shows a schematic close-up view of the compositional (a) and thermal distribution (b) encountered at the (s)-(l) interface. When considered in conjunction with figure 3.3 (a), it becomes clear, that the increased amount of solute in (l) (c.f. equation 3.10) leads to a reduction of the liquidus temperature T_{liq} following the composition dependence of the liquidus line (see line T_e in figure 3.4 (b)). The actual temperature distribution in the melt $T_{(l)}$ remains unaffected. As introduced in this figure, a critical temperature gradient

$$\nabla T_{e,crit} = \frac{T_1 - T_3}{D_{(l)}/v_i} = \frac{T_{liq} - T_{sol}}{D_{(l)}/v_i} \tag{3.11}$$

can be defined and compared to the actual gradient $\nabla T_{i,(l)}$. For gradients larger than $\nabla T_{e,crit}$, planar solidification is kept stable. If the actual gradient falls below the critical one, the (l) ahead of the interface exists at a temperature below its T_{liq} and is thus undercooled. The amount of this *constitutional undercooling* introduced by chemical composition is $\Delta T_c = T_{liq} - T$. Moreover, the interfacial stability is compromised enabling the growth of protrusions. *Cellular structures* form depending on the decline of $\nabla T_{i,(l)}$, small gradients of which produce *dendrites*.

In the course of this section, several implications concerning solidification have been introduced which will prove useful when dealing with rapid solidification conditions. First, temperature distribution, interface curvature and chemical composition were shown to contribute to the undercooling necessary to create the driving force for the transformation:

$$\Delta T_i = \Delta T_{th} + \Delta T_r + \Delta T_c \tag{3.12}$$

Second, equations 3.10 and 3.11 show an evident influence of the solidification rate v_i on the growth process and the resulting microstructure. This velocity dependence is the first hint as to the rapid solidification mechanisms, to be discussed in the oncoming section. Furthermore, the processes of accommodating atoms into the moving (s)-(l) front cannot be neglected, making *interfacial kinetics* a critical factor especially when large velocities are involved.

3.2. Interfacial kinetics and metastable thermodynamics

For the further theoretical treatment of rapid solidification, the previous section introduced three decisive factors: undercooling ΔT_i, thermal gradient $\nabla T_{i,(l)}$ and solidification velocity v_i. Bormann argues in his review on non-equilibrium phase reactions, that it

is the (s)-(l) interface which governs the degree of undercooling and heterogeneous nucleation. Moreover, its mobility exerts more control over phase formation than their respective energetic stabilities do [86]. Aziz and coworkers, as well as Boettinger and Perepezko confirm this observation, when deriving functions for the local composition and temperature conditions at the moving interface [33][90][35][34][30]. Hence, it holds the key to approaching an explanation for the selection of phases and microstructure encountered in experiments. To this end, the first part of this section deals with the kinetic aspects of the accommodation of atoms into a front moving at high velocities. The other contribution consists of competing processes in nucleation and growth, which at the same time influence the microstructure evolution.

3.2.1. Interfacial kinetics

Most of the theoretical and experimental work related to non-equilibrium interface kinetics encountered in rapid solidification processes was performed from the 1970s to the mid-1990s. Especially the groups of Turnbull, Aziz, Perepezko, Boettinger, Thompson, Kurz and Trivedi contributed substantial insight to this field. Their work mostly concentrated on pure semiconductors or metals and dilute alloys of both[5]. Following the basic treatment of Aziz [33], a *rate theory* approach is employed to describe the atomistic processes at an advancing front. This is schematically depicted in figure 3.5 (a), where a one-dimensional movement is assumed. Both solute and solvent atoms in (l) independently jump across the interface and are built into (s). Rate theory then sums up the individual jump rates of both species to and from (s). The length of those jumps, assuming a convenient potential well in (s), is less than the distance denoted l_D (compare arrows 1 to 5 in 3.5 (a)). The latter is on the order of interatomic distances a_0 in (s) and corresponds to the length of diffusive jumps in (l) [33].

[5] *Dilute* refers in this context to alloys containing less than 10 % of solute atoms in order to maintain the approximation of linearised phase boundaries (c.f. figure 3.3 (a)) [34].

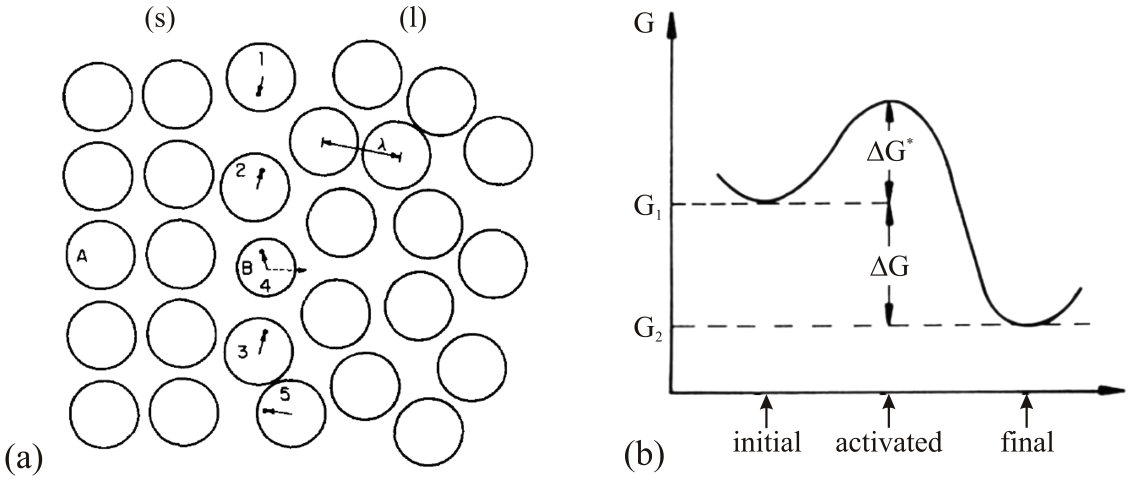


Figure 3.5.: Schematic atomic arrangement during growth of a solidification front from left to right (a) depicting the trapping a solute atom (no. 4) into (s) (taken from [33]). (b) general free energy characteristic for transformations involving an activated state of higher free energy (modified from [93]).

Solute atoms, such as no. 4 in the same figure, exhibit a different behaviour regarding their inclusion in (s) depending on the type of interfaces and thus the growth mode of the material (see section 3.1.1). In ledge growth, the interface steps laterally and the solvent atoms take on their new (s) positions in a time smaller than $\tau = l_D/v_i$, making this process instantaneous. τ corresponds to the time needed to solidify a step or a monolayer of atoms. During this time, the solute atom tries to diffuse back to (l). If this should take longer than τ, the next monolayer is solidified and stays at this position, since (s) diffusion is neglected. According to Aziz, continuous growth in turn shows a seemingly reversed motion. There, the solute located in (l) is dragged to a site in (s) during this period of time, while it tries to impede this by diffusing away [33].

Rate theory for a kinetic description of interfacial velocity v_i, affords a closer look at the energetic disposition of the atoms located there for a duration τ. Figure 3.5 (b) shows a general schematic of the Gibbs free energy of solvent atoms applicable for this

purpose [93]. There, the difference in molar free energy between (l) and (s) is given by ΔG, being equal to the already introduced driving force for solidification. Before a solvent atom can change from (l) into an (s) site, it needs to overcome an energy barrier ΔG^*, making this a thermally activated process. The interface velocity v_i results from the net jump rate between (s) and (l) and thus from the difference between the respective fluxrates $j_{(\cdot)\to(\cdot)}$ [97][93]:

$$\begin{aligned} v_i &= a_0 \cdot \left(j_{(l)\to(s)} - j_{(s)\to(l)}\right) \\ &= a_0 \cdot A \cdot \nu \cdot \exp\left[-\frac{\Delta G^*}{RT_i}\right] \cdot \left(1 - \exp\left[-\frac{\Delta G}{RT_i}\right]\right) \\ &= v_0 \cdot \left(1 - \exp\left[-\frac{\Delta G}{RT_i}\right]\right) \end{aligned} \tag{3.13}$$

with accommodation factor A describing the fraction of possible (s) sites accepting atoms crossing the interface, ν the frequency of atomic vibration and v_0 as a kinetic prefactor of the interface mobility. According to Aziz et al., the latter equals a hypothetical maximum in growth velocity for the case of an infinite driving force [34]. A approaches unity for rough (s)-(l) interfaces and assumes low values in the case of sharp ones. Thus, the slowest process in the competition between diffusion to and accommodation in the interface dominates the behaviour [93]. Thompson et al. and Aziz et al. follow Turnbull´s approach in relating the kinetic prefactor to liquid diffusivity $D_{(l)}$ [98][34]. This is based on the assumption, that the rate of atoms being built into (s) is approximately the same as the rate of solvent atomic diffusion in the melt[6]:

$$v_0 = v_D = c_1 \frac{D_{(l)}}{a_0} \tag{3.14}$$

where c_1 is a geometrical factor close to unity [34]. Moreover, the *Stokes-Einstein relation* can be employed to relate v_0 to the shear viscosity η_S representing an experimentally accessible value:

$$v_0 = c_2 \frac{k_B T}{\eta_S} \tag{3.15}$$

[6]It shall be emphasised that those equations contain material parameters which are strictly temperature dependent.

with c_2, another geometrical factor on the order of unity [34]. Finally, a useful expression of the prefactor can be formulated to

$$v_0 \cong \frac{Ak_BT}{3\pi a_0^2 \eta_S} = \frac{A}{a_0} D_{(l)}. \tag{3.16}$$

[99][97][38][98]. Inserting this into equation 3.13, the competition between kinetics and thermodynamics, which was mentioned above only in qualitative terms, becomes evident [68]. For high (l) temperatures, where diffusion is easily possible, the undercooling is insufficient to generate the driving force needed for phase transformation (compare equation 3.1 for pure metal solidification). Consequentially, the exponential containing ΔG determines growth under those conditions. Low temperatures on the contrary effect high undercooling ΔT_i, which increases ΔG. Now the kinetic prefactor is rate limiting due to the exponential increase in viscosity η_S, which results from the significantly reduced diffusivity.

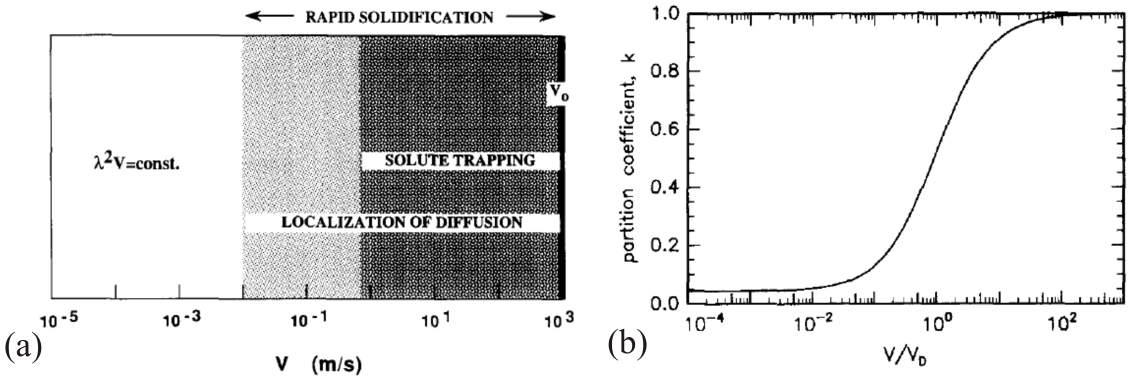


Figure 3.6.: Range of solidification front velocities typically encountered in rapid solidification (a) including distinct intervals of different dominating phenomena (according to [91]). Functional course of non-equilibrium patition coefficient k_v under rapid solidification conditions (b) in dependence of normalised interface velocity equal to the Péclet number (modified from [34]).

Apparently, the diffusive speed v_D plays an important role in interface mobility. Kurz and Trivedi examined its relation to the growth velocity v_i by observing the solidified

microstructure [91]. In their review, a distinction of three velocity regimes is introduced, based on a comparison of diffusive distance l_D to length scales characteristic for microstructure. Figure 3.6 (a) summarises their assessment for growth velocities ranging between 10^{-2} and 10^3 m/s, which is the typical interval in rapid solidification of semiconductors and metals [91]. On the lower branch of v_i up to 10^{-2} m/s, where cellular or dendritic growth can be observed (concurrent with the discussion in section 3.1.2), the characteristic length l_{crit} of microstructural features auch as dendrite radius or the spacings between cells and eutectic lamellae. In this regime, the product $l_{crit}^2 \cdot v_i$ is constant [93]. As long as l_{crit} surpasses l_D, unhindered bulk diffusion takes place and the *Einstein equation* can be used to calculate

$$l_D = 2\sqrt{D_{(l)}t} = 2D_{(l)}/v_i \tag{3.17}$$

analogously to the thermal diffusion length in equation 2.19 [91]. As soon as l_{crit} approaches l_D or even falls below it, the size of the diffusional field is constrained by the microstructural feature.

In the range between 10^{-2} and 1 m/s the transition to steady state growth is observed. Our previous discussion of this case in section 3.1.2 already introduced the appropriate critical length. Equation 3.10 gives the concentration profile in (l) directly ahead of the interface having a width of $D_{(l)}/v_i$. With increasing solidification rates, l_D approaches this value, finally leading to the loss of local interfacial equilibrium. Introducing the *Péclet number* β_{Pe}, a boundary value can be derived yielding a straightforward means to assess the conditions leading to the loss. β_{Pe} is a well known dimensionless number in fluid dynamics describing the relation between convective and diffusive flow of mass or heat [78]. Here, it is calculated by relating the velocities of growth and atomic diffusivity in (l) [33][91][100]

$$\beta_{Pe} = \frac{v_i}{v_D} = \frac{v_i l_{crit}}{2D_{(l)}}. \tag{3.18}$$

As soon as the interfacial velocity reaches the diffusive speed defined in equation 3.14, β_{Pe} approaches unity and therefore steady state conditions, i.e. local equilibrium, are

no longer valid [25]. From an atomistic perspective as depicted in figure 3.5 (a), the interface then travels so fast that the diffusional motion of the atoms cannot outrun it. Hence, solute atoms can be extensively incorporated into (s), possibly exceeding equilibrium solubility limits. This so called *solute trapping* is one of the remarkable features of rapid solidification [33][91][100][34].

Once again, it was Turnbull and coworkers who proposed an upper limit to v_i based on the sound velocity v_S. It was shown to be applicable for melts of pure metals and simple monomolecular substances. They argue that crystallisation under those conditions is *collision limited*, meaning that every collision of an atom in (l) with the approaching interface results in a crystallisation event. This holds especially for metals having activation barriers ΔG^* significantly smaller than the driving force ΔG. Thus, the solidification rate is limited by the rate of impingement only, resulting in large interface mobility, which is in turn restricted by v_S. A rule of thumb applicable to (l) metals, states that v_S is three orders of magnitude larger than v_D. In terms of the growth modes introduced in section 3.1.1, interface velocities lower than v_D are characteristic for diffusion-controlled processes. For higher velocities, interface control is established, which then translates to collsion-limited growth when v_S is reached [101][34][30].

Returning to the compositional implications arising in solute trapping, a model relevant to the material systems under investigation here shall be introduced. Aziz and Kaplan developed an analytic approach describing single-phase continuous growth of rough interfaces in dilute disordered alloys (compare figure 3.3(a)) [102]. In order to account for the velocity dependence of the composition, β_{Pe} serves well to modify the equilibrium partition coefficient k_{eq} in equation 3.8 to

$$k_v = \frac{X^{neq}_{(s),i}}{X^{neq}_{(l),i}} = \frac{k_{eq} + \beta_{Pe}}{1 + \beta_{Pe}} \tag{3.19}$$

as kinetic partition coefficient governed by the non-equilibrium composition $X^{neq}_{(\cdot),i}$ of (s)

and (l) at the interface [33][100]. Figure 3.6 (b) shows the general behaviour of k_v as a function of normalised interface velocity β_{Pe}. Especially the high velocity branch of k_v at Péclet numbers way above unity hints at another decisive feature of rapid solidification: k_v approaches unity, which is equivalent to the melt and the formed (s) having the same composition. This finding is called *partitionless solidification* and will be of importance later on.

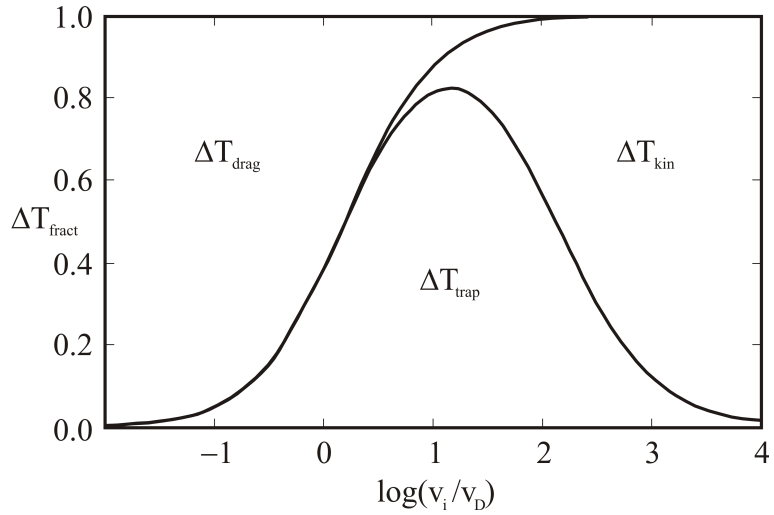


Figure 3.7.: Fractional contributions of solute drag, solute trapping and kinetics to the resulting interfacial undercooling as a function of logarithmic normalised interface velocity (equal to logarithmic Péclet number). As shown, for each velocity regime the atomic attachment is dominated by one of these undercooling contributions (modified from [103]).

As the compositional situation depicted in figure 3.4 (a) already infers, the solute accumulated in front of the (s)-(l) interface reduces the driving force for solidification. This is due to the transition of the diffusional behaviour from a diffusion absence in (s) to high diffusivity in the interface and the adjacent (l). The resulting increased solute concentration acts as an obstacle, thus slowing the migration down by *solute drag* effect [34][28][104][105]. The total energy dissipation at the moving interface is associated to

the acting driving forces via further additive contributions to interfacial undercooling ΔT_i as introduced in equation 3.12: kinetic undercooling ΔT_{kin}, and the addends due to solute trapping ΔT_{trap} and solute drag ΔT_{trap}. Clearly, these undercooling addends are also velocity dependent, which has been elaborated by Aziz and Boettinger from a kinetic standpoint [34][103]. Depending on the underlying mechanism, each contribution has an interface velocity regime in which it is most effective. Figure 3.7 summarises this depicting fractional undercooling as a function of β_{Pe}. As expected, solute drag works best at low velocities where diffusion is still decisive. Transition to steady state growth at $\beta_{Pe} \approx 1$ makes solute trapping dominant. Velocities approaching the collision limit lead to kinetic undercooling suppressing the other components. Assadi and Greer transferred the impact of these undercooling contributions to thermodynamics, which is dealt with in the next section [103].

3.2.2. Thermodynamic considerations and metastability

Based on the theory of regular solutions in heterogeneous systems, the free energy of an alloy G_{alloy} with a solution of B in A is given by

$$\begin{aligned} G_{alloy} &= X^A_{(s)} G^A + X^B_{(s)} G^B + \Delta G_{mix} \\ &= X^A_{(s)} G^A + X^B_{(s)} G^B + \Delta H_{mix} - T\Delta S_{mix} \end{aligned} \tag{3.20}$$

where ΔG_{mix} corresponds to the change in free energy due to the mixing of both components $j = (A, B)$ and $X^j_{(s)}$ to the respective (s) composition[7]. Figure 3.8 (a) depicts an idealised free energy vs. composition characteristic of an alloy system with a mixing tendency. Adding to this the G-X curve of the melt as shown in figure 3.8 (b), a graphical

[7] In this framework, the enthalpy of mixing $\Delta H_{mix} = \Omega X^A_{(s)} X^B_{(s)}$ stems from the theory of regular solutions, whereas the theory of ideal solution gives the entropy of mixing $\Delta S_{mix} = RT\left(X^A_{(s)} \ln\left(X^A_{(s)}\right) + X^B_{(s)} \ln\left(X^B_{(s)}\right)\right)$. The parameter Ω accounts for the binding energy of the A-B system and assumes negative values for preferred mixing (exothermic reactions) while positive values stand for demixing tendencies (endothermic reactions)[93].

method for the determination of thermodynamic equilibrium between these two phases can be employed. Under said condition, the chemical potentials $\mu^j_{(\cdot)}$ of all components j in all phases $(\cdot)$ must be equal [68][93]. For a given temperature T and composition $X_{(l)}$, this prerequisite is graphically expressed by a common tangent to both G curves as shown in figure 3.8 (b). Applying this *common tangent rule* to a system for different temperatures yields the equilibrium phase diagram.

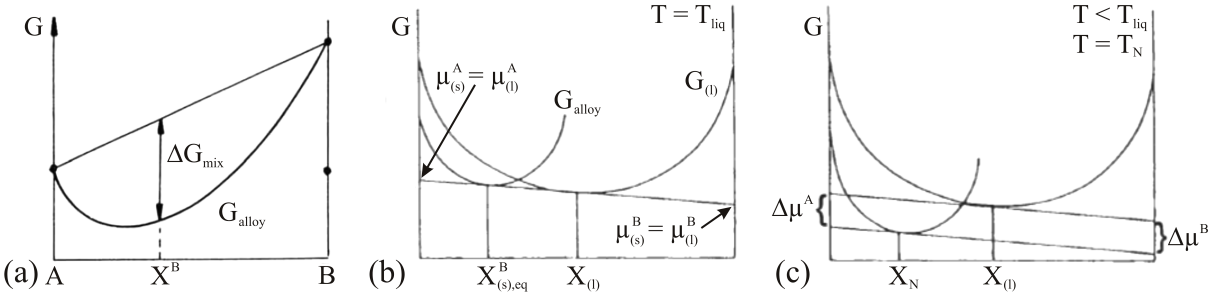


Figure 3.8.: Molar free energy curve (a) for a solid solution, where the pure components A and B share the same crystal structure (modified from [93]). Concept of the rule of parallel tangents: (b) schematic free energy diagram of two phases at liquidus temperature T_L and (c) the situation for an arbitrary nucleation temperature $T_N < T_L$ (modified from [98][37]).

In order to determine the driving force for the nucleation of a (s) phase, Hillert, Thompson and Spaepen proposed the *rule of parallel tangents* and labelled it as a 'partly thermodynamic approach' [98][37]. Figure 3.8 (c) depicts its application to an alloy melt undercooled to temperature T_N below T_{liq}. The *maximum driving force* $\Delta G_{alloy,max}$ for alloy formation is reached when the formed (s) has a composition leading to equal differences in chemical potential between (s) and (l) for both components [98][37]:

$$\Delta\mu^A = \left(\mu^A_{(s)} - \mu^A_{(l)}\right) = \left(\mu^B_{(s)} - \mu^B_{(l)}\right) = \Delta\mu^B. \tag{3.21}$$

This equality corresponds graphically to the difference in the G-X plots between the common tangent of the system at equilibrium and the parallel at T_N (see figures 3.8 (b)

and (c) in comparison)[8]. Not only does this provide $\Delta G_{alloy,max} = \Delta\mu^A = \Delta\mu^B$; the most probable composition X_N of the first stable (s) nuclei can be determined from the tangent point of G_{alloy} and the constructed parallel[9]. [98][37].

As already stated in the introduction to this chapter, material processing employing ultra-short pulsed laser radiation generates strong non-equlilibrium conditions. Von Allmen and Greer attribute this tendency to the short heating and cooling time scales promoting small length scales of material modification. Together, these contributions generate large magnitudes of thermal gradients $\nabla T_{i,(l)}$ and irreversible heat flow. Both heat and mass flows act simultaneously in the same volume and influence each other [39][68][106]. Such short transient processes can effect local equilibria at the (s)-(l) interface, in which stable or metastable phases are formed or even lead to a complete loss of equilibrium. Consequentially, the application of equilibrium phase diagrams for the assessment of potential resulting phases is not advisable. For this purpose, metastable phase diagrams can be employed to some extent. Those can be calculated using e.g. CALPHAD methods, when thermodynamic data on the involved phases is experimentally available. Then, the parallel tangent rule introduced before, can be used to assess and compare driving forces for possible transformations in the system of interest, even if metastable states are involved [36][107][108][86].

The cause for the stable existence of thermodynamically unfavoured, *configurationally frozen states* can be found when considering kinetic barriers for transformations to other states. Overcoming those hindrances requires thermally activated jumps of atoms [36][37]. For our discussion, both composition and structure resulting from solidification

[8]Naturally, this task is not as simple as it seems, since it requires knowledge on the thermal and compositional behaviour of free energy of both alloy and melt, which is not readily available for all phases and situations.

[9]Assuming B has vanishing solubility in A, the maximum driving force calculates to $\Delta G_{alloy,max} = (T_{liq} - T) \cdot \left(\Delta S_m^A - R\ln(X_{(l)}^A)\right)$ [98].

play decisive roles as will be made clear in this theoretical part and the oncoming experimental discussion. Another energetic perspective was brought on by Bormann. He argues, that even in the case of non-equilibrium phases resulting from highly undercooled (l)-(s) transitions, the energetic difference between those states and the thermodynamically stable one is rather low. Accordingly, the driving forces for the transition to the stable state are also reduced [86].

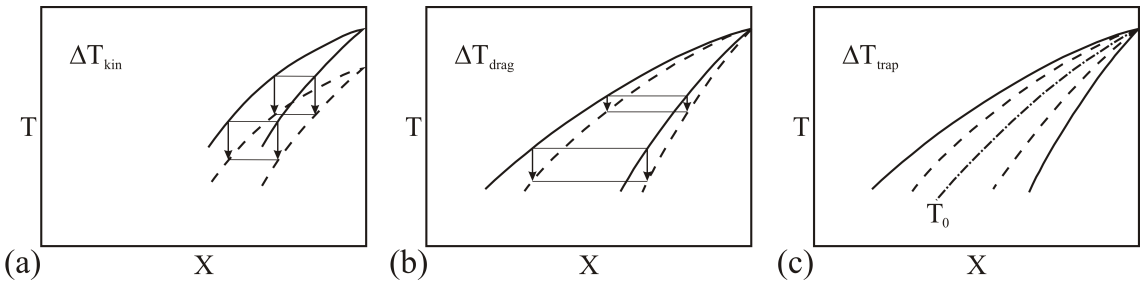


Figure 3.9.: Effect of the different contributions to interfacial undercooling as introduced in figure 3.6 on the shape of a hypothetical phase diagram: true kinetic undercooling (a) shifts the phase boundaries to lower temperatures, solute drag (c) effects skewing and the boundaries fall on the T_0 line for solute trapping (c) in effect (modified from [103]).

In order to assess the implications imposed by the undercooling contributions effected by the moving interface (see section 3.2.1) on phase diagram shape, Assadi and Greer analysed a simple hypothetical alloy system. They argued, as did Turnbull, that alloy solidification genuinely is a collision-limited process. The driving force for propagation of the (s)-(l) interface is reduced by dissipation mechanisms. Hence, the growth velocity v_i is reduced, making the process appear diffusion-limited. From the standpoint of interfacial undercooling ΔT_i^{total}, this means that the kinetic undercooling ΔT_{kin} that is promoting the growth is reduced by the undercooling addends ΔT_{drag} and ΔT_{trap}, which can be seen as a different way to interpret the statements in figure 3.7. Concluding their theoretical treatment, Assadi and Greer transferred these findings to assess the consequences on phase diagrams imposed by the individual effects. This yields accord-

ingly modified *kinetic liquidus and solidus lines* as depicted in figure [103]. Since kinetic undercooling is independent of interfacial composition, it produces a translation of the phase boundaries in the negative T direction without altering their shape and curvature. It is obvious that solute drag cannot take place in pure components, which skews the boundaries to lower temperatures while maintaining the partition coefficient and their intersection at T_m. When both $X^{neq}_{(l),i}$ and $X^{neq}_{(s),i}$ approach the same value, as observed in solute trapping, the liquidus and solidus curves collapse onto one common line, denoted as T_0 *line* [103].

Biloni and Boettinger (see chapter 8 in [37]) describe this line as the thermodynamically highest possible interface temperature allowing for *congruent solidification*, thus defining a limit for *polymorphous phase transitions* [35]. The latter are characterised by the formation of any phase without changing the actual composition. During solidification, this constrains an alloy system to maintain chemical homogeneity during the transition from (l) to (s), which was already introduced as partitionless solidification. Based on this, Johnson argues that polymorphous transitions only consist of topological rearrangements of atoms. This fits the discussion above, since solute trapping occurs at interface velocities v_i on the order of or larger than solute diffusion velocity v_D (see equation 3.17 and figure 3.7), effectively inhibiting the long-range mass transport needed for compositional changes [36].

Hence, T_0 can be seen as a boundary of the enhanced solute concentration encountered in rapidly solidified alloys under solute trapping conditions [35]. In order to actually work with the T_0 *concept* as a means to estimate possible phase formation, it is necessary to be able to construct this boundary line. To this end, two approaches can be pursued. One relies on the use of known thermodynamic data of all involved phases [107][108], while the other is used if this information is not available and represents an approximation based on the equilibrium phase diagram [109]. In the case of known free energy vs. compostition functions for (l) and the possible (s) phases, the T_0 line is constructed

by looking at the corresponding $G_{(\cdot)}$-X curves at a set of different temperatures. By connecting the intersection points between the $G_{(l)}$ and $G_{(s)}$-X curves, where the free energy of (l) and (s) phases is equal (ΔG=0), the progression of T_0 as a function of composition can be evaluated. The advantage of this approach lies in its applicability to thermodynamically known metastable (s) phases. On the contrary, the above-stated simplified approach introduced by Ishihara and coworkers, is not capable of including those phases since it relies on equilibrium phase diagrams. Here, the T_0 line is achieved by connecting the midpoints between solidus and liquidus lines for a set of temperatures. Evidently, this only holds above eutectic or peritectic temperatures [109]. To estimate the behaviour encountered below these limits, metastable liquidus and solidus lines are assumed to continue the curvature of the stable lines into the low temperature region. Clearly, this corresponds to an extrapolation of the equilibrium phase boundaries and thus caution is to be taken whilst employing this method [90][35].

3.2.3. Microstructure and phase selection

During the discussion of growth under steady state conditions and heat flow into the newly formed (s) in section 3.1.2, the role of the interfacial temperature gradient $\nabla T_{i,(l)}$ on the stability of the advancing front was pointed out. Equation 3.11 introduced critical temperature gradient $\nabla T_{e,crit}$ as the lower boundary for planar growth without segregation processes. Since this value obviously is a function of v_i, it is straightforward to deduce that the different regimes of interfacial velocities presented in section 3.2.1 not only influence the chemical composition of the resulting (s). Clearly, they contribute to the control over the formed microstructure and thus need to be considered in conjunction with the effects of thermal gradients and alloy composition [25][84]. Kurz, Trivedi and coworkers authored a set of useful review publications on these issues and their mutual interactions in the 1990s [110][111][100][91]. Figure 3.10 (a) and (b) summarise the general findings on microstructural development as a function of growth velocity v_i, temperature gradient $\nabla T_{i,(l)}$ and alloy composition X_0 respectively.

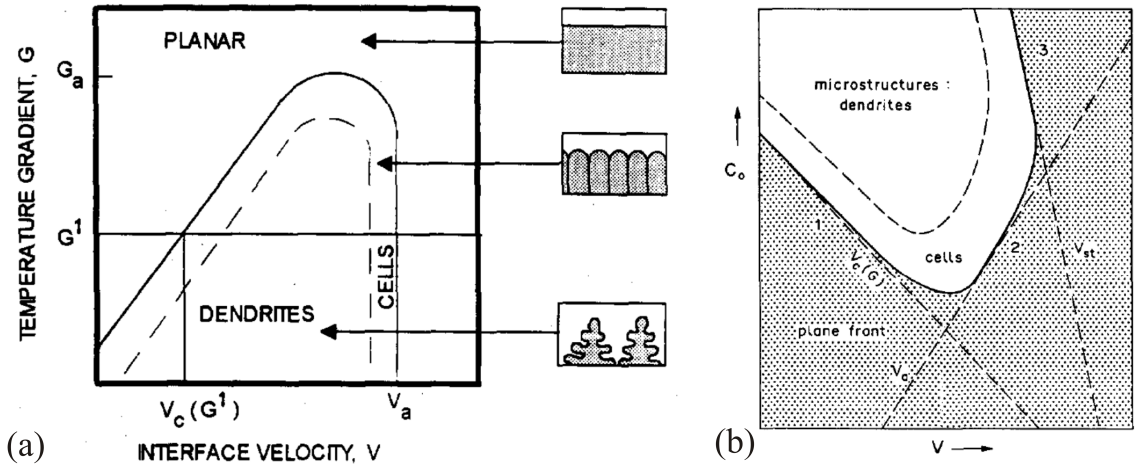


Figure 3.10.: Schematic representation of regions of different resulting solidifcation microstructures for different selections of solidification parameters: (a) temperature gradient vs. interfacial velocity (taken from [84]) and (b) alloy composition vs. interfacial velocity (taken from [110]).

Those results are based on theoretical considerations concerning interfacial temperature and composition similar to those presented in the previous two sections and were experimentally confirmed for laser-induced resolidification of doped semiconductors and dilute metallic alloys. Both figures show regions where dendritic, cellular or planar growth is favoured by the corresponding pair of parameters. The regions in turn are separated by boundary lines, whose characteristcs can be calculated with the knowledge given so far in this text.

Looking at the $\nabla T_{i,(l)}$-v_i diagram on the left hand side, two limiting cases for a fixed alloy composition X_0 can be distinguished. On the low velocity branch constitutional undercooling governs the transition between cellular and planar growth. The critical velocity is found by simply reorganising equation 3.11

$$v_{e,crit} = \frac{\nabla T_{i,(l)} D_{(l)}}{T_{liq} - T_{sol}} \tag{3.22}$$

which is a function of the equilibrium solidification interval (see denominator) and the interfacial temperature gradient. On the high velocity side exists an upper limit for v_i,

which clearly is independent of the temperature gradiend at hand. The *limit of absolute stability* v_a alike marks the transition to segregation-free solidification:

$$v_a = \frac{(T_{liq}^{neq} - T_{sol}^{neq})D_{(l)}}{k_v \Gamma} \tag{3.23}$$

where the corresponding non-equilibrium values are employed along with Gibbs-Thomson coefficient Γ of equation 3.7. Replacing $v_{e,crit}$ in equation 3.22 with v_a, the appendant upper limit to the temperature gradient ∇T_a follows directly:

$$\nabla T_a = (1/k_v \Gamma) \cdot (T_{liq} - T_{sol}) \cdot (T_{liq}^{neq} - T_{sol}^{neq}) \tag{3.24}$$

Explicitly, for a fixed intermediate temperature gradient, increasing v_i leads to a microstructural evolution from initially planar, over cellular and dendtritic, back to planar growth at high velocities [84][100][91]. Figure 3.10 (b) represents the complementary situation for a fixed interfacial temperature gradient, and thus as a function of v_i and X_0. Here, the limiting lines of constitutional undercooling $v_{e,crit}$ and absolute stability v_a are supplemented by the boundary of solute trapping v_{trap} at higher velocites. The lower part of this figure evidences that planar growth is preferred by dilute alloys. For higher concentrated solutions, cellular or dendritic structures are formed, which effectively are suppressed only when the trapping mechanism evolves at high v_i according to figure 3.7 [110].

Kurz ultimately reasoned that a system being rapidly solidified under local equilibrium conditions is likely to prefer those microstructural morphologies which exist at the highest possible interfacial temperature. Furthermore, he extended this notion to the prediction of phase selection [100]. Concerning this topic, Bormann emphasised the role of the interfacial undercooling on the driving force for nucleation of (s) phases. He pointed out, that interface mobility plays a more influential role than considerations of energetic stability of the candidate phases [86]. This was confirmed by Spaepen, who attributes the control over phase selection to such kinetic factors and additionally assigned a cooling rate $\dot{T}$ and nucleation probability [8]. The latter was of special interest

for Perepezko and coworkers, who contributed analyses on the role of nucleation and on the *competition* between phases during nucleation and growth [112].

Directly related to nuclei formation is one of the most widely used criteria for phase selection brought forward by Turnbull. He reasoned that the reaction paths most probable to be favoured by kinetics are those associated with the least amount of atomic rearrangement or movement. This corresponds to fast transitions where only small differences in entropy between parent and product phase are observed. The resulting arrangement of atoms in (s) is thus likely to exhibit short range order, be it topological or compositional in nature, and can either be amorphous or crystalline [85]. For the latter, Turnbull proposed that kinetics favour the formation of simple isotropic crystal structures with small unit cells [8]. Moreover, Greer suggested that phases are favourably nucleated if they exist over wide composition intervals, allow high interdiffusivities and enable fast interface mobilities. Concerning the selection between amorphous and crystalline (s) phases, he noted that amorphous phases are preferred when kinetic hindrances are in effect, while the formation of crystalline metastable phases is due to thermodynamic reasons [106]. In sum, the selection of phases and the microstructure resulting from rapid solidification are governed by competing processes during nucleation and growth of all possible (s) phases, stable or metastable, whose free energy is lower than that of the (l) state [27].

Finalising these general considerations on kinetics and thermodynamics, the application of these concepts to the main field of interest of this thesis ensues, namely, the pulsed laser treatment of metallic thin films. To this end, it is necessary to couple these findings with the temporal and spatial implications inherent to pulsed laser treatments on the one hand and the energetic and diffusional peculiarities of confined media on the other [113]. This was summarised by Greer in a treatise devoted to a comprehensive discussion about the role of diffusion on reactions in such arbitrarily designed systems as multilayered thin film media [106].

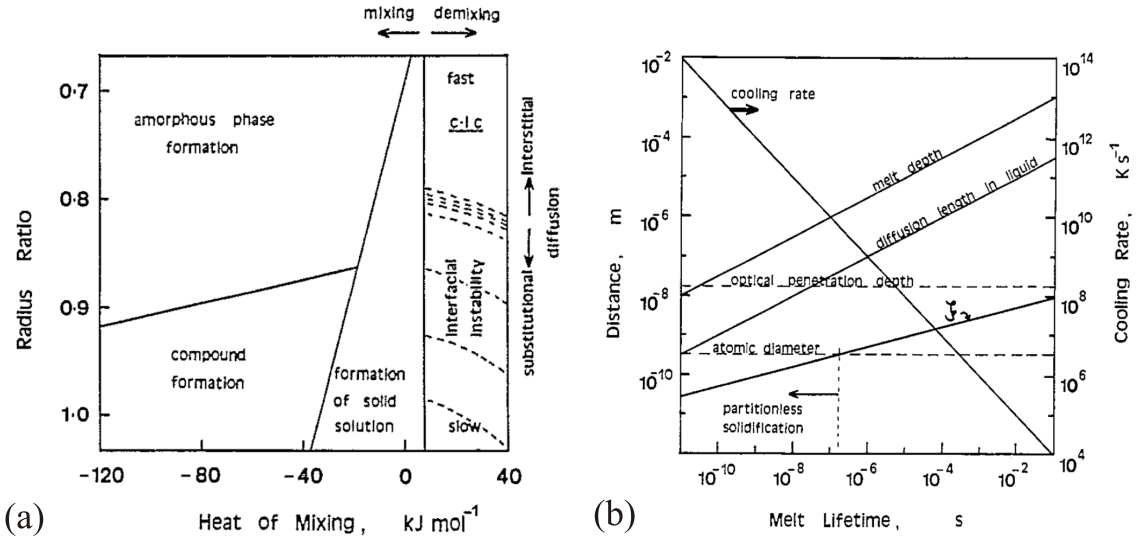


Figure 3.11.: Greer´s simplified master curves on (a) thermodynamic interaction and diffusional mass transport of pure multilayer components and (b) pulsed laser treatment parameters with critical diffusional and microstructural dimensions (both taken from [106]).

Greer´s approach consists in relating the thermodynamic interaction between the pure elements forming the multilayer with their possibilities to perform diffusional mass transfer as governed by kinetics. Hereunto, he joined up the most important parameters characterising these processes in one plot, depicted in figure 3.11 (a). There, the heat of mixing ΔH_{mix} (introduced in equation 3.20) as a thermodynamic quantity of the alloy and the ratio between the constituent atomic radii ($r_{at,s}/r_{at,l}$) outline the regions of the different phases and microstructures formed[10]. The latter suggests that these two parameters normally cannot be considered independently. According to the theory of regular solutions [93], the region of $\Delta H_{mix} \approx 0$ corresponds to ideal mixing conditions leading to the formation of chemically random solid solutions. While positive values are associated with demixing and clustering (due to increasing $\gamma_{(s)-(l)}$), negative ΔH_{mix}

[10]Greer pointed out, that ΔH_{mix} can be used irrespective of the mixing taking place in (s) or (l). Furthermore, he employed Goldschmidt radii as atomic radii, knowing that these deviate from accurate values especially when large negative ΔH_{mix} are involved [106].

favours the formation of chemical order or even compounds. To account for entropic effects associated with Gibbs free energy of mixing, the demarcation between these regions is slightly shifted from $\Delta H_{mix} = 0$ towards positive values. Increasingly negative mixing enthalpies are likely to promote the quenching of amorphous phases. This happens especially when the radii of the mixing components exhibit a large difference and thus small radius ratios. The plot here is restricted to a lower radius ratio of 0.59 which corresponds to the classical limit of interstitial diffusion[11]. With increasing radius ratio, the interstitial mechanism is displaced by the substitutional one. The aforementioned condition for solid solution formation is naturally supported by ratios approaching 1.0. Hence, figure 3.11 (a) can be seen as a master curve enabling the assessment of the possibilities of phase formation in a given matching material.

Greer complemented this by coupling the most decisive parameters of pulsed laser treatment with the critical dimensions of material transport and microstructure discussed above. Figure 3.11 (b) is thus the master curve for different processing regions as delineated by dimensional and temporal constraints. The associated demarcations are given as straight lines in the graph and were estimated by a set of simplified equations originally devised by Spaepen et al. and von Allmen et al. [39][42][43]. Since they were only considering the case of laser irradiation normal to metallic alloy thin films on substrates, one-dimensional heat transfer towards the substrate was scrutinised. Thus, the melt depth d_{melt} is the characteristic processing parameter, governed by pulse duration τ_p, irradiation power P and the material´s thermal properties. Especially the latter effect further heating of the already molten layer taking place for times $t > \tau_p$, leading to a superheating of (l) and thus $\nabla T_{i,(l)} > 0$. The double logarithmic scale of figure 3.11 (b) simplifies the depiction of the functions $\dot{T}$, $l_{th,(l)}$ and l_{mono} to straight lines. Herein, the transition to partitionless solidification is achieved when $l_{mono} < 2r_{at}$, which is favoured

[11] Deviating from this limit, Greer reports observations of interstitial diffusion at ratios approaching 1.0 taking place in binary systems with large negative ΔH_{mix}.

by high cooling rates. Moreover, the behaviour of d_{melt} shows, that short $\tau_{(l)}$ and thus high $\dot{T}$ generate comparatively low melting depths, leading to a more surface-confined heat treatment with reduced possibilities of diffusional intermixing as in concordance with experimental findings [25].

Combining the curves in figure 3.10 with those in figure 3.11, a set of four clearly simplified *master curves* might be at hand which could support the interpretation of experimental results from microstructure and phase composition after laser processing. Vice versa, it might enable a more guided approach to the design of dedicated microstructures by appropriately selecting materials and processing parameters beforehand.

4. Materials selection

The objectives of this thesis require the materials selection process to be tackled from different vantage points and background data. Based on the described governing mechanisms of rapid solidification, the foremost prerequisite for their systematic application in the microstructural design of metallic alloys is a precise à priori knowledge on a different set of thermodynamic, diffusional and kinetic material parameters. Preferably, these data need to be present as functions of temperature and composition. As intended, the combination of the pure elements forming the multilayer thin film not only governs the possibilities of phase and microstructure formation. Consequentially, it controls the resulting functional properties of the modified material, both by structural characteristics of the solid and the microstructural dimensions formed [1]. In order to reasonably reduce the complexity of the problem, only binary material combinations shall be in focus of the analysis here.

In addition, the possibility to arbitrarily design the multilayer-substrate combination opens up the opportunity to exert influence on the heat transfer process away from the superheated melt. Hence, both melt lifetime $\tau_{(l)}$, limiting diffusional intermixing, and solidification front velocity v_i are likely to be affected by purposedly choosing convenient substrate materials. Simultaneously, an appropriate adhesion behaviour to the multilayer must be ensured. In order to systematically assess the prospects of controlling the outcome of LIMET treatments, it is necessary to reasonably narrow down the possible candidate combinations to well-investigated material systems.

4.1. Substrate materials

Besides ensuring integrity of the metallic thin film during laser treatment, the main purpose of the substrate is to extract heat from the processed region. Thus, the thermal properties introduced in section 2.2 play the decisive role. To impede disturbances to the melting and resolidification process of the multilayer, the substrate must ensure stable geometrical conditions at its surface. Phase transitions in (s) or the transition to (l) state can effect alterations in density or a softening of the elastic coefficients, both of which can jeopardise this condition. Obviously, an intermixing between the multilayer and the substrate elements is also to be impeded, in order to keep impurity contents as low as possible. To this end, the substrate should not exhibit phase transitions in the temperature interval from room temperature to the melting points of the multilayer constituents. From an application point of view, the use of MEMS materials is recommendable, since their properties are well known and their production methods are established and yield reproducible results [64][114]. Furthermore, their successful use as LIMET-capable substrates could repeatedly be shown, also in conjunction with applications in small scale mechanical and tribological composite behaviour [17][115][65].

A set of standard MEMS materials was assessed accordingly with respect to their melting temperature, softening point, thermal conductivity and diffusivity. As soon as the presence of a disturbing phase transition was ruled out, the parameters governing heat conduction were used to refine the search. In order to systematically analyse the possibility to control melt lifetime $\tau_{(l)}$, it was intended to achieve a reasonably wide interval, preferably spanning some orders of magnitude in conductivity and diffusivity. Single-crystalline silicon (sc-Si), amorphous silicon nitride (Si_xN_y) and fused silica (SiO_2) representing the most frequently employed MEMS material systems [64], show convenient characteristics at room temperature. Table 4.1 summarises these data and rounds them up with relevant thermodynamic values. Since both Si_xN_y and SiO_2 are

Property	Substrate materials		
	Silicon (sc-Si)	Silicon nitride (Si_xN_y)	Fused silica (SiO_2)
λ_{th} (W/mK)	150.0	30.0	1.4
ρ (kg/m^3)	2330	3170	2210
D_{th} (10^{-5} m^2/s)	9.04	1.33	0.09
c_P (J/kgK)	702.2	710.6	745.0
T_{soft} (K)	/	/	1953
T_m (K)	1687	2173	2003
T_b (K)	3538	/	2473
Literature	/	[116]	[117]

Table 4.1.: Relevant thermal and thermodynamic properties of the employed MEMS substrate materials at room temperature along with their literature sources. T_m is amended by boiling point T_b and softening temperature T_{soft} if applicable (Si_xN_y decomposes at 2173 K). Until otherwise stated, the data are valid for bulk material and stem from [118].

employed in their amorphous form (see section 5.1), no relevant phase transitions are likely to be observed in the temperature range of interest for all selected substrates. Most importantly, the spread in thermal properties spans three orders of magnitude in conductivity λ_{th} and in diffusivity D_{th}, making these substrates the ideal choice for the purposes of this thesis.

4.2. Metallic multilayer systems

The necessity to base the search for convenient binary metallic systems both on the availability of comprehensive thermodynamic data and desirable functional properties, considerably narrows down the number of candidate metal combinations. Moreover, Turnbull´s kinetic argument of phase selection (see section 3.2.3) suggests to concentrate

on prospective phases with comparatively simple crystal structures. In addition, the implications on driving the force discussed in conjunction with the T_0 concept (c.f. section 3.2.2) indicate a preference towards systems exhibiting intermetallic phases with large existance range over compound phases with narrow composition intervals.

Property	Multilayer components		
	Aluminum (Al)	Nickel (Ni)	Titanium (Ti)
λ_{th} (W/mK)	237.0	90.7	21.9
ρ (kg/m^3)	2700	8910	4510
D_{th} (10^{-5} m^2/s)	9.91	2.29	0.93
c_P (J/kgK)	897.0	444.0	523.0
T_m (K)	933	1728	1941
T_b (K)	2792	3186	3560
α_{th} (10^{-6}/K)	23.1	13.4	8.6
r_{at} (pm)	124.6	144.8	143.2
R (1)	0.935	0.428	0.440

Table 4.2.: Relevant thermal and thermodynamic properties at room temperature of the metallic materials employed for multilayer deposition (from [118]).

A literature survey accounting for these issues points to three of the best-investigated systems with respect to their thermodynamics as well as their functional characteristics: Ni/Al, Ti/Al and Ni/Ti. All three have in common, that an intermetallic phase fulfilling these preconditions is located at the stoichiometric composition of the constituent elements (see figures 4.1 to 4.3) [119][120][121][122]. Moreover, it is possible just by combining only three different pure metals (atomic radii; see table 4.2) to access a multitude of different thermodynamic, diffusional and kinetic behaviours. Thus, the applicability of Greer´s master curves to à priori microstructural design can systemati-

cally be assessed. Adopting the multilayer approach to the design of the metallic thin film allows for an arbitrary selection of composition and potentially unusual material combinations [8][106]. The following brief description of the candidate material systems will be restricted to the phases at and adjacent to the stoichiometric composition. More detailed information on the relevant involved phases is given in appendix V.

4.2.1. Nickel-Aluminium System (Ni/Al)

The Ni/Al system is mostly known for its remarkable mechanical properties and good corrosion resistance even up to the elevated temperatures encountered in turbine applications. Desai et al., Ansara et al. and Pasturel and coworkers summarised the thermodynamic data necessary to calculate the phase diagram (figure 4.1) and free energy characteristics [123][124][125][126].

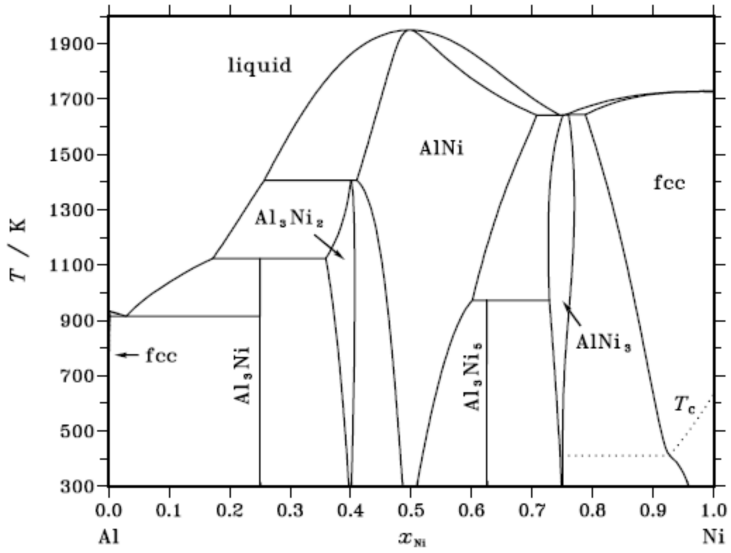


Figure 4.1.: Equilibrium phase diagram of Ni/Al system (taken from [127]).

Especially the intermetallic phases NiAl, referred to as β with cubic B2 structure, and Ni_3Al, also called γ' exhibiting a fcc ordered $L1_2$ structure, were subject to intensive

research (see figure 4.1(b)). [120][127][128][129]. β-NiAl shows the desired extended compositional range and melts congruently at 1950 K for compositions close to stoichiometry, while keeping its order.

For compositions on the Ni-rich part of its range, a thermally induced martensitic transformation to a tetragonal $L1_0$ structure is observed, which was first noticed during the 1960s [130][131][132][133][134]. Its associated Martensite start temperature M_S is strongly composition-dependent and ranges approximately between 33 and 1273 K for contents of 60 to 70 at.% Ni, and can further be modified by adding Mn and/or Fe [120][135]. It is worth mentioning, that cosputtering and self-propagating exothermic solid-state reactions (SHS) in multilayers can yield metastable phases [128][136]. Especially the process mentioned last, benefits from the β-phase exhibiting an appropriate energy density (861 kJ/cm^3) and enthaply of formation (59 kJ/mol) to enable a self-sustaining reaction front [137][138][139][140].

4.2.2. Titanium-Aluminium System (Ti/Al)

Alloys based on titanium aluminide phases share the same properties and application fields with those of the Ni/Al system [120][141]. Intensive research was devoted to assessing the phase diagram (see figure 4.2 (a)) and thermodynamic equilibria especially by Kainuma et al. and Desai and coworkers [142][123][143][144][145][146][147][148] while Colinet summarises the associated formation enthalpies [149]. Both phases exhibit comparatively large existence ranges as depicted in figure 4.2 (a).

γ-TiAl keeps its ordered $L1_0$ structure up to the melting point and is also known for its capability to be formed in exothermic self-propagating reactions during combustion synthesis like β-NiAl [120][150]. Therein, an energy density of 788 kJ/cm^3 and an enthaply of formation 40 kJ/mol are observed [151][152]. Like in the Ni/Al system, the differ-

ence in melting points of the constituent elements is large, but only β-Ti(Al) exhibits a melting transition above those temperatures.

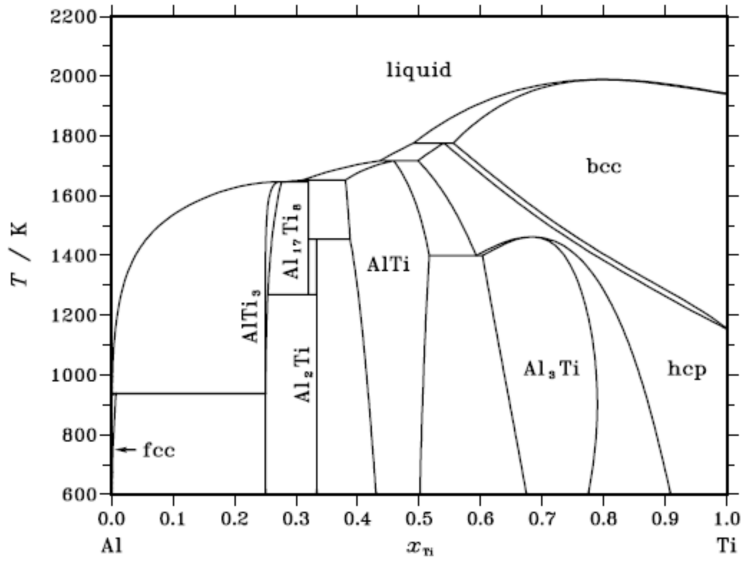


Figure 4.2.: Equilibrium phase diagram of Ti/Al system (taken from [141]).

4.2.3. Nickel-Titanium System (Ni/Ti)

The system Ni/Ti is well-known for its capability to perform a thermally induced shape memory effect due to a (s) state transition between the ordered austenite B2 NiTi and martensite tetragonal B19' ($P2_1/m$) phases located in an existence range at the equiatomic composition (see phase diagram in figure 4.3). Since the first publication by Buehler et al. in 1962 [153], intensive research on this martensitic transformation and the factors influencing its efficiency was performed both with respect to bulk and thin film applications. This progress and the resulting technical applications are reviewed in the following publications [154][155][156][157][37] (there chapter 16). The thermodynamic data and free energy characteristics are reviewed in [158][159][160][161][162][163].
With respect to the existence ranges, the phase diagram only shows hexagonal Ni_3Ti phase as possible candidate besides B2 NiTi and the disordered solid solutions of the

constituent elements. Moreover, like the phases in the vicinity of the stoichiometric composition in the material systems discussed before, B2 NiTi can be formed during self-propagating reactions in (s) state, with an energy density of 563 kJ/cm^3 and an enthaply of formation of 34 kJ/mol [164][165].

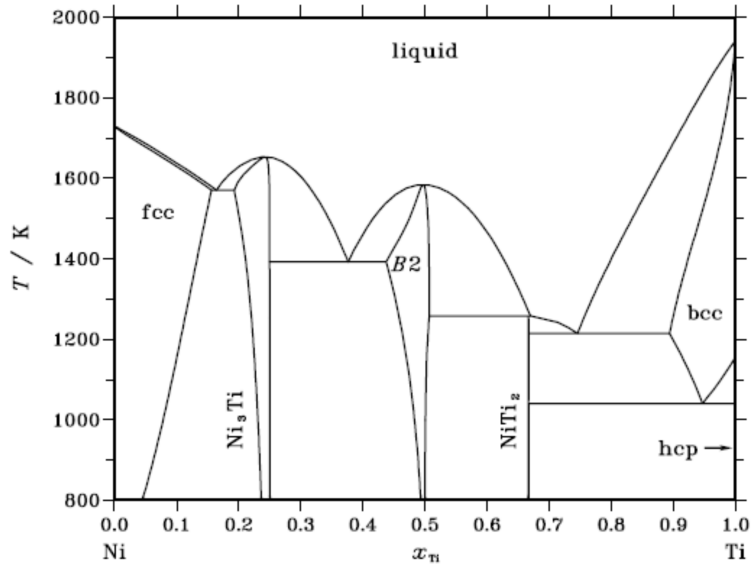


Figure 4.3.: Equilibrium phase diagram of Ni/Ti system (taken from [163]).

Part III.

Experimental part

5. Experiments and methods

5.1. Design of experiment

As the master curves depicted in figures 3.10 and 3.11 infer, a set of key parameters is thought to determine both the outcome of microstructure morphology and phases in rapid solidification: solidification velocity v_i, interfacial temperature gradient $\nabla T_{i,(l)}$, cooling rate $\dot{T}$, alloy composition X_0, enthalpy of mixing ΔH_{mix} and the ratio of the atomic radii. Section 3.2.3 revealed some hints on how to manipulate them by an appropriate selection of experimental conditions. Transferred to the possibilities of LIMET, three main levers can be identified: The *materials* used for substrate and multilayer, the actual *design of the thin film stack* (regarding total t_{tot} and bilayer thickness Λ) and the *laser processing parameters* employed (irradiation intensity I, embodied by fluence F, and pattern periodicity d). Their individual impact and their mutual relation need to be considered while planning systematic experiments, especially when taking into account the prospective number of parameter variations, which is needed to be kept at a reasonable minimum.

Since the role of the underlying substrate in adjusting v_i and $\nabla T_{i,(l)}$ is already clearcut, the multilayer design shall be in focus here. By selecting the individual layer thicknesses t_i of the constituents and adjusting their mutual ratio, its overall composition X_0 is controlled. Since it is intended to willingly trigger the formation of intermetallic phases with reasonable grain size and volume fraction, X_0 is chosen bearing in mind Turnbull´s criterion on phase selection [85]. Hence, it is situated in a region of the binary phase

diagram, where a phase with a large existence range and a preferably simple crystal structure can be found. For the three binary systems under discussion here, section 4.2 showed $X_0 = 0.5$ to be the appropriate choice, which is maintained constant throughout this thesis. Very much like ΔH_{mix} and the radius ratio, the sum of the thicknesses of two adjacent layers, bilayer period Λ, governs the extent of achievable intermixing during the laser processing. If it is chosen too large, say on the 100 nm order, ns-pulsed laser is likely to yield an incomplete mix of the metals (compare with equation 3.17 describing diffusion length). In turn, adopting a narrow Λ of approx. 3 nm as in Spaepen´s early studies [42][43], the probability of an increased intermix to be achieved already during the deposition process is increased [166]. Therefore, an intermediate Λ of 50 nm is adopted for all material systems, as in Daniel´s thesis, which enables a good basis for comparison [19]. Concluding the matters of materials selection and specimen design, total multilayer thickness t_{tot} is addressed. It is chosen to be on the order of 400 nm both to increase the likelihood of achieving the through reaction and to be able to assess substrate influence.

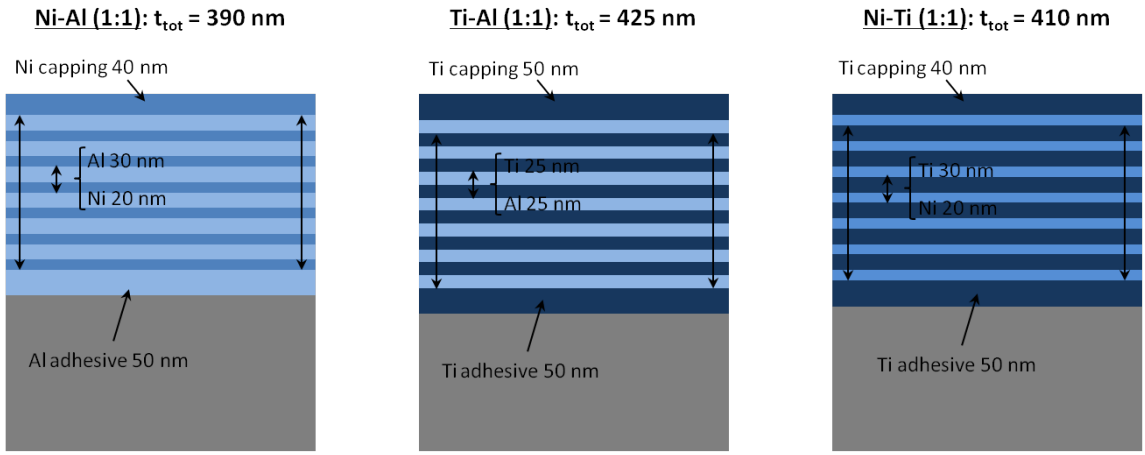


Figure 5.1.: Intended specimen stack design with respective capping and adhesive layers including the devised nominal values for individual layer t_i and total stack thicknesses t_{tot}.

Figure 5.1 shows the specimen stack design for all systems. The multilayer contains at least six bilayers, which are deposited onto an adhesion-promoting layer. Each stack is completed by a capping layer made of the component with a higher melting temperature, consistent with the findings of Lasagni [79]. To ensure that absorption of the laser radiation takes place in a volume where no transition to another material takes place, the thickness of the capping is selected according to the corresponding skin depth δ (see equation 2.8). Here, $2t_i$ is sufficient.

LIMET offers fluence F and periodicity d as experimental variables. Since pulse duration τ_p is a fixed value for the ns-pulsed laser in use, its impact on $\dot{T}$ cannot be systematically varied. As Baeri summarised [27], the irradiation area density F not only determines the temperature in the interference maximum position T_{max}, it also governs the duration of the melt $\tau_{(l)}$ together with the substrate material. Hence, the impact on $\dot{T}$ and $\nabla T_{i,(l)}$ can be expected. Periodicity d comes into play when considering the role of proximity between adjacent interference maxima. The closer they are to each other, the less effective the lateral heat transport, due to modified $\nabla T_{i,(l)}$ and thus prolonged $\tau_{(l)}$ as well as reduced v_i are in disposition. A misplaced selection of those parameters can either lead to an incomplete processing of the multilayer, or in combination with a disadvantageous adhesion to the substrate, to damaging the thin film by ablation. Thus, a convenient *processing window* for F and d must be determined, both by experiment and by simulation.

The result of LIMET patterning is observed post-mortem by a combination of standard and dedicated high-resolution imaging techniques. Especially for the latter ones, like TEM and APT, rather tedious preparation and analysis procedures are necessary to ensure good quality data. Their use is thus restricted to selected cases, whereas the standard methods were readily applied. Nevertheless, in order to cover the large parameter space presented above, it makes no sense to try to analyse all possible variable

combinations. Looking at only one composition per material system and three different substrates already implies a vast variety with regard to the basic specimen settings themselves. By means of FEM simulations, it is intended to identify suitable combinations of F and d within the processing window, which lead to a through-reaction with minimum F and a stable lateral (s)-(l) front propagation. Since Ni/Al already has a comparatively large body of LIMET-related results, most of the experimental work of this thesis will be concentrated there, dealing with smaller intervals of F and d in order to get reliable data for a conclusive comparison and a subsequent improvement of the FEM simulations. To cross-check with the other material systems, their modification will be assessed at individually chosen combinations of F and d.

5.2. Specimen preparation, Laser processing and characterisation

5.2.1. Ion beam Physical Vapor Deposition

The thin film specimens needed for this thesis were prepared using *ion beam physical vapour deposition* (I-PVD), an easily controllable and reproducible deposition technique. Its main difference with other PVD techniques is the absence of an electric field between the target and the substrate [167][168]. The PVD equipment used here is a modified Roth&Rau UniLab system, the schematics of which can be seen in figure 5.2 (a). The original filament ion source was replaced by a HF-generator-driven ion gun (Hüttinger Elektronik PFG 300 RF) for plasma creation, operating with a *forward power* P_{fwd} of 110 W at a *frequency* ν of 13.54 MHz. The geometrical setup of the system, i.e. the sputter target mounting, allows for a sequential layer deposition. It supports water-cooling and hydraulic rotation for two separate 10 cm-diameter sputter target discs, bonded on

a Cu holder plate with bayonet fixing, as depicted in figure 5.2 (a). Single-metal targets with 99.6 to 99.995 at.% purity were used. As indicated, the distance between ion gun and target is approximately 20 cm with an inclination of roughly 40 ° between the ion beam and the target´s normal direction.

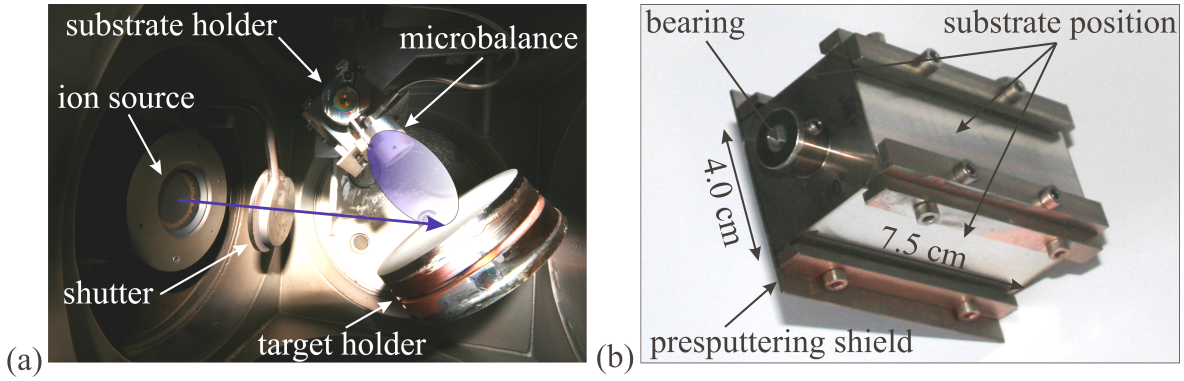


Figure 5.2.: General outline of (a) the I-PVD chamber used (ion beam direction and sputter plume indicated schematically) and (b) the custom-made rotation holder for the different substrates.

The process chamber was generally kept at a *base pressure* p_{base} of $7.7{\cdot}10^{-7}$ to $2.6{\cdot}10^{-6}$ mbar. Especially the deposition of Ti is prone to oxidation during the process if the chamber pressure is worse than 10^{-6} mbar [169]. The custom-made square *rotation holder* allows for target pre-sputtering and *consecutive deposition* on three substrates without breaking the vacuum of the process chamber. Due to the limited space inside the chamber, the maximum substrate size is restricted to $75 \times 25 \times 1\,\mathrm{mm}^3$. The optimum orientation of the substrate surface with respect to the sputter plume is parallel to the target material surface (see figure 5.2 (a)) at a fixed distance of 6 cm.

In order to ensure result comparability, every sample set was sputtered in one session. Identical deposition parameters and boundary conditions could thus be guaranteed for

the whole sample set. The *main process parameters* of this PVD system, besides the aformentioned HF and base pressure settings are summarised in table 5.1. Keeping these conditions, the production of oxide- and porosity-free as-deposited thin films could be achieved as shown in section 6.2.1.

P_{fwd} (W)	P_{ref} (W)	U_{beam} (V)	j_{beam} (mA)	U_{acc} (V)	j_{acc} (mA)	f_{Ar} (sccm)	p_{Ar} (10^{-3} mbar)
110	5 - 11	450	17 - 22	120	2	8.0 - 8.5	3.5 - 3.8

Table 5.1.: Optimum process parameters for I-PVD deposition of metallic multilayered thin films applicable to all employed target materials.

Pre-sputtering was performed for each target for 600 s at U_{beam}=600 V and j_{beam}=23 mA, while all other parameters were set as given in the table above. Online monitoring of the deposition process was performed using in-situ thickness measurements by a *quartz crystal microbalance* (type TecTra MTM-10). Calibration of the microbalance was achieved in a separate set of deposition experiments by SEM imaging of FIB-prepared cross sections.

5.2.2. Laser interference metallurgy

The theoretical basis of a precise and adjustable spatial intensity distribution of light with periodicities on the μm scale lies in the use of the *superposition principle* [70][79][170]. This distinguishes *Laser interference metallurgy* (LIMET) from other laser surface patterning techniques. It states that the algebraic sums of a number n of wave functions j solving the wave equation are solutions to the wave equation themselves:

$$\vec{E}_{sum}(\vec{r},t) = \sum_{j=1}^{n} c_j \vec{E}_j(\vec{r},t) \tag{5.1}$$

is the general notation, where c_j represents a weighting coefficient (here, c_j=1 is convenient). Equation 5.1 calculates the inhomogeneous spatial distribution of the electromagnetic field $\vec{E}_{sum}$ resulting from the interaction of n overlapping waves, with special interest on the region where *interference* takes place [70]. In general, linear superpositions are applicable only with light intensity low enough to avoid a non-linear optical response from the medium in which it is travelling [70].
This is the case for the Nd:YAG ns-pulsed solid state laser (NEWPORT-SPECTRAPHYSICS QUANTA-RAY 290) used here. In order to design a spatial arrangement of $\vec{E}_{sum}$ and intensity I_{sum} via equation 2.2, an *inverse problem* approach is generally necessary. The desired intensity distribution is transformed into Fourier space, yielding n waves and their individual geometrical arrangement to form the desired *interference pattern* [79][170].

As presented in section 1, a hierarchically ordered pattern of periodic parallel lines is the basis for the envisioned biomimetic composite thin films. Therefore, the controlled interference of but two sub-beams (n=2) of the aforementioned laser is necessary, allowing a simpler way to calculate the pattern. As discussed in section 2.2, the light emitted by the laser is best described as a linearly polarised monochromatic electromagnetic plane wave. Then, equation 5.1 yields

$$\vec{E}_{line}(\vec{r},t) = \vec{E}_{0,1}\exp\left[i(\vec{k}_1\cdot\vec{r}-\omega t)\right] + \vec{E}_{0,2}\exp\left[i(\vec{k}_2\cdot\vec{r}-\omega t)\right] \tag{5.2}$$

since both interfering waves originate at the same source. Using equation 2.2 the intensity I_{line} is calculated [70]

$$I_{line}(\vec{r},t) = 2c^2\epsilon_0|\vec{E}_0|^2(1+\cos(\phi)) = 4I_0\cos^2\left(\frac{\phi}{2}\right) \tag{5.3}$$

representing the intensity distribution of an interference of two beams (see figure 5.3 (a)) having the same electric field magnitude and polarisation ($\vec{E}_{0,1} = \vec{E}_{0,2} = \vec{E}_0$ and $I_2(\vec{r},t) = I_1(\vec{r},t) = I_0$). Complete *destructive* ($I_{line} = 0 = I_{min}$) and complete *constructive* ($I_{line} = 4I_0 = I_{max}$) interferences occur for even and odd integer multiples of 2π

values of ϕ, respectively [70]. For pulsed laser systems, the intensity I_0 is experimentally determined in terms of the energy flux per unit area known as *fluence*

$$F = \frac{\eta P}{fA} \equiv I_0 \tag{5.4}$$

with optical setup efficiency η, laser beam power P, pulse repetition rate f and beam area A.

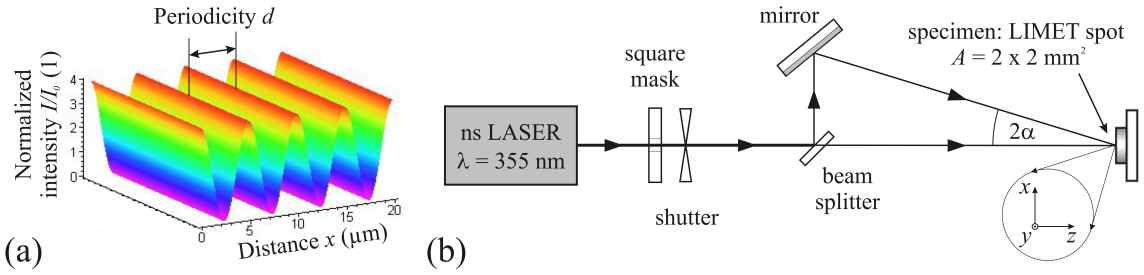


Figure 5.3.: Calculated two-beam interference pattern (a) according to equation 5.3 (modified from [171]) and general two-beam LIMET setup (b) with general coordinate frame used in this thesis (modified from [172] and [173]).

Looking at the experimental interference setup used in this thesis and its coordinate system as displayed in figure 5.3 (b), it becomes clear that the phase argument ϕ is only determined by the divergence angle 2α between the two beams coinciding at the sample surface, with

$$\phi = 2x|\vec{k}|\sin(\alpha) \tag{5.5}$$

where $|\vec{k}| = 2\pi/\lambda$ [79]. A parallel line interference pattern of alternating maximum I_{max} and minimum I_{min} intensity lines is thus generated on the sample surface plane $(x-y)$, with a spatial periodicity d:

$$d = \frac{\lambda}{2\sin(\alpha)}. \tag{5.6}$$

Applying the superposition principle to a technical application like surface patterning, requires the generation of a stable interference pattern at the sample surface, which is achieved when coherency between the sub-beams is maintained.

As discussed in section 5.1, the optical properties of Ni and Ti at the multilayer surface suggest the use of the laser´s third harmonic having a wavelength λ of 355 nm. The pulse duration τ_p amounts to 10^{-8} s and a maximum fluence of F_{max}=1.9 J/cm^2 (according to equation 5.4) can be achieved. Due to the fact that periodicites d in the μm-range are intended, incidence angles 2α on the order of 1 ° can be expected for the second sub-beam. Therefore, reflectance can be treated as in normal incidence. The actual spot size was determined using both *dark-field imaging* in a light microscope (OLYMPUS BX60) and *white light interferometry* (WLI, ZYGO NEWVIEW 7300). The latter was also employed for topographical analyses of the irradiated areas. For the structuring process itself, the sample was aligned perpendicular to the primary beam direction and mounted on a customised *x-y translation stage*.

Concluding, the *main process parameters* of LIMET for the present thesis were the *periodicity d* and the *laser fluence F*, which were systematically varied in order to attain a comprehensive understanding of their effects on the thermally induced modification of the multilayer microstructure and its underlying mechanisms as discussed in section 3. Three periodicities (4.0, 8.0 and 16.0 μm) were adjusted by modifying the geometrical LIMET setup according to equation 5.6. The criterion was the formation of sufficiently separated interference maxima to allow for a correct analysis of the lateral heat flow as a function of both periodicity and substrate material. For each selected period, the nominal fluence F was varied from 50.0 to 750.0 mJ/cm^2. This corresponds to an interval of 0.26 to 40 % of F_{max} according to prior investigations [174][171][172][80][175]. The fluence was incremented 25.0 mJ/cm^2 for fluences below 300.0 mJ/cm^2 and 50.0 mJ/cm^2 for values above. While the last interval was mainly used to determine the ablation

threshold fluence of each substrate-multilayer-periodicity system, the first interval served to deliver controlled amounts of energy to the interference maxima positions.

5.2.3. Scanning electron and focused ion beam microscopy

Combining high-resolution scanning electron microscopy (SEM) with focused ion beam (FIB) into one *SEM/FIB dual beam microscope* has had a strong impact on microstructural characterisation since its advent in the early 21st century. The possibility to use the well-developed analytical methods of SEM while locally removing specimen material on the μm/sub-μm scale with FIB, enhanced the methodological spectrum not only in solid state physics and microelectronics, but also in biology and especially in materials science [176][177]. As a consequence, nowadays SEM/FIB not only represents a characterisation technique capable of imaging, chemical and structural analysis of surfaces and the underlying volume; it is also a versatile patterning tool, which proves useful in site-specific sample preparation for localised analyses using other techniques like *transmission electron microscopy* (TEM) or *atom probe tomography* (APT). In light of this and the discussion in section 5.1 it becomes evident, that the successful application of SEM/FIB is the backbone of the microstructural analyses of this thesis.
To this end, two different dual beam systems were employed: a *FEI Helios 600 Nanolab* and a *FEI Strata DB 235*. Both are equipped with a field emission gun as an electron source, a Ga liquid metal ion source and diverse gas injectoion systems allowing for electron- or ion-induced chemical vapour deposition (E-CVD or I-CVD) of protective coatings necessary to reduce ion beam damage to the regions of interest [176]. Besides *top-view imaging* of individually selected laser spots in secondary electron (SE) contrast, the SEM/FIB technique was employed in dedicated site-specific sample preparation.

TEM sample preparation of selected microstructural features is one of the key achievements of the SEM/FIB technique [176]. Today, its general procedures are regarded as an established standard operation mode and are summarised in [178]. Introducing a

low-kV ion irradiation as a final step of the preparation, both Ga contamination and ion beam damage are significantly reduced, thus contributing to an improved TEM foil quality [179][178][180]. As section 5.2.5 will elucidate, the production of cone-shaped samples suitable for APT is increasingly performed by the use of SEM/FIB systems. The tip radii needed for electric field-induced evaporation of atoms are on the order of 50 nm. Conventionally, those specimen tips can be achieved by electrochemically thinning a wire prepared by macroscopic cutting techniques [181][182][183]. Besides the sometimes troublesome search for convenient etching solutions, this procedure fails to provide a site-specific preparation. In contrast, the SEM/FIB approach used here is basically derived from the TEM foil machining [184][181][185]. A preliminary wedge-shaped specimen with 25.0 μm length, 2.0 μm width and 60 ° opening angle is extracted from the sample[1].

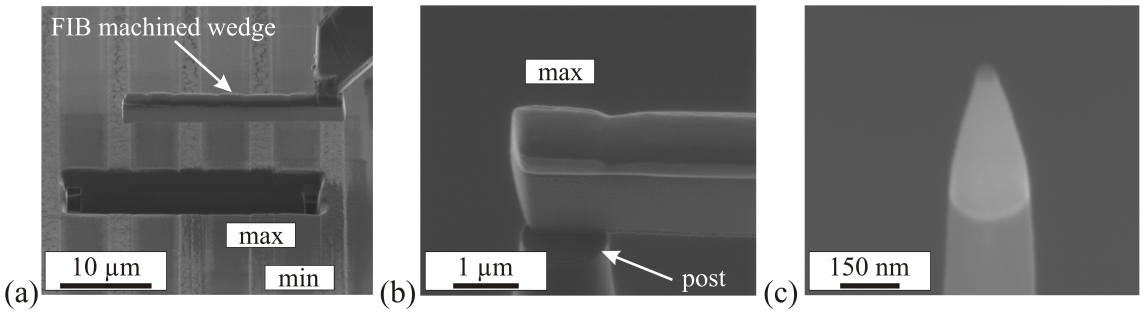


Figure 5.4.: Sequence of SEM micrographs depicting FIB machining of APT specimens: preliminary wedge-shaped specimen attached to micromanipulator directly after site-specific lift-out (a). LIMET maximum location at microtip array post prior to Pt-deposition (b) and final APT specimen tip of this region (c) after annular milling and low-kV polishing.

By means of the micromanipulator, the wedge is transferred to a commerically avail-

[1]In order to better identify the top layer of the multilayer specimen in SE images of the subsequent preparation steps, the protection coating used here consists of a 200 nm thick E-PVD C deposition which itself is protected by the usual E- and I-CVD Pt coatings used in TEM foil preparation.

able tip holder called *microtip array* [181]: a Si 7.0×3.0×1.0 mm^3 plate which has been micromachined by deep reactive ion etching to expose 36 equally spaced cylinders 2.0 μm in diameter and 110.0 μm in height in a six by six array at its surface. The flat top of each cylinder, also called *post*, serves as a mounting base for individual APT tips. Using the micromanipulator, the free end of the extracted wegde is carefully placed in the centre of a post and attached there by I-CVD Pt depostion. After this, it is cut off the remaining wedge by the ion beam and the procedure can be repeated until all of the wedge has been distributed onto posts. On average, a wedge of the size discussed here yields up to eight APT tips. The final tip shape as discussed above is formed when the post is aligned parallel to the ion beam direction such that the latter can perform a sequence of annular milling steps with decreasing inner radius and ion beam voltage. In analogy to the final step of TEM foil machining, a low-kV milling is performed at 2 kV [184][181].

5.2.4. Transmission electron microscopy

TEM is an established method for microstructural, chemical and structural analysis enabling lateral resolution in the sub-nm range, especially since the development of aberration-corrected electron optics [186][187][188][189]. Its use in this thesis is of special importance, because it ensures site-specific determination of present phases. Moreover, it is crucial in identifying microstructural features discovered in APT analysis and therefore plays the role of a complementary technique. For the aim of this work, the data gathered in TEM serves as basis for the correlation of post-LIMET microstructure with FEM simulation results, as a means to better assess the APT-derived local elemental distributions and as a guide to the interpretation of the phases formed, their location with respect to the interference maximum and their relation to the thermodynamic and kinetic mechanisms presented in the theoretical part (cf. chapter 3.2).
Site-specific preparation of TEM foils as introduced above was the prerequisite of the analyses performed using a conventional, non abberation-corrected *JEOL 2010* TEM.

Its electron source is a LaB_6 cathode thermal emitter and its acceleration voltage was 200 kV. The main operation modes of the TEM in this project were *Z-contrast imaging*, *selected area diffraction* (SAD) for structural investigations and subsequent *bright-field* (BF) and *centred dark-field* (C-DF) imaging. All images were recorded using a CCD camera (type *Gatan*) with 1024×1024 pixels and data acqusition software GATAN DIGITAL MICROGRAPH V3.10.1. Phase identification through SAD patterns interpretation was a central issue. To this end, the TEM grids were mounted in a *double tilt holder* allowing for a convenient orientation of the TEM foil with respect to the direct electron beam for recording *zone-axis SAD patterns*. Only the latter were taken as a reliable source of structure information and were manually analysed using the vector graphics software *CorelDraw X4* along with the sources of crystallographic data [190]. Moreover, correct calibration of the TEM system was ensured in each session by taking zone-axis SAD patterns of a foil made of single-crystalline Si and comparing the measured d-spacings to the corresponding ICDD pattern (27-1402 [190]).

5.2.5. Atom probe tomography

Kelly and Miller characterised *atom probe tomography* (APT) as a specially suitable method for quantitative examinations of interfaces in layered materials, since it is able to unveil chemical intermixing and interface morphologies by sub-nm resolved imaging and compositional information with < 10 ppm sensitivity at the same time [182][191]. Thus, its use as a complementary technique to the crystallographic and microstructural analyses obtained by TEM makes it an ideal option to complete the characterisation of the present multilayers and their chemistry [192][185][183]. In particular, the alteration of the elemental distributions as a function of the distance to a laser interference maximum was of interest. APT was derived by combining some principles of *field-ion microscopy* (FIM), which is a lensless point-projection technique for atomically resolved imaging of ideally shaped needle-specimens, with *time-of-flight mass-spectroscopy* (TOF-MS) for compositional analysis regarding elements and isotopes [193][192]. A representation of

the main setup of the latest development of the APT technique is depicted in figure 5.5. It shows the schematic of a *local electrode atom probe* (LEAP) as used in this thesis (CAMECA LEAP 3000X HR).

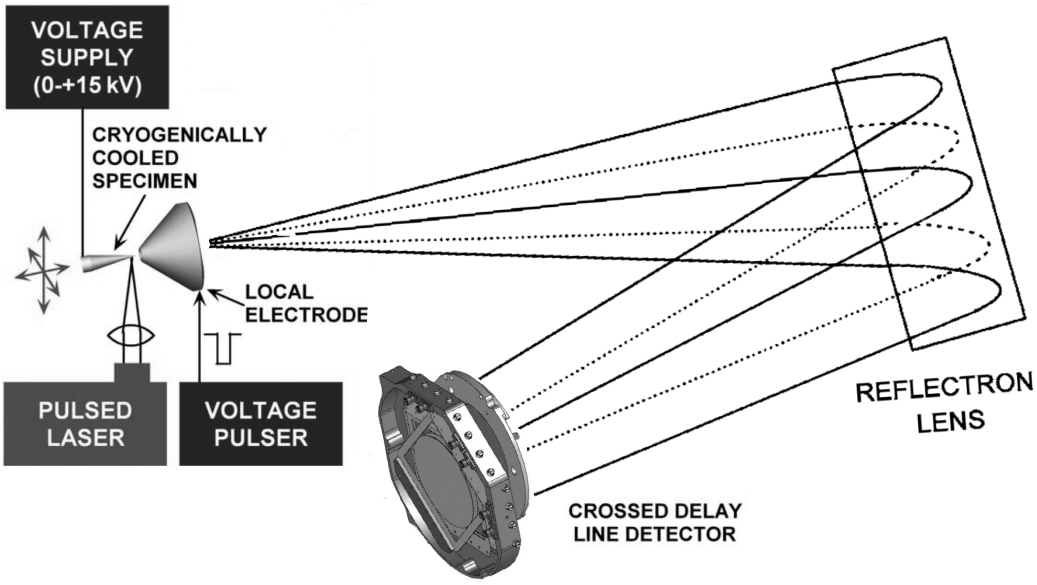


Figure 5.5.: Schematic representation of the general setup of the APT system employed in this thesis. The trajectory of the ions through the reflectron lens is indicated by the curved lines (modified and rearranged after [182][192][183]).

The FIB-milled specimen tip (see section 5.2.3) is brought into a UHV chamber at a pressure $p < 10^{-8}$ Pa and cooled down to cryogenic temperatures between 20 and 70 K [185][183]. Its apex, having a radius r_{tip} of approximately 50 nm, is positioned opposite to the 30 to 50 μm circular opening of a cone-shaped counter-electrode (*local electrode*) at a distance less than the aperture diameter. Applying a high positive DC potential U_{DC} of 2 to 15 kV to the specimen, the average electric field at its tip calculates to

$$E_{tip} = \frac{U_{DC} + U_{pulse}}{k r_{tip}} \tag{5.7}$$

where $k \approx 3.3$ represents a geometrical factor necessary to correct for the deviation of the cone-like specimen from a perfect sphere [194][193][195]. Typical electric field magnitudes

range between 15 and 65 V/nm. Depending on the specimen material and its atomic binding energies, these values are sufficient to remove atoms at the tip´s surface by *field evaporation* [183][195]. Upon leaving the tip, the positively charged ions can change their charge state by *post-ionisation* within the enhanced electrical field in the vicinity of the tip [196]. Subsequently they are accelerated by the field and attain their final velocity v within a distance roughly corresponding to a few tip radii. v is assumed constant on the whole path [182]. They then travel along diverging trajectories to a position-sensitive detector at a distance s from the specimen, where imaging magnifications M exceeding 10^6 can be achieved as calculated by

$$M = \frac{s}{\kappa r_{tip}} \tag{5.8}$$

with $\kappa \approx 1.65$ as the *image compression factor* according to [194][192][193][195]. In order to use these processes to obtain reliable spatially resolved elemental distribution maps, a precise control of the evaporation is mandatory. To this end, two different approaches are useful to trigger the evaporation:

- Voltage pulsing: Limited to conductive materials (with conductivities larger than 10^4 S/m), the standing positive DC voltage U_{DC} at the tip can be superimposed by applying a negative polarity voltage pulse to the local electrode as shown in figure 5.5. Hence, it enhances the effective electric field at the tip and thus triggers the trace of the mass spectrometer for chemical analysis. Common values for the amplitude of the voltage pulse U_{pulse} are on the order of 0.15 to 0.2 U_{DC} and its duration is on the order of ns. These parameters and applied temperature T, need to be chosen such that no atoms are preferentially evaporated by the standing voltage and that all surface atoms have the same probability to be removed during a pulse [182][185]. Depending on the ionisation state n of the removed atom, energy conservation as the basis for the TOF analysis is formulated as follows:

$$\frac{m}{n} = \frac{2q_e}{s^2} \left(U_{DC} + U_{pulse}\right) t_{TOF}^2 \tag{5.9}$$

with ion travel time t_{TOF} and *mass-to-charge ratio* m/n in Daltons or amu representing the elemental or isotopical information [193][182].

- Laser pulsing: A certain evaporation rate can be attained with a lower total potential field compared to voltage runs by irradiating the end tip with a focused pulsed laser beam of energy per pulse E_P. To date, lasers with pulse durations in the ps and fs scale and wavelengths between 355 and 532 nm are utilised. The physical mechanisms of this laser-induced atom evaporation are still under discussion, but range between the mere addition of *thermal energy*, *direct photo-ionisation* and the generation of a *pulsed electric field* at the specimen apex. As with voltage pulsing, here the laser pulse represents the trigger event for field-evaporation. Introducing this operation mode, the spectrum of materials analysable with APT could be widened to even include insulators. It needs to be mentioned, that especially the geometry of the specimen tip needs to be adapted suitably to laser pulsing, since its mass resolution is sensitive to the duration of heat extraction from the tip [194][182][185].

Both pulsing methods effectively remove atoms layer by layer from the tip, which gradually increases r_{tip} thus yielding an increase in U_{DC} (equation 5.7) in order to maintain a constant evaporation rate. Ultimately, this leads to early sample fractures when the mechanical stresses imposed by the electrical field overcome the cohesive forces of the tip material, which is more likely to happen in voltage pulse APT since higher field magnitudes can be expected [194][185].

Looking at the flight path of the ions in figure 5.5, three components that are important for the superior performance of the LEAP system over preceding APT instruments can be discerned. The *local electrode concept* reduces the standing voltages and U_{pulse} necessary to induce evaporation and it enables the use of higher pulse frequencies between 50 and 250 kHz. The latter significantly reduces measurement time and thus enhances the

accessible field-of-view [182][185]. Introducing an electrostatic mirror (*reflectron*) into the flight path, the ion trajectories are altered mainly in their length. The resulting energy compensation enhances the possible mass resolution when compared to straight-flight-path APT systems. Finally, the ions hit a position sensitive detector consisting of a *multichannel plate* (MCP) and *delay line detectors*. There, the TOF signal carrying information on chemistry and original location of the ion in the depth direction z is combined with its impact location on the MCP yielding the complete $(x, y, z, m/n)$ data needed for a computerbased three-dimensional reconstruction of the specimen tip [192]. The current design of the MCP restricts the detection efficiency of the LEAP systems to 60 % due to ions hitting insensitive wiring [182]. The actual efficiency of the system employed here amounts to ca. 37 % due to the reflectron mesh. Moreover, evaporation rates larger than 2 % increase the probability of multiple ion hits at the same time, which makes them indiscernible. With these characteristics and under ideal conditions, actual LEAP systems are able to reach detection rates on the order of 5×10^6 ions/min and mass resolutions $m/\Delta m$ FWHM of 1200 [185].

Pulse energy E_P (nJ)	Pulse frequency f (kHz)	Temperature T (K)	Evaporation rate (%)
1.0	50	40	0.5

Table 5.2.: Optimum process parameters for laser pulsing APT analyses of metallic multilayered thin films. An effective charge-state-ratio (CSR) of 0.024 was obtained.

As already stated, a great deal of experimental effort needs to be placed into estimating optimum measurement conditions for APT tips. Especially the material and temperature dependent evaporation fields need to be taken into account [196]. The present multilayer specimen mostly consisted of elemental combinations with significantly different fields leading to inhomogeneous evaporation and thus to problematic reconstructions of spatial distributions. Preliminary tests showed that the tips were prone

to early fracture when measured with voltage pulsing. Most probably this was due to the multilayer-substrate adhesion being weak compared to the electric field strengths. Hence, all specimens were scrutinised using laser pulsing APT at $\lambda = 532\,\mathrm{nm}$ and $\tau_p = 10\,\mathrm{ps}$, which automatically restricted the analyses of those multilayer stacks deposited on Si for thermal conductivity reasons (see above). The parameters given in table 5.2 proved reliable irrespective of the type of multilayer under investigation.

5.3. Finite element thermal simulations

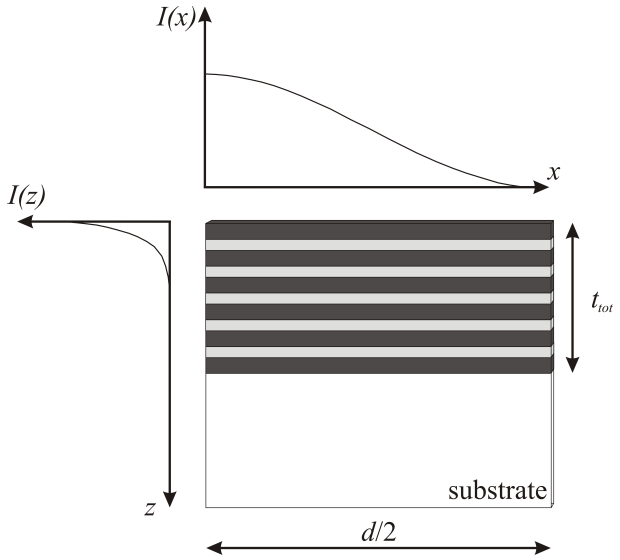


Figure 5.6.: Schematic depiction of a half-period of multilayer stack and substrate as used in the FEM simulations along with the spatial intensity distribution effective during LIMET: $I(x)$ representing the lateral and $I(z)$ the depth component (modified from [80]).

Trying to explain the microstructural evolution induced by LIMET only through post mortem characterisation would be an incomplete approach. This would omit the *thermal history* of the specimen embodied by the spatial and temporal temperature distribution $T(\vec{r}, t)$, which gives a clue to possibly initated phase transformations and microstruc-

tural changes within the heat-affected volume. The small dimensions both in space and time associated with this problem of ns-pulsed laser heat treatment of thin films hinder a reasonably well resolved experimental determination of $T(\vec{r},t)$. Hence, former projects dealt with this problem by providing estimations obtained by performing numerical approximations combining the *Finite Element Method* (*FEM*) with convenient analytical solutions for selected input data [19][79][171][80].

Their general approach was adopted here for the sake of comparison, yet adapted to the present materials and multilayer stackings. The aim is a possible explanation for the observed phase formation and its dependence on the relevant parameters periodicity d, fluence F and most notably the substrate material selected. Only a thorough correlation and interpretation of the resulting $T(\vec{r},t)$ datasets with the aforementioned microstructural information can deliver the insights needed.
Section 2.2 described the physical mechanisms underlying the use of laser radiation as a heat source. Combining these with the geometrical interference setup used for LIMET and its resulting spatial intensity distribution (see equation 5.3), the calculation of the spatial and temporal distribution of heat within the metallic thin film (geometry see figure 5.6) can be achieved by solving the homogeneous heat diffusion equation according to *Fourier´s second law* [68][67][83][81][79]

$$\rho(T)c_p(T)\frac{\partial T(\vec{r},t)}{\partial t} - \nabla\left(\lambda_{th}(T)\nabla T(\vec{r},t)\right) = Q(\vec{r},t) \tag{5.10}$$

with $Q(\vec{r},t)$ representing the heat source term given in equation 2.12. Here, all relevant material parameters are introduced as values depending on temperature T, which must be accounted for when trying to solve equation 5.10 by means of FEM[2]. The software package used here (*Comsol Multiphysics V3.5a*) already provides a database with temperature-dependent functions of density ρ, specific heat capacity c_p and thermal conductivity λ_{th} for most of the materials under investigation in this thesis.

[2]For the sake of clarity, the temperature dependent notation of the variables will be omitted in further equations.

Those not covered can be introduced by the user when adequate literature data is available to generate sectionally continuously differentiable functions for the interval from ambient to boiling temperature. Solving this differential equation 5.10 leads to a normal parabolic diffusion of heat in a body, where the thermal diffusion length of equation 2.19 is valid [67][81]. The following necessary boundary conditions and assumptions form the basis of the simulations performed here according to successfully applied approximations in prior theses [19][79][171][80]:

- Geometrical setup: The two-beam interference pattern used for LIMET allows some simplifications with respect to dimensionality and size of the specimen portion that is simulated. Hence, the simulations could be run more efficiently from a numerical standpoint. Due to symmetry, only a two-dimensional cut in the (x-z) plane needs to be considered, where x denotes the base vector perpendicular to the interference lines and z the vector in the depth direction (cf. coordinate system in figure 5.3 (b) and the cross-section model in figure 5.6).

  As shown by [80], the lateral dimensions of the simulation can sufficiently be restricted to the distance between an interference maximum and an adjacent interference minimum location $x \in [0, d/2]$ and depth $z \in [0, 5\mu\text{m}]$. While the first was introduced due to symmetry, the latter was established considering the thermal diffusion length of the materials forming the multilayer-substrate system with respect to the time interval of the simulation ($t \in [t_0 = 0, t_{sim}]$). Adjusting the interference pattern given in equation 5.3 to this simulation of a half-period yields

  $$I(x, y, z = 0, t) = 4I_0 \cos^2\left(\frac{\pi}{d}x\right) \tag{5.11}$$

  as a convenient representation of the intensity distribution at the surface introduced in equation 2.15.

- The simulation time t_{sim} was selected to be 250 ns and thus 2.5 times longer than the simulations of [171][80] due to the introduction of fused silica as additional

substrate material. By this, a closer examination of the temporal temperature decay was possible. The laser pulse itself was initiated at $t = t_p$=30 ns.

- The boundary conditions for the initial temperature assumed the specimen in thermal equilibrium with its surroundings: $T(x = 0, z = 0) = T(x = d/2, z = 0) = T_{amb}$=298 K and the same for the temperatures at maximum depth z=5 μm. Moreover, $\frac{\partial T}{\partial z}|_{z=0} = 0$ impeding heat conduction through the surface (see also the last two items of this list).

- Phase transformations are included only with respect to transitions from solid to liquid and liquid to vapour (and vice versa), thus introducing contributions Q_m and Q_b to U_{trans} in equation 2.12. Accounting for other transitions, e.g. of intermetallic phase formation, would require exact knowledge, not only of the phases formed, but also of their respective volume fractions. In analogy to [79][171][80] the temperature functions at phase transitions, which normally exhibit numerically problematic discontinuities, are rendered continuously differentiable by introducing the *error function*. 50 K was taken as temperature interval $\Delta T_{0,trans}$, during which the latent heat of the transition is added or released in concordance with [79][80]:

$$Q_j = L_j \rho \frac{\partial}{\partial t} \left(\frac{1}{2} \mathrm{erfc} \left(\frac{T - T_j}{\Delta T_{0,trans}} \right) \right) \tag{5.12}$$

  with $j = (m, b)$ when considering melting or boiling with their respective transition temperatures T_j and latent heats L_j.

- Radiation losses at the specimen surface are not taken into account, yielding U_{rad}=0 (see equation 2.12).

- Convection losses both due to the surrounding atmosphere and due to molten material moved by surface tension gradients, gravitation or electromagnetic forces are neglected, yielding U_{conv}=0 (see equation 2.12).

Especially the last two issues can be explained as consequences of the limitations of the FEM approach to this problem. Calculating radiative losses at the surface would require a dynamical adaptation of the surface emissivity as a function of temperature and present phases. Convection in turn can be introduced in Comsol Multiphysics, but the necessary heat transfer coefficient α_{conv} is not straightforward to determine as stated in section 2.2. Including both into a suitable FEM code would require substantial simulation effort, which was beyond the scope of this thesis.

These above-summarised assumptions along with equations 2.15 to 2.17 were used to reformulate equation 2.12 to describe the heat source term $Q(\vec{r},t)$ of the parabolic heat diffusion in equation 5.10 for the present laser irradiation:

$$\begin{aligned} Q(\vec{r},t) &= -\nabla I(\vec{r},t) + U_{trans} \\ &= 4I_0 \cos^2\left(\frac{\pi}{d}x\right)(1-R)\,\delta \exp\left[-\delta z\right] P(t) - Q_m - Q_b \end{aligned} \tag{5.13}$$

where pulse duration function P(t), the surface´s optical properties, reflectivity R and absorbance A(z), are introduced as discussed in section 2.2. Here, the absorption coefficient β of equation 2.16 is replaced by the skin depth δ (see equation 2.8) of the topmost metal layer in concordance with the design of the multilayer stack, cf. section 5.1. In the same section, the dependence of the optical properties on the actual temperature was pointed out. As already discussed in [79], especially the reflectivity R regulates the heat introduced into the material and its variation with temperature needs consideration. Literature, however, shows that in the case of relatively low reflectivity at room temperature, its impact on the resulting heating of the sample can be neglected [197][198][199][200][201]. This is valid in the present situation of either Ni or Ti assuming the toplayer and for a laser wavelength of 355 nm. These and all other material properties relevant for the simulations are taken from the materials library of Comsol Multiphysics V3.5a and [118].

The simulations performed here served in a dual role. On the one hand, their results were interpreted in conjunction with microstructural SEM and TEM analyses, especially when looking at the expansion of molten material volume both in the lateral and the depth directions (see section 6.2.2). On the other hand, they were intended to deliver a broader overview of the impact of the critical processing parameters reaching beyond the scope of the LIMET experiments and their subsequent microstructural evaluation.

6. Results

6.1. FEM thermal simulations

Prior to actually laser-patterning the multilayers, thermal simulations were performed in order to assess the spatial and temporal temperature distribution $T(\vec{r}, t)$. It serves as a basis for subsequent assumptions concerning the *dimensional expansion* of the heat-affected material volume in which a sufficient intermixing of the constituent elements and a through reaction can be achieved. Moreover, approximations of the melt time interval $\tau_{(l)}$ can be extracted, enabling an estimation of the relevant *processing time scale*. The ultimate motive of these simulations is to define a reasonable LIMET processing window regarding fluence F and periodicity d, wherein comparable material modifications are likely to be achieved. Since the simulations do not contain contributions of processes which lead to the damage of the multilayer by delamination or dewetting, a more complete view of the processing window is attained only when coupled with microstructural observations. To get a feeling for the influence of the substrate material, the fluence and the periodicity, the Ni/Al system is taken as the principal system. The differences in behaviour arising in the other multilayer material systems are discussed later on. A critical prerequisite to the simulation tasks here is the knowledge on temperature-dependent heat transport properties of all involved materials as inferred by section 2.2. An according literature research revealed, that sufficient data is available for all components in question except for thin film a-Si_xN_y. Most studies of their transport behaviour are restricted to temperatures up to 400 K [202][203], and thus not suitable for the temper-

ature range to be expected here based on prior results [19]. Hence, a-Si$_x$N$_y$ is excluded from the simulation tests, but serves as a comparison in actual experiments because its room temperature heat transport properties are situated between those of the other two substrates (see table 4.1).

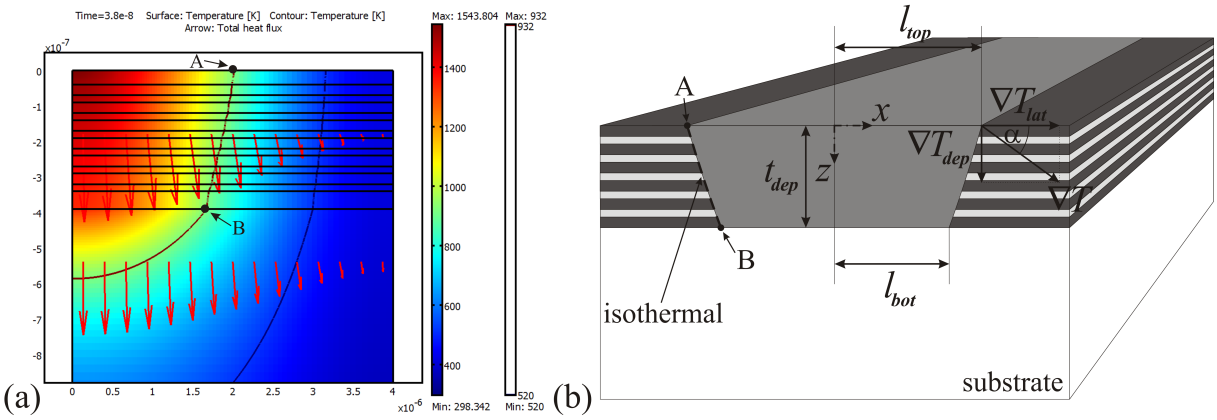


Figure 6.1.: 2D representation of the $T(\vec{r}, t)$ results (a) of the FEM thermal simulation obtained for Ni/Al on sc-Si irradiated using a nominal fluence F of 275 mJ/cm^2. General coordinate frame used in the following for the description of the FEM results (b) introducing the propagation coordinates of the (s)-(l) interface (points A and B of the component with smaller T_m) as well as the effective thermal gradient ∇T there.

Figure 6.1 (a) depicts a representative simulation of the two-dimensional temperature distribution at the maximum lateral and depth expansion of the heat-affected zone. To clarify the type of spatial heat propagation, lines of constant temperature, *isotherms* (e.g. see line between points A and B) are included. They are selected to match critical temperatures of the metallic components, like the melting point T_m and $0.3 \cdot T_m$, which are of interest in assessing the melting and the diffusion behaviour, respectively. Obviously, the almost perpendicular alignment of the isotherms with respect to the multilayer surface, points to a pronounced lateral propagation of the heat as expected for SLG conditions [57]. In a first approximation, the volume which is bounded by the

isotherm representing the melting temperature of the metallic component with lower T_m is treated here as an *ideally intermixed region*. Therein, the temperature is higher than the melting temperature, thus a more complete blend is expected to be achieved due to an enhanced mobility of atoms in (l) phase and possible convection effects. Moreover, the corresponding region in actual specimens can readily be identified by cross-sectional imaging of the microstructure. In figure 6.1 (b) a simplified schematic of the intermixed region is given along with a definition of experimentally accessible values needed for a quantitative comparison between the thermal simulation and the laser processing. The lateral expansion along the x-axis is primarily measured by l_{top}, describing the position of point A. Point B describes the isotherm propagation both in depth t_{dep} and laterally l_{bot}. As long as the isotherm only intersects the z-axis, t_{dep} is the sole measurable value. When the isotherm reaches the multilayer-substrate interface, which is indicative of a through reaction, t_{dep} is constantly equal to t_{tot} while its intersection point B then travels parallel to x in the interfacial plane at a distance l_{bot}. To reasonably compare specimens with different periodicities and/or multilayer thicknesses, these three values are normalised with respect to $d/2$ and t_{tot}.

6.1.1. Influence of substrate, periodicity and fluence – Ni/Al

Besides the melt life span $\tau_{(l)}$ and the normalised coordinates of points A and B, other primary values to compare the different processing influences can be extracted from the temperature distribution field $T(\vec{r}, t)$. These are the surface temperature at the centre (0,0) of the interference maximum T_{max} and the fractional portion $f_{(l)}$ of molten low-T_m metal, here Al. Based on previous simulation studies of LIMET processing [19][79][171][80], the range in F and d can be narrowed down to 100 to 300 $\mathrm{mJ/cm^2}$ and 2 to 24 μm, respectively. The following figure 6.2 compiles the (d,F)-dependence of T_{max}, $f_{(l)}$ and $\tau_{(l)}$ encountered in Ni/Al multilayers deposited onto sc-Si (highlighted by □). It is brought together with the corresponding data for a-SiO_2 (designated with ■) allowing for a direct comparison of the substrate effect.

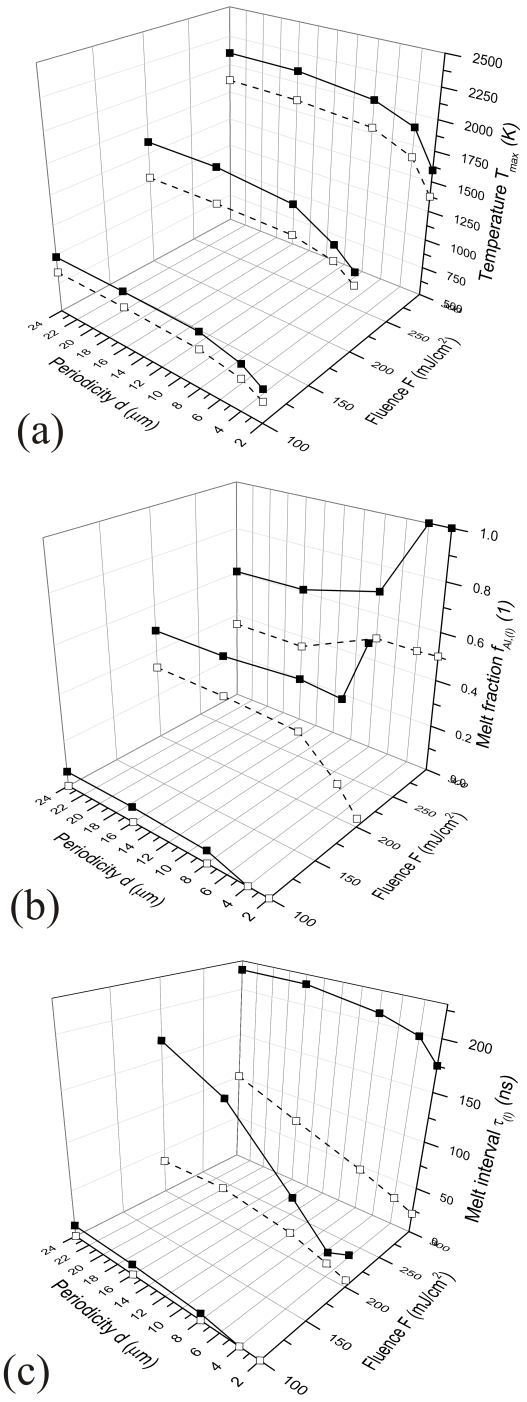


Figure 6.2.: Direct comparison of the thermal simulation results obtained for Ni/Al on sc-Si (□) and fused silica (■) when varying d and F: (a) maximum temperature T_{max} at the multilayer surface of the interference maximum location. (b) fraction of molten Al and (c) duration of the Al melt.

Obviously, T_{max} as a function F and d (shown in 6.2 (a)) follows the same functional trend for sc-Si and a-SiO_2, except for the fact that the result surface[1] representing the latter is shifted to higher temperatures by approximately 20 to 30 %. This does not seem surprising when taking into account the considerably large difference between the involved thermal transport parameters. The much lower λ_{th} and D_{th} of fused silica does not allow for a quick removal of the delivered heat, leading to this behaviour. The result surface is exemplarily described for the case of the sc-Si substrate. Increasing the fluence leads to an almost linear increase in T_{max}. In turn, with rising periodicity, an increase in T_{max} can be observed, which saturates to a constant value for d equal or greater than 8 μm. If restricted to the stationary part of the result surface, calculated T_{max} increases with F from ca. 900 to 1900 K for Si and ca. 1000 to 2100 K for fused silica.

Conversely, while a fluence of 100 mJ/cm^2 is not sufficient to melt a significant part of the Al layers in the case of sc-Si irrespective of d (c.f. figure 6.2 (b), wherein the corresponding molten fraction $f_{(l)}$ is depicted), on a-SiO_2 already 10 % of the topmost Al is molten, when the 8 μm threshold is exceeded. In contrast to $T_{max}(d,F)$, the result surface for $f_{(l)}$ of both substrates shows a different behaviour. For intermediate fluences, $f_{(l)}$ increases with increasing d in analogy to the corresponding T_{max} characteristic, leading to a stationary melt fraction of ca. 35 %. Looking at the same irradiation conditions for a-SiO_2, a strikingly different course of the function is revealed. At 2 μm periodicity, already 70 % of the Al layers are in (l) state. With rising d, the fraction sharply drops to a then constant value of 50 %. A possible explanation for this difference lies in a co-operative hindrance on heat transport imposed both by the poorly conducting substrate and the close proximity of the adjacent interference maxima at d=2 μm. Under these conditions, lateral and depth heat transfer are just as difficult.

[1] The term *result surface* in the following will refer to the 3D representation of a simulation result for a certain substrate as a function of d and F.

This is even more pronounced at 300 mJ/cm^2 irradiation, where a complete melting of Al is calculated even for a 4 μm periodicity, followed by a similar drop to a constant 60 %. Then, even on the sc-Si substrate the influence of the proximity of the interference maximum can be observed, albeit with a significantly smaller molten portion of 50 %, which reduces by ca. 10 % upon entering the stationary d range. Hence, figure 6.2 (b) infers to preferably employ fluences above 200 mJ/cm^2 and it strengthens the argument for the already derived 8 μm periodicity threshold.

Figure 6.2 (c) compares the calculated melt life spans $\tau_{(l)}$ within the same (d,F) parameter field. Once again, for Si a behaviour analogous to its $T_{max}(d,F)$ surface is a result of the simulations. At 200 mJ/cm^2 fluence, $\tau_{(l)}$ increases from 7 to 40 ns, while a similar course ranging between 25 and 100 ns is seen for 300 mJ/cm^2 with both curves appearing to follow a linear function. As expected, fused silica exhibits significantly larger melt durations. With intermediately intensive irradiation, a similar increase is observed there, but ranging from 25 to 170 nm, corresponding to an approximate increase by a factor of four. Only at the smallest periodicity, an increased melt duration of 35 ns is registered in concordance with the diminished heat transport capabilities. The data from the 300 mJ/cm^2 fluence can be assessed only up to d=8 μm, since the melt duration of higher periodicities exceeds the total simulation time t_{sim}. Attempts to increase t_{sim} were unsuccessful due to convergence problems in COMSOL´s solver routine and were not pursued further. Even so, $\tau_{(l)}$ increases from 175 to 210 ns for lower d if not in a linear manner. Taking into account the findings on d-related behaviour so far, it seems reasonable to narrow down the associated interval to 4 to 16 μm.

For comparison with cross-sectional micrographs later on, the normalised dimensions of melt expansion need to be considered, which are compiled in figure 6.3, continuing the combined depiction of the two substrates under consideration.The lateral position of point A at the multilayer surface (cf. figure 6.1) is given in figure 6.3 (a).

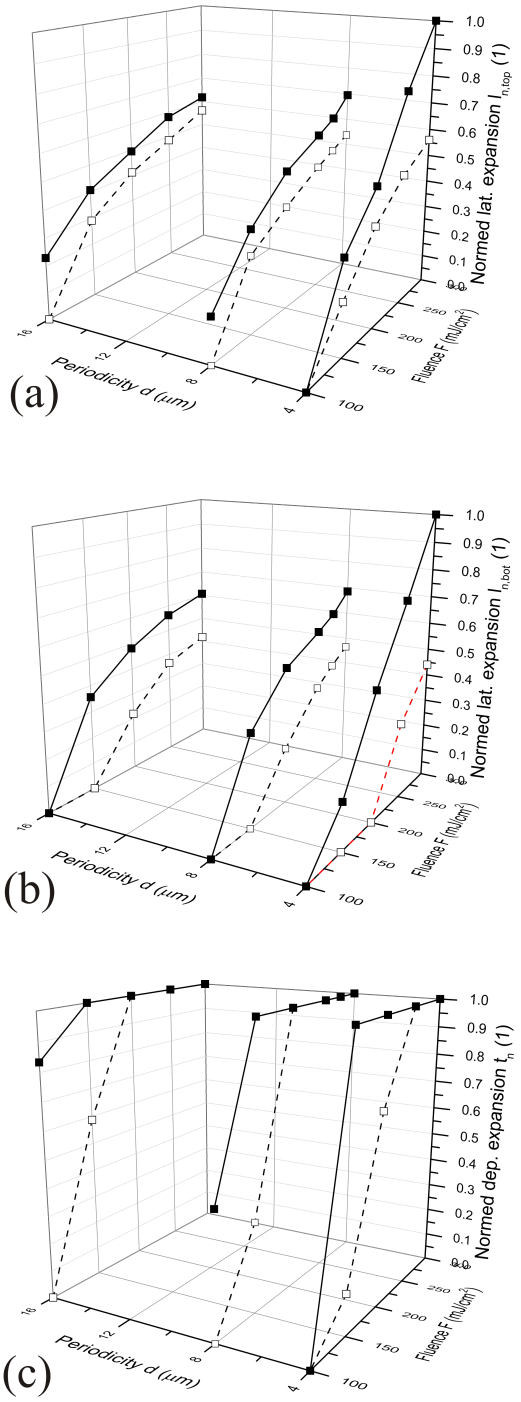


Figure 6.3.: Direct comparison of the thermal simulation results obtained for Ni/Al on sc-Si (□) and fused silica (■) when varying d and F: normalised lateral propagation of point A l_{top} (a) and normalised propagation of point B in lateral l_{bot} (b) as well as in depth direction t_{dep} (c) (all quantities introduced in figure 6.1 (b)).

For sc-Si the F dependence of normalised l_{top} takes on the same functional form for all selected periodicities. A non-linear increase with F is observed, which reaches a saturation at approx. 50 to 60 % of $d/2$ for fluences above 250 mJ/cm^2. Moreover, thanks to the normalised representation, it is clearly visible that even the fraction of lateral expansion assumes the same values irrespective of d, supporting earlier findings on $f_{(l)}$. Looking at the normalised lateral position of point B located at the multilayer-substrate interface (see 6.3 (b)), a similar behaviour can be seen, except for a slightly lagging lateral travel, first setting in at fluences above 150 mJ/cm^2 and finally reaching only 40 to 50 % of $d/2$. This means that on sc-Si a through reaction is to be expected for F exceeding 200 mJ/cm^2. This is confirmed by figure 6.3 (b), showing the normalised travel in depth of point B. It reaches 100 %, and thus a complete melting down to the substrate for the fluence threshold stated above. Returning to the interpretation of the lateral lag of point B, conclusions can be drawn concerning the alignment of the isotherm with respect to the z-axis representing the normal of the film plane. Here, the isotherm seems to be slightly inclined with respect to the z-axis, which can be interpreted as follows: a superposition of velocity components in x- and z-directions dictates the overall propagation of the isotherm.

Turning to the expansion behaviour of a-SiO_2, similar functional shapes can be observed, which nonetheless exhibit two considerable differences. First, the two lateral characteristics shown in figures 6.3 (a) and (b) are shifted to higher $d/2$ fractions. For periodicities equal or greater than 8 μm, the shift amounts to ca. 30 %. Analogously, a threshold fluence for a through reaction can be observed there and with the aid of figure 6.3 (c). Its value is approximately located at 150 mJ/cm^2 and thus 50 mJ/cm^2 less than the corresponding value for sc-Si. Moreover, for d=4 μm, no saturation in lateral propagation both at the surface and the interface is visible. Here, a rather linear behaviour with respect to F can be observed. Second, except for F=100 mJ/cm^2, the fractions of lateral travel both of point A and B assume the same value. In the sense of the

discussion above, this indicates the isotherm propagation in multilayers on fused silica to take place purely laterally. The interpretation of the lag in lateral travel between points A and B as an indicator for the isotherm orientation already implies that more data can be extracted from the simulations dealing with the actual direction of the heat flow within the given coordinate frame.

Returning to figure 6.1 (b), the location of point A is depicted as a reference coordinate for two thermal gradient vectors, ∇T_{lat} and ∇T_{dep}, whose superposition yields the effective gradient vector ∇T. In line with the basic theories of heat transport, ∇T points in the direction of the actual heat flow. Both of its vector components at A (see figure 6.1 (b)) can be calculated by conveniently fitting the local thermal distribution along the two coordinate axes[2] and subsequently differentiating with respect to x and z. The results of these calculations as a function of F and d for both substrates are shown in figures 6.4 (a), for ∇T_{lat} and (b), for ∇T_{dep}. Both are estimated to be situated mostly on the order of intermediate 10^8 to lower $10^9\,\mathrm{K/m}$ values. The most striking insight can be gained in figure 6.4 (a).

Apparently, the two substrates do no effect a significant difference in the lateral component of the thermal gradient. Both $\nabla T_{lat}(F, d)$ result surfaces match each other exactly with relative deviations on the order of only 10 %. They show a non-linear decline with increasing d, which saturates at 0.10 to $0.25{\cdot}10^9\,\mathrm{K/m}$ for periodicities above $8\,\mu$m, irrespective of F. Increasing fluence in turn effects a pronounced rise in magnitude of the gradient component at lower periodicities. At d=2 μm it ranges between 0.50 and $1.00{\cdot}10^9\,\mathrm{K/m}$. The effect of substrate selection only becomes evident when looking at the depth component (see figure 6.4 (b)). Here, only the shape of the $\nabla T_{dep}(F, d)$ result

[2] As equation 5.3 describing the spatial distribution of intensity generated by LIMET implies, the thermal distribution along x is fitted best by a function proportional to $\cos^2(x)$. In the depth direction, a linear fit served well.

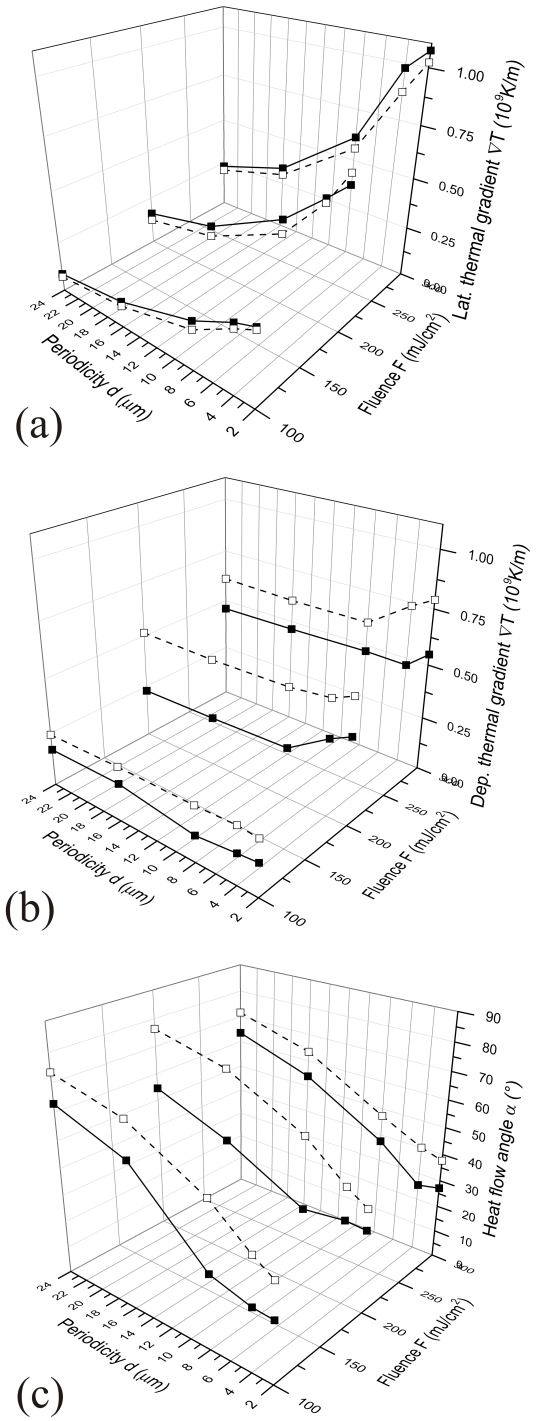


Figure 6.4.: Direct comparison of the thermal simulation results obtained for Ni/Al on sc-Si (□) and fused silica (■) when varying d and F: Thermal gradient at A-B boundary in lateral (a) as well as in depth direction (b). Corresponding heat flow angle α (c) (all quantities introduced in figure 6.1 (b)).

surfaces is the same, which shall be described exemplarily for sc-Si. Increasing d does not significantly affect the magnitude of ∇T_{dep}, giving a constant value, which rises from 0.25 to approximately $0.70{\cdot}10^9\,\mathrm{K/m}$ with increasing F. The result surface associated with fused silica is shifted to values 40 to 50 % of those of sc-Si, restoring the intuitive perception of the situation.

In order to figure out the orientation of the resulting heat flow vector, figure 6.1 (b) introduced angle α between the multilayer surface and effective thermal gradient ∇T. To perform a first order approximation, the composite effect of multilayer stacking on the heat transport properties (introduced in section 2.2) must be assessed according to equations 2.20 to 2.24 and the data of the individual components given in table 4.1. In the case of Ni/Al at room temperature, the lateral composite thermal diffusivity amounts to $59\,\mathrm{m^2/s}$ and $58\,\mathrm{m^2/s}$ in depth, while the conductivities are calculated to 180 W/mK and 145 W/mK, respectively (see table 4 in appendix V). Their differences are negligible, hence it is sufficient to calculate α based on the geometric relation between both gradient components, as summarised in figure 6.4 (c).

When taking into account the results of the two individual gradient components, it can be expected, that once again the resulting functional shape is the same for both substrate materials, which is the case. Apparently, F does not exert a significant influence on the magnitude of α for both substrates; rather, periodicity mostly dictates its behaviour. Both $\alpha(d, F)$ result surfaces are displaced by roughly 10 to 20 °. For d below $8\,\mu$m, α is considerably low, with a constant 25 ° for a-SiO_2 and 40 to 50 ° for sc-Si. With increasing d, a steep rise in α takes place reaching 65 ° and 75 °, respectively. The smaller angles between the effective heat flow vector and the multilayer surface for d equal or less than $8\,\mu$m point to a more pronounced lateral flow component. This confirms the findings described above concerning the hindrance exerted by the close proximity of heat sources at lower d. The significance of heat propagation in depth finally rises with

increasing periodicities and especially on sc-Si with its more favourable heat transport capabilities.

Summarising these initial approximations, first indications on a desirable processing window can be derived. Depending on substrate choice, the intended through reaction can be achieved when F exceeds a certain threshold value, which mostly is independent of d. As could expressly be shown in figure 6.3 (c), this value lies at $150\,\mathrm{mJ/cm^2}$ for fused silica and $200\,\mathrm{mJ/cm^2}$ for sc-Si. Their F vicinity should preferably be targeted during LIMET experiments. Moreover, the difference of these thresholds might point to a rule of thumb on how to identify reasonably comparable specimen states in the different substrate situations. In order to impede the discussed proximity problem, to achieve a more constant fraction of molten material (especially according to figure 6.2 (b)) and thus a more stable expansion of the heat-affected volume, periodicities above $8\,\mu\mathrm{m}$ are of interest. Clearly, these statements can only represent lower boundaries, since the effects of damaging phenomena are not seriously accounted for in the simulations.

6.1.2. Influence of multilayer material combination

Based on these perceptions, the effort put into simulating the effect of the combination of metallic elements can further be reduced. Following the concluding argument of the previous section, it seems reasonable to assume that restricting the perspective only to the F dependence at $d = 8\,\mu\mathrm{m}$ yields sufficient results for a meaningful comparison. Figure 6.5 lines up the according results of T_{max} (a), $f_{(l)}$ (b) and $\tau_{(l)}$ (c), where the individual material combinations are designated as 1 (Ni/Al) serving as reference, 2 (Ti/Al) and 3 (Ni/Ti) as well as empty (sc-Si) or filled (a-SiO_2) symbols for the allocation of substrate material. Like Ni/Al, the two other binary systems exhibit a linear rise in T_{max} with increasing F, with the exception that the T_{max} characteristics of the different substrates are not separated by 20 to 30 %. In fact, the difference in both curves for those systems does not exceed 3 %.

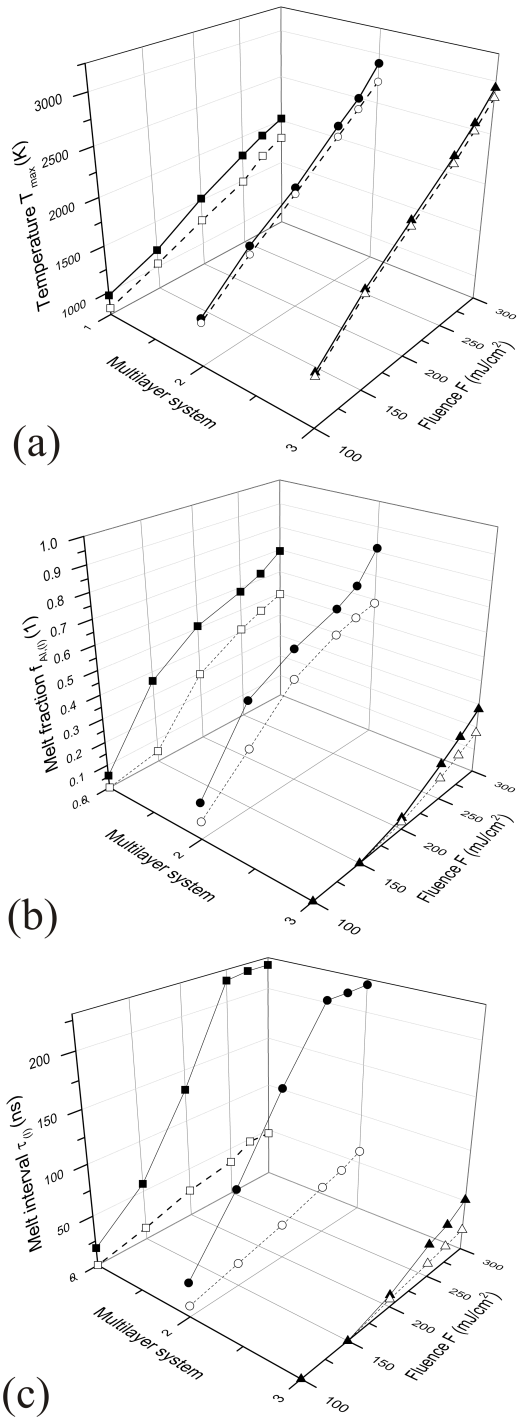


Figure 6.5.: Direct comparison of the thermal simulation results obtained for the three multilayer material systems (1-Ni/Al, 2-Ti/Al and 3-Ni/Ti) on sc-Si (open forms) and fused silica (filled forms) when varying F for a constant periodicity of 8 μm: (a) maximum temperature T_{max} at the multilayer surface of the interference maximum location. (b) fraction of molten $T_{m,low}$ component and (c) corresponding melt duration.

Directly compared with Ni/Al, they show a steeper rise and a significantly elevated temperature level. The latter is calculated to almost reach 3000 K for F at 300 mJ/cm^2 and thus is slightly lower than the boiling point of the respective topmost material layer (c.f. table 4.1). Apparently, both the reduced thermal transport capabilities of the capping layer alone in the case of Ti/Al and the combination of two materials with bad conduction and diffusivity like Ni/Ti lead to the same effect (see table 4 in appendix V). The heat deposited at the interference maximum cannot be efficiently transported away leading to more increased surface temperatures due to its accumulation close to the surface.

Turning to the volume fraction of molten low-T_m material shown in figure 6.5 (b), the behaviour of Ti/Al is equal to the already described characteristic of Ni/Al even with respect to both substrates. This also holds for their melt life spans $\tau_{(l)}$ depicted in figure 6.5 (c). For obvious reasons, Ni/Ti deviates from this in both parameters. There, significant portions of melt are only formed when F surpasses 250 mJ/cm^2. On sc-Si, 20 % of Ni is molten during 25 ns for $F = 300\,\mathrm{mJ/cm^2}$. Under the same irradiation conditions but on fused silica, 30 % $f_{(l)}$ can be achieved for twice the time interval. The discussed near-surface accumulation of heat for Ti/Al and Ni/Ti should also be visible in the normalised dimensional expansion of the heat-affected volume shown in figure 6.6. Here also, the coordinate convention as well as the nomenclature of points A and B introduced in figure 6.1 (b) is applied. On a-SiO_2, Ti/Al once again closely matches the behaviour of Ni/Al in all normalised parameters (see 6.6 (a) to (c) and compare characteristics 1 and 2). sc-Si largely follows this similarity, especially with the lateral movement of A exactly following the trace of its fused silica counterpart. As for point B´s travel in x-direction, figure 6.6 (b) reveals its initiation at fluences increased by 50 mJ/cm^2 compared to a-SiO_2, but finally assuming a comparable fraction of $d/2$ of roughly 40 %. It seems likely, that these two observations together, can be attributed to the accumulation effect. A look at the normalised depth expansion in figure 6.6 (c),

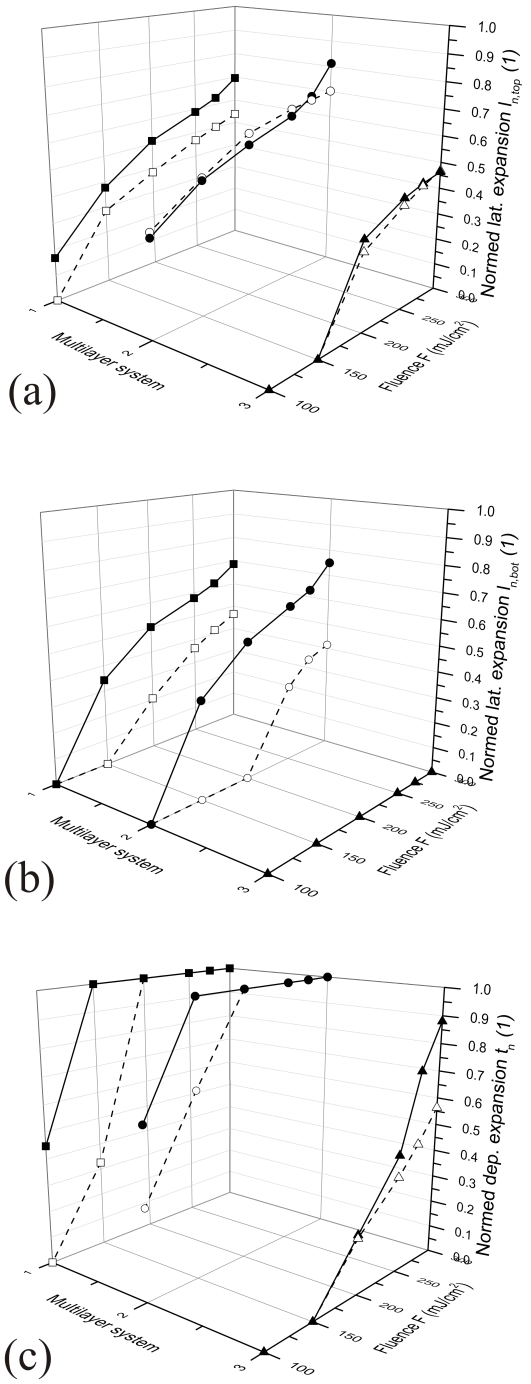


Figure 6.6.: Direct comparison of the thermal simulation results obtained for the three multilayer material systems (1-Ni/Al, 2-Ti/Al and 3-Ni/Ti) on sc-Si (open forms) and fused silica (filled forms) when varying F for a constant periodicity of 8 μm: normalised lateral propagation of point A l_{top} (a) and normalised propagation of point B in lateral l_{bot} (b) as well as in depth direction t_{dep} (c) (all quantities introduced in figure 6.1 (b)).

evidences that Ni/Al and Ti/Al are similar even with respect to the threshold fluences for a through reaction on both substrates. Ni/Ti, as the most unfavourable material combination with respect to heat transport capabilities, not surprisingly exhibits a different expansion behaviour. Within the F interval under investigation here, no through reaction is expected to be achieved according to figures 6.6 (b) and (c). The normalised depth expansion depicted in (c) shows no major difference between sc-Si and fused silica up to 250 mJ/cm^2. Upon reaching 300 mJ/cm^2, the heat-affected zone on Si expanded approximately 60 % of t_{tot} in depth, while it attains a value of almost 90 % on a-SiO_2.

Concerning the propagation of point A (in 6.6 (a)), the substrate choice has no apparent influence. In contrast to the other binary systems, which incorporate Al, the comparatively diminished heat transport properties lead to an accordingly reduced normalised lateral expansion of only 45 % at best. These observations also are in concordance with the notion of near-surface heat accumulation. In conclusion, these FEM-based estimations can be interpreted such that the choice of the metallic multilayer components dictates the expansion of the heat-affected zone.

To some extent, their influence is even more pronounced than that of the substrate selection: The presence of a high-T_m metal with unfavourable heat transfer deteriorates both the transport of laser energy away from the interference maximum and the achievement of a good mixture of constituent atoms. As for Ti/Al, this can be compensated by Al, leading to similar simulation results and thus the same conclusions regarding threshold fluences for through reaction on both substrates. Ni/Ti in turn affords the use of higher fluences above 300 mJ/cm^2 to yield the desired heat-affected volume, which in the case of sc-Si is likely to effect boiling of the capping layer at the interference maximum position, unwanted due to impending damage to the multilayer. These findings are included in the implementation of the subsequent LIMET experiments.

6.2. Microstructural characterisation and structure determination

6.2.1. As-deposited multilayers

To meet the requirement of specimen comparability, the specimen holder described in section 5.2.1 was crucial, since it enabled serial deposition of each multilayer set onto the three substrate types without breaking the vacuum of the I-PVD chamber. Initial tests to discover optimum deposition conditions showed that the sputter plume exhibited a directional characteristic leading to inhomogeneous film thicknesses on the substrates compared to macroscopic length scales. By a systematic assessment of local thickness distribution using FIB cross-sections, it could be shown, that this variation was negligible for areas on the order of a masked LIMET pattern. Thus, macroscopic areas with thicknesses ideal for the treatment could accordingly be identified and were focused on exclusively. Directly after deposition, all thin films presented untarnished metallic reflection and showed no macroscopic flaws like delamination or propagating cracks [204][205][206][113], irrespective of the substrate employed. This spoke in favour of the employed vacuum conditions and process gas quality as well as adhesive layer selection.

Ni/Al specimen sets

TEM cross-section imaging (as figure 6.7 (a) shows exemplarily for the case of Ni/Al on sc-Si) confirmed clearly distinct layers of the constituent metals Ni and Al in as-deposited state. No traces of other phases, like possible intermetallics or oxides could be found. This was confirmed by global structure analysis of the different substrates via GIXRD (for sake of brevity not shown here). Obviously, the grain sizes both in and out-of-plane (along normal direction n) did not exceed the respective t_i. Grain morphology thus was mostly globular and in concordance with structure zone models of thin film deposition for the I-PVD parameters used [207][208][209][210].

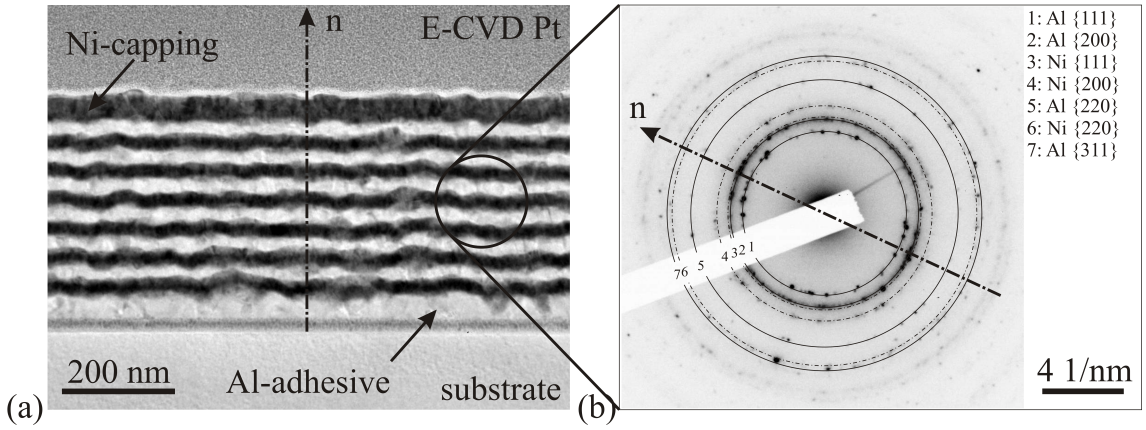


Figure 6.7.: Ni/Al as-deposited multilayer on sc-Si: TEM micrograph (a) and corresponding SADP (b) with qualitative phase analysis.

The cross-section moreover revealed several instances critical for the interpretation of the microstructural modifications issued by LIMET later on. Table 5 in appendix V compares the intended with the actually reached layer thicknesses as measured in the micrograph. Especially the Al layers, exhibited an enhanced film topography. Seen in conjunction with common theories of thin film growth as summarised by Thompson et al. [211], this was interpreted as a result of Al´s growth behaviour.

After initial cluster formation, island growth and their coagulation in the substrate surface plane, growth along normal direction sets in. Here, Al seemed to exhibit a reduced coagulation leading to spatially separated islands which then individually grew along the n direction. The gaps between them were filled with other incoming Al atoms, finally closing them up but lagging behind in n growth. Literature mainly attributes this observation to the surface energy of the deposited species, which governs the wetting and thus the coagulation behaviour [211]. As a result, a strong layer topography was formed, which was transferred to all subsequently deposited layers.

As can be inferred from table 5, the intended 1.00 overall composition ratio of the multilayer was shifted to the Ni-rich part of the phase diagram. Based only on the mean t_i values and also accounting for the actual contributions of the capping and the adhesive layer, a ratio of Al to Ni atoms of 0.66 (i.e. approximately Al 40 at.% and Ni 60 at.%) was achieved, which still was within the targeted composition range of B2-NiAl thus making this difference less important[3]. It is necessary to note, that this approach to estimate thin film chemical composition can only be treated as a zero order approximation, since it is based on employing bulk densities which seldom are present in thin film regime [206][113].

Temperature measurements by thermocouple and temperature-sensitive adhesive stripes performed in situ during deposition at the site of the mounted substrate showed the specimen to remain at 50 to 60 ° throughout the whole process[4]. Hence, thermal energy imposed by deposition was too low to initiate diffusion at the layer boundaries leaving only the topographic effect as an explanation for the observed diminished contrast. Besides these microstructural observations, local diffraction analysis with SAD patterns (SADP) was undertaken. Figure 6.7 (b) depicts the SADP taken in the central part of the multilayer using the smallest possible SAD aperture having an approximate diameter of 180 nm. It is shown to scale along with its location in figure 6.7 (a). Using star-quality ICDD reference charts, the qualitative phase analysis was performed.

The SADP exhibits a ring-like distribution of the principal reflections showing no clear orientation relation with respect to the substrate normal vector n thus emphasising the

[3] Attempts to confirm this result by EDX measurements in SEM were not conclusive. This was due to the unideal experimental conditions associated with using normal-incidence electrons for generation of characteristic X-rays, which is usually encountered when dealing with thin films and multilayers of this thickness range. The same held for analogous measurements of the other sample systems.

[4] The same temperature level was consistently recorded for the deposition processes of the other multilayer material systems.

notion of an untextured as-deposited multilayer. Here also, no signal of other phases could be accounted for. In the vicinity of the overlapping Ni {111} and Al {200} reflections a slightly diffuse background signal could be detected. Attempts to perform a meaningful analysis of deposition residual stresses based on X-ray diffraction methods were rendered impossible due to the diminished diffracted X-ray intensity of the higher-indexed planes of both phases.

Ti/Al and Ni/Ti specimen sets

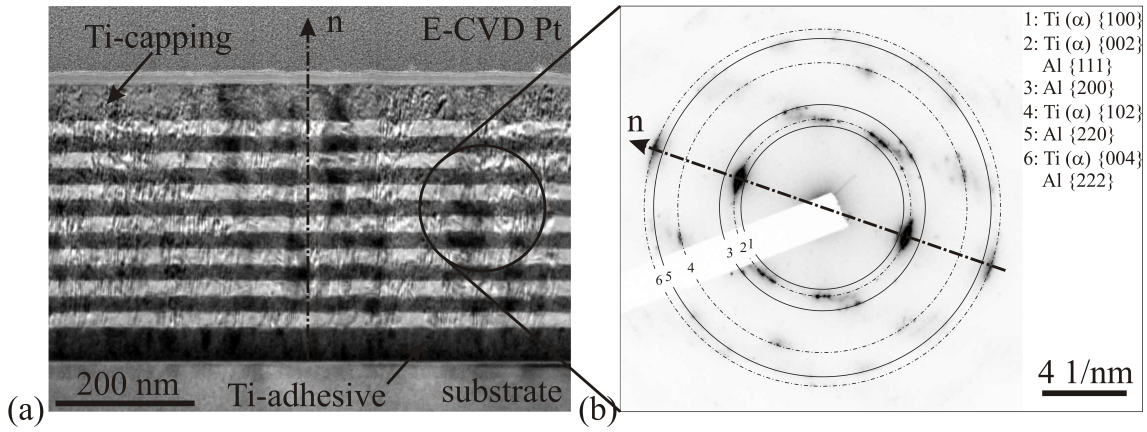


Figure 6.8.: Ti/Al as-deposited multilayer on sc-Si: TEM micrograph (a) and corresponding SADP (b) with qualitative phase analysis.

The same analysis procedure was performed on Ti/Al and Ni/Ti specimens. FIB cross-section imaging of all specimen types showed comparable deposition results within the respective sets. Figure 6.8 (a) shows the TEM bright field micrograph taken from the Ti/Al multilayer deposited on sc-Si, which exhibited distinctly different features when compared to Ni/Al. Likewise, globular grains with sizes corresponding to the individual layer thicknesses (see table 6 in appendix V) were seen. Looking at the adhesion layer, here made of Ti, it was striking to observe its comparatively homogeneous thickness and thus low topography. This effected the clearly more smooth growth of all following layers,

closely resembling the intended multilayer design. Considering the aforementioned table 6, the calculation of the actual overall multilayer composition ratio led to 0.87 Al to Ti atoms (i.e. approximately Al 46 at.% and Ti 54 at.%) still lying at the Ti-rich border of the $L1_0$-TiAl phase field.

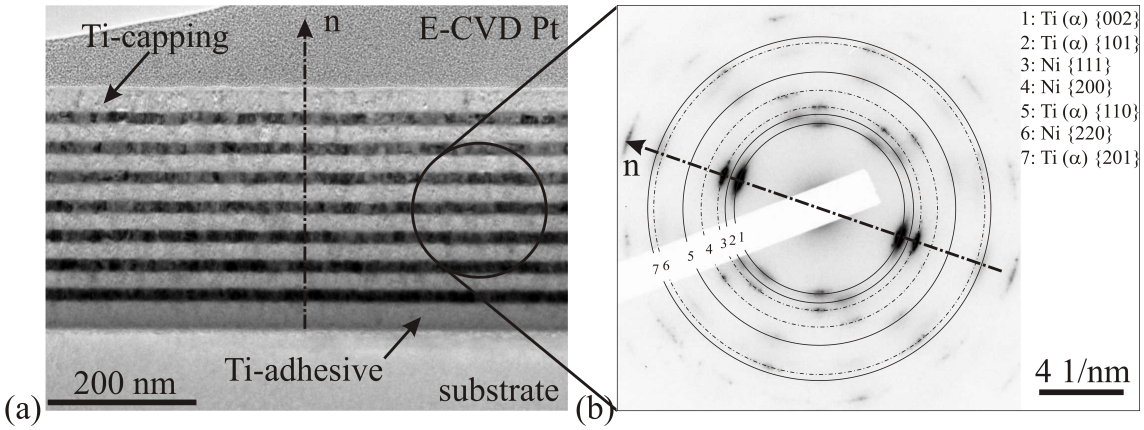


Figure 6.9.: Ni/Ti as-deposited multilayer on sc-Si: TEM micrograph (a) and corresponding SADP (b) with qualitative phase analysis.

Similar observations on layer topography and grain morphology were made in the cross-sectional TEM micrograph of Ni/Ti on sc-Si as shown in figure 6.9 (a). The selection of Ti as adhesion promoter here also proved useful in supporting desirable growth conditions (see table 7 in appendix V). Unfortunately these could not be brought on for Ni/Al specimens also, since the I-PVD facility employed in this study only allows for mounting of two different targets. It would afford breaking vacuum after deposition of the adhesion layer onto the substrates before multilayer growth, which cannot be recommended due to Ti being prone to fast oxidation when exposed to ambient atmosphere. The actual ratio of Ti to Ni atoms in the whole stack was calculated to 0.89 corresponding to ca. 53 at.% Ti and 47 at.% Ni thus being situated at the Ti-rich phase boundary of the intended B2-NiTi phase field. Local structural characterisation of Ti/Al and Ni/Ti by SAD patterns (see (b) of figures 6.8 and 6.9) essentially yielded the same result.

In both cases, only diffraction peaks of crystalline constituent metals were detected and verified by star-quality ICDD data. Ti always appeared in its low-temperature α form. Interplanar spacings $d_{\{hkl\}}$ of all reflections were close to the reported standard values. The most striking difference with Ni/Al´s as-deposited SADP was found when considering the distribution of diffraction peaks with respect to the specimen normal direction n. Along the indicated n vector, only spots of α-Ti {002} and Al {111} as well as α-Ti {002} and Ni {111}, respectively, were aligned. All other reflections were at the correct angular locations as set by crystallography. In those two cases, the expected PVD growth texture with the close-packed planes of the constituent phases lying in the substrate plane was visible. Clearly, the growth of these planes occurred along the incident direction of the sputtered ions finally leading to *fibre textures*. Most of the reflections showed an angular distribution slightly below 15 ° around n pointing to a slight texture spread.

6.2.2. LIMET-processed multilayers

Surface characterisation

Section 5.2.2 already introduced the experimental systematics for the LIMET processing of the multilayer stacks. A fluence series between 50 and 750 mJ/cm^2 was performed employing the three periodicity setups (4, 8 and 16 μm) identified by thermal simulations (see section 6.1) on all sample types. The aim of this was to get information on critical irradiation density thresholds for damage and ablation as well as on quality and homogeneity of the interference pattern. To this end, the individual spot areas were examined in top-view both by light microscopy (in bright and dark field mode) and SEM. Ablation represented a reasonable choice as a parameter to sort the irradiation spots, since it bears twofold significance. First, increased ablation obviously impedes the use of the LIMET-treated multilayer in real applications.

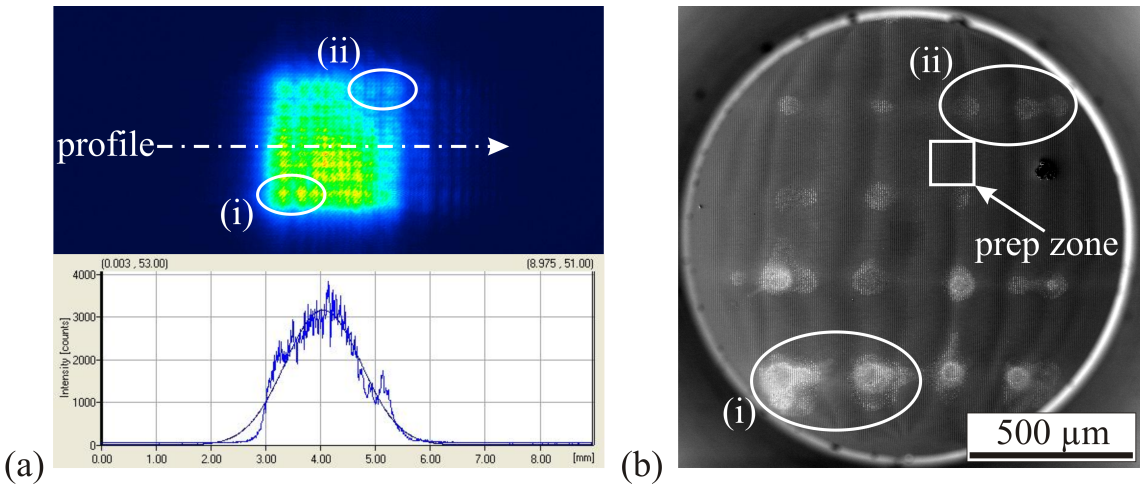


Figure 6.10.: Characterisation of the spatial intensity distribution of a LIMET spot obtained by beam profiling (a) (modified from [172]): 2D colour coded representation (top) and 1D profile measured along the dash dot line (bottom). SEM top-view micrograph of a typical LIMET spot (b): zone suitable for site-specific specimen preparation (*prep zone*) indicated.

Second, it can rather easily be made experimentally accessible by means of bright-field light microscopy and an according subsequent image data processing. Since ablation exposes the underlying substrate, the bright-field image shows a well-detectable difference in greyscale with respect to the intact regions showing metallic reflection. This difference can be utilised in defining a convenient greyscale threshold which separates these distinct regions in the spot. Before going into further detail on these procedures, it is instructive to take a closer look at the spatial distribution of the laser intensity within the irradiated spot. Figure 6.10 (a) shows quantitative information on this in 2D (top) and 1D (bottom) obtained by beam profiling measurements of a single laser pulse using a MetroLux, beamlux II basic area detector system [172].

Without anticipating the oncoming results, the situation depicted in this figure gave clues necessary to comprehend not only the practical assessment of ablation and the definition of a degree still tolerable for the purposes of this thesis. It also evidenced a

critical limitation of the LIMET setup used. As visible in the top part of figure 6.10 (a), the intensity distribution within the square-shaped spot showed neighbouring dot-like areas of locally increased intensity (yellow-red) directly embedded into low-intensity regions (green-blue). The high-intensity dots were arranged in a clear geometrical pattern, which could be described as a regular 2D square array with a dot-spacing of approximately 350 μm in both dimensions. Obviously, the LIMET optics were not capable of transferring a homogeneous distribution of laser intensity to the specimen surface. This was confirmed by the intensity profile shown below, which was recorded along the indicated dash-dot line passing through the centre of the spot.

There, a more or less Gaussian beam shape could be visualised being in concordance with the characteristics of the initial laser beam before passing through the interference setup. The larger fluctuations of actual intensity around the inserted Gaussian fit function seem to coincide with the high-intensity dots observed in 2D view. A look at the SEM top-view micrograph taken from a correspondingly treated multilayer in figure 6.10 (b), shows regions of material damage (bright contrast), which exactly match the positions and the geometrical pattern of the dots recorded by beam-profiling. From a standpoint of optics, the physical origin of their arrangement seemed to be straightforward and explained by near-field or *Fresnel-diffraction* at the square mask used to form the shape of the LIMET spot [70]. Thus, both the laser system´s inherent intensity distribution perpendicular to the propagation direction and the diffraction effects taking place at the optical elements jointly contributed to a flawed *inhomogeneous irradiation* of the spot area. Considering these circumstances it was assumed, that ablation was likely to take place in the dots even for fluences at the lower end of the series. Hence, a trade-off between through reaction and the degree of ablation was to be expected and to be taken care of by finding an appropriate compromise between sufficient heat energy delivery and damage induction. FIB cross-section micrographs to measure the processing depth together with the proposed greyscale threshold in light microscope top-views

for ablation area assessment were utilised to look for suitable fluence levels. Aim of this procedure was to assure that the heat-affected zone of the interference maxima spanned the complete stack thickness t_{tot} for most of the spot area, while keeping ablation at a low level. For sake of brevity, only the final results of this combined approach shall briefly be summarised here.

Ni/Al specimen sets

It was found for fluences effecting 10 to 15 % ablation of the spot area, that patterning led to a sufficient modification in depth of the multilayer. For Ni/Al specimens, this meant that depending on the substrate, different threshold fluences were identified: specimens on fused silica 150 mJ/cm^2, a-Si$_x$N$_y$ 175 mJ/cm^2 and sc-Si 275 mJ/cm^2 met the stated requirements. This further narrowed down the range of employable fluences predicted by the thermal simulations, still lying well within the projected interval. Figure 6.11 portrays a line-up of SEM micrographs obtained from Ni/Al specimens on the different substrates which were LIMET-treated at fluences above the tolerable 15 % ablation area limit. The type of damage inflicted is essentially the same. At the centre of a dot,

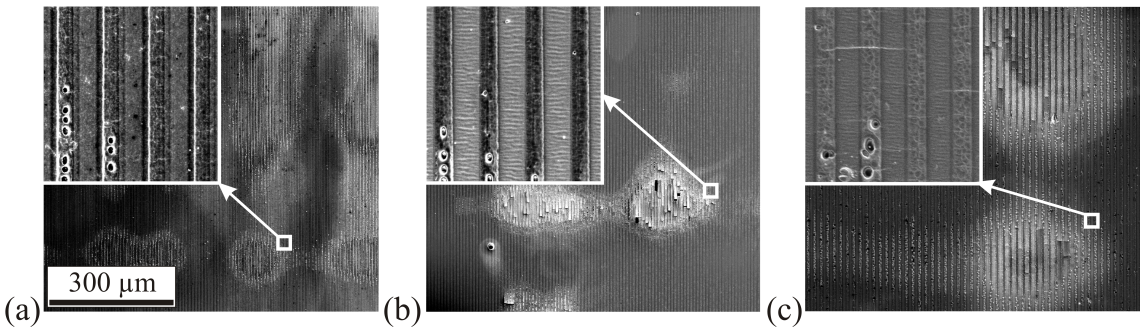


Figure 6.11.: SEM top-view micrographs of the damage inflicted to Ni/Al multilayers on the different substrates (sc-Si (a), a-Si$_x$N$_y$ (b) and fused silica (c)) when using fluences slightly above the identified ablation limit. The inserts show close-up images to the scale of the highlighting boxes.

the energy delivered to the maximum site led to an increase in temperature up to the boiling point of the component metals. Convection effected the melt to move away from the maximum towards the minimum sites thus exposing the underlying substrate. Most probably, the thermal stresses acting on the interface between the unmolten multilayer and the substrate at the interference minima caused the remaining stack to delaminate. To confirm these suppositions, the inserts shown in the top-left corner of the individual images were taken from regions located at the transition from the dot to neighbouring areas as indicated by the white boxes. By this, the initial stages of the damage mechanisms could be visualised due to the slightly reduced local intensity compared to the dot itself. Apparently, increased temperature levels at the maximum location initiated material flow leading to formation of holes (see lower left corner in all inserts), a step prior to the already observed complete material removal.

In contrast to the specimen on sc-Si, those on the substrates with worse heat transfer capabilities exhibited two remarkable damage features besides hole formation. First, in the interference minima a ladder-like surface morphology was formed. Their *rungs* were oriented parallel to each other and perpendicular to the interference maximum lines, corresponding to the orientation of the heat flow direction simulated for these cases in section 6.1, figure 6.4. Second, two types of cracks appeared at or in the vicinity of the interference maxima sites.

While a-Si_xN_y (b) only showed cracks exactly at the maximum centre expanding through the whole film thickness and parallel to the interference line, fused silica (c) in addition exhibited cracks threading perpendicularly. The initiation site of both types was unclear at this stage of the investigation, whereas it seemed sound to speculate that their physical origin seemed to be linked to differences in thermal expansion of the present phases (post-treatment thermal stresses).

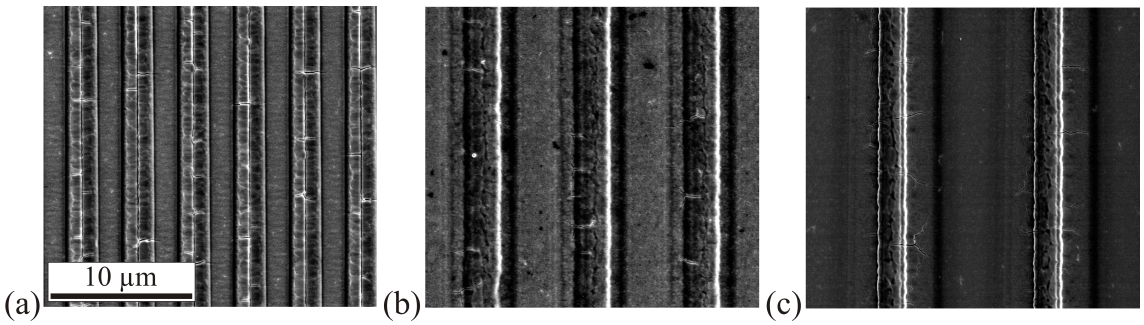


Figure 6.12.: SEM top-view micrographs of the damage inflicted to Ni/Al multilayers when using different periodicities (4 μm (a), 8 μm (b) and 16 μm (c)) at a constant fluence of 275 mJ/cm^2.

In order to reduce the overall amount of these damage types, the above stated fluence limits were kept for the patterning of the different Ni/Al specimen types. Due to that, the effect of periodicity was checked on Ni/Al on sc-Si at $F = 275\,\mathrm{mJ/cm^2}$ as shown in figure 6.12. The results depicted there stem from the same type of location as the inserts of figure 6.11, which is confirmed by the absence of the damage patterns encountered there. In concordance with the FEM findings (see section 6.1), an increase in width of the interference maxima was observed[5].

The SE-contrast observed at and within the maximum lines already gave hints as to the thin films´ topography being altered by the Marangoni convection effects imposed on the melt, which were analysed by FIB cross-sections (see following section). Only the specimen with 4 μm periodicity (c.f. (a)) exhibited the ladder pattern observed before at the multilayers on substrates with restricted heat transport capacities, supporting the discussed interpretation of this effect.

[5] A more in-depth and quantitative assessment of the relation between simulation and actually encountered dimensions of the heat-affected zones is discussed in the following section.

Ti/Al and Ni/Ti specimen sets

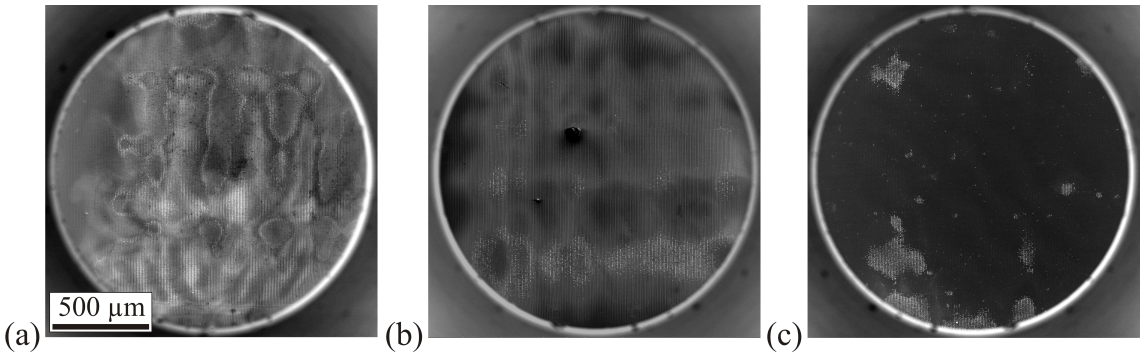


Figure 6.13.: SEM top-view micrographs of the damage inflicted the three multilayer material systems deposited on sc-Si (Ni/Al (a), Ti/Al (b) and Ni/Ti (c)) when using the same (d,F) conditions.

Following the same experimental approach, the resulting surface morphologies of the other multilayer material systems were also assessed. Figure 6.13 lines up SEM micrographs obtained from all three candidates deposited on sc-Si substrates and irradiated under the same conditions[6]. It was evident that the same set of irradiation conditions (d,F) had a less pronounced effect on the surface quality in comparison to the observations made on Ni/Al. Both Ti/Al (b) and Ni/Ti (c) experienced a much lower degree of ablation, for the same fluence that had led to over 15 % ablation in Ni/Al (a). Nevertheless, due to its physical origin, the spatial pattern of damage within the spot corresponded closely to the already encountered form.

In a first appraisal, the reason for this result was thought to be associated to the comparatively inferior heat transport properties of these two multilayer systems. To be able to produce comparable results between the sample sets during the following experiments,

[6] An according cross-examination of substrate influence on these specimen sets essentially yielded the same effects and relations already observed in the Ni/Al sets. Therefore, a more detailed description is skipped here in order to focus more closely on the differences in multilayer behaviour.

a conservative approach concerning the threshold fluences was pursued. Following the *principle of the weakest link*, this would imply applying the previously determined values for Ni/Al to the other material systems. With the simulations showing the need to use slightly higher fluences to achieve a through reaction there (see figure 6.6), this principle was employed in a lesser version: For all specimens, an interval of fluences around the indicated threshold was analysed concerning the cross-sectional microstructure. The width of the interval laid between 50 and 75 $\mathrm{mJ/cm^2}$ depending on the structuring results encountered. Unanimously, all these results emphasise the critical role that pattern homogeneity played in the further course of this thesis.

The FEM findings discussed before strictly assumed a totally equal distribution of laser intensity throughout the spot area. Experimental reality, in turn, pointed to additional limitations of the simulations, imposed by the optical implications of the LIMET setup. Irradiation inhomogeneity further implied that a comparable examination of the resulting microstructure and the phase formation as well as local chemistry by TEM and APT afforded to search for an area within the spot, which could reproducibly be identified in all samples and was situated in a region representing the average patterning result of the spot. Based on the top-view micrographs in conjunction with the beam-profiling analysis depicted in figure 6.10, a reasonable workaround for this situation was devised.

In the top-part of figure 6.10 (a), two areas representing the extreme opposite in irradiation density are encircled: (i) showing increased ablation even in the vicinity of the high-intensity dots and (ii) with only weak effects in the dot surroundings. As figure 6.10 (b) proves, both regions were visible in the SEM micrographs for intermediate and high fluences. Of them, only (i) even appeared at lower F, making it the perfect landmark for a reproducible identification of a suitably selected *preparation area* for comparable site-specifically prepared samples. The latter was defined according to the 2D inten-

sity distribution measured by profiling and comparing it with regions of homogeneous greyscale representation in the corresponding SEM top-views. In figure 6.10 (b), the area more closely meeting these conditions is highlighted (*prep zone*) and henceforth served for these purposes.

Cross-sectional characterisation of microstructure and structure

By means of cross-section imaging, data critical for the interpretation of microstructure and phase evolution were made accessible. Moreover, its results on actual expansion of the heat-affected zone at the interference maxima were directly compared to the numerical predictions attained by FEM. Especially the latter represents a novelty with respect to the experimental scope and the systematic of the approach already introduced in section 6.1. Since site-specific FIB preparation of cross-sections and TEM foils are both time-consuming and, from time to time, tedious procedures, only a limited amount of specimen and interference maxima therein could be analysed. Mostly, the lateral field of view of these two views contained at best three neighbouring interference maxima. Hence, the dimensional measurements presented in the following section were calculated as mean values of the visible features, discarding associated standard deviations due to the reduced data set at hand. Nevertheless, the following section will be able to draw a reliable picture of the relation between reality and simulation.

Ni/Al specimen sets

At first, the patterning result of Ni/Al multilayers on the different substrate materials was analysed within a $50\,\mathrm{mJ/cm^2}$ interval around the above discussed fluence thresholds for intermediate d=$8\,\mu$m. The modifications to the thin film stack encountered at the interference maxima of the presumed optimum irradiation density are shown in figure 6.14. The SE contrast images given there were taken from FIB cross-sections of interference maxima for each of the substrates. Evidently, the contrast conditions within the interesting part of the section did not allow for a meaningful analysis of grain

morphology or even size. In turn, adhesion and interface conditions between stack and substrate, resulting topography and the sought-after expansion of heat-affected volume were accessible.

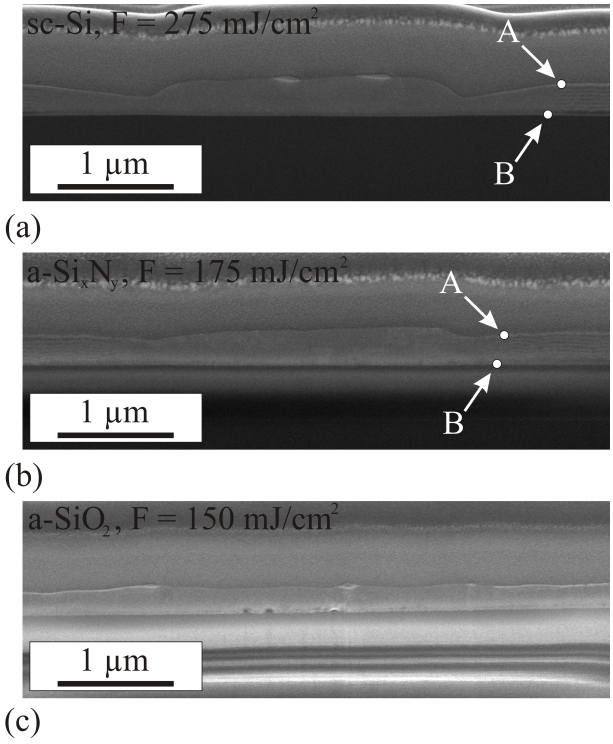


Figure 6.14.: SEM/FIB cross-section micrographs obtained for Ni/Al multilayers on the different substrates (sc-Si (a), a-Si_xN_y (b) and fused silica (c)) for LIMET processing at $d = 8\,\mu$m using the individual optimum fluences for LIMET given there.

Section 5.2.2 already introduced the experimental systematics for the LIMET processing of the multilayer stacks. A fluence series between 50 and 750 mJ/cm^2 was performed employing the three periodicity setups (4, 8 and 16 μm) identified by thermal simulations (see section 6.1) on all sample types. The aim of this was to get information on critical irradiation density thresholds for damage and ablation as well as on quality and homogeneity of the interference pattern. To this end, the individual spot areas were examined in top-view both by light microscopy (in bright and dark field mode) and SEM.

As figures 6.14 (a) and (b) show, a layered microstructure was visible in the left- and rightmost parts of the cross-section, which abruptly vanished approaching the interference maximum, where no distinct contrast was recorded. The latter was interpreted as thin film volume wherein significant, if not total intermixing of the constituent metallic elements was achieved. Hence, it was easy to discern these two regions and to attribute their boundary with points A and B as indicated in the figure. In a first approximation, it was assumed that this condition could be achieved, if one of the components was molten and thus the more efficient atomic mobility within (l) phases could be exploited.

A look at the cross-section obtained from the fused silica (figure 6.14 (c)) reveals that FIB cross-sections were not always capable of yielding sufficient contrast to unequivocally recognise remaining multilayer structures. In most cases, this was due to charging effects encountered in the vicinity of the substrate and could only be circumvented by extracting these data from TEM foils instead. Fortunately, the micrographs unanimously confirmed that the optimum fluence derived by simulation and ablation degree was sufficient to extend the heat-affected zone throughout the whole multilayer thickness. Another common denominator was found considering the evolution of the topography along the lateral coordinate of the cross-section. When seen from minimum to maximum, the total thickness of the stack started to drop gradually as soon as point A was reached. This trend continued up to the closer vicinity of the maximum location, but did not leave the substrate exposed. Then, a sudden increase in thickness was visible, merging into a plateau of almost constant thickness, which even surpassed the stack´s original t_{tot}. Qualitatively, it can be stated, that the degree of induced topography change increased for substrates with inferior heat transport capabilities. Here, the multilayer on fused silica (figure 6.14 (c)) was the extreme case showing no significant alteration.
According to von Allmen et al. [68], the general shape encountered there corresponds closely to topographic modifications induced by Marangoni type convection flow in the

melt. Due to the well-known relation between convection flow and gradients in melt temperature and surface energy discussed by Marangoni, it seemed worthwhile consulting the FEM results described in section 6.1. Figure 6.4 there, summarised the findings on local temperature gradients in the lateral and depth directions for the extreme cases of sc-Si and a-SiO_2. Looking at the calculated heat flow angle α (c) of the respective irradiation conditions (d,F) it could be seen, that the melt on sc-Si experienced a pronounced flow in the depth direction (approx. 50 °), while on fused silica the lateral flow component (ca. 25 °) is stronger in effect. Hence, one might argue the differently formed degree in topography.

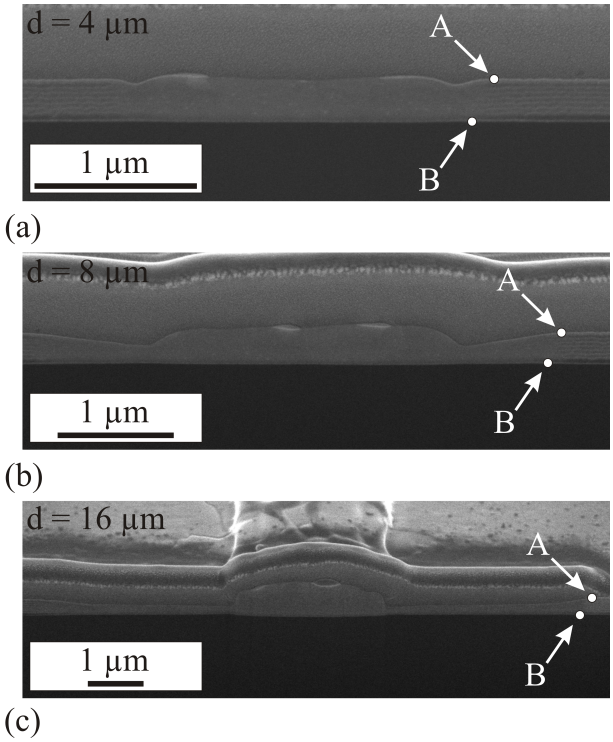


Figure 6.15.: SEM/FIB cross-section micrographs obtained for Ni/Al multilayers on sc-Si substrate for different LIMET periodicities (4 μm (a), 8 μm (b) and 16 μm (c)) using the optimum fluence 275 mJ/cm^2.

Finally, the presence of these topographic shapes proved that beside (l) diffusion, convection was active in the melt which additionally contributed to a more efficient intermixing of the component metals. Similar observations were made when analysing the effect of periodicity on the cross-sectional morphology of the interference maxima when keeping the fluence constant. The behaviour encountered there will exemplarily be discussed for the sc-Si specimen set (at optimum 275 mJ/cm^2), since the above mentioned findings on substrate-related phenomena could be reproduced for the other periodicities. Figure 6.15 delineates FIB cross-sections obtained at 4, 8 and 16 μm periodicity, wherein a sufficiently clear contrast was achieved allowing for an unequivocal identification of points A and B. Shape and course of the topography modification closely resembled the one encountered in the substrate variation analysis. Here, the degree of topography was found to increase with increasing periodicity d. This fell in line with the simulated results on heat flow angle α given in figure 6.4 (c). With increasing d, α increased from ca. 35, over 50 to finally 60 ° for the periodicities analysed here, which perfectly fitted to the experimental results.

Due to the fact that the drop in topography was generally gradual and that its onset could be related to the location of point A, it was assumed that the results of the thermal simulations with respect to the expansion of the heat-affected zone (c.f. section 6.1) could still be utilised despite their lack in accounting for these fluid-dynamic effects. Obviously, the definition of points A and B was devised sufficiently general to fit the needs of different effects. Therefore, a comparison of the estimated and the actually measured dimensions of heat-affected zones seemed appropriate. To the author´s knowledge, no LIMET-related study conducted so far tackled this question on the basis of an extended parameter set as considered here. The comparisons were made based on the data depicted in figure 6.3, where the lateral and depth coordinates of A and B are given relative to $d/2$ and t_{tot}, respectively. For the sake of clarity, the results for sc-Si (see figure 6.16) and a-SiO_2 (figure 6.17) will be discussed separately, with micrograph results designated with ■ and those of FEM with □.

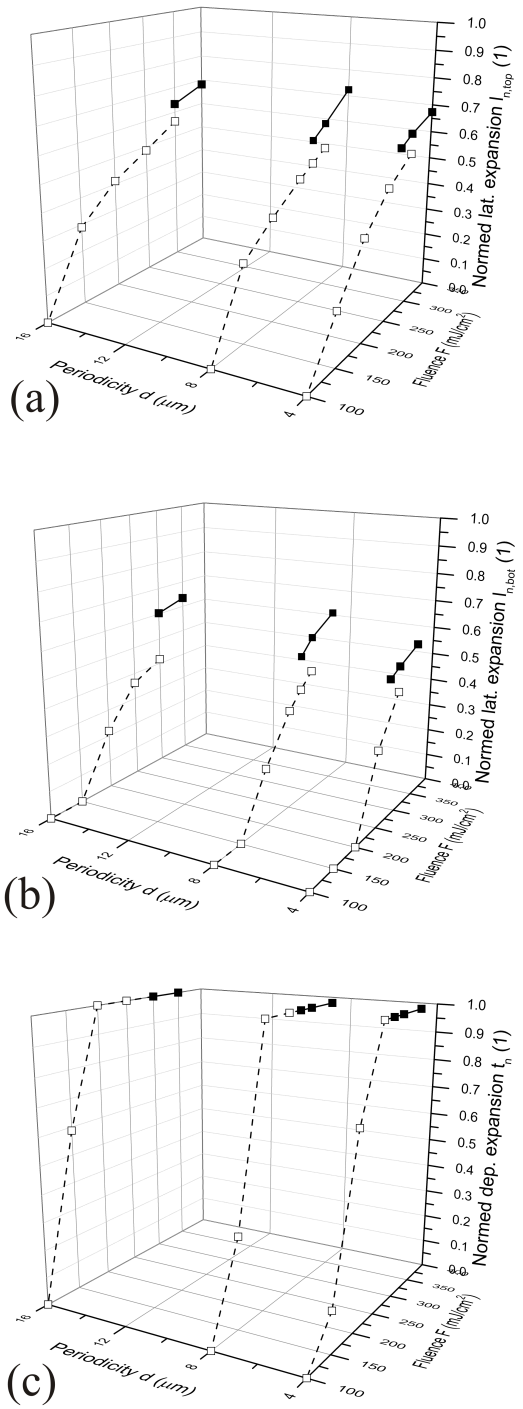


Figure 6.16.: Direct comparison between FEM estimated normalised dimensions of the heat-affected zone (designated □) and the corresponding results obtained by cross-sectional imaging (■) for Ni/Al on sc-Si substrate: lateral expansion at the multilayer surface l_{top} (a), lateral expansion at the substrate interface l_{bot} (b) and depth expansion t_{dep} (c).

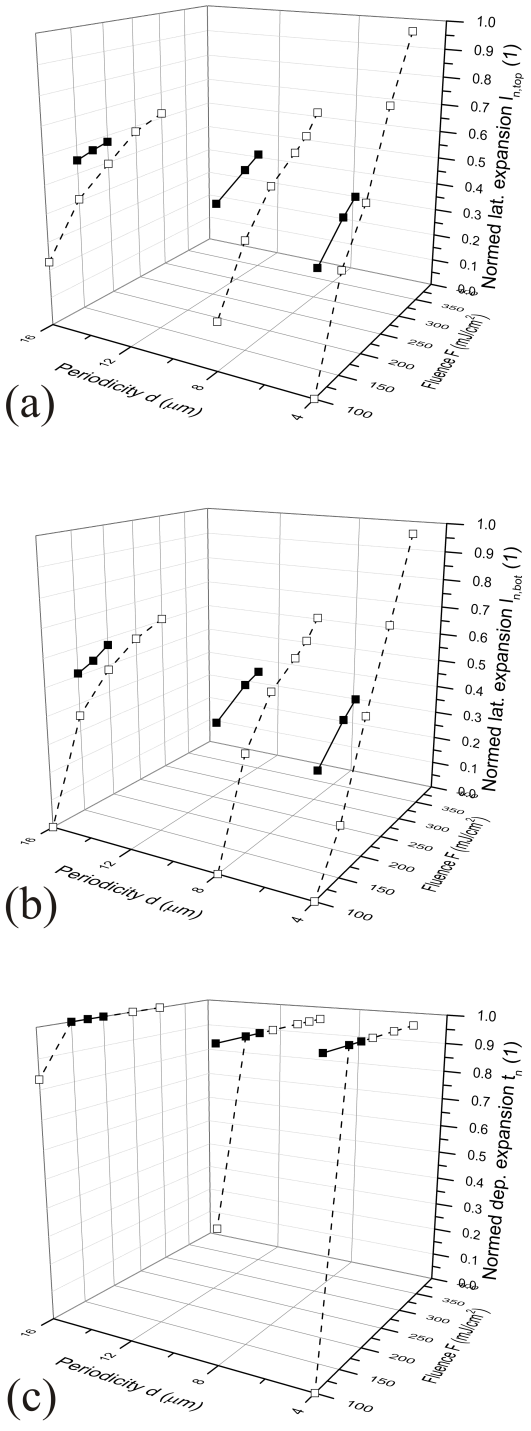


Figure 6.17.: Direct comparison between FEM estimated normalised dimensions of the heat-affected zone (designated □) and the corresponding results obtained by cross-sectional imaging (■) for Ni/Al on a-SiO_2 substrate: lateral expansion at the multilayer surface l_{top} (a), lateral expansion at the substrate interface l_{bot} (b) and depth expansion t_{dep} (c).

Irrespective of the applied periodicity, the actually measured normalised lateral expansion surpassed the FEM estimated value by 0.1 to 0.2 in absolute terms. The same difference was observed for the corresponding value at the multilayer-substrate interface (b). Moreover, a close resemblance of the functional course between simulation and reality was visible. Concerning the depth expansion (c), both results overlapped predicting a through reaction for the fluence range in question. Nevertheless, the relative deviation of the values amounted to 20 to 40 %, which exceeded the range of tolerable deviation when compared to typical experimental errors.

The data on a-SiO_2 substrates depicted in figure 6.17, essentially yielded the same picture concerning the relation of functional course and deviation in values. Only the normalised depth expansion posed an exception, since the simulation predicted the through reaction to set in at slightly lower fluences (less by 50 mJ/cm^2). Considering these comparisons jointly, the following conclusions were drawn. Both the similar functional shape and the fact that FEM systematically underestimated the real situation made the overall result appear nevertheless promising. Two possible reasons were proposed.

First, the actual heat transport properties of the multilayer material could be even worse compared to the tabulated data in literature. This seemed reasonable, since it is well-known that thin film media might exhibit different physical properties than their bulk counterparts. Especially density can differ due to deposition-inherent phenomena. Nevertheless, these influences were assessed not likely to yield significant differences like on one order of a magnitude. Second, the design of the FEM thermal simulations was not capable of accounting for additional heat sources. As previously implicitly assumed, a significant amount of elemental intermixing was likely to have taken place within the volume of the interference maximum delineated by the A-B boundary. Since mixing of Ni and Al is an exothermic process, at least the release of enthalpy of mixing of the respective components should be considered. Hence, it was seen worthy to undertake

energetic estimations based on thermodynamic data of the original and the final phases in order to try to balance the deviations. This in turn afforded more detailed local data on local phase composition (TEM) and chemistry describing the outcome of the different phenomena contributing to elemental intermixing. For the latter, APT was employed, whose results are given in the following section 6.3. Therefore, the description and implementation of this approach are postponed to the discussion (c.f. chapter 7).

A more clear view on grain morphologies and sizes resulting from the LIMET-induced resolidification was obtained by TEM imaging along with localised phase analyses. Following the joint insights provided by FEM and the cross-sectional microstructure characterisation so far, a specimen set was selected, which was deemed representative for the different introduced parameter selections (d,F). Thermal simulations (see especially figure 6.2) indicated less significant variations in the heat flow conditions for periodicities larger than 8 μm. Both FEM and FIB cross-sections showed effective through reactions for the projected optimum fluence value. Hence, TEM analysis was performed on this selection of LIMET parameters for the individual substrate systems. The attained through reaction was essential in order to achieve grains sufficiently large to yield zone-axis SADPs, an achievement not yet reached in related studies. Especially this processing result ensured that phase identification could be performed under controlled and reproducible conditions.

Only unequivocally indexed zone-axis SADPs with correctly measured angular relations between the reflections of a phase as given by crystallography were considered sufficiently reliable for this task. Preferably, these were recorded along different zone axes within the same grain as a confirmation, but not all will be shown in the following text for the sake of clarity. Figure 6.18 compares the same set of cross-sections already shown in figure 6.14 but here in the form of TEM bright-field images with a clearer contrast. As visible in figure 6.18 (c), for multilayers deposited on a-SiO_2 even the A-B

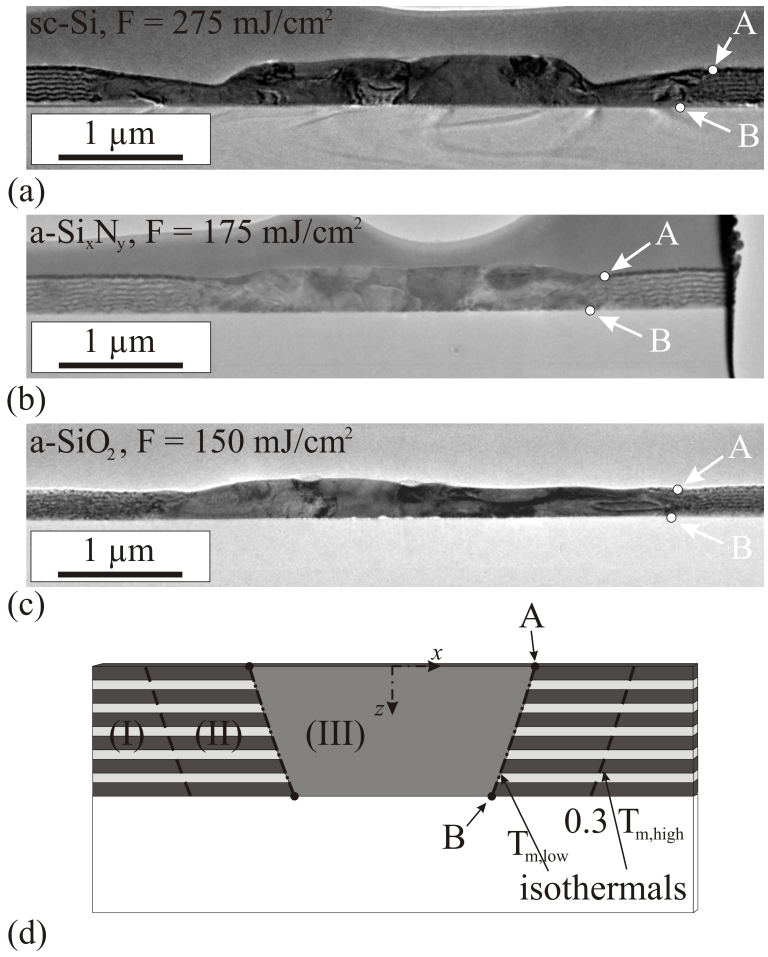


Figure 6.18.: TEM micrographs obtained for Ni/Al multilayers on the different substrates (sc-Si (a), a-Si_xN_y (b) and fused silica (c)) for LIMET processing at $d = 8\,\mu$m using the individual optimum fluences for LIMET given there. The schematic representation of the heat-affected zone and its surroundings (d) introduces the designation of three distinct regions with different processing result ((I) to (III)) along with the A-B boundary representing the $T_{m.low}$ isothermal.

boundary could readily be discerned. Without going into further detail, all three TEM images (a) to (c) exhibited grain sizes significantly surpassing the as-deposited state. Looking at the *centre region* of an interference maximum (centred part of the micrographs, region (III) in the schematic representation given in figure 6.18 (d)), most of its volume was composed by a only limited number of grains, which spanned the whole

thickness of the stack and whose lateral expansion corresponded to several t_{tot}. A more in-depth analysis on present morphologies and sizes will be discussed at each close-up analysis of the different regions encountered in individual specimens, but it already can be stated that the observed growth followed a SLG mode. The schematic representation of an interference maximum and its surroundings shown in figure 6.18 (d) introduces two additional regions (I) and (II) besides the centre region (III). As will be cleared up in the following discussion, these portions also show clearly distinct microstructural features, whose properties were useful in deducing a hypothesis on the nature and path of effects taking place during the resolidification process. Together with the region (III) microstructure, clues on processing history could be derived.

First, figure 6.18 (a)´s case of Ni/Al on sc-Si was considered. To this end, close-up imaging was performed starting in the section of the remaining multilayer microstructure (see figure 6.19) and ending in the centre region (c.f. figure 6.20). In the following, the images summarising the TEM findings are organised as follows. The top-left corner (a) shows the micrograph of the cross-sectional region in question along with specimen normal direction n and the areas targeted for SAD analysis, given to scale with the employed aperture. The corresponding recorded diffraction patterns are associated to the individual areas by black arrows. Figure 6.19 shows the situation encountered at the *transition region* (II) between the still visible and *apparently unmodified multilayer* (I) and the onset of complete intermixing (III). Comparing the SADPs in clockwise order starting from (b) the top-right (corresponding to a path from the interference minimum to the maximum location), a significant alteration in the present phase composition could be observed.

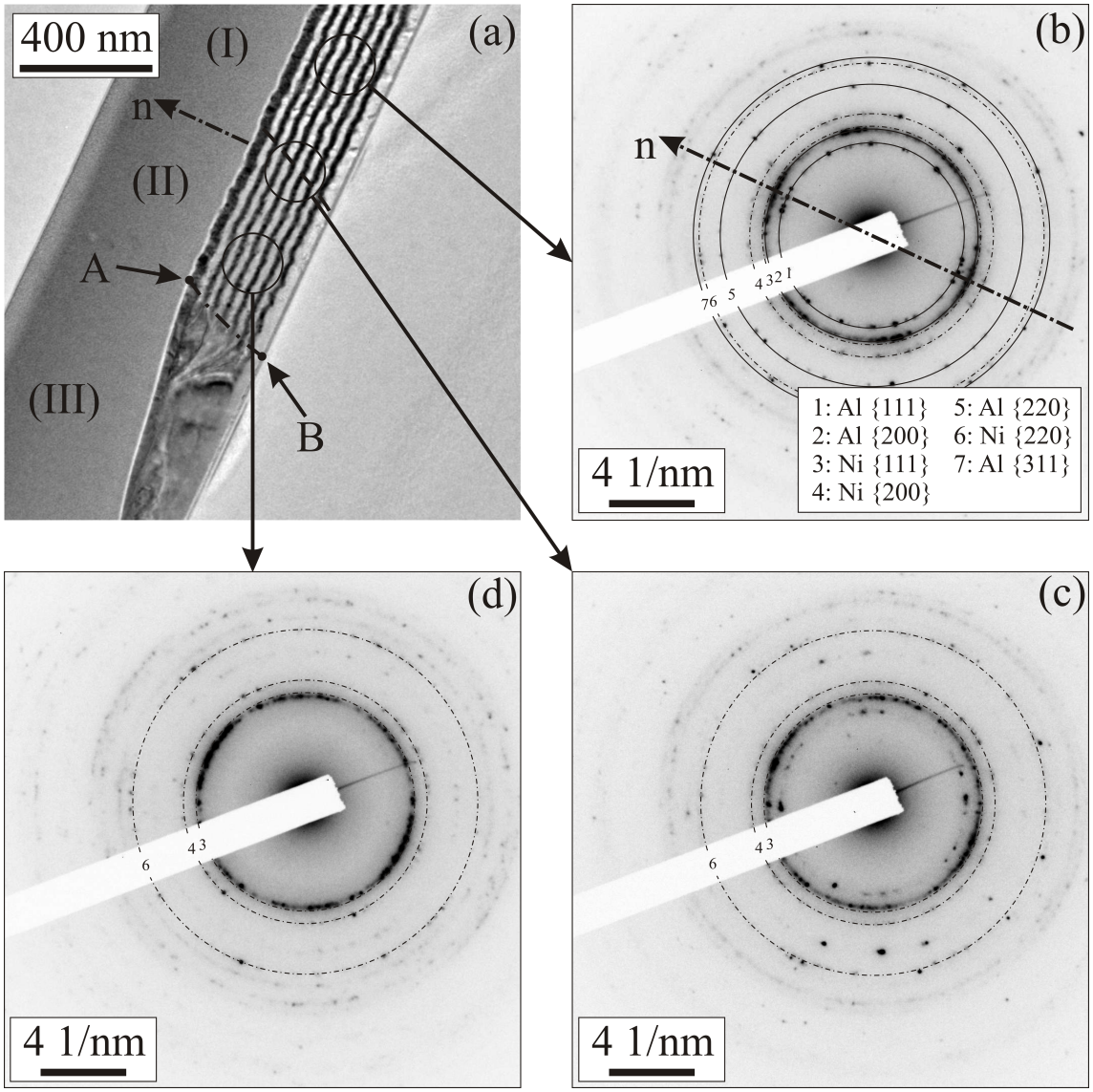


Figure 6.19.: TEM structural analysis of the vicinity of an interference maximum obtained for Ni/Al on sc-Si after LIMET treatment using $d = 8\,\mu$m and $F = 275\,\mathrm{mJ/cm^2}$: TEM micrograph (a) indicating the different processing regions and the location of the site-specific SAD analyses. SADP of the unmodified region (I) (b), the transition between regions (I) and (II) (c) as well as region (II) alone.

While the diffraction pattern taken in region (I) not surprisingly resembled the one recorded in the as-deposited sample state (compare with figure 6.7 (b)), the other two SADPs differed from it despite the fact that they obviously were taken from regions, where the multilayer still seemed intact. When approaching the border to region (III), the remaining stack exhibited an evolution with respect to the diffraction signal stemming from the Al phase. Its signal at first gradually decreased and blurred, as can be seen in the SADP from the transition between regions (I) and (II) (figure 6.19 (c)). In region (II) in turn (figure 6.19 (d)), it totally vanished leaving behind crystalline Ni reflections and an elevated background in the vicinity of the interplanar spacings of low-indexed Al planes. This finding could be correlated directly to the evolution of the greyscale signal visible in the micrograph 6.19 (a). Following the same path, the Al layers appeared increasingly darker when compared to the contrast situation encountered in region (I), where Al yielded a bright signal.

Taking into account the Z-contrast underlying the employed type of TEM imaging, a hypothesis concerning the effects taking place was devised. Clearly, a darker greyscale representation directly corresponded to an increase in mass density in the region under question. It seemed therefore sound to assume, that the species with higher atomic number, Ni, diffused into the Al layers. For those located in region (II) a homogeneous greyscale signal was encountered, pointing to a very efficient atomic exchange process taking place in a significant magnitude. Its extent could only be assessed by the use of APT, whose results are discussed in the following chapter. Region (II) stretched over the whole stack thickness and measured approximately 500 nm in in-plane length. Interestingly, the form of its boundary to region (I) was aligned exactly parallel to the A-B boundary (both demarcations are highlighted in the micrograph 6.19 (a) as dash-dot and dash line, respectively). Remarkably, the equilibrium phase diagram of the Ni/Al system (see figure 4.1), clarifies that an α-Al solid solution only accepts limited amounts of Ni in its lattice. Bearing in mind the implications of the FEM results (see section

6.1), in this region a thermal field magnitude sufficient for such intensive atomic movements could possibly be achieved only for a very limited amount of time, on the order of several ns. In a first approximation it was deemed likely that this kind of intermixing could be attributed an enhanced mobility of Ni species within the still (s) Al layers. The latter were subsequently quenched as amorphous solid solution thus freezing in the Ni atoms, which was corroborated by the already discussed blurred Al diffraction signal in the SADPs of transition (I)-(II) and region (II). Especially the fact that the TEM micrograph did not reveal any signs of dewetting from the substrate and that no significant alteration to layer topography could be found, supported the assumed (s) state reaction.

Furthermore, considering figure 6.1 (a) helped in assessing this situation. There, the 2D temperature distribution exactly for this combination of multilayer, substrate and LIMET parameters is given: a blue isotherm is depicted which corresponds to $0.3 \cdot T_m^{Al}$. It is also oriented parallel to the A-B boundary, but at a distance of approximately 1 μm. This isotherm was selected such that it accompanies the one associated to the actual melting point. Together they confine a volume of enhanced diffusion in concordance with standard theories. The closer to A-B, the higher the local temperature and thus an increased diffusion is qualitatively predicted by the Stokes-Einstein equation (see equation 3.15). Especially in the vicinity of the yellow isotherm representing $0.3 \cdot T_m^{Ni}$ these phenomena are likely to be even more effective. Its distance from the A-B boundary is approximately 580 nm, which perfectly fits to the in-plane elongation of region (II) stated before. Within this volume a sufficiently high temperature for these two phenomena is in effect over significantly longer times than those associated with the melting duration alone. Under these conditions, enhanced diffusional transport of Ni into (s) Al and the subsequent loss of crystalline order of the latter is the most likely explanation of these findings.

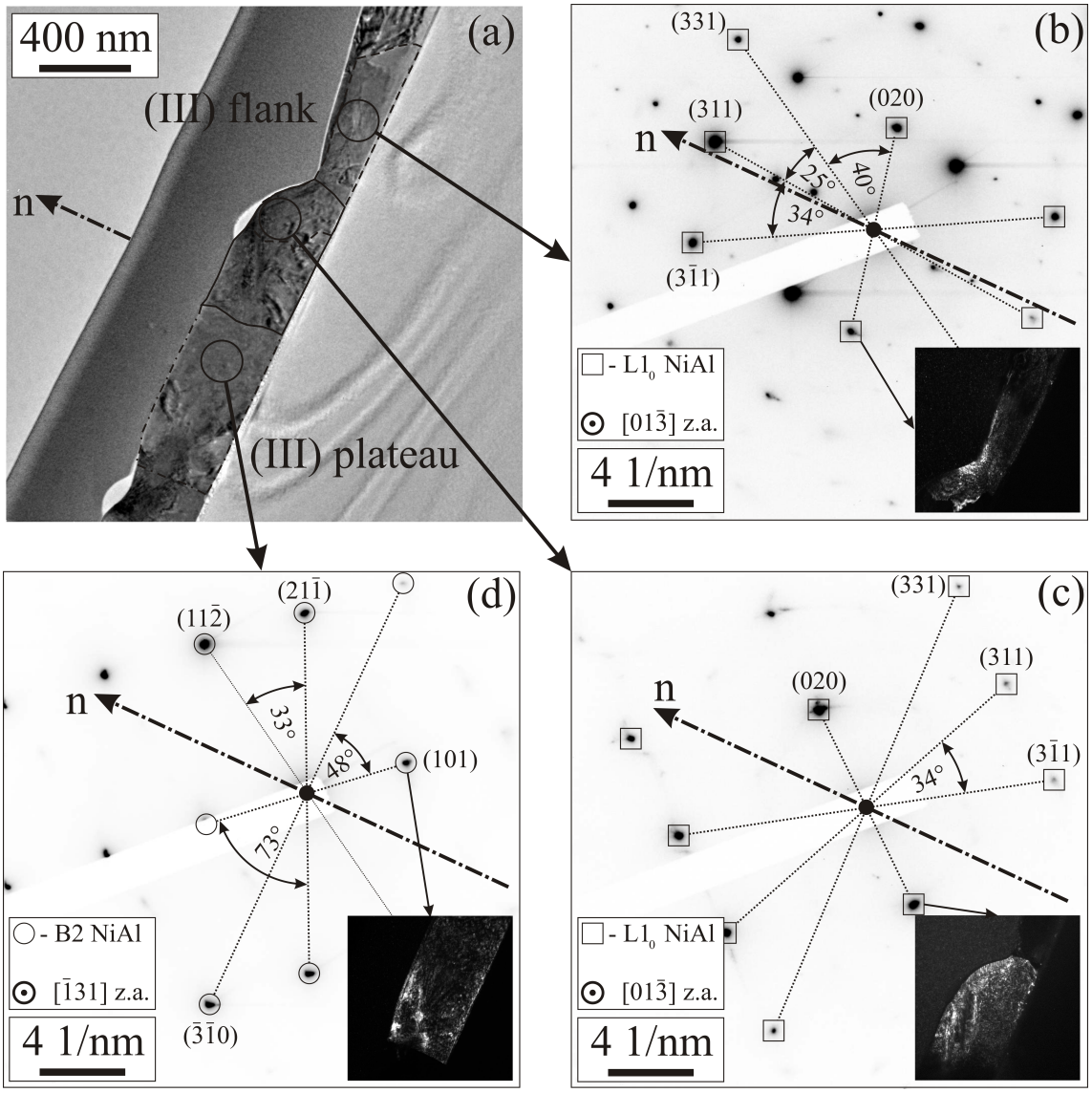


Figure 6.20.: TEM structural analysis of an interference maximum obtained for Ni/Al on sc-Si after LIMET treatment using $d = 8\,\mu$m and $F = 275\,\mathrm{mJ/cm^2}$: TEM micrograph (a) indicating the location of the site-specific SAD analyses. SADP zone axis images of region (III) flank (b), and two individual grains within region (III) plateau (c) and (d).

Micrograph 6.19 (a) also revealed insights into the microstructure of region (III) directly at the A-B boundary. According to the working hypothesis, it is assumed that the resolidification front originates there and subsequently travels back to the interference maximum site. Hence, more data on nucleation and growth could be extracted by examining this onset. Apparently, the whole region consisted of a single grain next to a material portion exhibiting residual traces of former Ni layers. In depth, these residues were seen to bend upwards to the stack´s surface. There in turn, the Ni capping layer still seemed to have remained intact (see darker greyscale representation) up to the location of the topography depression deep within region (III) as can be seen in the micrograph of figure 6.20 (a). A structural analysis of the single grain (figure 6.20 (b)) revealed a zone-axis SADP of the martensitic low-temperature NiAl phase ($L1_0$ structure). Using the $(0\bar{2}0)$ reflection, a TEM dark-field image was taken as shown in the insert. The dark-field both confirmed the martensite grain to stretch through the whole thin film thickness (except for the residual Ni capping) and over 750 nm in-plane up to the point of lowest topographic depression. Deviating from usual materialographic procedures of grain size determination, the geometric arrangement of both the multilayer stack and the simulated lateral travel of the resolidification front afforded the selection of a more convenient coordinate frame of measurement. Here, the dimensions were captured parallel to depth z and lateral coordinate x, respectively.

Once again looking at the microstructural features from the onset of region (III) up to the interference maximum centre, two more grains could be imaged. The first one, directly adjacent to the $L1_0$ grain, stretched over the whole thickness (ca. 370 nm) and reached from the topographic depression well into the constant thickness plateau, over a length of approximately 700 nm. Its corresponding zone-axis SADP also identified the NiAl $L1_0$ phase (figure 6.20 (c)). Only the third grain, finally reaching the original site of the interference maximum, could be attributed to another phase: the high-temperature austenitic B2-NiAl (see figure 6.20 (d)). A (101) dark-field image (see insert there) ex-

hibited a depth coordinate size equal to the plateau value of 370 nm and an in-plane size of 780 nm. Besides their *comparable in-plane sizes*, another remarkable common denominator of these three grains was identified in the *orientation of their grain boundaries*. All of them were aligned perfectly parallel to the specimen normal vector n. Taking these two observations together, a strong indication for a planar solidification front travelling laterally in the film plane was at hand pointing to the growth mode most probably in effect here. Moreover, comparing the orientation of individual (hkl) reflections with respect to the n vector, those crystallographic planes parallel to the grain boundaries would be identified: (020) for the $L1_0$ grain in the onset, (331) for the one adjacent to it, and finally (310) for the B2-grain in the centre. Obviously, the phases discovered at the interference maximum allowed to draw two conclusions concerning phase formation: First, the phases located in the targeted part of the phase diagram were formed during the LIMET processing of a stoichiometrically designed multilayer. Second, their location relative to the lateral coordinate reaching from the interference minimum to the maximum can be taken as sign of the thermal history of the laser treatment and thus of the phase selection processes.

The same analyses were performed on the Ni/Al stack deposited onto a-Si_xN_y and essentially yielded similar results showing only slight deviations. For the sake of brevity, the results obtained there shall be discussed shortly. Here, directly at the A-B boundary two drop-shaped grains were spotted on top of each other (see figure 6.18 (b)), both having comparable sizes of 200 nm in depth ($\approx t_{tot}/2$) and 930 nm in-plane. Each of them was identified to be formed of $L1_0$ phase. Closing in to the centre only one other grain was discerned with a depth of 380 nm (thus corresponding to t_{tot}) and a width of 600 nm. Like on sc-Si, B2-NiAl could be assigned to this centre grain.

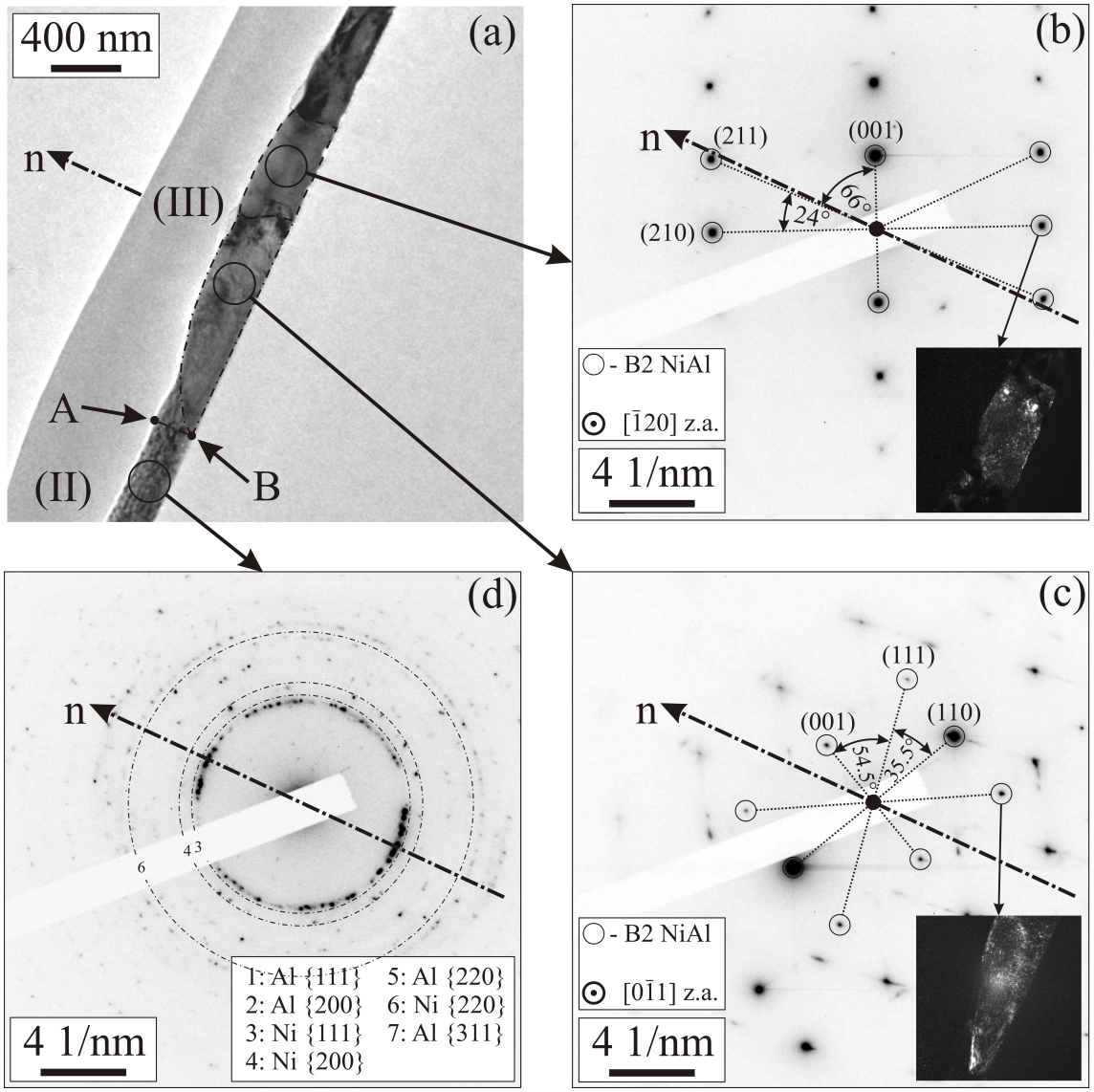


Figure 6.21.: TEM structural analysis of an interference maximum obtained for Ni/Al on a-SiO_2 after LIMET treatment using $d = 8\,\mu$m and $F = 150\,\mathrm{mJ/cm^2}$: TEM micrograph (a) indicating the location of the site-specific SAD analyses. SADP zone axis images of two individual grains within region (III) (b) and (c) as well as region (II) (d).

Turning to the specimen set on fused silica, more pronounced deviations in the microstructural and structural outcome were observed, which are summarised in figure 6.21. The micrograph given there (a) depicts an interference maximum cut in half, with the residuals of the multilayer located at the lower part of the image. Thus, following the SADPs from there but in counter-clockwise sense, the same path from minimum to maximum is followed as before. In figure 6.21 (d), the diffraction pattern taken from the remaining multilayer only consisted of crystalline Ni signal and diffuse background close to the $d_{\{hkl\}}$-spacing of Al. This was consistent with the findings on early intermixing beyond the A-B boundary as discussed for the case of Ni/Al on sc-Si (c.f. figure 6.19). Not shown here is the SADP obtained at the interference minimum location, which yielded exactly the same result. The Z-contrast encountered in the layers corresponding to the original Al deposition confirmed this result. Obviously, the same effect leading to this enhanced diffusional transport of Ni into (s) Al took place but to a more pronounced extent. Since the same result was obtained from a-Si_xN_y, it was sound to assume that the inferior heat transport of these two materials was the origin of this finding.

A FEM-simulated 2D thermal distribution for the stack on a-SiO_2, comparable to those shown in figure 6.1 (a), showed the $0.3 \cdot T_m$ isotherms of both of Ni and Al even reaching the interference minimum location and keeping a sufficiently high temperature level for a longer period of time. The microstructure in region (III) here exhibited only two grains spanning the whole in-plane length from the A-B boundary to the centre of the interference maximum. Both of them expand completely over t_{tot} in depth. The outward grain (figure 6.21 (c)) had an in-plane length of ca. 820 nm and was identified as a B2-NiAl austenitic phase, in contrast with the discovery of $L1_0$ at the corresponding sites of sc-Si and a-Si_xN_y. The inner grain (figure 6.21 (b)), in turn, once again fitted to the already encountered situation of B2-NiAl at the interference maximum centre. Its lateral expansion was measured to 420 nm. In concordance to the sc-Si result, here also the grain boundaries were aligned parallel to the specimen normal vector n, thus confirming the

assumed planar lateral growth of the resolidification front. The crystallographic planes parallel to the grain boundary were identified as (111) for the outer and (213) for the inner grain.

Ti/Al and Ni/Ti specimen sets

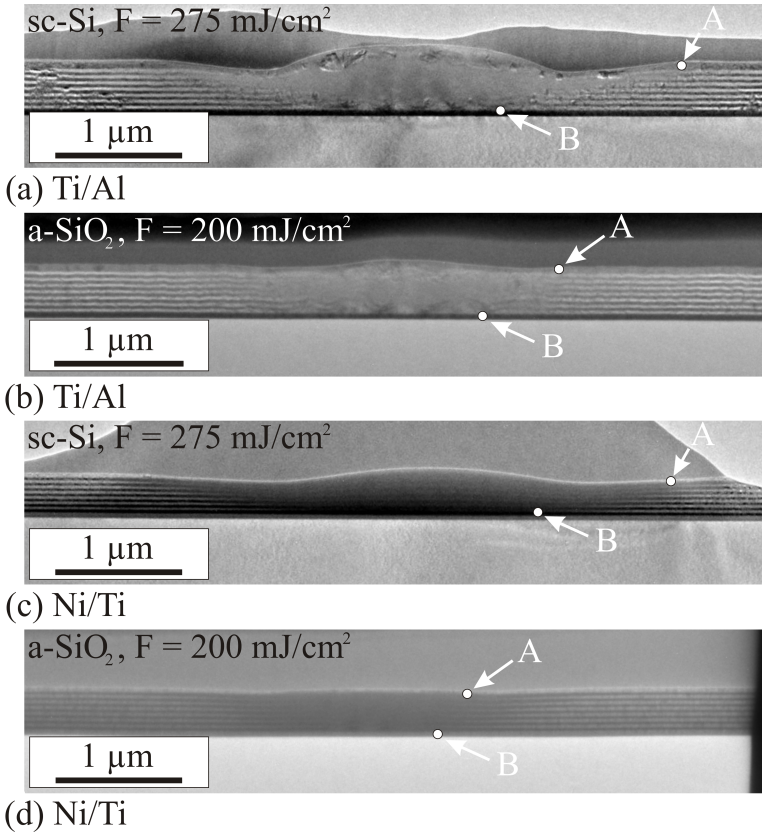


Figure 6.22.: TEM micrographs obtained for Ti/Al and Ni/Ti multilayers on the different substrates (sc-Si (a) and (c) as well as fused silica (b) and (d)) for LIMET processing at $d = 8\,\mu$m using the individual optimum fluences for LIMET given there. The identified A-B boundaries are indicated.

Figure 6.22 depicts bright-field TEM cross-sectional views on the patterning result obtained at the other multilayer component/substrate material combinations. Following the discussion on selection of LIMET parameters in sections 6.1 and 6.2.2, cross-sections were prepared on specimens which were patterned using a fluence lying within a 50 to 75 mJ/cm^2 wide interval around the assumed fluence threshold. Each of the images given there, represents the structuring result for optimum F at d=8 μm. Especially for those sample sets deposited on a-SiO_2, the simulation result of figure 6.6 held true, since the intended through reaction could only be achieved when the fluence level sufficient for Ni/Al was increased by 50 mJ/cm^2. The induced topography shape at the interference maximum site corresponded closely to the one observed for Ni/Al (see figure 6.14) and even fitted to the substrate influence discovered there. The sole but consistent difference in shape could be found at the maximum (see 6.22 (a) for Ti/Al on sc-Si), which exhibited a convex curved form instead of the plateau seen in Ni/Al.
Once again the multilayer on a-SiO_2 (see 6.22 (b)), did not exhibit a significant modification of topography. Ni/Ti essentially behaved in the same way but showed an even further reduced degree of topographic alteration. Like before, on fused silica (d) no depression was visible. Looking at the expansion of the heat-affected zone, a significant difference to Ni/Al could be found which was revealed by direct comparison with figure 6.18.

Considering the composite heat transport properties assessed by equations 2.21 to 2.23, it became clear that the heat introduced was preferably transported within the film plane than along the depth direction. This was reflected in the extended displacement of point A compared to the one of point B as visible there. Moreover, the multilayer morphology encountered at the transition from the interference minimum to the maximum was found to be exactly the same as in the case of Ni/Al: The closer to the A-B boundary, the more blurred the original layer structure appeared also pointing to a region of initial intermixing in front of the assumed (s)-(l) interface.

A more quantitative view on the differences in expansion behaviour of the heat-affected zone could be achieved by performing the same comparison between FEM simulations and cross-section analyses as depicted in figures 6.16 and 6.17 but accounting for the different multilayer systems. In line with section 6.1.2, the analysis here was restricted to the case of 8 μm periodicity (see simulation results depicted in figure 6.6), as can be seen in figure 6.23 for the case of the sc-Si substrate and figure 6.24 for fused silica. As already introduced, the different material systems are designated by Ni/Al (1), Ti/Al (2) and Ni/Ti (3).

Compared to Ni/Al on sc-Si, where the simulation results consistently underestimated the actually attained expansion by 20 to 40 %, the situation found for Ti/Al and Ni/Ti was quite heterogeneous. Ti/Al simulations always overestimated the affected volume by at least 50 % in the lateral displacement of both A and B, while the depth coordinate was well met. Ni/Ti, in turn, showed acceptable agreement in the case of the normalised lateral expansion at the stack surface, with a 30 % underestimation. Looking at the corresponding value at the stack-substrate interface in the depth direction, the simulation did not predict a through reaction to occur, while cross-sectional imaging confirmed its presence.

The fused silica (see figure 6.24) did not yield better agreement. The comparison there rather reflected the one already discussed for sc-Si. At least in the case of Ni/Ti (3), a change from under- to overestimation of the simulation results was observed for the position of point A. At this stage of the thesis it was unclear, which effects contributed to these findings, especially when taking into account the quite promising outcome observed in the case of Ni/Al for both substrate materials under investigation.

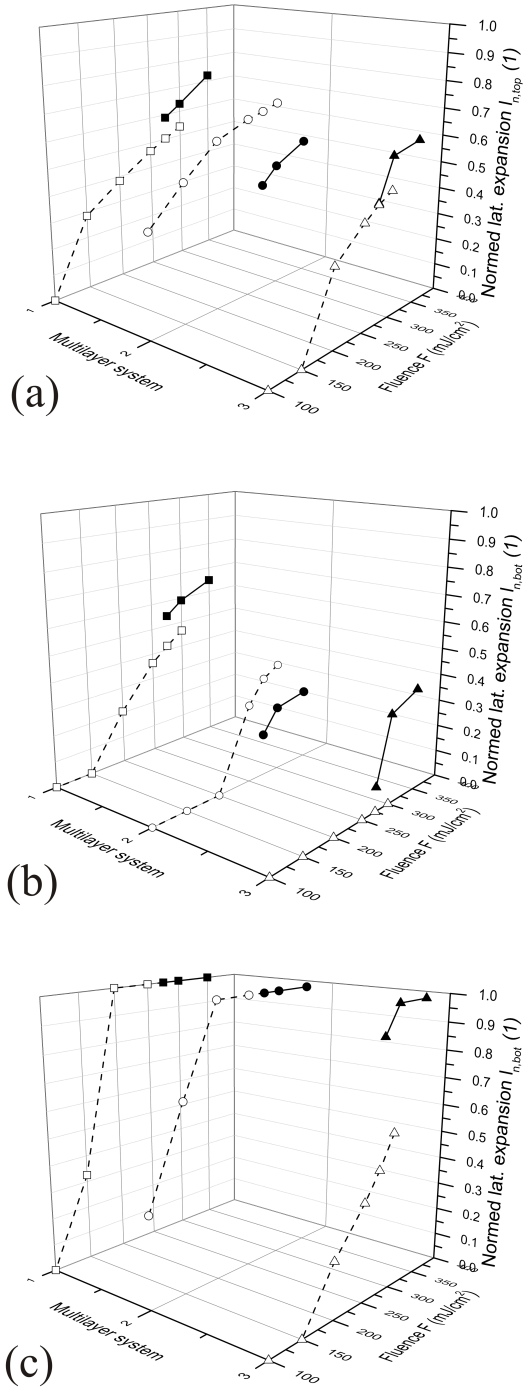


Figure 6.23.: Direct comparison between FEM estimated normalised dimensions of the heat-affected zone (open forms) obtained for the three multilayer material systems (1-Ni/Al, 2-Ti/Al and 3-Ni/Ti) and the corresponding results obtained by cross-sectional imaging (filled forms) on sc-Si substrate when varying F for a constant periodicity of 8 μm: lateral expansion at the multilayer surface l_{top} (a), lateral expansion at the substrate interface l_{bot} (b) and depth expansion t_{dep} (c).

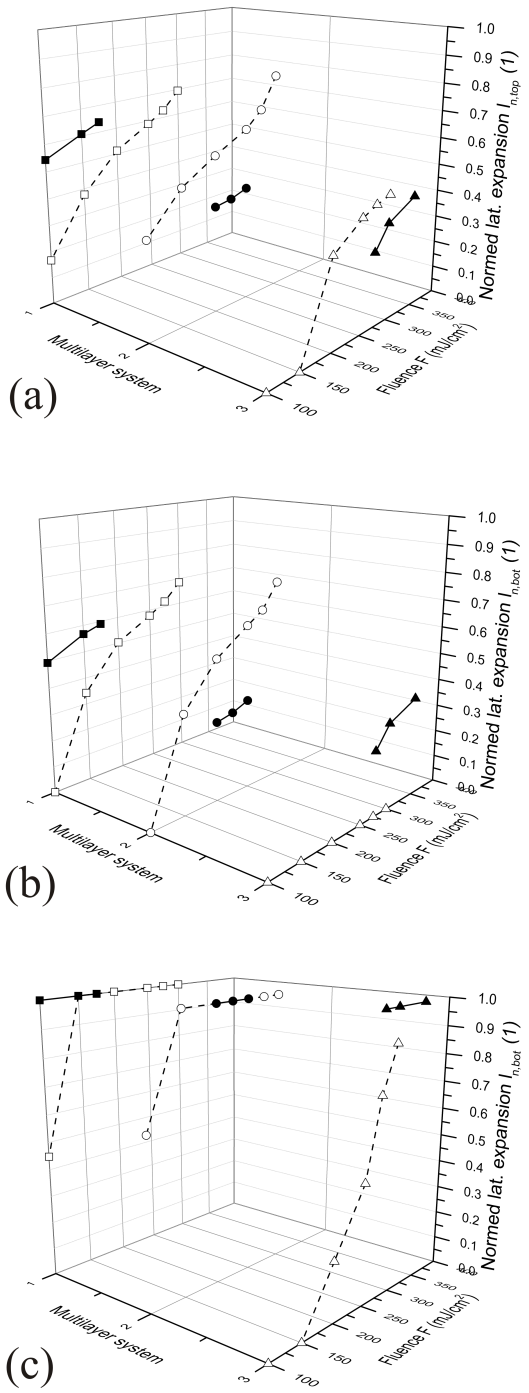


Figure 6.24.: Direct comparison between FEM estimated normalised dimensions of the heat-affected zone (open forms) obtained for the three multilayer material systems (1-Ni/Al, 2-Ti/Al and 3-Ni/Ti) and the corresponding results obtained by cross-sectional imaging (filled forms) on a-SiO_2 substrate when varying F for a constant periodicity of 8 μm: lateral expansion at the multilayer surface l_{top} (a), lateral expansion at the substrate interface l_{bot} (b) and depth expansion t_{dep} (c).

Figure 6.25 shows the situation encountered at an interference maximum site and its direct vicinity for Ti/Al on sc-Si after irradiation with 275 mJ/cm^2 fluence. Following the resolidification path from the residual multilayer microstructure in region (II) to the maximum region (III), the SAD images revealed a significantly different outcome of phases concerning present crystallinity. While all Ni/Al specimen sets were composed of crystalline phases in region (III) irrespective of the substrate employed, the micrograph of Ti/Al´s maximum (figure 6.25 (a)) showed a portion of homogeneous contrast spanning the whole lateral expansion of the heat-affected zone without any signs of internal boundaries or individual grains. While reaching the film-substrate interface, this portion was found to be covered by drop-shaped domains at the thin film´s surface. Those showed a darker Z-contrast signal due to higher mass density.

The SADP taken from the homogeneous formation (see figure 6.25 (c)) only consisted of blurred, homogeneous diffraction rings embedded into an elevated diffuse background signal. The rings were located at the $d_{\{hkl\}}$-spacings of the lower-indexed planes of both constituent phases, α-Ti {100} and {002} as well as Al {111}. Their appearance and shape could only be explained by the homogeneous formation consisting of an amorphous phase based on the constituting metals. According to the literature, the Ti/Al system is known to form metastable amorphous phases when prepared by ball-milling or mechanical alloying [212]. Especially the work of Bonetti at al. and Gerasimov et al. with the last mentioned technique produced a metastable hcp structure within the stoichiometry field of γ-TiAl ($L1_0$), the targeted at hand [213][214]. Here, the contrast and the background in the SADP only allowed to unequivocally image the aforementioned ring, thus impeding a deeper analysis.

Turning to the SADP stemming from one of the drop-shaped formations at the film´s surface (see 6.25 (d)), discrete reflections of two neighbouring crystals were recorded. They both could be identified as high-temperature β-Ti(Al) solid solution by zone axis

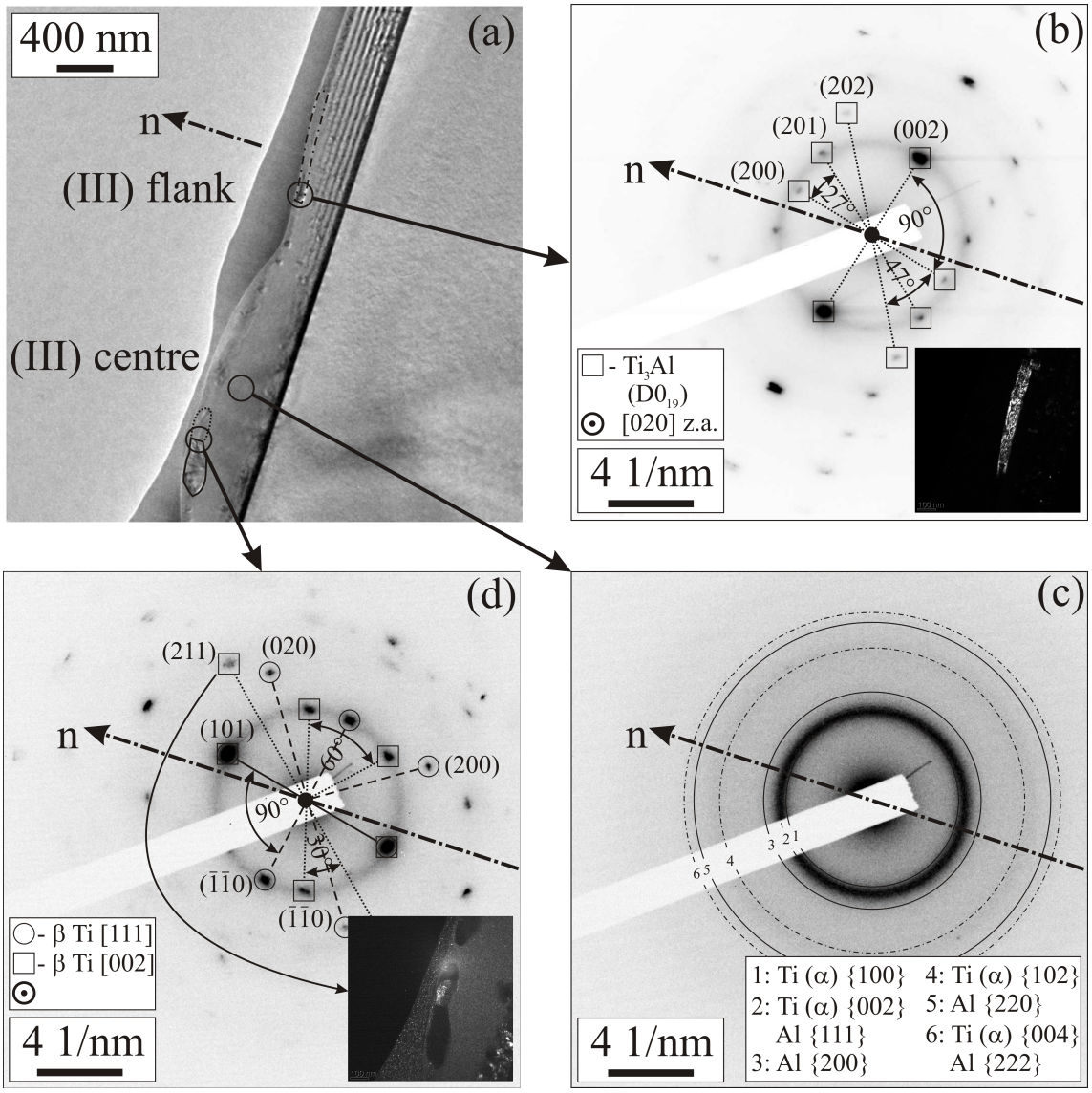


Figure 6.25.: TEM structural analysis of an interference maximum obtained for Ti/Al on sc-Si after LIMET treatment using $d = 8\,\mu$m and $F = 275\,\mathrm{mJ/cm^2}$: TEM micrograph (a) indicating the location of the site-specific SAD analyses. SADP zone axis images of region (III) flank (b), and region (III) centre at the thin film surface (c) as well as close to the substrate interface (d).

determination. The dark-field image shown in the insert revealed the respective grain to correspond to a singular drop-formation. These drops were not equiaxed and showed dimensions on the order of approximately 400 nm along the lateral and 150 nm along the depth coordinates. Looking more closely at the topographic depression, the amorphous formation was covered by an elongated grain which seemed to have evolved from the original Ti capping layer. Its SADP is given in 6.25 (b) and surprisingly shows the grain consists of a α_2-Ti_3Al ($D0_{19}$) intermetallic phase. As the corresponding dark-field image in the insert shows, the grain had an in-plane length of ca. 800 nm, while its thickness of 60 nm only slightly surpassed the original capping value. Considering the structure results of the crystals only, no metastable phase could be identified and the present phases mostly are associated to the Ti-rich part of the equilibrium phase diagram (c.f. figure 4.2). Apparently, the local chemical composition of the achieved intermix played a decisive role in determining the phases formed, a supposition affording confirmation by APT.

Analogous analyses performed on Ti/Al deposited onto fused silica and irradiated with 200 mJ/cm^2 fluence (micrograph see figure 6.26 (a)) yielded quite similar results with respect to he encountered phases. Despite the less convenient heat transport of the substrate material, the core of the maximum portion still consisted of the amorphous phase (see 6.26 (b)), but its size was reduced compared to the situation on sc-Si. In turn, the crystals covering the amorphous portion were found to be significantly larger and their outward shape no longer resembled drops. Instead, they turned out to be polygonal grains now entirely covering the whole surface of the interference maximum location. Their grain boundaries were found to be in contact exactly at the centre of the maximum and were aligned parallel to the specimen normal vector n. Like in the case of Ni/Al, this was taken as proof for a planar solidification front propagating laterally in the film´s plane.

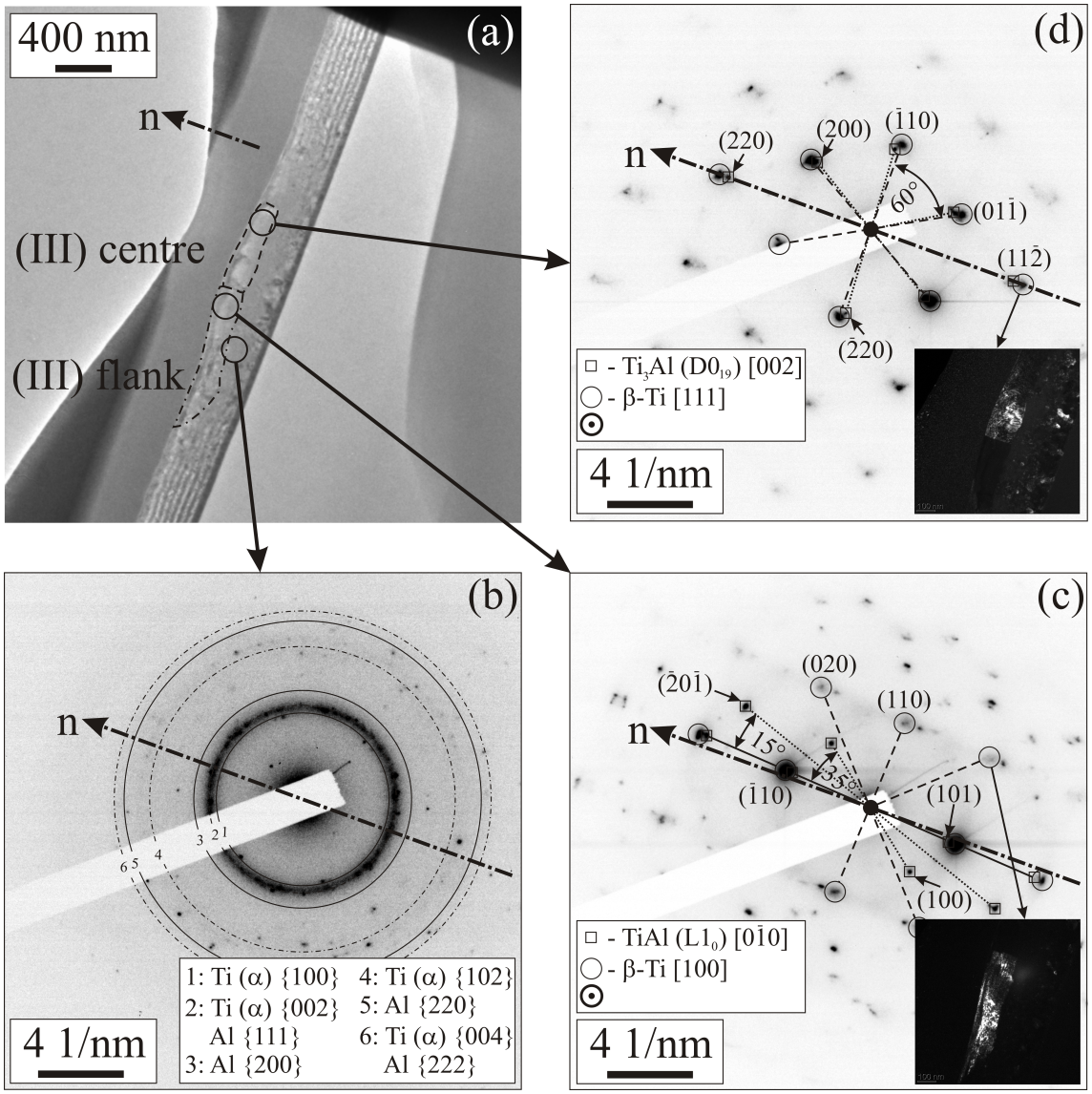


Figure 6.26.: TEM structural analysis of an interference maximum obtained for Ti/Al on a-SiO_2 after LIMET treatment using $d = 8\,\mu$m and $F = 200\,\mathrm{mJ/cm^2}$: TEM micrograph (a) indicating the location of the site-specific SAD analyses. SADP zone axis images of region (III) flank close to the substrate interface (b) and at the thin film surface (c) as well as region (III) centre (d).

The SADP taken from the left-hand side grain (see 6.26 (c)) shows two overlapping zone-axis diffraction patterns, which could be assigned to β-Ti(Al) in solid solution and intermetallic γ-TiAl ($L1_0$). Unfortunately, the respective diffraction spots were located so close to each other, that a dark-field image would be composed of signals stemming from both phases, thus impeding separate images of the original grains (see insert). Hence, instead of a single grain, the size of the crystalline zone was estimated to 1030 nm in-plane and 170 nm in depth elongation. Considering the relative orientation of diffraction spots to the direction of the normal vector n, β-Ti(Al) (110) planes were identified to be aligned parallel to the grain boundary. The diffraction information on the right-hand side (see figure 6.26 (d)) was determined to consist of overlapping β-Ti(Al) solid solution and α_2-Ti_3Al intermetallic zone axes. Like before, the spots were located too close to each other for individual imaging of the grains (see insert) and the crystalline portion measured 670 nm laterally and 180 nm in depth. Here, β-Ti(Al) ($\bar{1}10$) and Ti_3Al ($\bar{2}20$) planes were found to be parallel to the grain boundary. Both the close vicinity of the diffraction spots and the identified zone axes of the phases showed an orientation relation between the β and α_2 crystals. The crystallographically equivalent hexagonal basal plane of α_2 and the octahedron plane of β were also found to be parallel.

The microstructural morphology of the Ni/Ti sample sets (see micrographs in figures 6.22 (c) and (d)) seemed to be in line with the progression from crystalline products (Ni/Al) over a mixture of crystalline and amorphous phases (Ti/Al) to a completely amorphous product. Within both cross-sections a homogeneous contrast was visible and no distinct grain structures could be discerned. This was confirmed by close-up micrographs taken from specimens on both substrate materials (see bright-field image (a) of figures 6.27 for sc-Si and 6.28 for a-SiO_2, respectively). Following the minimum-maximum path in figure 6.27 (counter-clockwise order of the SADPs), diffraction imaging confirmed a gradual transition from crystalline educt phases to an amorphous product at the interference maximum site. Already at the border between region (II) and (III)

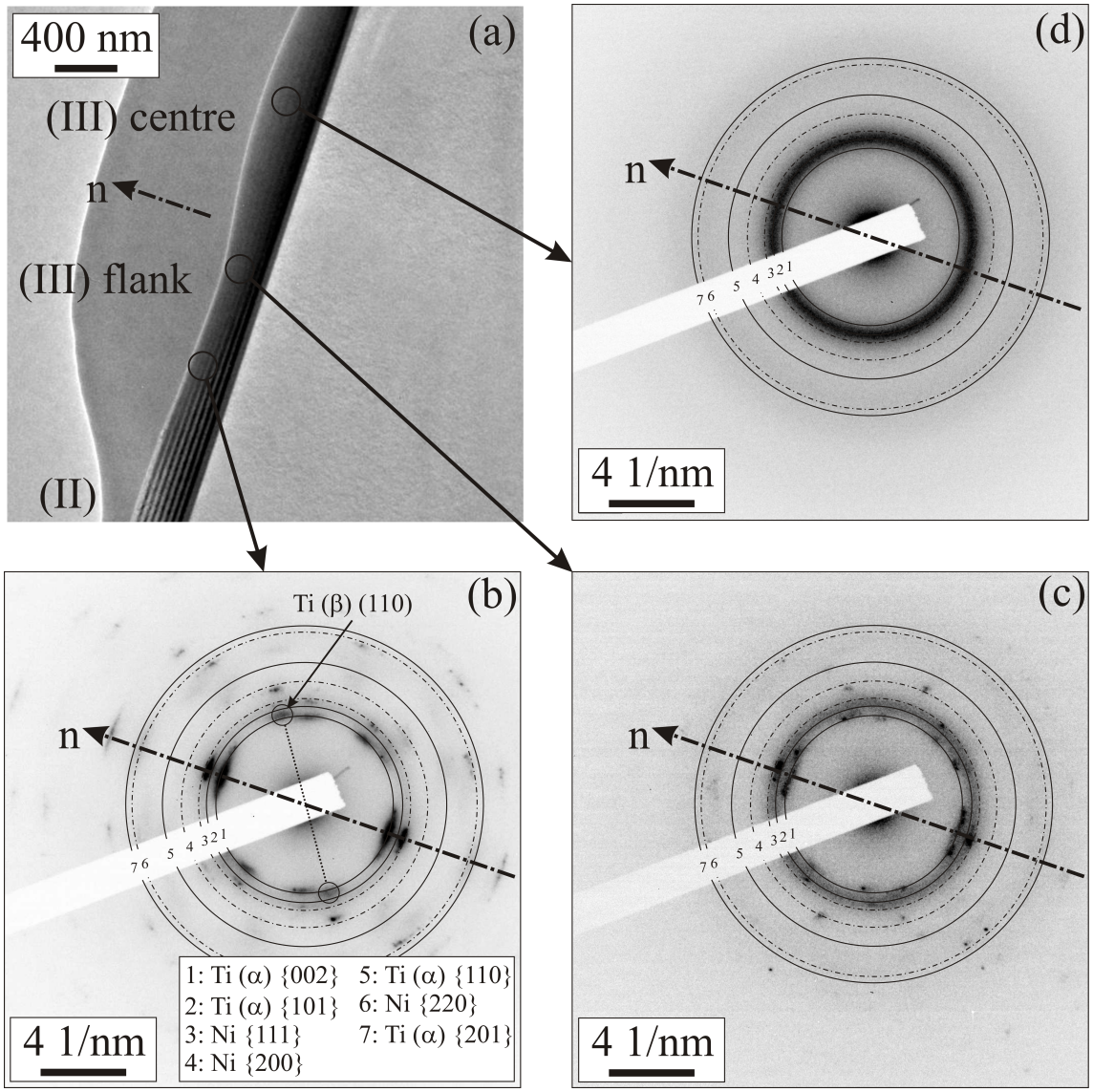


Figure 6.27.: TEM structural analysis of an interference maximum obtained for Ni/Ti on sc-Si after LIMET treatment using $d = 8\,\mu$m and $F = 275\,\mathrm{mJ/cm^2}$: TEM micrograph (a) indicating the location of the site-specific SAD analyses. SADP zone axis images of region (III) flank (b) and (c) as well as region (III) centre.

(figure 6.27 (b)), the SADP showed slight differences compared to the as-deposited state shown in figure 6.9 (b). Reflections associated with Ni appeared more diffuse, while α-Ti still yielded a pronounced signal. Nevertheless, their orientation relative to specimen normal vector n was unaltered thus showing the persistence of the aforementioned fibre texture. In addition, two β-Ti reflections (110) emerged. Apparently, the introduced heat led to the transformation of Ti from α to its high-temperature β modification. Closing in to region (III)´s onset (see 6.27 (c)), both Ti and Ni signals got more diffuse. While Ti only showed blurred individual reflections, Ni assumed a homogeneous ring-shaped distribution pointing to the loss of texture. It was assumed that this stemmed from the same effect observed in the case of Ni/Al: Ti atoms from the adjacent layers diffused into (s) Ni layers, finally being buried there during quenching.

At the maximum centre (6.27 (d)) only one homogeneously diffuse and broad ring was visible located between the $d_{\{hkl\}}$-spacings of β-Ti {110} and Ni {111}. This finally confirmed the assumed presence of an amorphous phase, most probably a quenched-in Ni(Ti) amorphous solid solution, since the ring was found at a larger $d_{\{hkl\}}$-spacing than the one of Ni {111}-planes. The possibility to form amorphous alloys in the Ni/Ti system via mechanical alloying or melt quenching is known since the work of Schwarz et al. and Bormann et al. in the 1980s [215][159]. The group of Hollanders employed mechanical alloying to produce amorphous alloys [216]. The metastable phase diagram applicable to this system was determined by thermodynamic calculations and confirmed by XRD in Bormann´s group [159], while Aliaga et al. determined the ideal glass forming conditions in this system [217].

In principle, the LIMET-patterning of Ni/Ti on fused silica yielded the same result, as figure 6.28 reveals. Once again following the SADPs in counter-clockwise sense, the evolution towards the maximum zone was visualised. Here, already in the transition between region (II) and (III) both the transition from α- to β-Ti and a pronounced blur

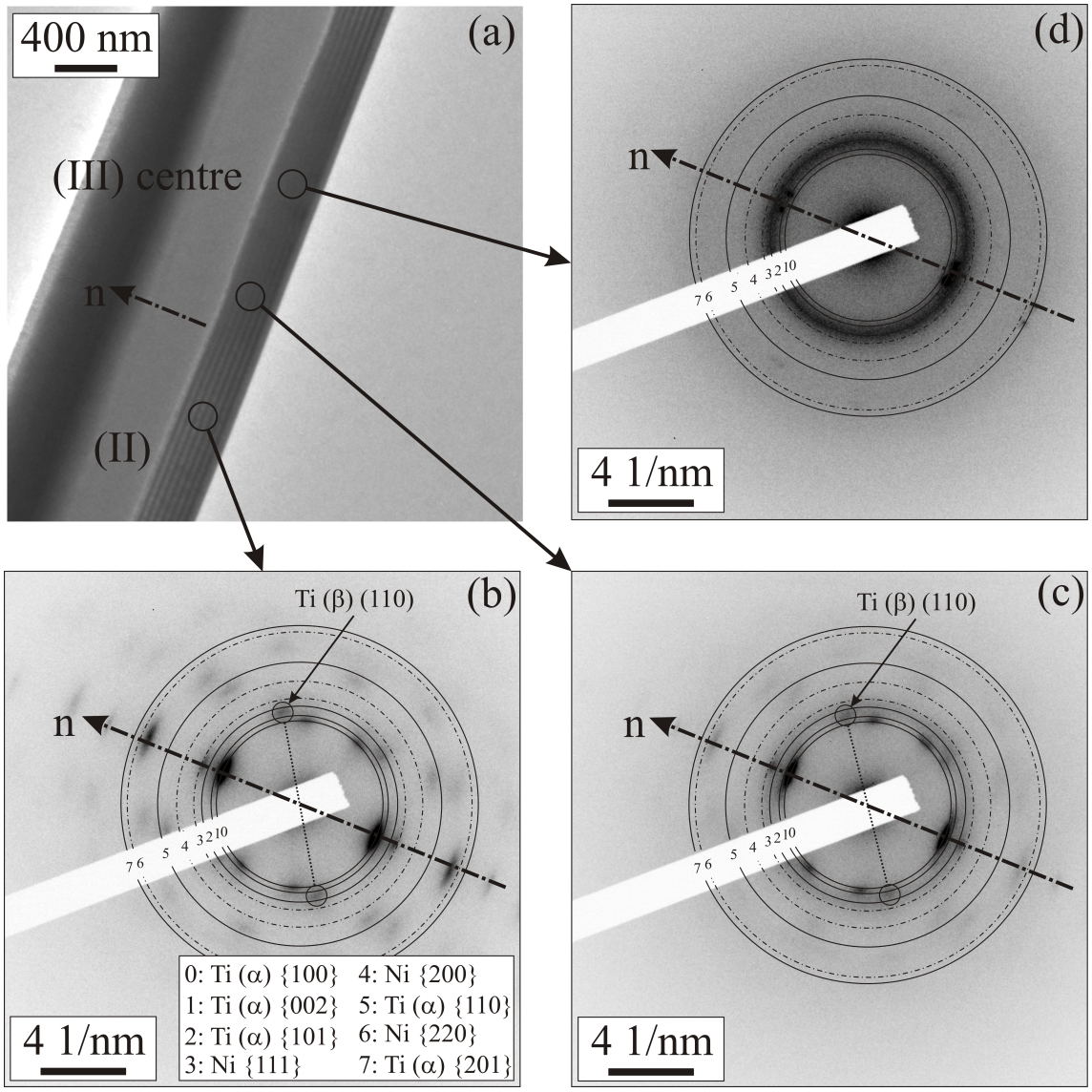


Figure 6.28.: TEM structural analysis of an interference maximum obtained for Ni/Ti on a-SiO_2 after LIMET treatment using $d = 8\,\mu$m and $F = 200\,\mathrm{mJ/cm^2}$: TEM micrograph (a) indicating the location of the site-specific SAD analyses. SADP zone axis images of the transition between region (II) and region (III) flank (b), region (III) flank alone (c) as well as region (III) centre.

of Ni-reflections could be confirmed (figure 6.28 (b)). Reaching the onset of region (III), a generally elevated background was found along with an increasingly ring-shaped diffuse Ni signal also exhibiting an enlarged $d_{\{hkl\}}$-spacing (figure 6.28 (c)). At the maximum´s centre (see figure 6.28 (d)) the same completely diffuse ring-pattern was found as in the case of sc-Si. Here, only minute traces of residual α-Ti could still be found in the vicinity of the specimen normal direction n.

6.3. Localised chemical analysis by APT

Especially the initial intermix observed in region (II) (e.g. see figure 6.19 for respective micrographs and SADPs recorded from Ni/Al on sc-Si) afforded the use of APT to image the elemental distribution with reasonable spatial resolution and chemical sensitivity. In concordance with literature [195], the type of substrate significantly determined the ability to measure APT sample tips. Since laser-assisted evaporation yielded stable conditions (see table 5.2), the substrate's heat transport capability governs the quality of the obtained mass spectrum and the peak shapes therein [218]. Essentially, all APT measurements were restricted to sc-Si specimen sets because of two reasons. First, the peaks consistently exhibited reduced thermal tails effected by retarded evaporation due to inhibited heat flow from the APT sample. Second, as the microstructural examination given in the section before revealed, only these allowed for a clear distinction between the processing regions (I) to (III) as introduced in figure 6.18 (d). Hence, sc-Si allowed for a more comprehensive view of the different intermix results.

In advance, it shall be mentioned that all attempts to run APT specimens extracted at the interference minimum position and within region (I) failed. In all cases, the samples ruptured and were lost when the evaporation reached the interface between the individual as-deposited layers. This could be attributed to differences in the evaporation fields of the respective metallic components according to image hump theory and post-ionisation

theory [196][195]. While measuring, the standing DC voltage U_{DC} is increased due to the changing tip radius r_{tip} in order to maintain a constant evaporation rate. During the transition from an Al layer requiring low fields for evaporation (19 V/nm) to Ti or Ni layers both affording higher field values (26 and 35 V/nm respectively), U_{DC} is increased further to maintain a constant evaporation rate. As soon as the next layer made of the species with lower evaporation field is reached, U_{DC} is already too high and exerts high mechanical stresses on the sample tip. Cohesion forces between the atoms can be exceeded thus causing tip fracture and catastrophic failure of the measurement. Successful measurements could first be obtained when tips were extracted from region (II). There, the close vicinity of an individual atom was composed of a mixture of both species thus reducing the effective difference in evaporation field. Conversely, this finding could be taken as an indication of the quality of the I-PVD deposition process. The failure of region (I) samples pointed to a low or even negligible amount of intermixing between the individual as-deposited layers, representing the intended reference situation. Following the same sequence of description, the results on Ni/Al shall be addressed first, being followed by Ti/Al and Ni/Ti. Initial results obtained from Ti/Al multilayers on sc-Si were already published by the author and coworkers in [65] and will be discussed in revised manner here. In contrast to the measurements performed on the other two material systems, these data were obtained at the experimental facilities of CAMECA using the systems LEAP 3000X HR and LA-WATAP.

Ni/Al on sc-Si

Figure 6.29 displays a typical mass spectrum recorded during an APT measurement of a Ni/Al specimen tip. Besides the main elements of the multilayer, both single and complex ionic species of other contributions were detected. Mainly these stemmed from the sputtering chamber, either from residual gases adsorbed onto walls or moving parts in the line of sight of the ion beam during sputter deposition (C^+, N^+ and O^+) or from the stainless steel chamber material itself (Cr^+, Mn^+ and Fe^+). As table 6.1 confirms,

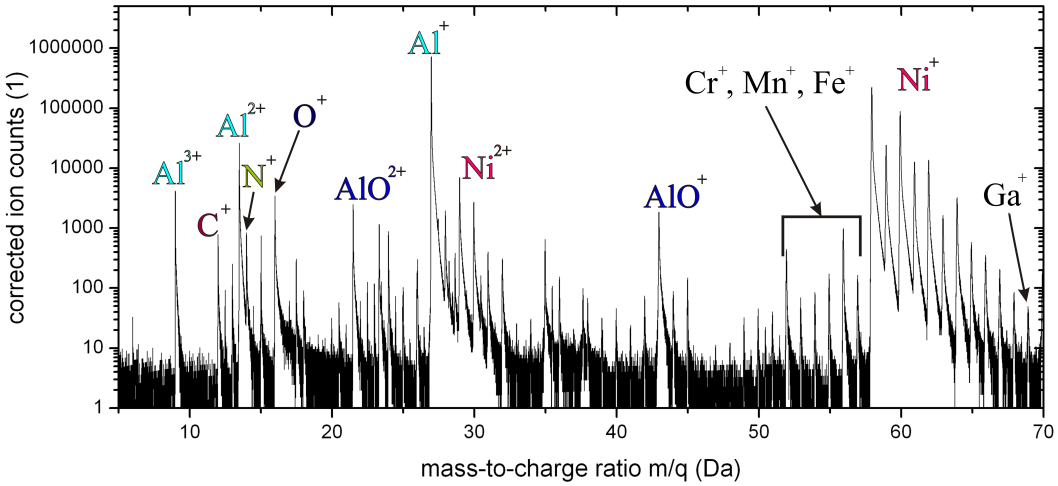


Figure 6.29.: Background corrected mass-spectrum typical for the Ni/Al multilayer specimens (correction based on protocol contained in analysis software IVAS): 58.2 Mio ions recorded, 47.8 Mio analysed, background level 2.68 ppm/ns with peak characteristics FWHM 1201.7 and FWTM 575.5.

APT sample tip extraction location	Component fraction c_i (at.%)							
	Ni	Al	C	N	O	Fe	Mn	Cr
region (II)	51.69	46.55	0.17	0.04	1.06	0.35	0.02	0.09
flank (III)	49.23	49.11	0.16	0.05	1.04	0.33	0.02	0.10
plateau (III)	47.48	51.00	0.12	0.02	0.90	0.29	0.03	0.10

Table 6.1.: Decomposed atomic composition of the overall recorded ions for the Ni/Al APT specimens (rounded to two digits).

their contribution to the overall chemical composition was considerably minute, mostly below 1 at.% for all recorded specimens. The same held for traces of Ga^+ ions which were introduced to the sample tips during the FIB annular milling routine. The presence of complex ionic species like AlO^{2+} was attributed to the rather high laser energy of 1 nJ

employed to assist evaporation. In line with the argument Dmitrieva et al. elaborated, the increased presence of 1+ in relation to 2+ charge states of the constituent species was taken as an indication of high laser energies [219]. Here, the detected low CSR of 0.024 for both principal elements confirmed the increased laser energy level. Despite this, the peaks of the mass spectrum did not show pronounced thermal tails confirming the appropriate choice of APT parameters and sample geometry. As the table shows further, irrespective of the extraction position and thus the processing state, the intended compositional relation between Ni and Al atoms was met quite well[7]. Even the undesirable incorporation of O was kept to a reasonable minimum of approximately 1.0 at.%, speaking in favour of the deposition process.

Looking at figure 6.30, the tip extraction positions within an interference maximum (see TEM bright-field image (a)) are designated along with respective SEM micrographs of APT specimen and 3D reconstructions of the encountered elemental distribution. Following the individual depictions there in clockwise order, the images follow the solidification path from region (II) into the lower (*flank)* and higher topography (*plateau)* parts of region (III). For visualisation reasons, the reconstructions were restricted to the two principal metallic elements (of which only 0.3 % of the recorded atoms are shown there) and the O distribution (100 % visibility).

In figure 6.30 (b), the situation in region (II) is given. Apparently, the individual metallic layers still could be discerned and the O atoms were not distributed homogeneously throughout the tip. Instead, O seemed to have aggregated to a compact layer which was always found atop a Ni layer. Entering region (III) in the flank part (figure 6.30 (c)), the traces of individual layers vanished leaving a qualitatively homogeneous

[7] This finding emphasises the problems associated with layer thickness based composition determination discussed in section 6.2.1.

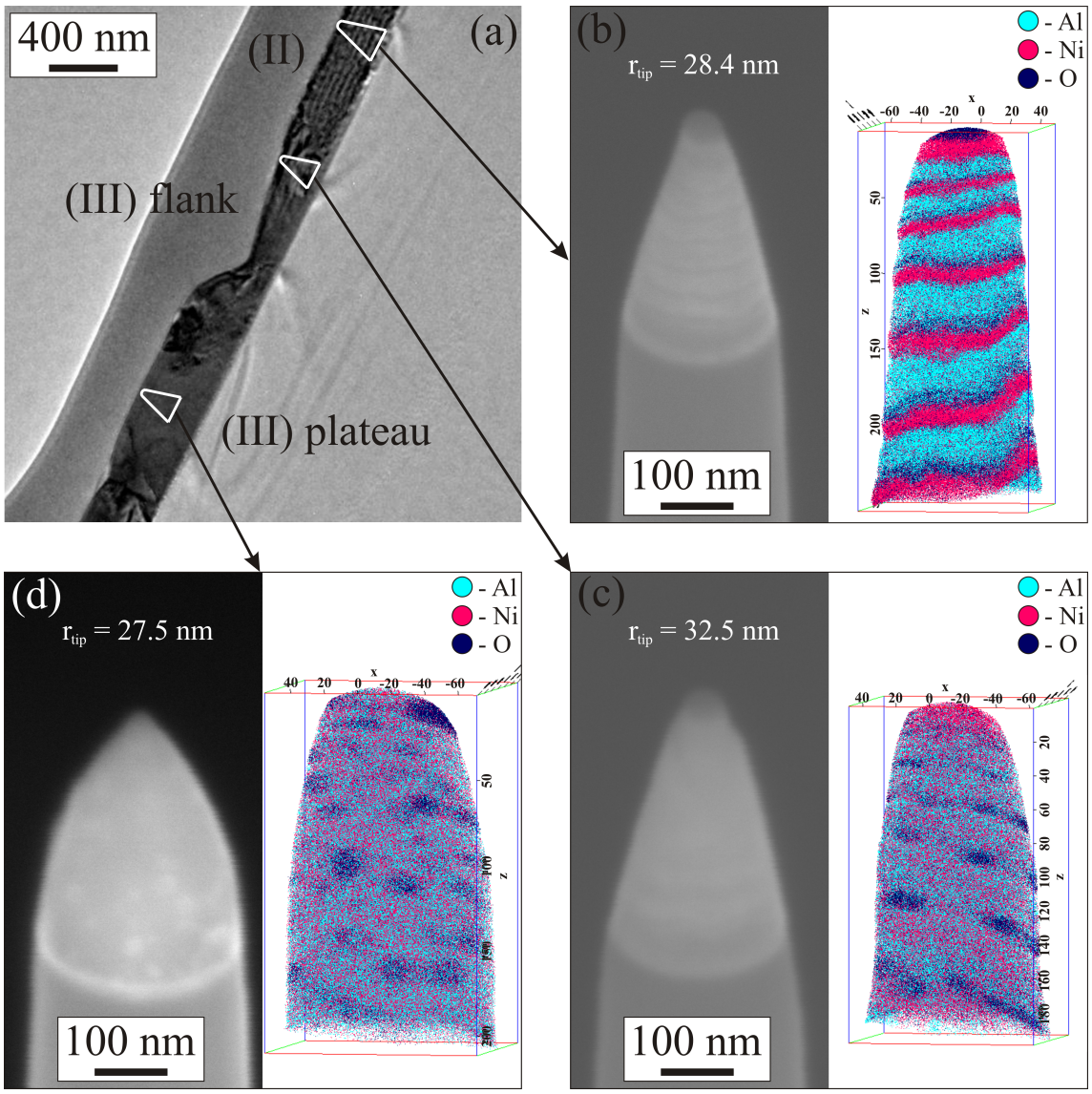


Figure 6.30.: Site-specific APT analysis of distinct processing regions of LIMET treated Ni/Al on sc-Si substrates: The TEM micrograph (a) indicates the approximate extraction locations for the subsequently analysed APT specimen tips. The latter are shown along with their corresponding APT 3D reconstructions in (b) for region (II), (c) for region (III) flank and (d) region (III) plateau. For the sake of better visibility 0.3 % of the Ni and the Al atoms and 100 % of the O atoms are visualised there.

mixture of Ni and Al. The only exception to this observation was the seemingly unaffected Ni capping layer at the top of the reconstructed tip. Also, the O distribution was altered to larger, separated aggregates whose arrangement resembled the original stack layering. At the centre part of the maximum (figure 6.30 (d)), the homogeneous dispersion of Ni and Al even included the region of the former capping layer. O in turn further continued its aggregation to finally form globular clusters being distributed homogeneously within the measured tip. These rather qualitative descriptions of the 3D reconstructions were backed both by the accompanying micrographs and the close examination of the elemental distribution by 1D concentration profiles (see figure 6.31).

Those profiles are given along with the *region of interest* (ROI) they were calculated from. Consistently throughout this thesis, the ROIs were selected to be of cylindrical shape with 40 nm diameter and length spanning through the whole tip height. The data inside these ROIs was sampled using fixed counts to account for any slight density variation. As the inserts to each 1D concentration profile reveal, it was intended to orient the ROIs perpendicularly to the layers forming the stack. This proved difficult due to layer morphology, thus causing some inaccuracies in the 1D profiles. The profile of region (II) shown in figure 6.31 (b) impressively confirmed the assumption of (s) Ni dissolving into (l) Al, which was so far only deduced from Z-contrast observations in figure 6.19. Here, Ni very clearly entered into the surrounding Al layers to be finally buried at approximately 20 to 30 at.% thus widely exceeding the equilibrium solubility of Ni in Al (0.11 at.% at the eutectic temperature [220]). Depicted in the same figure, this nicely shows the gradual change from a crystalline to an amorphous diffraction signal for Al. The latter, in turn, seemed not to have crossed the layer interfaces into Ni as its maximum content there could be quantified between 0 to 2.5 at.%. This variation might also be attributed to the initially present layer topography as found in the TEM cross-section in figure 6.7 (a).

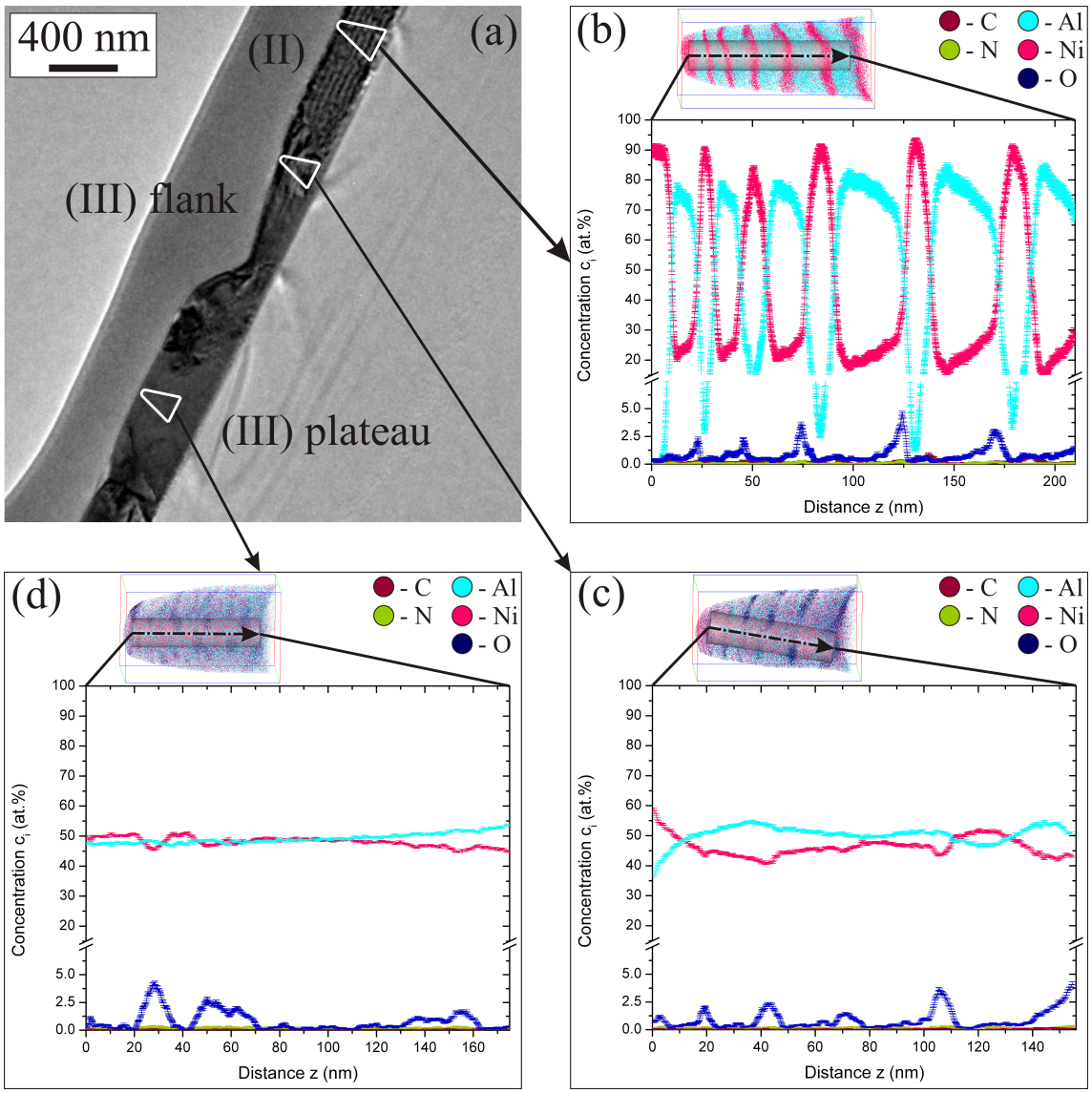


Figure 6.31.: Site-specific APT analysis of distinct processing regions of LIMET treated Ni/Al on sc-Si substrates: The TEM micrograph (a) indicates the approximate extraction locations for the subsequently analysed APT specimen tips. The 1D-concentration profiles calculated from a 40 nm-diameter cylindric ROI of the latter are shown in (b) for region (II), (c) for region (III) flank and (d) region (III) plateau.

Returning to the functional course of the components´ composition c_i, the signal of Ni and Al showed interesting individual features, which were linked by the calculation method for the individual fractional portions. Looking at the width of the layers, it could be stated that it increased with an increasing z-coordinate in depth. After the third bilayer from the left (counting from the top) the layer width assumed a constant value of ca. 34 nm up to the end of the APT measurement[8]. According to pertinent literature, this effect can be attributed to dynamic effects taking place during an APT measurement, such as varying tip radius r_{tip}, tip geometry factor k or image compression factor κ [221][222][195].

With the voltage curve of this particular APT measurement exhibiting pronounced oscillations associated with the evaporation propagating into layers of materials with significantly different evaporation field (not shown here), this notion was confirmed. The evolution to the constant layer width representation might then be interpreted as an effect of more stable measuring conditions. Considering the large compositional variation within the Al layers given before, another feature was revealed in all bilayers. While Ni increases by 10 at.% with increasing z-coordinate, Al is reduced by the same amount. This finding was taken as an artefact of the reconstruction associated to the variation of layer widths discussed above. Studies of Vurpillot et al. dealing with APT reconstructions of precipitations in a metal matrix provide a possible explanation. They report variations in recorded atomic density at the interfaces between materials having a large difference in evaporation field. Those *depleted zones* were observed within the low-field material, which was also the case here in those parts of Al layers close to the interface with Ni (2D density plot not shown here). These observations fit the concept of *local magnification* representing the most prominent artefact known in APT reconstruction [223][224].

[8]The width was measured by calculating the difference between the intersection coordinates of the c_i-plots of Ni and Al.

The lower concentration part of this graph is given magnified in order to depict the distribution of trace elements more clearly. While the traces of C were found to be homogeneously distributed within the ROI, the signal of O and N followed the layering sequence as stated qualitatively earlier. Since O yielded the prominent contribution, its course shall be described here more closely. The O content was found to rise from a minimum 0.3 to a maximum between 3.5 and 4.5 at.% within a Ni layer when approaching the boundary to the underlying Al layer[9]. This was consistently reported for every bilayer within the specimen tip, which could be analysed using proximity histograms (*proxigrams*) calculated from 50 at.% isoconcentration surfaces (*iso-surface*) of Ni in figure 6.32 (a). There, two mean composition traces entering a Ni layer from the top (figure 6.32 (b)) and from the bottom (figure 6.32 (c)) are depicted.

A possible explanation for this distribution was devised when considering the deposition sequence of the I-PVD sputtering for multilayer production. As figure 5.2 (a) clearly shows, the targets were mounted onto a rotating holder. While one target was sputtered, the other faced the opposite wall of the chamber and thus was exposed to residual gases which the vacuum system was not able to effectively remove from the chamber. Target materials known for their potential as O getters like Al and Ti are especially likely to be covered by adsorbate layers within short time periods. A single layer deposition took around 5 min., enough to completely cover the Al target. As soon as the target was turned to face the ion beam, the adsorbate layers were removed before the actual target material was reached. Therefore, the initial parts of an Al layer were composed of a mixture of O, N and Al which evolved into dominating Al content with

[9] O content was determined using the O^+ peak at 16 Da alone. Following the argument of Bachhav et al., this peak was assumed to correspond to O^+ rather than O_2^{2+} due to the low number of multiple hits observed during the APT measurement [225]. Moreover, at 32 Da the peaks of Ni^{2+} and O_2^+ overlap, affording a peak deconvolution. Since the absolute peak height there amounted to less than 10 % of the 16 Da-peak, its contribution was deemed negligible.

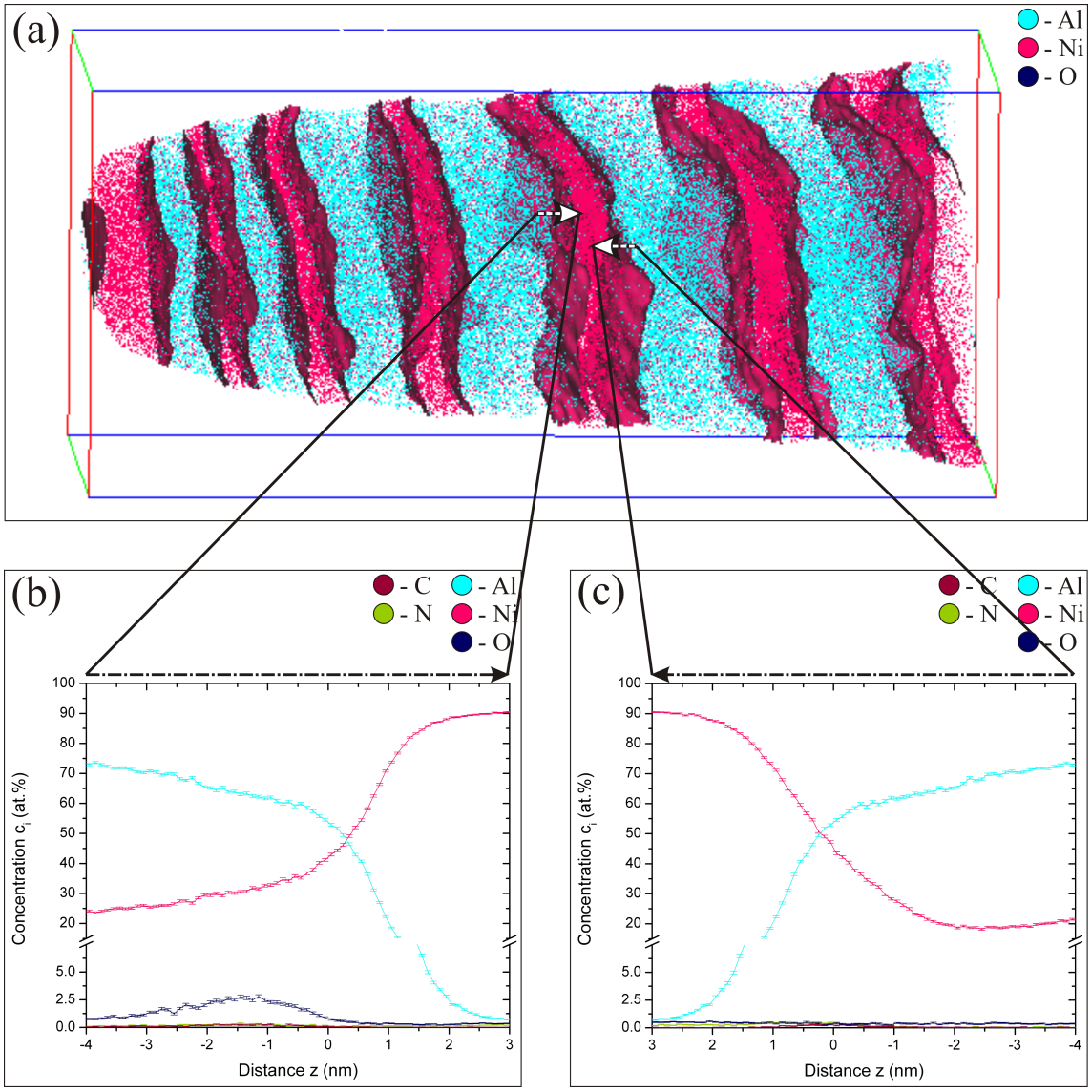


Figure 6.32.: Dedicated analysis of Ni/Al region (II) APT specimen tip: 3D reconstruction (a) of the specimen showing 50.0 at.% Ni iso-surfaces. (b) and (c) show proxigrams of these iso-surfaces summarised over upper (b) and lower (c) layer interfaces.

the ongoing sputter cleaning. Table 6.1 shows that the overall O content nevertheless was considerably low throughout the stack, making alterations to the deposition process unnecessary. Turning to the 1D concentration profile of the flank portion of region (III) shown in figure 6.31 (c), the compositional distributions both of Ni and Al turned into a more homogeneous intermixed state. As the qualitative view on the reconstructed tip in figure 6.30 inferred, Ni capping still was present at the top of the APT specimen which thus could be quantified at approximately 60 at.% Ni and 40 at.% Al. Following the z-coordinate in depth, the fractions of both elements varied around 50 at.% in an interval of ca. ± 5 at.% width. The variation of the trace elements still resembled the original stacking sequence, with the exception of the width of the O aggregates increasing in comparison to the situation encountered in region (II). Even the O content itself was found to be equal in magnitude. Within the plateau of region (III), the concentration profiles of the constituent metals (figure 6.31 (d)) were even more flattened to 50 at.% over the whole depth in a more narrow composition interval.

Only towards the end of the tip at a considerable distance from the multilayer surface, did the mixture depart from this ideal situation with a linear increase of Al to 55 at.% and an according decrease of Ni to 45 at.%. The O aggregates in turn enlarged further, keeping their general composition, but now showing no residual traces of the original stack. Taken together, these findings confirmed the LIMET process to have effected a complete intermix of the metallic constituents to the intended stoichiometry within the reach of region (III). It was seen reasonable to assume, that at least two different atomic exchange processes led to this result. The situation encountered in region (II) could be attributed to fast diffusion processes in (s) state, which also have taken place in region (III) before the laser irradiation effected even higher temperatures. As soon as these set in, the Ni layers transformed to (l) state, leaving behind a pool of completely molten material.

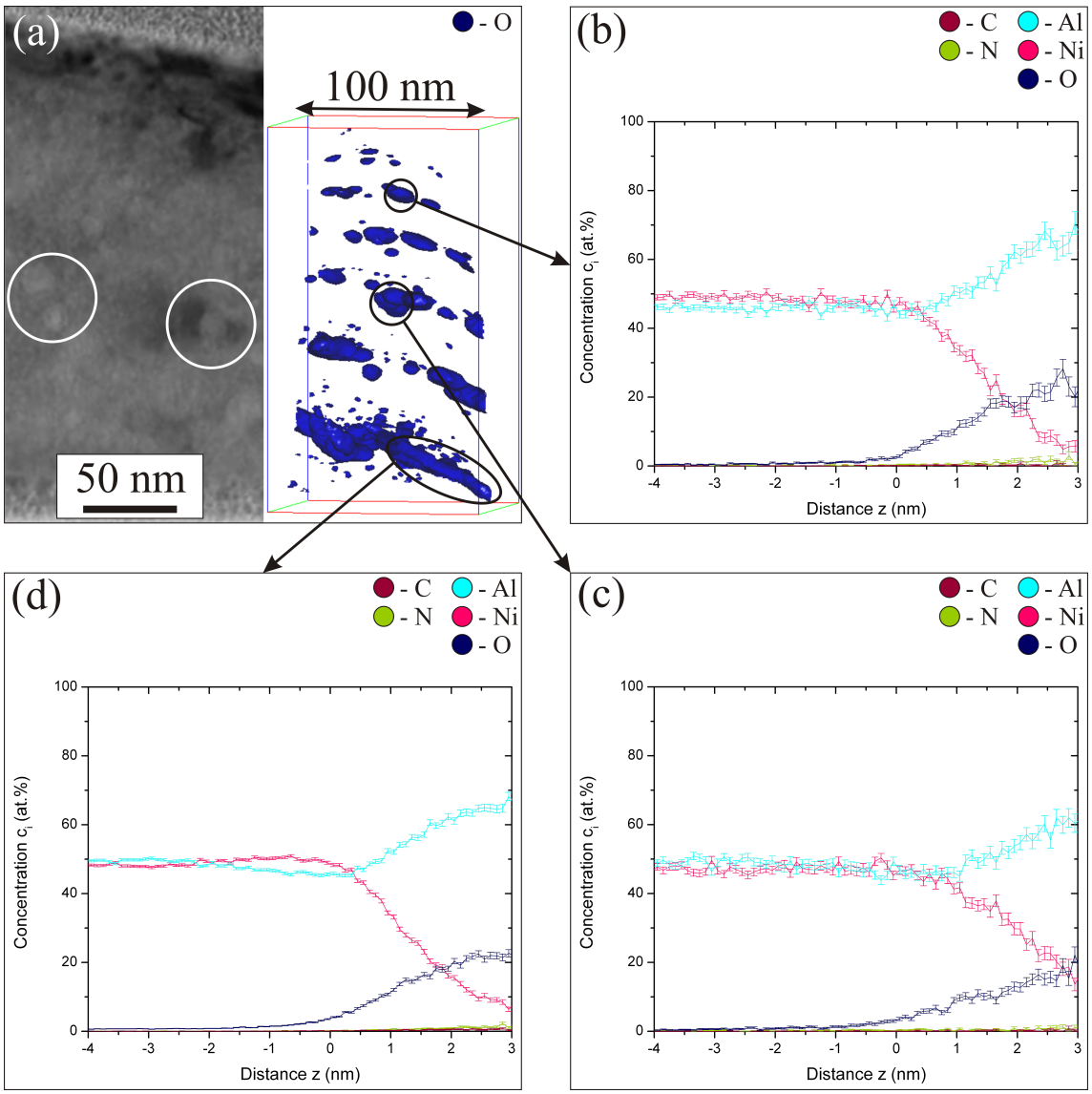


Figure 6.33.: Dedicated analysis of Ni/Al region (III) flank APT specimen tip: close-up TEM micrograph and corresponding 3D reconstruction (a) of the specimen showing only the O 4.0 at.% iso-surfaces. The latter are confirming the presence of differently shaped O aggregates. (b) to (d) show proxigrams of individual O aggregates found at different depth coordinates z of the specimen tip.

Together with the topography observed in the cross-sectional micrographs (see figure 6.14), it was obvious to assume that Marangoni convection was active in this region, thus leading to even more efficient intermixing. Using the iso-surface approach, the O aggregates encountered in the two parts of region (III) were examined closer and compared to highly magnified TEM bright-field images. Figure 6.33 shows proxigrams calculated for 50 at.% Ni iso-surfaces taken from three different depth regions (from top to bottom of the APT sample tip in clockwise sequence). Obviously, the compositional distribution across the interface of the iso-surface exhibits the same behaviour. Coming from the left, the exterior of all iso-surfaces showed a 50:50 set Ni/Al mixture with a very low amount of residual gases. In the interior, the Ni content gradually dropped to approximately 5.0 at.%, while the ones associated to O and Al rose in the same manner to 20 and 70 at.%, respectively.

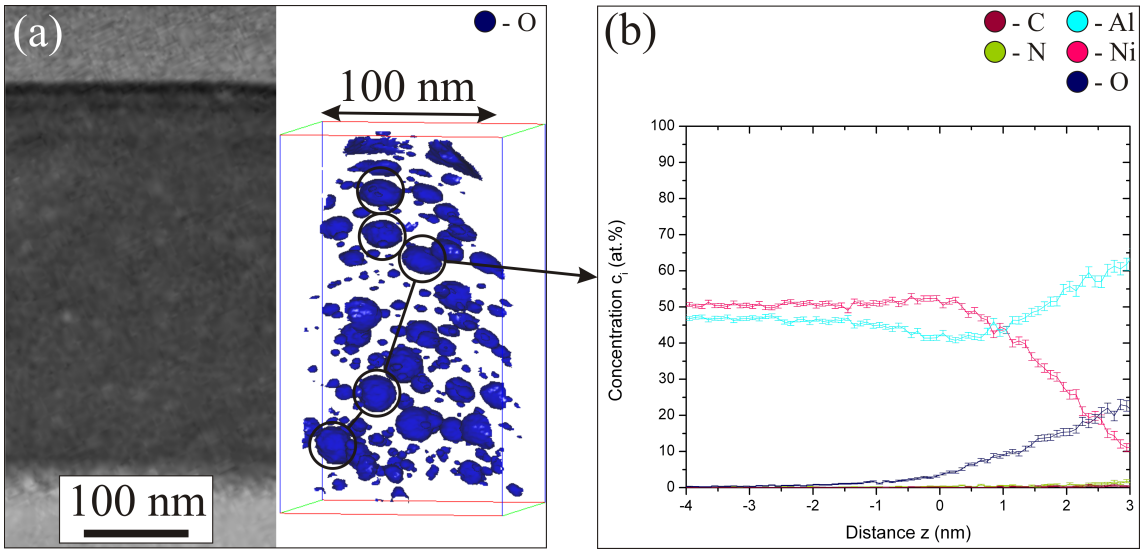


Figure 6.34.: Dedicated analysis of Ni/Al region (III) plateau APT specimen tip: close-up TEM micrograph and corresponding 3D reconstruction (a) of the specimen showing only the O 4.0 at.% iso-surfaces. Both images confirm the presence of globular O aggregates. (b) shows a proxigram calculated of five individual O aggregates.

Closer to the thin film surface, the shape of the iso-surfaces was more globular, while in the lower parts a gradual transition to flat ellipsoids and once again a compact layer could be visualised (see tip reconstruction in figure 6.33 (a)). The accompanying bright-field image taken from the vicinity of the thin film surface shows similar globular formations within the homogeneously contrasted matrix (see white circles). In the literature, no information on a crystalline phase of these elements is reported for the measured stoichiometry. The same results were obtained for the O aggregates encountered at the plateau of region (III). As figure 6.34 (a) reveals, the tip extracted there contained only globular aggregates, which were homogeneously distributed within the volume.

Ti/Al and Ni/Ti on sc-Si

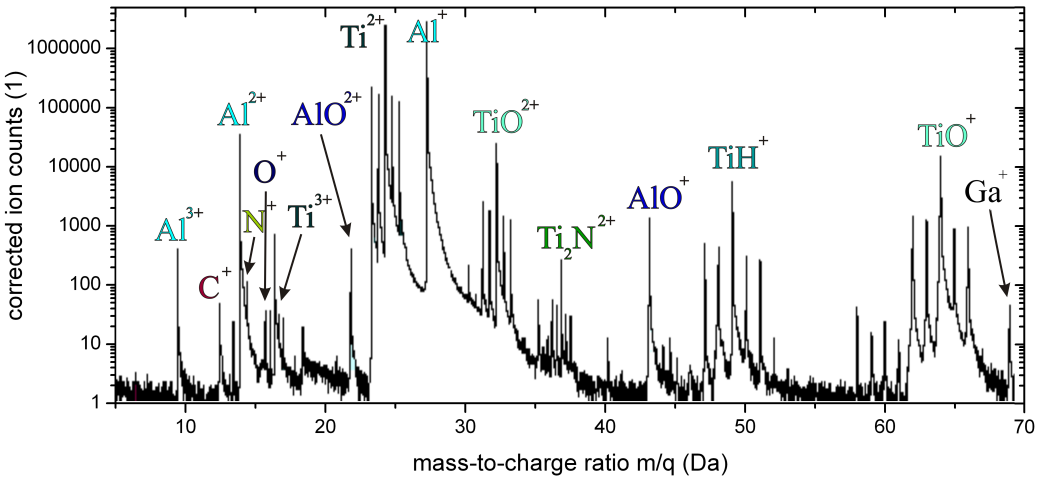


Figure 6.35.: Background corrected mass-spectrum for the Ti/Al multilayer specimens (correction based on IVAS protocol, courtesy of Cameca Instruments Inc.).

Due to the fact, that the measurements on Ti/Al were performed by personnel and facilities of CAMECA in the framework of preliminary tests, the analysis of the data was not as comprehensive as shown for the case of Ni/Al above and Ni/Ti discussed later. Unfortunately, the raw data was not transferred to the author, which would have

allowed pursuing this systematic approach autonomously. Nevertheless, the data furnished was useful to grasp the essence of the intermix result of Ti/Al in the different identified regions. Figure 6.35 shows the mass spectrum typically obtained from the Ti/Al APT specimens. Its principal shape and features are similar to those of Ni/Al (see figure 6.29): it contains single- and multiple-charged ions of the constituent metals, besides traces of residual gases (C^+, O^+ and N^+) and complex ionic species (most prominently formed of the metals in conjuction with H, O and N). In contrast to the spectrum of Ni/Al, here the peaks show pronounced thermal tails which could be an incentive to reevaluate the APT measuring parameters for this material combination.

The 3D reconstructions and 1D concentration profiles shown in figure 6.36 and 6.37, respectively were already published in [65]. Therein, figure 6 showed their relation to the microstructure of an interference maximum. In the light of the findings on Ni/Al described above, the author reviewed the TEM micrographs taken from the specific Ti/Al sample in order to correctly identify the three processing regions according to figure 6.18 (d). As the bright-field images (a) of both figure 6.36 and 6.37 reveal, the revised allocation differed from the published one. Especially, the paper´s statement to contain data on the interference minimum region was successfully refuted by the reasons discussed above. Hence, the bright-field images contain a slightly shifted assignment of the respective APT sample target areas. Both in figure 6.36 (b) and 6.37) (b) the situation formerly assigned to the interference minimum is depicted, which then was found to originate from region (II), as clearly could be deduced from the oscillating 1D-concentration profile. There, Ti could be proven to have entered the Al layers leading to a content between 35 and 40 at.%, thus exceeding the equilibrium solubility of Ti in Al (0.6 at.% at the eutectic temperature [226]). The Al content in Ti layers in turn did not exceed ca. 3.0 at.%. Even the spatial distribution of O showed a behaviour similar to the situation in Ni/Al. Here, O content increased from ca. 1.0 at.% in Al- to 10 at.% within the Ti layers also exhibiting maximum values for the layer portions being deposited first.

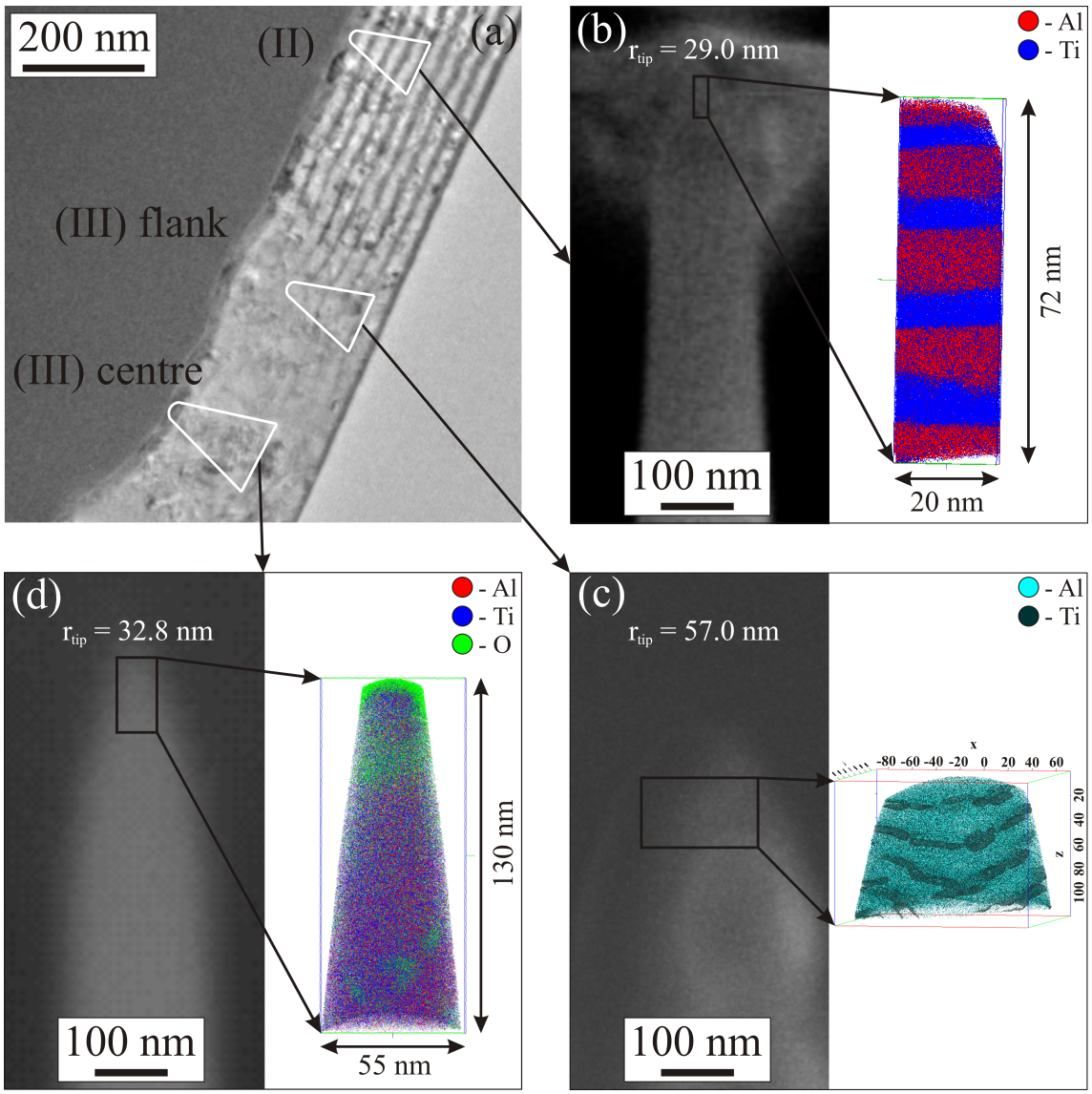


Figure 6.36.: Site-specific APT analysis of distinct processing regions of LIMET treated Ti/Al on sc-Si substrates (modified and corrected from [65]): The TEM micrograph (a) indicates the approximate extraction locations for the subsequently analysed APT specimen tips. The latter are shown along with their corresponding APT 3D reconstructions in (b) for region (II), (c) for region (III) flank and (d) region (III) centre (SEM micrographs of the specimen tips courtesy of Cameca Instruments Inc.; modified from [65]).

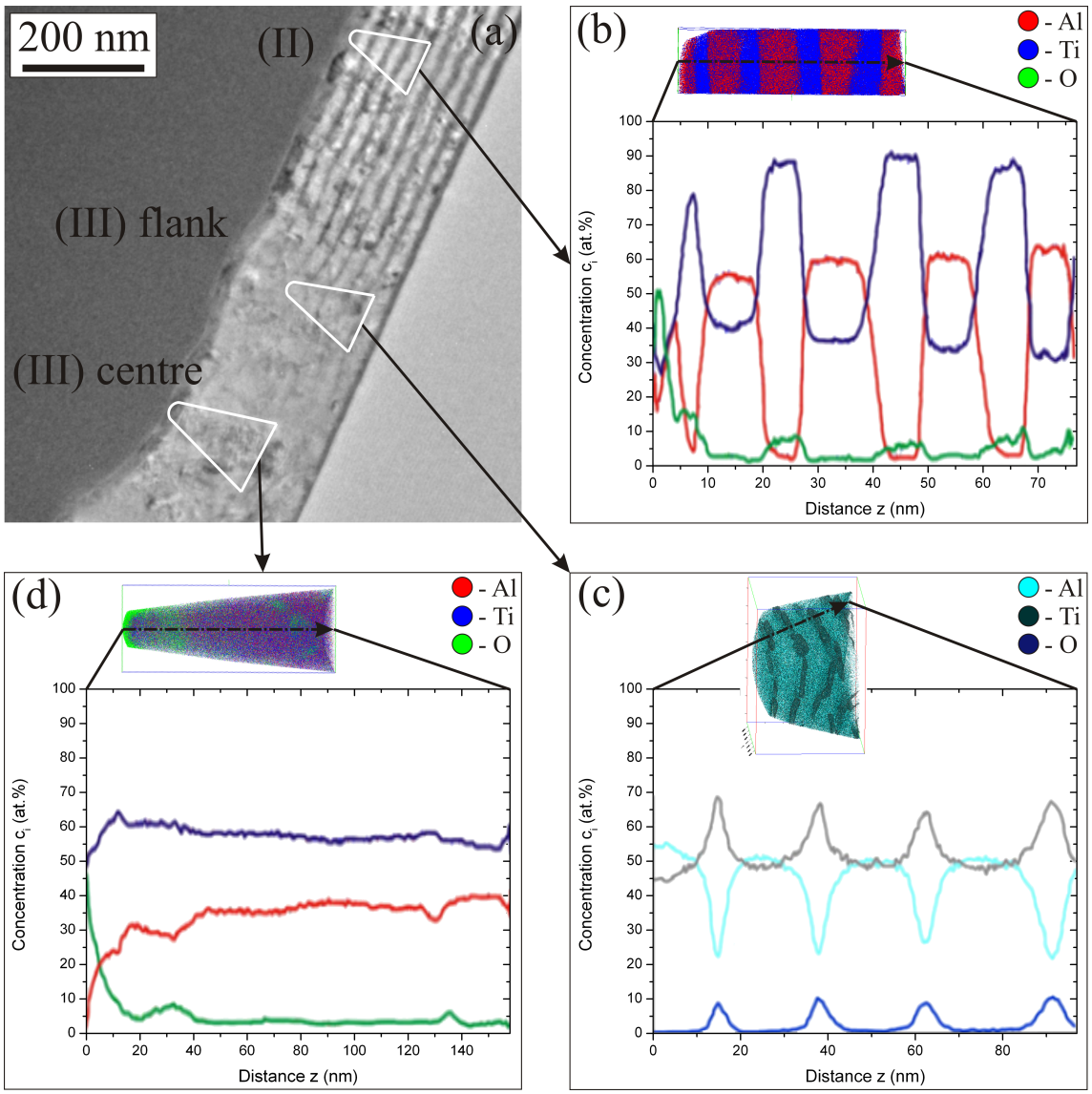


Figure 6.37.: Site-specific APT analysis of distinct processing regions of LIMET treated Ti/Al on sc-Si substrates (modified and corrected from [65]): The TEM micrograph (a) indicates the approximate extraction locations for the subsequently analysed APT specimen tips. The 1D-concentration profiles calculated from a cylindric ROI of the latter are shown in (b) for region (II), (c) for region (III) flank and (d) region (III) centre (modified from [65]).

The switch from Al to Ti containing O was straightforward due to Ti being widely known for its capability as O getter. Consequentially, the pronounced O content of 50 at.% could be attributed to the same material property. The second APT specimen ((c) both in figure 6.36 and 6.37) was extracted at the transition between regions (II) and (III), which was deduced from the still visible composition fluctuations for Al and Ti. Here, the former Al layers contained a 50:50 mixture of Ti and Al and were surrounded by residual Ti layers showing a reduced width of less than 10 nm which is the value found for region (II). The shape of the O signal further sharpened keeping those atoms within the narrower Ti layers, with the same maximum amount of 10 at.%. With the stack sequence still clearly visible, it was assumed that the specimen tip represented those parts of the multilayer located closer to the substrate interface. This was confirmed by the microstructure presented in the associated TEM bright-field image.

Approaching region (III) (see (d) both in figure 6.36 and 6.37), no residues of the original stacking were left in the 3D representation or the 1D concentration profile. At the top of the APT specimen an obviously large O content of 40 at.% was recorded, which sharply decreased within a z depth of 20 nm to a value of less than 5.0 at.% which then was mostly constant throughout the remaining depth. At the same location, both Ti and Al content rose comparably steep to a then constant 60 at.% and 35 at.%, respectively. Taking these findings together with the bright-field image here and the TEM analysis presented in figure 6.25, it was concluded that this specimen tip was extracted from a near-surface part of central region (III). The close similarity of the evolution of concentration profiles for Ni/Al and Ti/Al proved, that LIMET was able to activate the two discussed mass transport effects in this case also. Only the stoichiometric ratio of the metallic constituents was met differently depending on the depth from which the APT specimens originated. As a working hypothesis, this was attributed to the already widely discussed differences in heat propagation behaviour between the two multilayer systems on the one hand and along lateral and depth direction on the other hand.

Concluding the description of the APT results, the Ni/Ti sample sets shall be discussed in the following. The typical mass spectrum obtained for Ni/Ti samples is given in figure 6.38, in perfect concordance with the two mass spectra discussed before. Since Ni/Ti once again was measured using the APT facility at Saarland University, more tests were possible to determine better measurement parameters and specimen geometries. This is reflected in improved mass resolution and only minute thermal tail contribution.

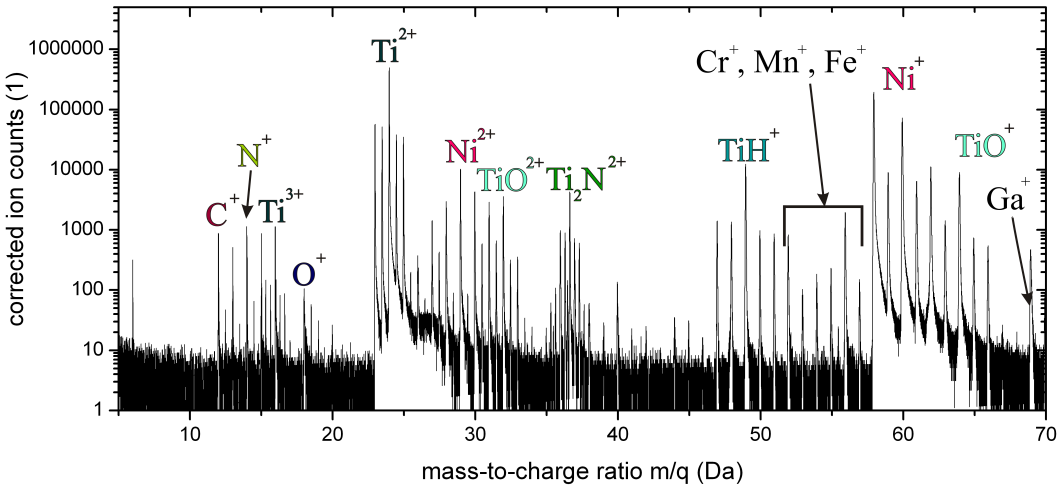


Figure 6.38.: Background corrected mass-spectrum typical for the Ni/Ti multilayer specimens (correction based on IVAS protocol): 55.9 Mio ions recorded, 34.7 Mio analysed, background level 5.74 ppm/ns with peak characteristics FWHM 1259.1 and FWTM 653.5.

In this case, APT measurements were successfully carried out for sample tips prepared from the region (III) flank and centre only, as figure 6.39 for the 3D reconstructions and figure 6.40 depict. The overall chemical composition encountered there is summarised in table 6.2 including the contributions of residues from gaseous species and chamber wall material. Within the probed volume of both specimens, the intended 50:50 ratio of Ni/Ti was achieved, once again confirming the stability of the deposition process. Besides the O content which reached ca. 2.0 at.%, all other contributions were significantly less than 1.0 at.% and were thus considered negligible. Looking at the actual spatial

APT sample tip extraction location	Component fraction c_i (at.%)							
	Ni	Ti	C	N	O	Fe	Mn	Cr
flank (III)	48.16	47.38	0.52	0.74	2.17	0.61	0.06	0.22
centre (III)	48.27	47.65	0.42	0.69	2.07	0.58	0.06	0.21

Table 6.2.: Decomposed atomic composition of the overall recorded ions for the Ni/Ti APT specimens (rounded to two digits)

distribution inside the volume measured from the APT specimen, essentially the same features can be found as in the two cases discussed before. The tip extracted from the flank part of region (III), see (b) in figures 6.39 and 6.40, showed two different regimes of intermixing along the depth coordinate z. The near-surface portion up to z=100 nm already exhibited a considerable exchange of atoms leading to a mean composition of ca. 48 at.% in both principal metallic elements. This exchange still was superposed with a weak oscillation stemming from the former stacking sequence. With increasing depth, the compositional amplitude increased for both elements pointing to a reduced intermixing due to lower local temperature in the near-substrate portion. This behaviour could also be visualised in the SEM micrograph of the specimen before the APT measurement (see figure 6.39 (b)), where the top region exhibited a homogeneous grey-scale representation, whereas the lower part showed a periodic contrast change associated with the residual multilayer structure.

In both APT specimens, the Ni content in Ti clearly exceeded the equilibrium solubility of Ni in Ti (10 at.% at the eutectic temperature [163]). As the magnified low-concentration part of the 1D concentration profile (see figure 6.40 (b)) reveals, the O content also oscillated with the original stacking sequence and showed maximum values of 3.0 to 6.2 at.% at the location of the former Ti layers. Within the adjacent former Ni layers, the O content did not exceed 1.2 at.%. This fitted quite well with the behaviour

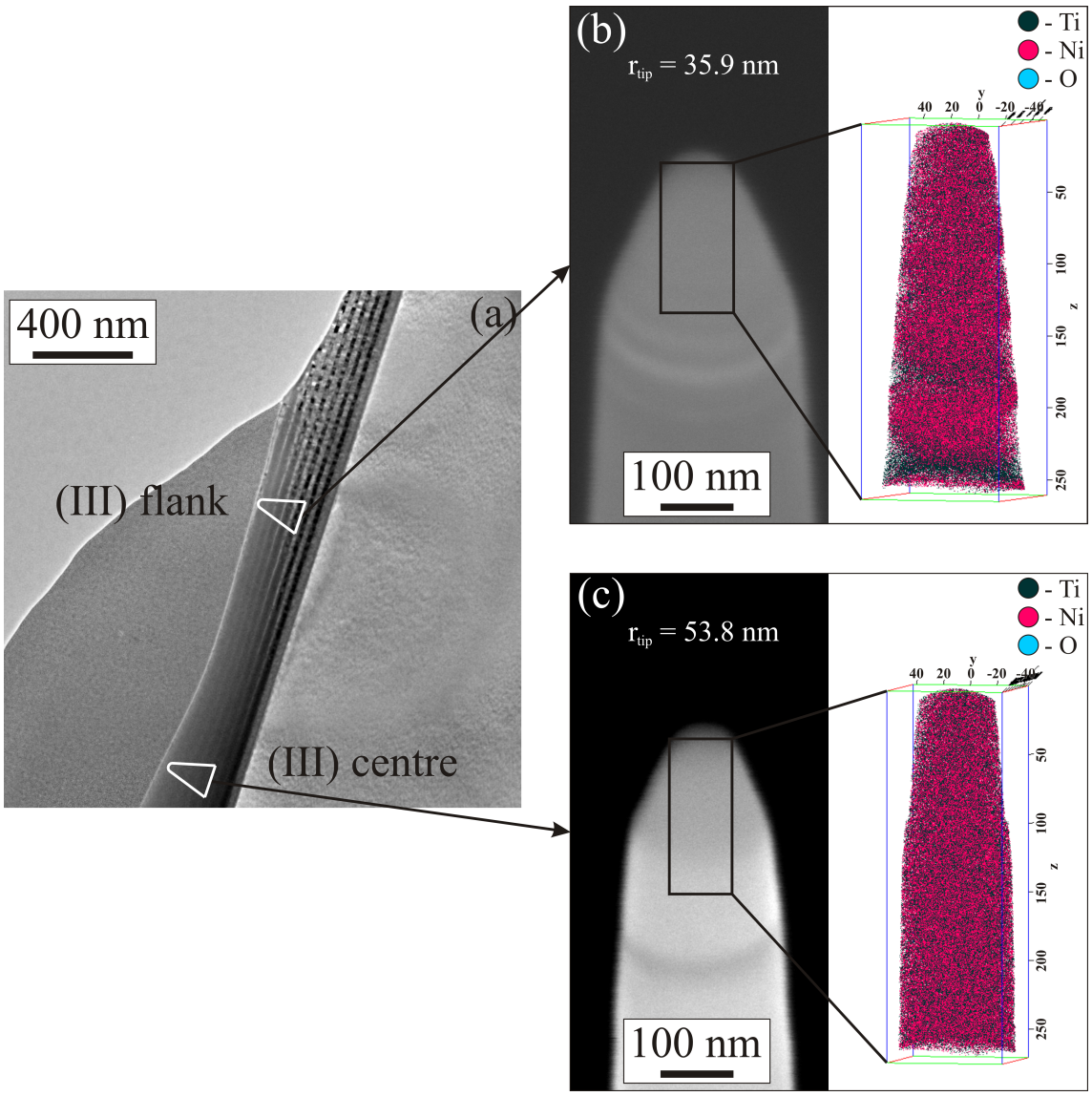


Figure 6.39.: Site-specific APT analysis of distinct processing regions of LIMET treated Ni/Ti on sc-Si substrates: The TEM micrograph (a) indicates the approximate extraction locations for the subsequently analysed APT specimen tips. The latter are shown along with their corresponding APT 3D reconstructions in (b) for region (III) flank and (c) region (III) centre. For the sake of better visibility 1 % of the Ni and the Ti atoms and 100 % of the O atoms are visualised there.

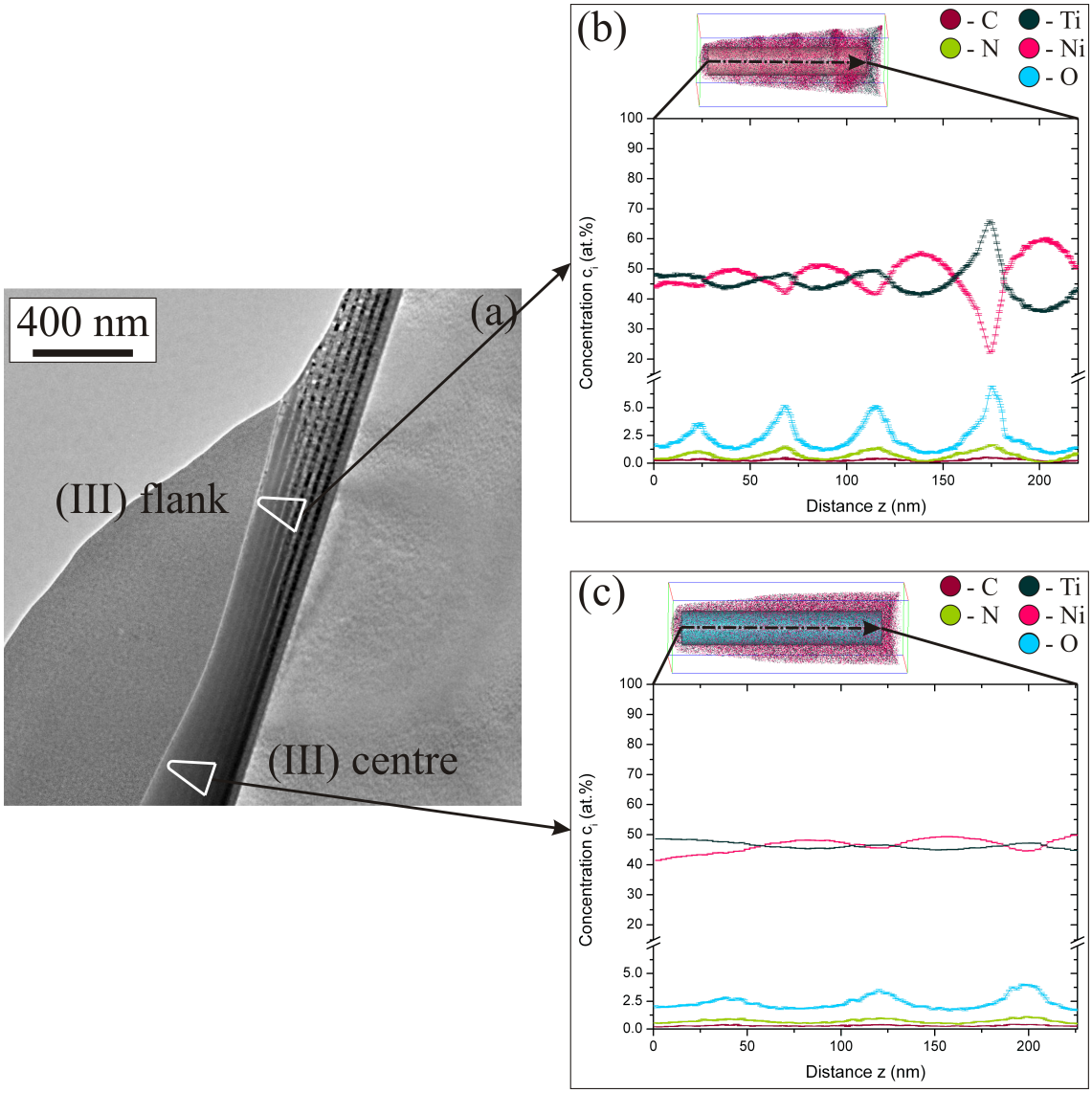


Figure 6.40.: Site-specific APT analysis of distinct processing regions of LIMET treated Ni/Al on sc-Si substrates: The TEM micrograph (a) indicates the approximate extraction locations for the subsequently analysed APT specimen tips. The 1D-concentration profiles calculated from a 40 nm-diameter cylindric ROI of the latter are shown in (b) for region (III) flank and (C) region (III) plateau.

of O encountered in the Ti/Al specimen and thus confirmed the interpretation given there. The same effect here could also be recorded for N atoms, which showed a maximum at the same locations, but only attained a maximum content of approximately 1.3 at.%. As could be expected following the findings so far, at the centre of region (III) the achieved intermixing was more complete (see (c) in figures 6.39 and 6.40). In contrast to Ni/Al and Ti/Al though, the composition signal of the metallic elements still showed an oscillating behaviour around the 48 at.% mean value, but with a significantly reduced amplitude of approximately 5.0 at.%. The SEM micrograph of the tip in figure 6.39 (c) confirmed this observation, since the tip showed no distinct contrast change. As for the gaseous species, the oscillation of O and N remained detectable. For both of them, the amplitude was reduced and the distribution within the former Ti layer broadened when compared to the flank portion. The maximum value for O attained 2.5 to 3.3 at.%, whereas the minimum was located at around 2.0 at.%.

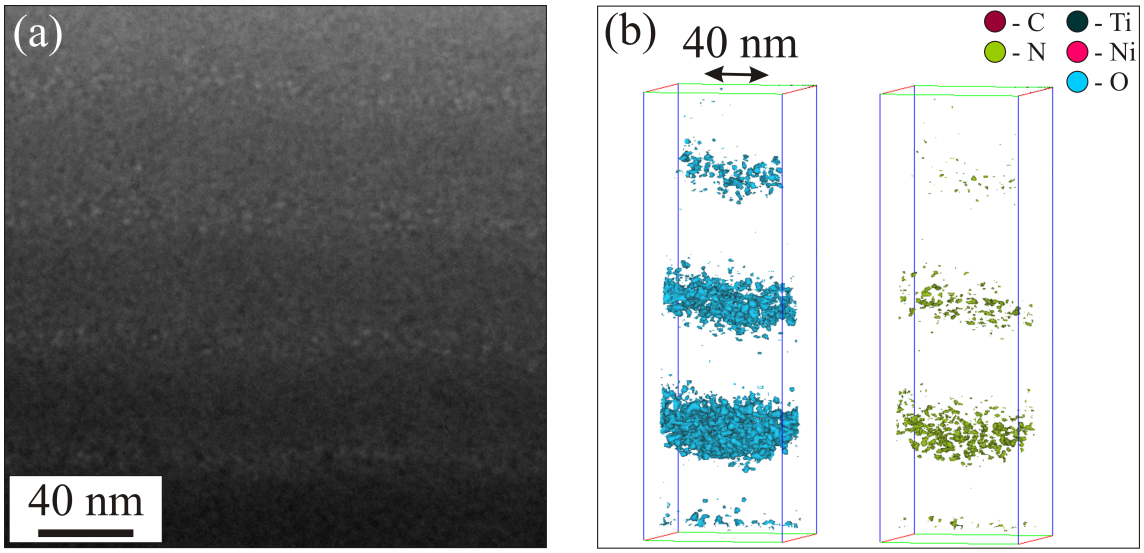


Figure 6.41.: Dedicated analysis of Ni/Ti region (III) centre APT specimen tip: close-up TEM micrograph (a) and corresponding 3D reconstruction (b) of the specimen showing only the O 5.0 at.% (left) and N 2.5 at.% iso-surfaces (right). Both images confirm the presence of globular aggregates taken as residues from the original Ti layer.

Using TEM bright-field imaging with high magnifications, it was attempted to visualise the microstructure at this part of the interference maximum, which is shown in figure 6.41 (a): bright-contrasted and apparently globular clusters could be found. These were arranged to parallel lines separated by a homogenous dark matrix and were spaced by ca. 50 nm, which exactly corresponded to the bilayer periodicity. Due to the projection effects associated with TEM imaging, it was deemed unreasonable to try to determine a mean size of those clusters. Taking these findings in conjunction with the oscillating O and N signals of the 1D concentration profiles, it was concluded that these formations were associated to remainders of the original Ti layers. This was further corroborated by iso-surfaces calculated for O and N as depicted in figure 6.41 (b). Therein it could clearly be visualised, that their spatial distribution, mutual arrangement and individual shape perfectly fitted to the agglomerations encountered in the TEM foil. Considering the comparatively low topographic modification effected by the LIMET processing in this material combination (see figure 6.22 (c) and (d)) together with the APT results clearly showing undeformed residues of the original stack structure, led to the assumption that Marangoni convection did not contribute to the intermixing process in Ni/Ti samples.

6.4. Correlative summary of the results

In order to be able to reasonably discuss the results described before, a comprehensive overview is afforded encompassing all local data obtained by the different techniques. Figure 6.42 shows the concept of this lineup for the case of the Ni/Al sc-Si (a) and a-SiO_2 (b) specimen sets. The TEM micrographs shown there span over a single LIMET half-period as do the simulated 2D temperature distributions directly below. For the sake of argument, the deviations between the simulation and the microstructural result (e.g. figures 6.16 and 6.17) were deemed acceptable to a first order approximation.

For sc-Si, at the centre of the interference minimum (region (I)) unaffected multilayers of crystalline Ni and Al were found, in agreement with the simulated temperature below $0.3 \cdot T_m^{Ni}$. Entering region (II) where this temperature was exceeded, SADPs showed an increasingly amorphous diffraction signal associated with Al, while Ni remained crystalline. The APT specimen extracted from this region revealed asymmetric diffusion taking place with Ni entering the Al layers at up to 30 at.%, while Al was immobile. The Al content of only 3 at.% within the Ni layers might as well be attributed to the layer topography analysed in section 6.2.1. As the close-up micrograph in figure 6.20 (a) corroborated, the multilayers in this region were still intact and showed no signs of deformation caused by convection effects or delamination from the substrate. Following this microstructural evidence, it was deduced that Al was not molten in region (II) as predicted by simulation. Looking at the exact location of the A-B boundary, the underestimation associated with the FE results in figure 6.16 is clearly visible.

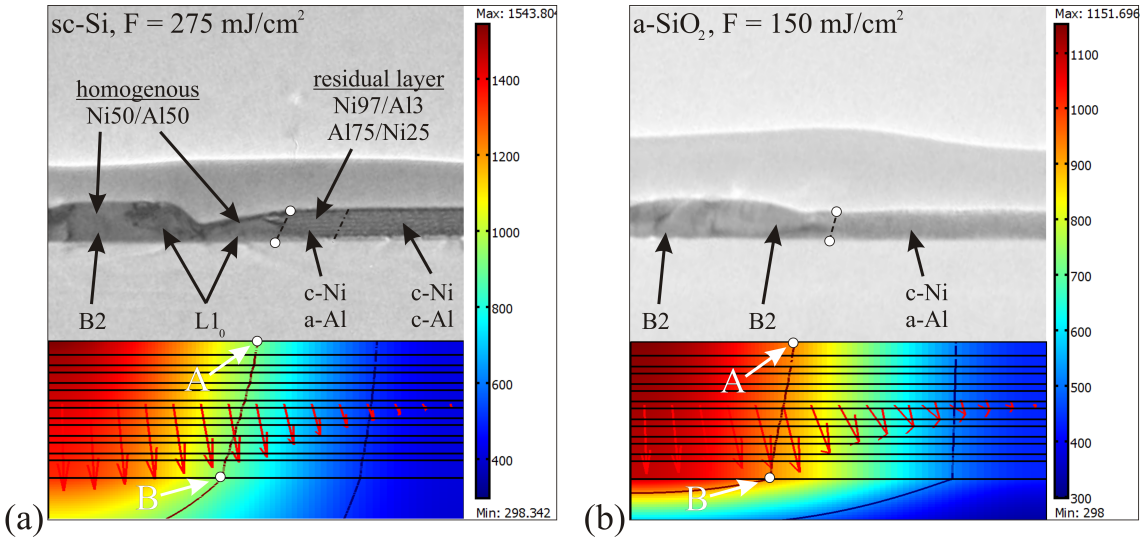


Figure 6.42.: Comparative overview of TEM, APT and FEM results obtained on Ni/Al multilayers on sc-Si (a) and a-SiO_2 substrate (b). Isotherms of T_m^{Al} (left) and $0.3 \cdot T_m^{Ni}$ (right) are included in each case.

Within region (III), the simulated temperature did rise to 1540 K at the maximum centre thus exceeding T_m^{Ni} only there. According to figures 6.2 (c) and 6.5 (c), the duration of the Al melt $\tau_{(l)}$ could be approximated to 40 ns with FEM. Both the homogeneous greyscale and the topography indicated an intermixing based on convection, which was confirmed by atom probe measuring the intended composition relation of 1:1 between the constituents. From a structural standpoint, it makes sense following the path taken by the (s)-(l) front during resolidification (to the left of the A-B boundary). From the indicated boundary of region (III) to the initial part of the topography plateau, the martensitic $L1_0$-NiAl was observed. Finally, the high temperature phase B2-NiAl was formed close to the interference maximum centre. Both findings fit the chemical composition encountered there. The same sequence of phases could be confirmed for the a-Si_xN_y specimen with $L1_0$-NiAl confined to a single grain directly at the A-B boundary.

For the multilayer on a-SiO_2 (see figure 6.42 (b)) both regions (I) and (II) showed undeformed residual multilayers in the TEM micrograph indicating a similar microstructural modification. As the encountered greyscale of the Al layers indicated, the asymmetric diffusion of Ni into Al already took place at the interference minimum (see right-hand edge) despite the lower fluence. Analogously to the former case, an underestimation of the extension of the heat-affected zone by FEM was visible when comparing the A-B boundaries. From a structural standpoint, the SADP of region (II) (figure 6.21 (d)) revealed the simultaneous presence of crystalline Ni and amorphous Al, in concordance with the simulated local temperature. In region (III) a maximum temperature of 1150 K was achieved. Large grains free of multilayer traces were formed there, identified as B2-NiAl equilibrium phase. The estimated $\tau_{(l)}$ amounted to ca. 60 ns lasting 50 % longer than in the sc-Si case. Using figures 6.2 (c) and 6.5 (c), the difference between the melt

duration effected by the substrate could be estimated for individual (d,F) selections[10]. Irrespective of the multilayer system under investigation, $\tau_{(l)}$ on sc-Si only amounted to 25 % of the duration achieved on a-SiO_2 for the same (d,F) combination.

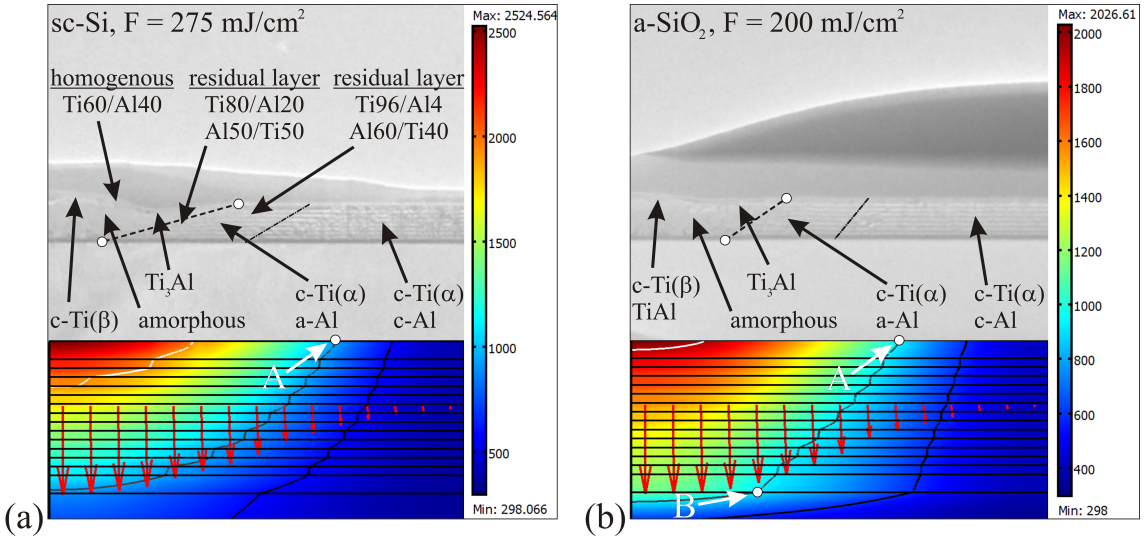


Figure 6.43.: Comparative overview of TEM, APT and FEM results obtained on Ti/Al multilayers on sc-Si (a) and a-SiO_2 substrate (b). Isotherms of T_m^{Al} (left) and $0.3 \cdot T_m^{Ti}$ (right) are included in each case.

Figure 6.43 (a) depicts the situation encountered in Ti/Al on sc-Si. Region (I) therein consisted of the unaffected multilayer structure, where only fibre-textured crystalline diffraction signals of α-Ti and Al could be recorded. Entering region (II), an undisturbed multilayered microstructure still was visible, with the Al layers showing evidence of asymmetric diffusion of Ti into them. This finding was confirmed both by TEM, with a crystalline signal of α-Ti and an amorphous one of Al; and by APT, showing a Ti content of up to 40 at.% in Al and 4 at.% of Al in Ti layers. Directly at the A-B boundary, a residual layer structure was imaged with the chemical analysis and revealed

[10]To this end, only those $\tau_{(l)}$ values not exceeding simulation time t_{sim} were used.

the Al layers to contain 50 at.% of Ti while the Ti layers accumulated up to 20 at.% of Al. Clearly, the FEM simulations overestimated the lateral travel of the A-B boundary. Within region (III), a maximum temperature of 2500 K was estimated representing an upper bound as does the melt duration of 50 ns. Both the homogeneous greyscale of the TEM micrograph and the 1D concentration profiles obtained by APT indicated an effective intermixing of both constituents. Together with the topography profile, convection was identified as an effective mechanism there. APT measured the near-surface composition at 60 at.% Ti and 40 at.% Al. This supported the discovery of a Ti_3Al equilibrium phase close to the thin film surface stretching from the A-B boundary to the topographic depression. At the maximum location, β-Ti solid solution was found at the surface. Both crystalline phases covered an amorphous mixture identified by SADP in the depth of the thin film.

The findings on Ti/Al deposited on a-SiO_2 are given in figure 6.43 (b). In contrast to Ni/Al, region (I) here exhibited an intact layer microstructure made of crystalline α-Ti and Al. Evidence of asymmetric diffusion of Ti into Al was discovered in region (II), wherein crystalline α-Ti and amorphous Al were confirmed by TEM. Here also, the A-B boundary from FEM overestimated the location discovered in the TEM micrograph. Within region (III), an upper bound maximum temperature of 2000 K was approximated along with a $\tau_{(l)}$ of 100 ns. Both the spatial sequence and composition of the phases corresponded to the situation encountered in the former case, as holds for the amorphous mixture in depth. Directly at the interference maximum, equlibrium γ-TiAl ($L1_0$) phase was formed at the film surface.

Finalising this summary, figure 6.44 lines up the results obtained for the Ni/Ti specimen sets. On sc-Si (a), the interference minimum exhibited the pristine multilayer microstructure consisiting of crystalline Ni and α-Ti. Crossing the $0.3 \cdot T_m^{Ti}$ isotherm, the TEM micrograph revealed an altered greyscale representation of the Ti layers pointing to

asymmetric diffusion of Ni. The simulated temperature within region (II) exceeded the transition temperature for the $\alpha \rightarrow \beta$ transformation of Ti (1150 K). With the SADPs of this region confirming the presence of β-Ti, the thermal simulations were proven to yield reliable first order approximations.

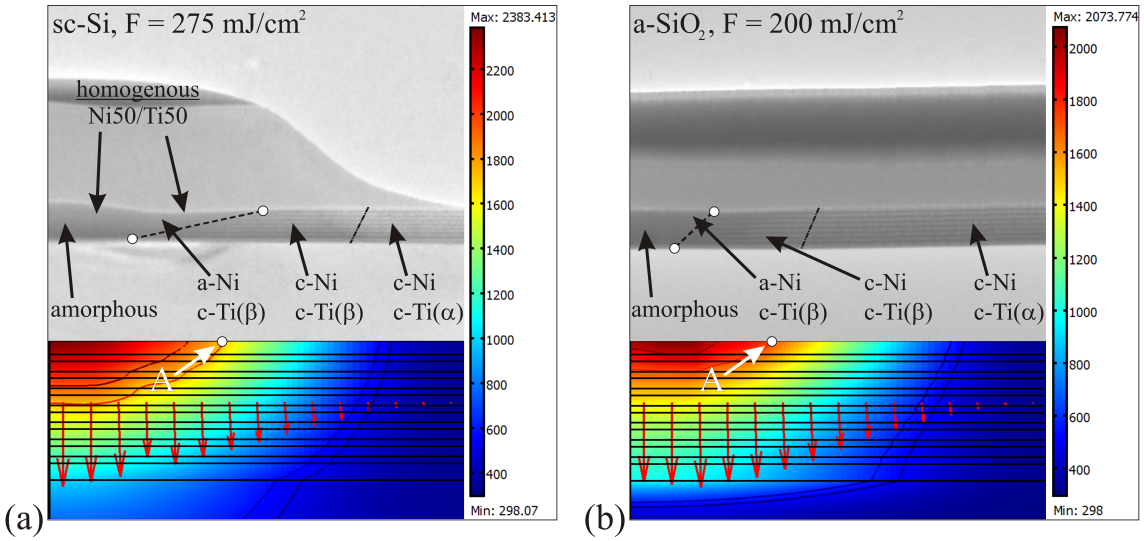


Figure 6.44.: Comparative overview of TEM, APT and FEM results obtained on Ni/Ti multilayers on sc-Si (a) and a-SiO_2 substrates (b). Isotherms of T_m^{Ni} (left) and $0.3 \cdot T_m^{Ti}$ (right) are included in each case.

Based on this, it was deemed worthwhile trying to pursue further improvements to them, which will be discussed in upcoming section 7.1.2. Passing the A-B boundary, the TEM micrograph showed a homogeneous greyscale within the whole thin film pointing to complete intermixing of both constituents, which was backed by two APT measurements. Phase analysis directly at the boundary exhibited a crystalline signal of β-Ti along with an amorphous one stemming from Ni. In region (III) an amorphous mixture was formed spanning the whole thickness. The maximum temperature there reached an approximate 2400 K and $\tau_{(l)}$ was simulated to 20 ns. Together with the comparatively low topography alteration achieved in region (III) this pointed to convection playing a

minor role in mass transport here. The result on a-SiO_2 (b) essentially yielded the same modifications concerning intermixing, formation of phases and their spatial distribution as well as topography. The simulated maximum temperature reached 2100 K while $\tau_{(l)}$ only amounted to 12 ns. In both situations, the duration of the melt was comparatively low. Nevertheless, the temperature level within region (II) and its holding time obviously were sufficient to efficiently promote diffusion throughout the heat-affected zone.

7. Discussion

7.1. Solidification and phase formation

Based on the joint assessment of the experimental data, it was possible to devise a working hypothesis on the processes taking place in a LIMET-treated multilayer. Figure 7.1 lines up a schematic representation of the temporal sequence of the heating cycle:

1. As the laser-pulse (a) started interacting with the pristine multilayer (b) at t_0, heating to T_{max} took place within half of the pulse duration τ_p. This corresponds to a heating rate $\dot{T}$ on the order of $10^{11}\,\mathrm{K/s}$. According to figure 6.4 (c), for periodicities $d \leq 8\,\mu\mathrm{m}$, most of the heat subsequently was transported laterally into the adjacent multilayer portions.

2. When the local temperature reached $0.3 \cdot T_m$ of the higher melting component, both TEM micrographs and APT measurements confirmed enhanced asymmetric diffusion leading to chemical compositions far from the equilibrium solubility range (see figure 7.1 (c) for t_1). As close-up TEM images of this region revealed (see figures 6.19 (a), 6.25 (a) and 6.27 (a)), the layers accepting the diffusing atoms did not exhibit any signs of grain boundaries within the intermixed zone. Moreover, no evidence of layer deformation or delamination could be found in the whole stack. In addition, APT revealed a peculiar distribution of O atoms covering the individual Ni layers. While the APT specimens taken from adjacent region (III) revealed individual coagulated O clusters (see figure 6.30 (c)

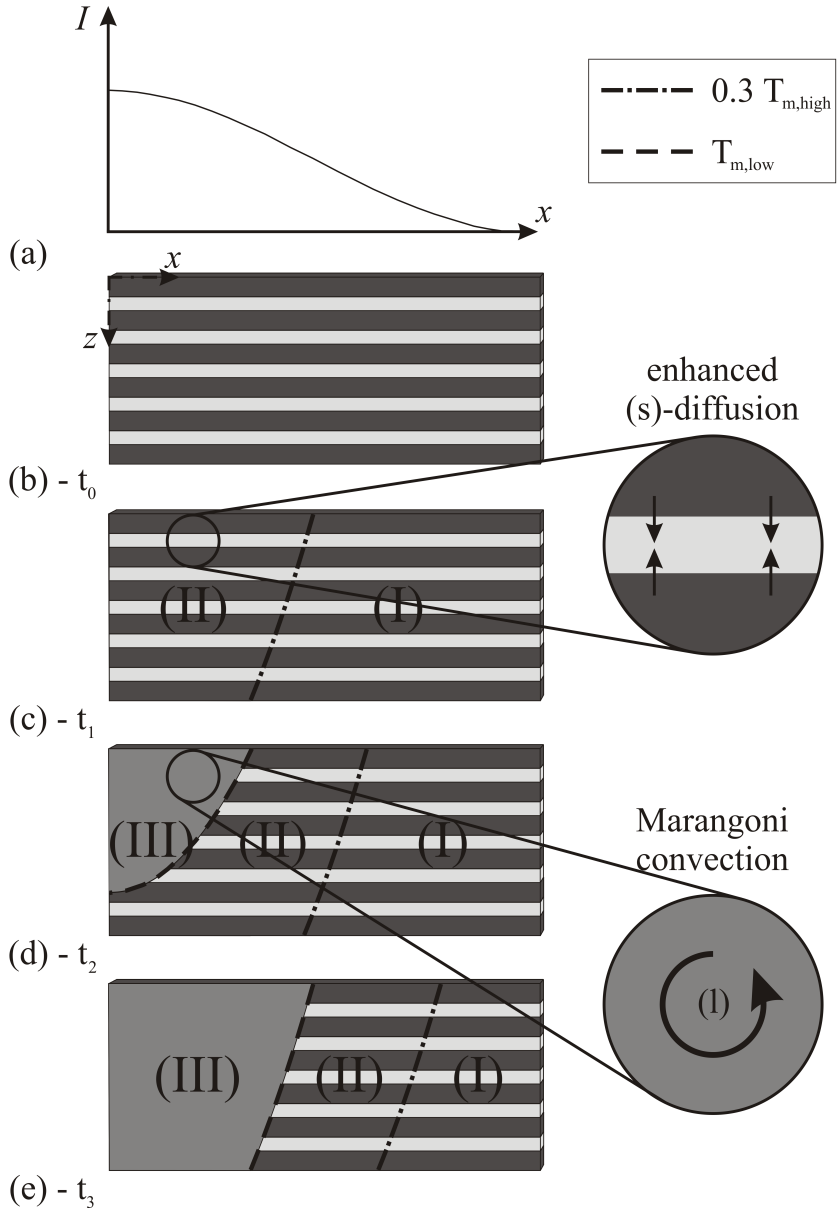


Figure 7.1.: Schematic visualisation of the working hypothesis on mass transport and solidification: spatial distribution of laser intensity (a) over a half-period of a pristine multilayer (b). Setting in of enhanced (s) diffusion and thus solid state amorphisation in region (II) (c). Subsequent formation of region (III) by melting of the low-T_m component (d) with Marangoni convection active. Situation of maximum expansion of the heat-affected zone before onset of resolidification (e).

and (d)), the one extracted in region (II) (see figure 6.30 (b)) showed a closed O layer. The latter could only be kept stable thoughout the LIMET process if it was not exposed to a (l) phase. Taking together these typical results of region (II), it was concluded that these processes took place in (s) state. While in the case of the multilayers containing Al, the higher melting component was mobile, in the Ni/Ti specimen sets the reverse situation was encountered. For all material systems, SADPs of region (II) confirmed the presence of an amorphous phase, which was formed within the layer of the immobile species. Hence, *solid state amorphisation* was inferred as the process characterising region (II).

3. As soon as melting of the component with lower T_m was achieved (figure 7.1 (d) for t_2), the melt front travelled laterally towards the interference minimum location. Within the volume delineated by the associated T_m isotherm, TEM and APT both yielded evidence of an efficient intermixing of the constituents. Obviously this took place despite the fact that the melting temperature of the other only component was reached in a confined volume at the interference maximum. This could be explained by the high-T_m layers in region (III) being completely dissolved in the low-T_m melt. Additionally, the topographic changes observed past the A-B boundary strongly indicated Marangoni convection to be the dominating mass transport process. This was supported by the aforementioned individual globular O clusters present in the formerly molten volume.

4. Depending on the melting point combination of the multilayer components, the LIMET parameters (d,F) and the substrate material employed, the molten volume is kept in (l) state for different time intervals $\tau_{(l)}$. At t_3, when the low-T_m isotherm reached its maximum lateral expansion, the post-mortem measurable heat-affected zone was attained and solidification set in (see (e)). The (s)-(l) front then travelled laterally back towards the interference maximum. Following Herlach et al. and Im et al., it is assumed that crystallites in region (II) located directly at the interface

act as crystallisation seeds. The latter effect *heterogeneous nucleation* and influence phase selection (c.f. section 3.1) [95][227]. Cross sectional microstructure analysis (see section 6.2.2) clearly proved that the crystalline phases formed within region (III) exhibited lateral grain sizes twice the initial multilayer thickness and showed no traces of segregation. The multilayers on a-SiO_2 even surpassed this factor. Moreover, the phase and grain boundaries were consistently found to be planar in shape and oriented parallel to the substrate normal direction (e.g. figures 6.20 (a) and 6.21 (a) for the situation in Ni/Al specimen sets). In consequence, *super lateral growth* (SLG) as introduced in section 1.2 was identified to take place in region (III) [45][46]. Since the simulated melt durations ranged between tens to hundreds of ns leading to approximate cooling rates on the order of 10^{10} K/s, *rapid solidification* was in effect. Hence, looking at the phase sequence and the local chemistry along its path opened up the possibility to make assumptions concerning phase selection and formation.

In the following, the results of section 6.4 will be discussed separately for regions (II) and (III) in the light of concepts on solid state amorphisation (briefly introduced there) and rapid solidification (as given in chapter 3 of the theoretical part). Qualitatively, it can be stated that the microstructural modification achieved for the three multilayer material systems reflects different degrees of superposition of these processes. Apparently, the impact of the substrate material was restricted to dictating $\tau_{(l)}$, the phase sequence and grain sizes. While Ni/Al presents dominating rapid solidification, Ni/Ti shows prevalent solid state amorphisation. Ti/Al in turn, can be regarded as a balanced mixture of both mechanisms.

7.1.1. Region (II) – Solid-state amorphisation

First observations of amorphisation reactions in multilayered metallic thin films subjected to conventional homogenisation heat treatment were made by Schwarz et al. in the early 1980s [228]. Au/La, the material combination under investigation there, was deposited by thermal evaporation to form thin film stacks with thickness characteristics comparable to those in the present study. Besides the multilayer approach, the literature reports other techniques to achieve amorphous phases in (s) state like high energy ball milling and ion irradiation [36][229]. As Saunders et al. emphasised in their treatment on thermodynamics of amorphous phase formation, this finding showed that quenching under large cooling rates is not necessary to trigger amorphisation [230].

Anomalous fast diffusion was discussed as the origin of this reaction taking place between initially crystalline materials at temperatures below the known crystallisation temperature of the amorphous alloy. The atoms entering the parent lattice introduce defects and disorder thus effecting amorphisation by nucleation and growth [36]. In this case, solute and self-diffusion data of crystalline La revealed Au to be significantly more mobile than La in its own lattice. Since only one component was highly mobile, diffusion yielded a pronounced asymmetric composition profile perpendicular to the layer plane. Moreover, mixing both constituents must yield an exothermic reaction with large energy output. Following the thermodynamic data available for the phases under consideration in this study and according to experimental evidence accessible in literature [107][159][231][232] and shown in section 6.4, solid state amorphisation is proven to be possible in all three systems. Thompson elaborated the impact of diffusional aspects in his review on interfacial reactions [233]. According to his summary, interdiffusion of the constituents in the direction perpendicular to the interface must precede nucleation and the subsequent growth of the new phase within the layer plane.

Phase selection in those reactions is constrained by thermodynamic and kinetic constraints, the latter encompassing competitive effects during nucleation and growth. Introducing interdiffusion as a prior step, this could be circumvented to base predictive calculations on barely known or even unknown kinetic constants or thermodynamic values. Thompson further emphasised the necessity of asymmetric diffusion as a constraint to polymorphic formation of metastable phases. Fast diffusion of one constituent into the lattice of the other together with low self-diffusion in the parent phase favours these transformations. The product phase is rich in the slow-moving component and exhibits a large range of stability with respect to compositional changes. Based on experimental data obtained on Ni/Zr, a material system known for its solid-state amorphisation capability, Thompson derived a rule of thumb allowing for an assessment of the diffusional behaviour of an exothermically reacting material combination with respect to solid-state amorphisation. In order to favour amorphisation, self-diffusion in the parent phase must be at least three orders of magnitude less than solute diffusion therein.

As for thermodynamic hindrances to nucleation, Desré and coworkers developed an approach based on the chemical gradient present at the interface between the layers of the different constituents [234][235][236]. Assuming that interdiffusion already formed an amorphous layer in between, figure 7.2 (a) shows a schematic representation of assumed composition profiles $X^i(z)$ in normal direction z within it. There, two different situations of compositional gradients are depicted with $\nabla X^i_{low}(z) < \nabla X^i_{high}(z)$. Figure 7.2 (b) below shows the associated free energy G-X^i for an amorphous (G_a) and an intermetallic phase (G_{IP}) of stoichiometry X^i_{IP}, in competition at the interface. Desré argued that the presence of steep concentration gradients reduces the driving force ΔG_{ac} for the nucleation of the intermetallic phase. Additionally, large negative enthalpies of mixing ΔH_{mix} and the alloy free energy ΔG_{alloy} of the amorphous phase ΔG_a contribute to the increase in stability of the metastable state. Assuming that crystallising the intermetallic phase affords a nucleus of radius $2r$, as in classical theory of homogeneous nucleation,

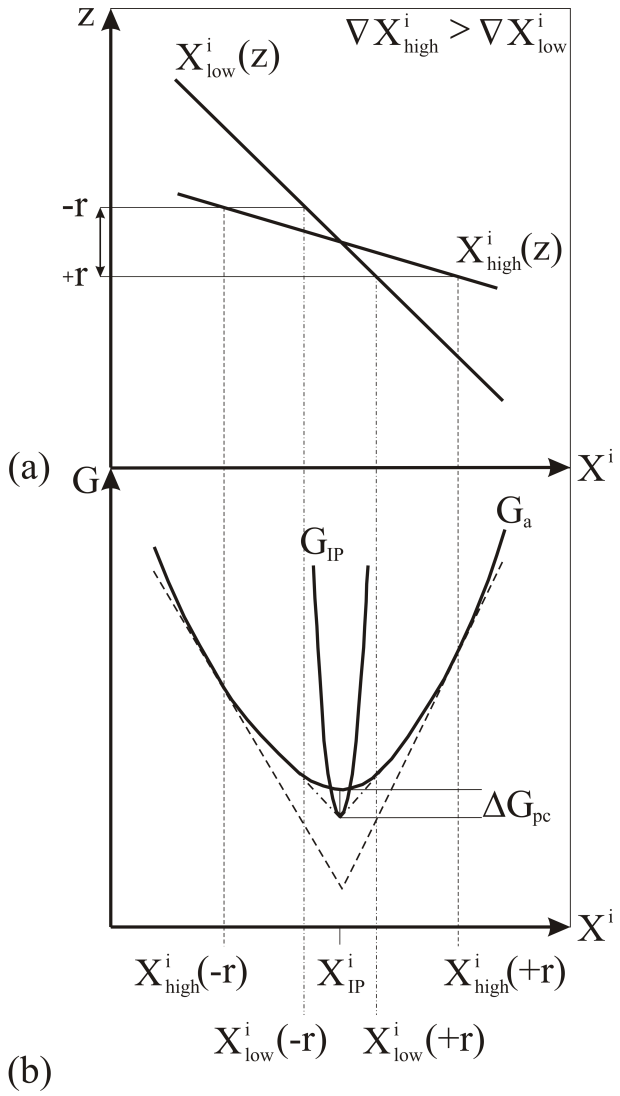


Figure 7.2.: Schematic visualisation of Desré´s treatment on thermodynamic nucleation barriers: two assumed compositional gradients $\nabla X^i(z)$ over an amorphous layer (a) (please note the counterintuitive selection of coordinate axes) and the G-X^i curves associated to the amorphous and the intermetallic phase under consideration (modified from [234])

figure 7.2 (a) allows to determine its chemical composition at opposite edges ($X^i(-r)$, $X^i(+r)$), whose magnitudes vary depending on the actual compositional gradient $\nabla X^i(z)$. Constructing tangents to the G_a curve at these compositions in figure 7.2 (b) allows a

graphical explanation of Desré´s hypothesis. In order to nucleate the intermetallic phase, the tangents must touch its free energy curve G_{IP}. As long as the chemical gradient does not fall below a critical value, the tangents fail to fulfil this requirement, which corresponds to the amorphous phase being stable. Clearly, with increasing magnitude of ΔH_{mix}, the curvature κ_X of G_a also increases thus further reducing the probability of the tangents intersecting G_{IP}. Apart from this catchy qualitative approach, Desré derived an expression for the free energy ΔG_N necessary for polymorphous nucleation of the intermetallic based on the free energy of nonuniform systems according to Cahn and Hilliard´s treatment as well as the theory of homogeneous nucleation [237][234]:

$$\Delta G_N = 24\gamma_{pc}r^2 + 8\rho\left[\Delta G_{pc}(X^i_{IP}) - N_A\chi(\nabla X^i)^2\right]r^3 + \frac{4}{3}\rho\kappa_X(\nabla X^i)^2 r^5 \qquad (7.1)$$

with γ_{pc} the interfacial energy of the polymorphous crystallisation front, ρ the atomic density, ΔG_{pc} the free energy of polymorphous crystallisation and χ a constant. The first addend represents the energetic contribution of a cubic nucleus surface. The second term, i.e. the volume and the third, i.e. the effect of the G_a curvature (κ_X), together stand for the driving force ΔG_{ac} for the crystallisation of the amorphous phase. Ignoring anisotropy and local variations of κ_X, the analysis of equation 7.1 with respect to the conditions that first give $\Delta G_N > 0$ yields an approximation for the critical composition gradient $\nabla X^i_{crit}(z)$. Based on experimental data and adapted estimations, Desré calculated this value for multilayers which were conventionally homogenised at 600 K. For Ni/Zr, $\nabla X^i_{crit}(z)$ amounted to $4.85{\cdot}10^7$ 1/m and for Ni/Al to $1.10{\cdot}10^8$ 1/m. The diffusional asymmetry in the latter system first was investigated by Ma et al. [238].

Different authors, including Johnson, Thompson, Saunders and Bormann, dealt with thermodynamic approaches to explain the presence of the amorphous phase making use of free energy diagrams G-X^i [36][230][107][233][108]. As Johnson compiled, the T_0 concept discussed in section 3.2.2 could be used to construct polymorphous phase diagrams to assess possible transformations, if and when the material processing led to a chemi-

cally homogeneous situation which did not allow for segregation. Those conditions are given when processing takes place sufficiently fast, as in this study, since polymorphic reactions are kinetically faster as they rely on topological rearrangements which do not require long-range mass transport. Consequentially, the latter corresponds to a kinetic hindrance to crystallisation. Polymorphous solidification of a phase is only possible when its free energy at the given composition and temperature is lower than the one of the liquid phase.

Using CALPHAD methods alongside experimentally determined thermodynamic functions, the free energy curves of the possible phases form the basis to assess possible transformations [108][239]. While obtaining these data for equilibrium phases is a rather straightforward task, metastable and amorphous ones require more effort. Especially for the latter, high temperature data are difficult to gather due to their instability under these circumstances. In case no experimental data are accessible, the use of an empirical approach devised by Miedema et al. is quite common, which yields only qualitatively reasonable data in the low-temperature range [240][241]. There, the amorphous phase is treated as an undercooled liquid with ideal solution entropy [107]. Thus, the free energy of (l) state $G_{(l)}$ is taken to represent the amorphous phase. As Bormann et al. and Saunders et al. emphasised, this method unfortunately underestimates the energy of mixing of the amorphous phase, since it neglects the short-range order which is responsible for the phase´s stability at low temperature [230][108]. As can be inferred from Desré´s discussion, the magnitude of the intermetallic phase free energy of polymorphous crystallisation can be estimated to be 10 % greater than the free energy of the amorphous alloy G_a [230][234]. This is qualitatively accounted for in the schematics of figures 7.2 (b) and 7.3 (a). Using the rule of parallel tangents as introduced in section 3.2.2, the maximum driving force for each transition can be assessed graphically. The mean chemical potential at the layer interface serves as a reference line as determined by the common tangent between the pure component G-X^i curves. Thus, from a

thermodynamic standpoint, the formation of intermetallic phases is always energetically preferred over amorphisation reactions. Here, the aforementioned nucleation hindrances exert their effects [36].

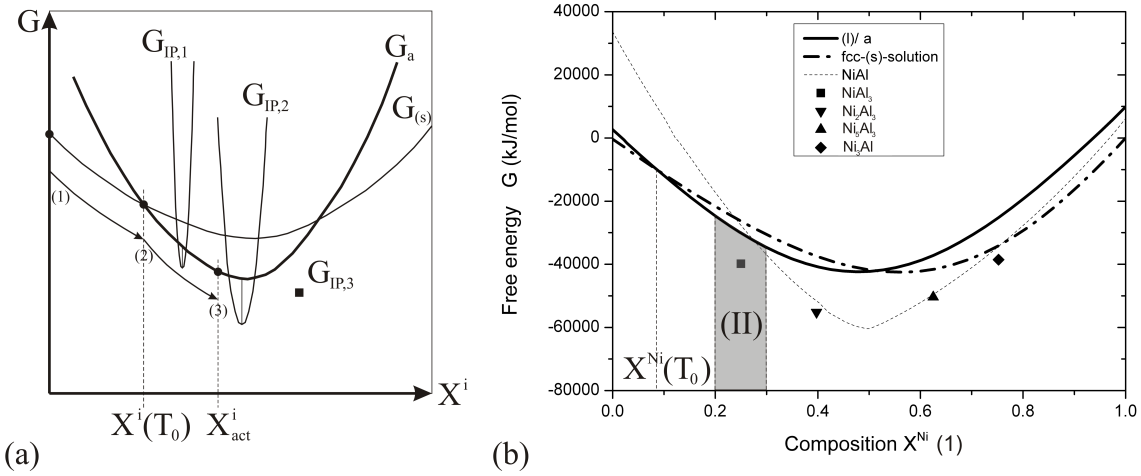


Figure 7.3.: General approach of using G-X^i curves to assess phase formation under metastable conditions (a) and corresponding G-X^{Ni} curve for Ni/Al system at T=700 K according to Thermocalc and [231] (b). Grey-coloured area corresponds to the APT-determined composition within the indicated region.

Since the time scale of LIMET processing generates cooling rates on the order of 10^{10} K/s, the common tangent rule of equilibrium thermodynamics cannot be applied to assess the resulting phases. Nevertheless, the G-X^i characteristics at the processing temperature T can still be employed for this purpose. Figure 7.3 (a) depicts an according hypothetical schematic containing curves of an amorphous phase G_a, a solid solution crystal $G_{(s)}$ and three intermetallic phases (two having existence range $G_{IP,1}$ and $G_{IP,2}$, one being a line phase $G_{IP,3}$). For argument's sake, an initial situation of two crystalline layers in direct contact made of pure components i and j is assumed. Heat treatment induces asymmetric diffusion of component i into the adjacent j layer, leading content X^i to rise from zero (see step (1) indicated in the schematic). Since the crystalline solid

solution is initially stable there, this process can be described by following the $G_{(s)}$-X^i characteristic. With increasing X^i an increasing amount of defects is introduced into the solid solution finally leading to a loss of lattice stability. This polymorphous amorphisation reaction sets in for X^i contents exceeding a threshold value $X^i(T_0)$. The latter is found according to the T_0 concept at the intersection point of the free energy characteristics of solid solution and the amorphous phase (see step (2) there). For further increasing X^i content, the amorphous phase is kept stable which is represented by following the G_a-X^i curve (step (3)) having a more negative free energy. Reaching the end of the heat treatment, a final intermix X^i_{act} is achieved. The amorphous phase will then either be frozen in or, if the composition is conveniently placed with respect to the stoichiometry of intermetallic phases and the hindraces can be circumvented, crystallisation sets in.

Turning to the experimental results achieved by TEM and APT on the different specimen sets (see section 6.4), the tools of metastable thermodynamics described above can be applied to explain the outcome discovered in region (II). As the effective temperature within this region, the midpoint of the temperature interval $[0.3 \cdot T_{m,high}, T_{m,low}]$ was assumed. Hence, for the Al-containing systems 700 K and for Ni/Ti 1100 K was used to extract appropriate G-X^i curves for equilibrium phases from the thermodynamic database THERMO-CALC (VERSION 4.1.2.37, 2006, courtesy of Saarland University, Chair of Metallic Materials). As for reliable data on the metastable amorphous phases, the literature provided studies on the amorphisation behaviour of these material systems at temperatures between 500 and 700 K performed by the group of Bormann [231][232] [159]. Since the temperature level encountered in Ni/Ti was comparatively elevated, the use of (l)-phase free energy to represent G_a was deemed appropriate after comparison of the G_a- and $G_{(l)}$-X^i curves in both sources.
Figure 7.3 (b) showing the characteristics at 700 K for the Ni/Al system also delineates the Ni concentration X^{Ni} encountered in the Al layers. Due to the discussed APT artefacts (see section 6.3), a range of compositions needs to be assumed, hence the rep-

resentation as a grey-coloured interval. Up to $X^{Ni}(T_0) \approx 0.10$, the fcc solid solution of Al remained in crystalline state. Beyond this threshold, an amorphous phase was stable, which also holds for the aforementioned compositional range. It is apparent that the rapid extraction of heat froze-in both the state of the intermix and the metastable amorphous phase, which was confirmed by the joint chemical and structural analysis (see figure 6.42 (a)), thus reinforcing this thermodynamics based argumentation. Energetically, the formation of the line-compound $NiAl_3$ would have been favoured but was inhibited by the hindrances discussed above.

Similar findings were made by Blobaum, whose study was dedicated to elucidating the thermodynamics and kinetics of magnetron-sputtered Ni/Al multilayers designed for SHS. There, an amorphous phase identified as Al_9Ni_2 was discovered to be the first phase formed at the interfaces during the reaction sequence [136]. The TEM micrographs there even confirmed the asymmetric diffusion of Ni into the Al layers. While the stoichiometry of this phase fits quite well to the composition range within Al layers found in this study, the SADPs of region (II) did not allow for its conclusive identification.

Turning to Ti/Al (see figure 7.4 (a)), the same approach can be utilised. In this material system, the difference in free energy between the undercooled (l) and the amorphous phase was significant at 700 K. The work of Kyllesbech Larsen on ion-irradiated multilayered Ti/Al yielded more accurate data on G_a, making it the appropriate source for the temperature range in question [232]. Here again, the Al fcc solid solution was initially stable and gave way to the energetically favoured amorphous phase at a Ti content of $X^{Ti}(T_0) \approx 0.37$. This intersection of the G-X^i curves was located within the compositional range encountered by APT in region (II) as figure 6.43 (a) confirms.

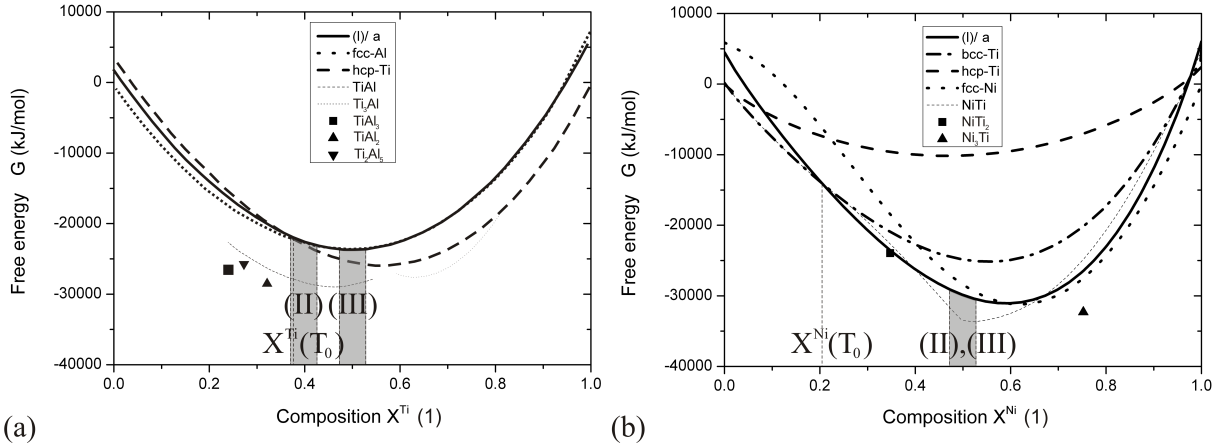


Figure 7.4.: G-X^{Ti} curve for Ti/Al system at T=700 K according to Thermocalc and [232](a) and G-X^{Ni} curve for Ni/Ti system at T=1100 K according to Thermocalc (b). Grey-coloured areas correspond to the APT determined compositions within the indicated regions.

The corresponding SADP showed the presence of an amorphous phase instead of the energetically favoured Ti_3Al intermetallic. As the TEM micrograph in figure 7.4 (a) revealed, region (III) also exhibited an amorphous portion close to the substrate interface. A closer look at its morphology (compare figure 6.25 (a) with 6.37 (a) and (c)) showed residual Ti layers and APT confirmed an optimum intermix in the Al layers. Within this compositional interval (see grey-coloured interval (III) in figure 7.4 (a)) the energetic difference between the amorphous phase and the two competing intermetallics (TiAl and Ti_3Al) is comparatively low. This kept the amorphous phase stable as confirmed by the SADP taken there.

The results obtained from Ni/Ti further reinforced the mutual affirmation of an experimental and a metastable thermodynamics approach. As Ni started entering the Ti layers, the bcc α-Ti solid solution was stable. Passing $X^{Ni}(T_0) \approx 0.20$, G_a exhibited the most negative free energy. Reaching the compositional range of intermix achieved in the Ti layers (see grey zone around $X^{Ni}(T_0) = 0.50$) both in region (II) and (III), the

amorphous phase competed with B2-NiTi and was frozen-in as shown by local structural analysis (see figure 6.44 (a)). Bormann´s analysis of Ni/Ti amorphisation showed that this reaction could be achieved for cooling rates on the order of 10^6 K/s, which clearly are surpassed by those estimated for LIMET [159]. It must be emphasised, that these results stand in contrast to those obtained by Hollanders et al. on Ni/Ti multilayers isothermally heat-treated at ca. 600 K for up to 220 h [216][242][243]. In the course of their diffusional studies it was shown that Ti dissolved into a crystalline Ni matrix, which is opposed by the present APT measurements and the TEM imaging in Z-contrast.

The discussion up to this point made it clear that the so far experimentally inferred solid state amorphisation could be confirmed via thermodynamic argumentation based on the established theories. Moreover, the discussed hindrances were effectively impeding the formation of any crystalline phase in region (II). Looking at the 1D concentration profiles obtained there for the individual material combinations (c.f. figures 6.31 (b), 6.37 (b) and 6.40 (b)) and estimating the interfacial width to ca. 4 nm (according to the proxigrams in figures 6.32 (b) and (c)), the actual composition gradient $\nabla X^i(z)$ was calculated to a range between 0.5 and $2.3{\cdot}10^8$ 1/m, well in the range of Desré´s estimations of the critical gradient for solid-state amorphisation $\nabla X^i_{crit}(z)$ given above. In fact, since these estimations were determined post-mortem, the initially effective chemical gradients surely surpassed the critical value necessary to impede nucleation of the crystalline phase.

As a preliminary conclusion, it can be stated that the use of thermodynamic data both on equilibrium and metastable phases, if experimentally known, allows for a reasonable post-processing explanation of the obtained results. Since diffusional mass transport forms the basis of these processes, the LIMET-induced intermix obtained in region (II) needs to be assessed from the standpoint of effective duration of the heat treatment. The literature dealing mainly with diffusion in multilayered thin film media in general is

focused on conventional long-term isothermal homogenisation at temperatures around $0.7 \cdot T_{m,low}$. First of all, the thin film diffusion behaviour of the material systems under investigation here is not well researched yet. Only the aforementioned study of Hollanders et al. concerning Ni/Ti contains data on bulk and grain boundary diffusion as well as on the mass transport in the amorphous phase [216][242][243]. Second, and most important, the studies do not fit to the boundary conditions of the ultra-short transient heating delivered by LIMET.

Still, the conventionally employed Einstein equation (see equation 3.17) might serve as a means to describe mass transport in (s) state. The thus estimated diffusivities may serve as a zero-order estimation of an effective $D_{(s)}$, which in turn can be compared with literature values of different possible diffusion mechanisms. Obviously, the abundant data on volume and grain boundary diffusion obtained from bulk specimens of the individual metallic components cannot serve for these purposes. For argument´s sake, the following assumptions were made based both on the present multilayer design and the measured intermix: as diffusion length, half the thickness of an individual layer $t_i/2$ was taken, since the diffusing species could enter from opposing interfaces. Moreover, the FEM simulated melt duration intervals $\tau_{(l)}$ were employed as lower-bound approximations for the heat holding time, which amounted to 50 ns for sc-Si and 200 ns for the a-SiO_2 substrate. Einstein´s equation then calculated an effective $D_{(s)}$ on the order of $10^{-9}\,\mathrm{m}^2/\mathrm{s}$.

The literature on bulk metallic glasses offers a basis of comparison to this limit. As Masuhr et al. summarise, viscosimetry performed on a set of different metallic melts together with Stokes-Einstein relation (equation 3.15) resulted in the same level of diffusivity at T_m [244]. Since Einstein´s equation is based on the underlying assumption of an isothermal processing this relation is known to yield overestimated values [245]. Hence, the estimated $D_{(s)}$ of region (II) can only represent an upper limit, which might be taken as further confirmation of solid-state amorphisation.

7.1.2. Region (III) – Rapid solidification

In order to conclusively show that region (III) underwent rapid solidification, the reasoning based on microstructural observations given so far needs further reinforcement. As discussed in the theoretical part (see sections 3.1 and 3.2), the parameters needed to assess both the resulting microstructure and phases are the thermal gradient at the (s)-(l) front $\nabla T_{i,(l)}$, the solidification velocity v_i, the interfacial cooling rate $\dot{T}_i$ and Péclet number β_{Pe}. Whether LIMET led to conditions for rapid solidification or not (see sections 3.2.1 and 3.2.3), should be tested by determining these values. Due to the typically small dimensions of heat-affected zones encountered there, in-situ and time resolved techniques like TCR (section 1.2) are not applicable.

A means to generate approximations might be found in the FEM thermal simulations since they provide $T(\vec{r}, t)$ data, which can be processed to yield the aforementioned values. According to the comprehensive summary given in section 6.4, the FEM data presented in section 6.1 can be trusted qualitatively. The inability to account for released portions of free energy, be it due to mixing of the constituent elements ΔG_{mix} or due to phase formation ΔG_f, directly within the model, led to a consistent underestimation of the volume of the heat-affected zone. This finding opened up a relatively simple workaround whose applicability will be shown exemplarily with the Ni/Al specimen sets. The latter were chosen since their region (III) consisted of solidified material only, where optimum (l) phase intermixing was achieved. Basically, the approach is constructed as follows:

1. A perfectly homogeneous LIMET spot is assumed, allowing for calculating the energy delivered to an individual interference maximum line E_L based on simple geometrical considerations and the employed nominal fluence F.

2. With the FEM results so far underestimating the heat-affected volume, the latter can be treated as a lower-bound approximation of the multilayer portion wherein

optimum intermixing took place. To this end, the calculated fraction of molten Al $f_{(l)}$ can be used. By this, the number of atoms of each species within this volume can be calculated based on the idealised multilayer geometry (see figure 5.1 (a)).

3. As region (III) was completely liquefied, the free energy characteristics of the melt $G_{(l)}$-X^i can be taken to represent the energetics of constituent intermixing. Here, the maximum temperature attained within region (III) was taken as a basis to check thermodynamic databases like Landolt-Börnstein or Thermocalc on according information. In this regime of elevated temperatures, the energetic difference between $G_{(l)}$ and G_{IP} is on the order of 10 %. Hence, $G_{(l)}$ alone can be taken as a source of released energy considering the local chemical composition.

4. Since a direct measurement of (l) phase composition was not accessible, the post-treatment data obtained by APT was assumed a reasonable approximation. This could be inferred due to the chemical composition of region (III) being homogeneous and equal to the average composition of the as-deposited multilayer.

5. Joining the molar free energy $G_{(l)}$ with the estimated number of atoms within $f_{(l)}$, an approximated energy release due to elemental mixing E_{mix} could be calculated. This amount was added to the energy per interference maximum E_L calculated before to yield a lower-bound estimate of the *total energy* E_{tot} present at an individual maximum line.

The nominal energy E_L was delivered within time τ_p and intermixing in region (III) took place during melt duration interval $\tau_{(l)}$ with both values being largely on the same order of magnitude. This similarity of time scales allowed the assumption, that the simulated laser could be treated as carrying E_L and E_{mix} simultaneously. In consequence, a modified *actual fluence* F_{act} could be calculated now accounting for both the energetic contribution of the laser and of the material, thus allowing to bypass the flaw of the FEM model in a first-order approximation. Since the simulation itself is based on balancing

the heat flow (see equation 3.6), one possible source of error remained: this energetic workaround is not capable of accounting for phase formation in the sense of replacing the multilayer in the altered volume with a material having different thermal transport properties.

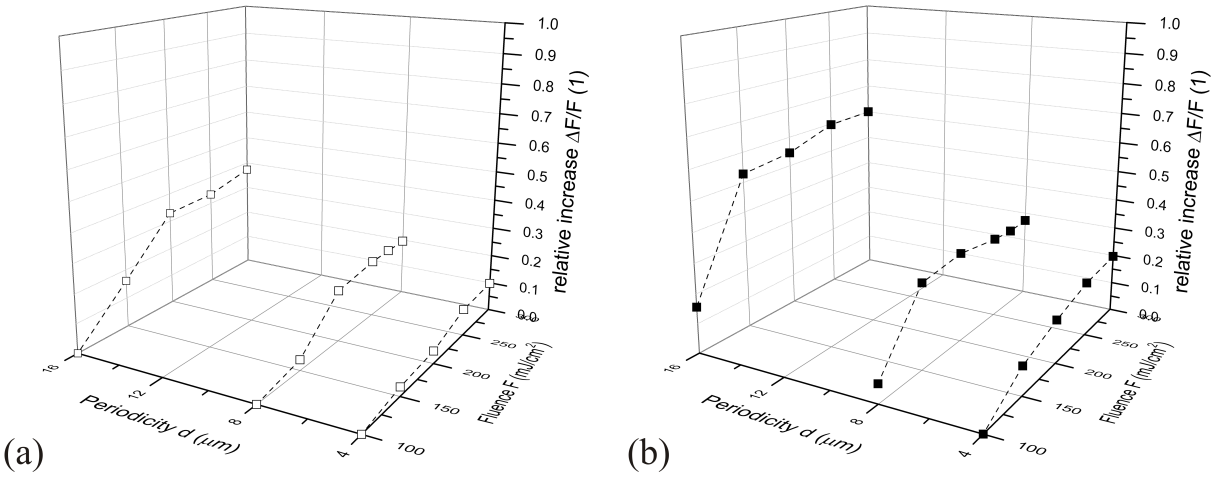


Figure 7.5.: Relative increase of fluence $\Delta F/F$ through the released ΔG_{mix} for Ni/Al on sc-Si (a) and a-SiO_2 (b). In both cases, the characteristic calculated for 4 μm, 8 μm and 16 μm periodicity are depicted (dashed lines).

The literature reports for bulk B2-NiAl a room temperature thermal conductivity of 92 W/mK and a diffusivity of $26{\cdot}10^{-6}\,\mathrm{m}^2/\mathrm{s}$ [246]. Both amount to half of the effective composite values calculated for the multilayer in section 6.1.1, thus being in reasonable proximity to each other effecting a negligible error, especially when seen in conjunction with according properties of the substrates. Figure 7.5 depicts the initial result of this approach by plotting the relative increase

$$\frac{\Delta F}{F} = \frac{F_{act} - F}{F} \tag{7.2}$$

thus representing the relative contribution of released free energy due to the mixing process as a function of LIMET parameters (d,F). Starting with the results obtained

on the sc-Si substrate, the functional behaviour of $\Delta F/F$ with respect to the nominal fluence F showed a similar course. With increasing F, the fraction of additional energy increased linearly up to a threshold fluence of $200\,\mathrm{mJ/cm^2}$ irrespective of the periodicity d. For higher F, $\Delta F/F$ assumes a constant value, which differs for each d. At $4\,\mu$m, the plateau settled at an energetic increase of 10 %, which increased to 20 % for $8\,\mu$m and reached ca. 35 % for $16\,\mu$m, with the rate of increase scaling almost linearly with the relation between the individual d.

Turning to a-SiO_2, the same functional behaviour could be observed, with the threshold already being reached for $150\,\mathrm{mJ/cm^2}$ and the plateau values being increased from 20 to 30 and then to 60 % with increasing d. These differences are straightforward when considering the fact that increasing d, increases E_L and that $\tau_{(l)}$ differed by a factor of four between both substrates. Conversely, the presence of a F threshold value which is dependent on the substrate choice only, allows to readily account for the added free energy. In the case of the Ni/Al specimens which underwent dedicated scrutinisation (see section 6.4, $d = 8\,\mu$m), the above presented analysis transforms nominal fluence $275\,\mathrm{mJ/cm^2}$ in the sc-Si case to a F_{act} of $330\,\mathrm{mJ/cm^2}$, while $150\,\mathrm{mJ/cm^2}$ for a-SiO_2 actually corresponds to $195\,\mathrm{mJ/cm^2}$. These modified values can then be used for further analysis of the simulation data obtained for these F_{act}.

Being able to calculate this relative increase, it is possible to reevaluate the comparison between FEM estimated and actually measured dimensions of heat-affected zones discussed in section 6.2.2 (c.f. figures 6.16 and 6.17) in order to assess the potential of this workaround. To this end, the F coordinate of the measured expansions is corrected by adding the mixing contribution, thus replacing F with the larger F_{act}. Figure 7.6 lines up the reevaluated comparison between FEM (designated by □) and the modified cross-sectional results (■) for sc-Si.

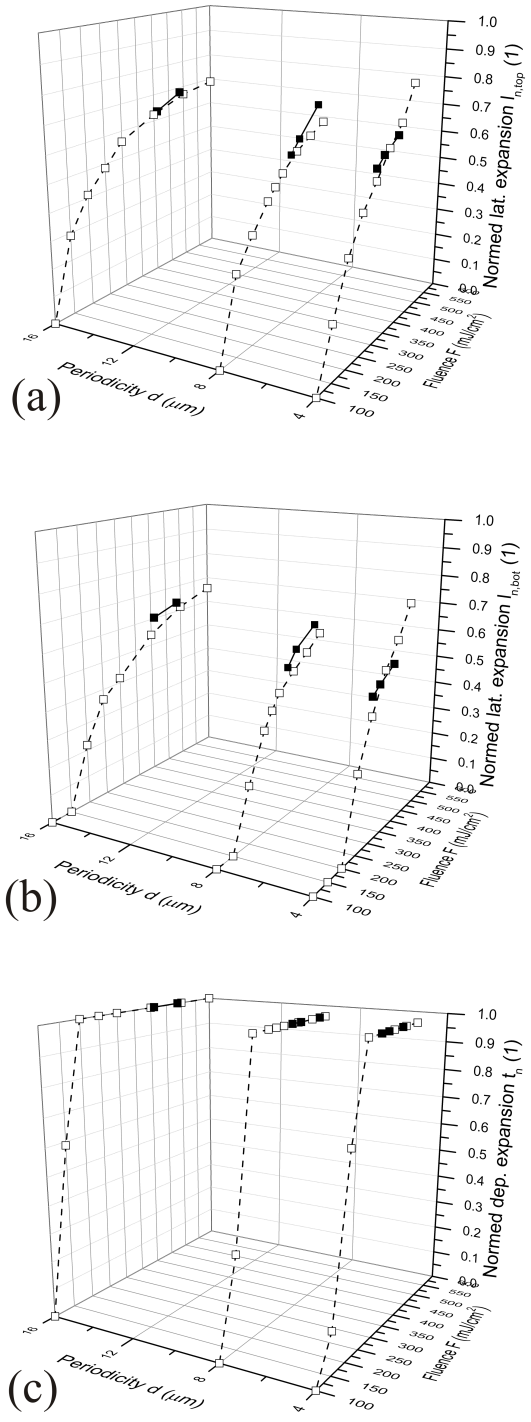


Figure 7.6.: Reevaluated direct comparison between FEM estimated normalised dimensions of the heat-affected zone (designated □) and the modified results of cross-sectional imaging (■) for Ni/Al on sc-Si substrate: lateral expansion at the multilayer surface l_{top} (a), lateral expansion at the substrate interface l_{bot} (b) and depth expansion t_{dep} (c).

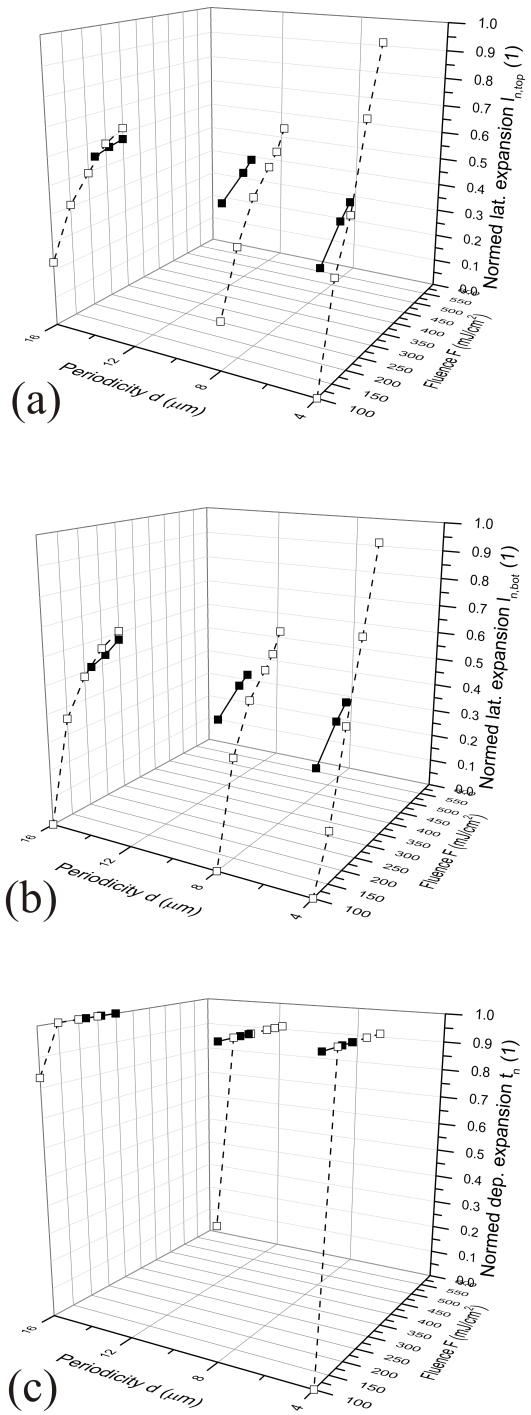


Figure 7.7.: Reevaluated direct comparison between FEM estimated normalised dimensions of the heat-affected zone (designated □) and the modified results of cross-sectional imaging (■) for Ni/Al on a-SiO_2 substrate: lateral expansion at the multilayer surface l_{top} (a), lateral expansion at the substrate interface l_{bot} (b) and depth expansion t_{dep} (c).

As before, the expansion lengths are normalised with respect to $d/2$ and t_{tot}. In contrast to the unmodified results, the workaround significantly reduced the relative difference between simulation and measurement for all expansion lengths and every selection (d,F). While in figure 6.16 the difference ranged between 20 and 40 %, the workaround consistently effected the functional courses to overlap closely with a relative difference of less than 10 %. Figure 7.7 depicts the same comparison for the a-SiO_2 substrate proving the same beneficial effect of the modification, but with a relative difference of ca. 15 % in the worst case.

The significantly lowered relative difference between measurement and simulation in both cases reveals that the proposed approach was capable of yielding more accurate estimations of F_{act} as well as heat-affected volume. It thus was concluded, that a deeper analysis of simulation results obtained from the respective (d,F_{act}) selections has the potential to extract reasonable approximations for the aforementioned decisive parameters governing solidification. In the following, special focus is laid on v_i and $\dot{T}_i$ as a function of the LIMET parameters.

Since the actual temperature at the (s)-(l) front was unknown, it was assumed that the T_m^{Al} isotherm could be taken as representation. Bearing this in mind, v_i thus was approximated by the velocity of this isotherm v_{iso}, which was determined using the x-t characteristics of the boundary demarcation points (A,B) and performing a linear fit within the time interval of stable back propagation. The calculated slopes yielded the respective v_{iso}, which was similar for both points under the same (d,F) conditions. Figure 7.8 shows the accordingly determined v_{iso} for point A as a function of the LIMET parameter field.

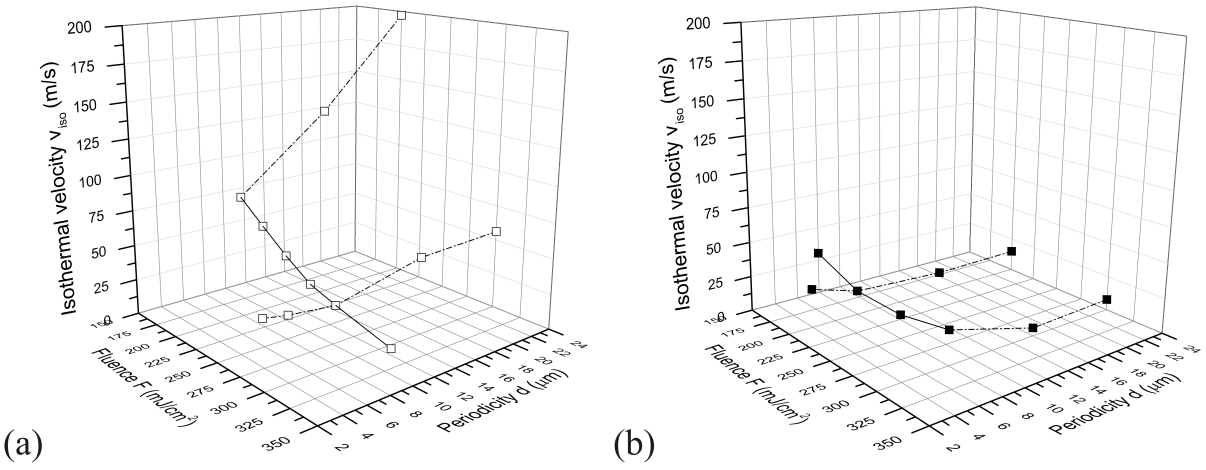


Figure 7.8.: FEM estimated isotherm velocities v_{iso} as a function of periodicity (continuous line for $d = 8\,\mu$m) and fluence (dash dot lines at $200\,\mathrm{mJ/cm^2}$ and $300\,\mathrm{mJ/cm^2}$, respectively) for sc-Si (a) and a-SiO_2 substrate (b).

The results obtained for Ni/Al sc-Si shown in figure 7.8 (a) reveal two superposed tendencies. In the example of v_{iso} as a function of F for a constant periodicity of $8\,\mu$m it can be seen, that lower fluences effect high isotherm velocities, here $86\,\mathrm{m/s}$ at $200\,\mathrm{mJ/cm^2}$. Increasing F led to an almost linear decrease of v_{iso}, reaching $30\,\mathrm{m/s}$ for $350\,\mathrm{mJ/cm^2}$. This is consistent with an observation of Baeri et al. made on pulsed laser melting and resolidification of bulk sc-Si [27]. They confirmed experimentally that v_{iso} principally depends on pulse duration τ_p, absorption length $1/\beta$ and energy density F. Modifying these parameters might effect a variation in v_{iso} within one order of magnitude or higher. Qualitatively, the velocity is increased for materials with large absorption coefficients β or by employing a pulsed laser with low τ_p. Baeri also observed, that the use of increasing energy density results in a reduction of v_{iso} in concordance with the present results. Looking at the behaviour of v_{iso} as a function of periodicity d two regimes could be identified. For low fluences ($200\,\mathrm{mJ/cm^2}$), the velocity increases in linear manner with rising periodicity, reaching up to $200\,\mathrm{m/s}$ at $24\,\mu$m. At constant $F = 300\,\mathrm{mJ/cm^2}$. the same functional course is revealed however, with a significantly lower slope. For $d = 2\,\mu$m a

v_{iso} of 46 m/s is calculated, which only mildly increases to 56 m/s at 24 μm. Turning to the calculations for a-SiO_2 substrate, a differently shaped $v_{iso}(d,F)$ field was found with a significantly lowered velocity magnitude irrespective of the selected (d,F) combination. For constant $d = 8\,\mu$m, the observation of Baeri once again is confirmed. At a low fluence of 150 mJ/cm^2, v_{iso} amounted to 30 m/s, which was reduced to a constant value of 20 m/s for fluences surpassing 200 mJ/cm^2. The d-dependent behaviour was analysed for 200 and 300 mJ/cm^2 fluence. Both showed a similar functional course with the low-d velocity at 30 m/s, which was reduced to a constant 15 m/s in the first and 7 m/s in the second case for periodicities larger than 8 μm.[1]

From these data it is straightforward to conceive that both fluence and periodicity control the energy density delivered to an individual interference maximum and thus govern v_{iso}. The influence of the fluence was already discussed above. Increasing d corresponds to an increasing amount of energy deposited per interference maximum. Hence, this should yield a decrease in v_{iso}, which was found for the simulations concerning the a-SiO_2 substrate. Looking at the sc-Si simulations, results presented here seem ambivalent in this respect. While the F-dependent behaviour fitted to the aforementioned conception, the variation of d effected a counterintuitive result. Especially at lower fluences, rising d yielded a steeply increasing v_{iso}. Yet seen in conjunction with the calculated thermal gradients at the (s)-(l) interface (c.f. figures 6.4 (a) and (b)) for both substrates, this could be attributed to the larger magnitude of heat extraction when sc-Si is employed.
Looking more closely at the $v_{iso}(d,F)$ fields for both substrates, another implication can be considered. Both the lowered magnitude and more constant v_{iso} values encountered on a-SiO_2 seem to be accessible for multilayers deposited on sc-Si as well. The $v_{iso}(d,F)$

[1] It should be noted, that rapid solidification studies performed on free-standing Ni/Al thin films using comparable fluences effected solidification front velocities on the order of 2 m/s. This value was determined by Bostanjoglo et al. using a Dynamic TEM technique [247].

field at fluences exceeding 350 mJ/cm^2 encountered there (figure 7.8 (a)) fits the magnitude and the d-dependence of the low F-branch of a-SiO_2. Hence, by increasing F the behaviour of both substrates might be adapted to each other, if multilayer adhesion to the substrate remains intact. Since a nominal fluence of 300 mJ/cm^2 (corresponding to an actual 360 mJ/cm^2) was already sufficient to inflict significant delamination, an experimental confirmation was not reasonable.

For the further discussion of the LIMET-induced microstructure and phase formation, a closer look at v_{iso} achieved by the employed actual fluences F_{act} is necessary. On sc-Si, an estimated 35 m/s were calculated, while on a-SiO_2, only 17 m/s were reached. In comparison to values reported in the literature (see section 1.2), these individual results are located at the upper bound of the TCR-measured solidification velocities for sc-Si (1 to 30 m/s according to [26][27]) and at the lower end of those encountered in metals (ranging from 30 to 100 m/s [44][51]). Considering however the results calculated for sc-Si as a whole, a good agreement with the measured values can be found. Bearing this in mind, these results can be related to the theoretical treatment of interfacial kinetics presented in section 3.2.1.

There, equation 3.18 introduced the Péclet number β_{Pe} representing the quotient between the velocities of interfacial growth v_i and solute diffusion in (l)-phase v_D. Using this value it can be determined whether conditions suitable for rapid solidification were achieved, which is the case when β_{Pe} reaches unity. In order to do so, it is necessary to calculate v_D by relating solute diffusivity $D_{(l)}$ to an estimated diffusion length within (l). In the present case it can be assumed, that region (III) can be described as Al melt wherein Ni atoms are dissolved. Considering the 10 % increase in volume taking place during the melting transition [93] and the data on solute diffusion in molten Al determined by Du et al. [248], v_D can be estimated. Accounting for the effect of the actual fluence on T_{max} in region (III), a maximum temperature of 1900 K can be as-

sumed (c.f. 6.2 (a)). $D_{(l)}$ then amounts to $18.4{\cdot}10^{-9}\,\mathrm{m}^2/\mathrm{s}$ leading to a diffusive speed of approximately 40 m/s. Thus, replacing v_i with the simulated v_{iso}, β_{Pe} for the example on sc-Si reaches 0.88, while on a-SiO_2 0.43 was achieved.

Both the absolute velocities v_{iso} and the respective β_{Pe} values can then be compared to the velocity-dependent solidification regimes depicted in figure 3.6. With both calculated absolute velocities being on the order of 10^1 m/s, the findings of Kurz et al. shown in figure 3.6 (a) confirm rapid solidification takes place with active solute trapping. With figure 3.6 (b) giving the functional behaviour of the non-equilibrium partition coefficient k_v (c.f. equation 3.19) in dependence on normalised velocity, embodied by the Péclet number, the degree of solute trapping is accessible [34]. With β_{Pe} of sc-Si being close to unity, an effective k_v of 0.9 was achieved which corresponds to partitionless solidification. Even for the slightly reduced β_{Pe} of a-SiO_2 where k_v approximately amounted to 0.8, the same can be concluded. Together with local chemical composition as well as microstructure and phases formed in region (III) given in figure 6.42, the argument in favour of partitionless solidification is further reinforced.

Final confirmation was achieved considering the temperature gradient at (s)-(l) interface ∇T_i for both F_{act}. Figures 6.4 (a) and (b) reveal that on sc-Si approximately $1.0{\cdot}10^9\,\mathrm{K/m}$ were obtained, while the multilayer on a-SiO_2 experienced a gradient of $0.5{\cdot}10^9\,\mathrm{K/m}$, when calculating the geometric mean of ∇T_{lat} and ∇T_{dep}. Mehrabian reports experimental observations on this value made during rapid solidification of dilute Al/Cu alloys [25]. There, planar partitionless solidification was achieved for an alloy containing 0.1 at.% of Cu when the processing yielded gradients on the order of $10^7\,\mathrm{K/m}$ and an interfacial velocity v_i of approximately 1 m/s. Both the interfacial velocities and the gradients effected by LIMET were sufficient to surpass the critical values for absolute stability of the (s)-(l) interface (v_a and ∇T_a, see equations 3.23 and 3.24 respectively).

So far, only the solidification mode and the microstructural evolution were addressed. In order to tackle issues of phase selection and formation, the information gathered on estimated solidification velocity v_{iso} needs to be accompanied by data on cooling rates present at the (s)-(l) interface [27]. The FEM studies performed on LIMET so far only calculated $\dot{T}$ directly at the centre of an interference maximum thus yielding exaggerated values [19][79]. In the course of this thesis, effort was made to improve this situation. Figure 7.9 lines up the $\dot{T}_i$ results obtained at the A-B boundary. They were extracted from simulated $T(\vec{r},t)$ data in the time instant, the demarcation reached its largest lateral travel. Hence, the $\dot{T}_i$ depicted there represent the cooling rate when resolidification is initiated.

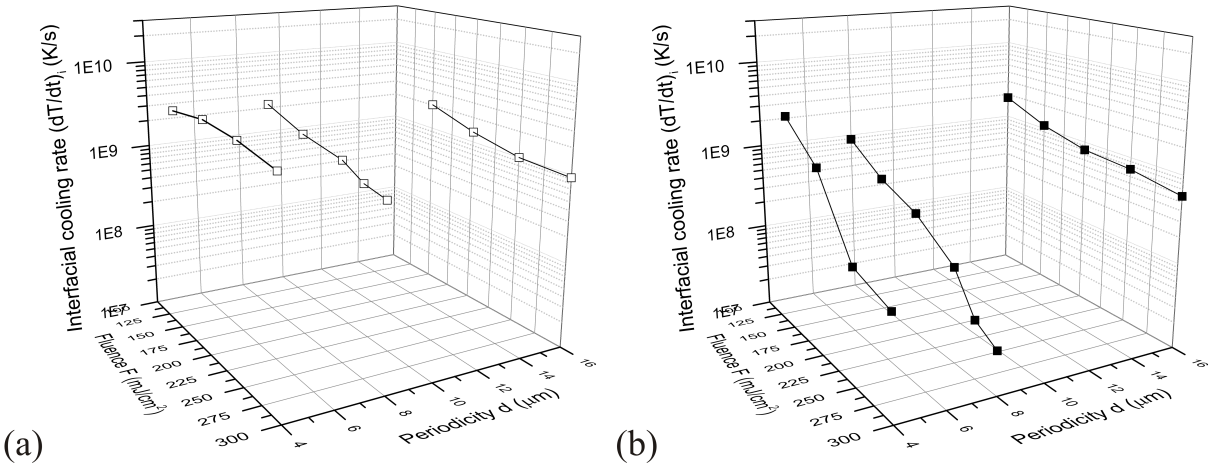


Figure 7.9.: FEM estimated cooling rates $\dot{T}_i$ at the T_m^{Al} isotherm at its maximum lateral propagation as a function of periodicity (continuous line for 4 μm, 8 μm and 16 μm) for sc-Si (a) and a-SiO_2 (b).

In figure 7.9 (a) the (d,F) charcteristics encountered for the sc-Si substrate are shown. $\dot{T}_i$ there seemed to be only slightly affected by variations in these parameters and ranged on the order of 10^9 K/s, thus being one order of magnitude lower than the estimation given while presenting the working hypothesis in section 7.1. It is apparent that both in-

creasing d and increasing F effect a slight reduction of $\dot{T}_i$ to the upper region of 10^8 K/s. In contrast to this, the results obtained for a-SiO_2 exhibited a differently shaped $\dot{T}_i(d,F)$ field. For periodicities equal or lower than 8 μm, the behaviour resembled the one encountered in sc-Si, but with a more steep loss of magnitude. Here, $\dot{T}_i$ was even reduced to values on the order of 10^7 K/s with increasing F. For $d = 16\,\mu$m both the same magnitude and functional course as for sc-Si were obtained. This is in concordance with the general result of the simulations (see section 6.1.1) showing stable conditions for periodicities larger than 8 μm. In the case of the actual fluences in question here, a cooling rate of ca. $1.0{\cdot}10^9$ K/s was determined for the multilayer on the sc-Si substrate while on a-SiO_2 only 30 % of this value was achieved.

This difference in cooling rate is likely to exert an influence on the phase sequence observed along the travel path of the solidification front. Figure 6.42 (a) and (b) already lined up the structural data needed to assess phase formation in the Ni/Al specimen sets. In the multilayer on fused silica (see figure 6.42 (b)), LIMET transformed region (III) to contain B2-NiAl only. On sc-Si (figure 6.42 (a)), martensitic $L1_0$-NiAl was identified as the first formed phase. According to literature on martensitic transition in Ni/Al system, the presence of this phase only is possible for compositions on the Ni-rich part of the NiAl-phase field (between 60 to 70 at.%). In the vicinity of the adjacent two-phase region, the crystal structure accommodates the off-stoichiometric composition by substituting Ni on the Al sublattice [131][249][250]. This stands in conflict with the compositional data obtained by APT within whole region (III) where Ni and Al were found to be intermixed 1:1. Consequentially, the LIMET-triggered reaction path leading to the formation of $L1_0$-NiAl cannot be based on the conventionally postulated (s)-state mechanisms. This notion is backed both by theoretical considerations devised Boettinger and Aziz [251] [252] and experimental evidence gathered in studies of Assadi and Greer [253][254]. In their work, a long-range ordered bulk intermetallic Ni_3Al specimen is molten by pulsed-laser radiation and subsequently resolidified. Boettinger

described the solidification of an intermetallic compound under non-equilibrium conditions. His studies included an approach to account for the degree of order as a function of solidification front velocity v_i. In analogy to the solute trapping treatment (described in section 3.2.1), a function describing the behaviour of the long-range order parameter η in dependence of v_i was developed on thermodynamic grounds [252]. Increasing v_i beyond a threshold value leads to a complete loss of order ($\eta = 0$), which corresponds to *disorder trapping* during solidification. The consecutive work of Assadi and Greer showed, that ordering takes place after the solidification front passed the specified volume. Both by simulation and actual experiments, they could confirm this hypothesis.

Transferred to the present situation, these findings were interpreted as follows. When the (s)-(l) front started receding and solidification set in, a disordered solid solution was formed first, which subsequently made a transition to either an ordered $L1_0$- or B2-NiAl. The selection between these two structural possibilities most likely is governed by a concurrence of two effects:

- Heterogeneous nucleation: Theoretical section 3.1 already introduced the concept of heterogeneous nucleation triggered by seeding crystals as devised by Herlach and coworkers [95][227]. Similar assumptions were made by Im et al. when explaining phase selection during laser-induced SLG-mode crystal growth [45][46]. In the present context, the remaining Ni-crystals within region (II) directly adjacent to the (s)-(l) interface were taken as possible seeds. Hence, the aforementioned disordered solid solution was likely to exhibit a face-centred cubic (fcc) structure as imposed by the seed since this process only affords short-ranged atomic displacements. Following Robertson and Wayman, the $L1_0$-structure can be treated as ordered tetragonal phase either of face-centred (fct) or of body-centred (bct) Bravais type [250]. Thus, the close similarity between fcc disordered solid solution and fct-martensite made a preferred transition to $L1_0$-NiAl more probable.

- Time interval available for achieving the ordering: It was deduced, that the high interfacial cooling rates at the A-B boundary encountered on Si substrates (see figure 7.9 (a)) support the initial martensite formation. As the (s)-(l) front propagated further, austenitic B2-NiAl was formed, especially at the interference maximum centre where the material was molten for most of $\tau_{(l)}$. Thus, a reduced $\dot{T}_i$ could be inferred, which fits this hypothesis.

A closer look at the interference maximum of Ni/Al on sc-Si (see figure 7.10 (a)) reveals an interesting feature supporting the argumentation of the first effect. The TEM dark-field image (b) taken at the onset of the topographic maximum of region (III), shows a twinned microstructure close to the thin film surface and right between $L1_0$- and B2-NiAl. The habit plane m clearly can be discerned in the image along with the orientation of both twin variants (s_1 and s_2). Perpendicular to both s_j a periodic modulation of the transmitted intensity could be seen, pointing to the presence of a fine-twinned substructure within the variants. This interpretation is supported by the SADP (c) taken from this $L1_0$ grain. There, streaking was observed along reciprocal [02h0]-direction. The streaks were oriented parallel to the intensity modulation within a twin variant, as indicated by the s_j vectors in (b) and (c).

Similar observations in LIMET treated Ni/Al multilayers were made during a preliminary study under supervision of the author [172]. From the standpoint of the geometric diffraction theory, streaking occurs when a relrod lies within the plane of the TEM foil, thus weakening the geometric diffraction condition [188]. Those relrods arise for example, when the crystal structure is modulated by planar faults to form a periodically recurring structure element with a modulation length larger than the interplanar spacing. Since the streaks here exhibited a diffuse intensity distribution without discrete and equally spaced reflections along s_j, the modulation here was not commensurate [186].

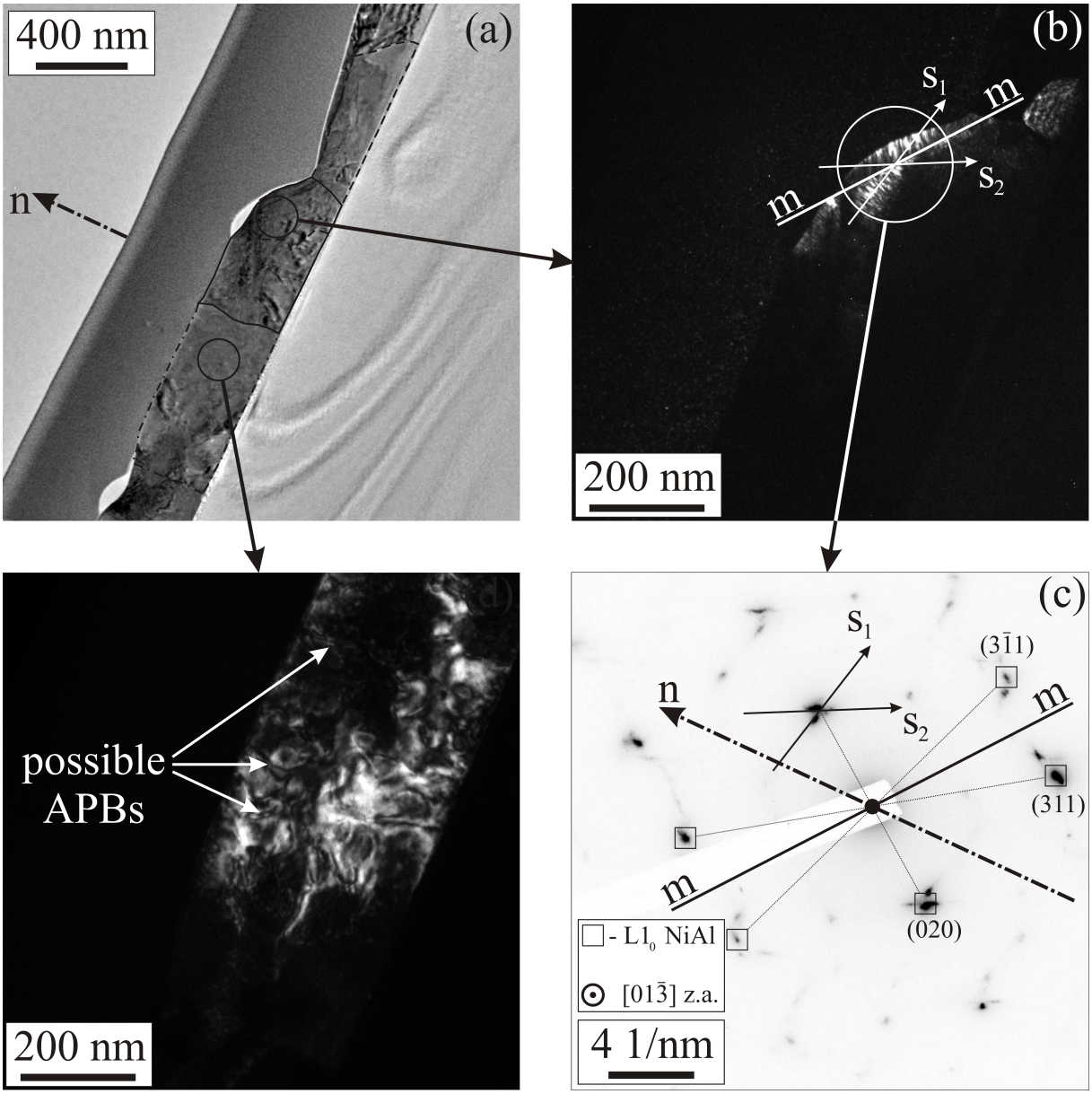


Figure 7.10.: TEM micrograph of Ni/Al region (III) on sc-Si substrate (a). dark-field imaging of $L1_0$-NiAl herring-bone morphology (b) and corresponding SADP (c): habit plane m and two twin orientation variants s_1 and s_2 indicated. Close-up dark-field imaging of central region (III) exhibiting prospective anti phase boundary (APB) structures in B2-NiAl (d).

According to literature on the martensitic transformations in Ni/Al, these streaks can be attributed to an intermediate phase being formed to accommodate the structural mismatch between B2 to $L1_0$. As Khachaturyan et al. elaborated, it is formed by a stacked structure, where the repeated element consists of seven layers having pseudo-orthorhombic structure. This *adaptive 7R phase* appears in order to reduce the elastic energy associated with the mismatch between the martensite and austenite phase [255][256]. The first observations of this structure in bulk Ni/Al were made by Robertson et al. and were called *tweed microstructure* [249][250]. In Ni/Ti related research, it is commonly referred to as *herring-bone morphology* according to Kockar and coworkers [257]. Both its presence and its location were taken as confirmation of the proposed transition sequence.

Dedicated TEM analysis of the centre of region (III) further revealed evidence supporting the aforementioned (s)-state ordering process. Assadi et al. both predicted numerically and proved experimentally, that a transition of this kind yields *anti-phase boundaries* (APBs) or domains of them. Figure 7.10 (d) shows a C-DF image taken in B2-NiAl, wherein a clearly visible domain structure was encountered which closely resembles an image taken from an APB network found in a rapidly solidified bulk Ni_3Al specimen [258]. Taken together with the 7R structure, it could finally be concluded that also in the case of LIMET the ordering step takes place in (s) state.

Concluding this discussion, the main statements on rapid solidification induced by LIMET shall be summarised. The presented improved interpretation of FEM data clearly confirmed polymorphous partitionless solidification in SLG regime. Phase selection is triggered by crystalline seeds at the boundary to region (II) enabling preferred heterogeneous nucleation. According to the joint analysis of local chemistry and structure along with the interfacial cooling rate, the resulting phases or even phase sequence could be conclusively explained. Irrespective of the cooling rate, the phases formed lie

exactly within the intended compositional range as imposed by the multilayer design. Hence, it was concluded that the local chemical composition within the melt dictates the stoichiometry of the possible (s) phases being formed upon cooling. The cooling rate in turn governs whether the subsequent polymorphous solidification yields a frozen in amorphous state or a crystalline phase.

In order to assess the applicability of these conclusions to other material systems, the results obtained from Ti/Al specimens (c.f. figure 6.43 (a) for sc-Si and (b) for the a-SiO_2 substrate) shall be discussed accordingly. For both substrates, only a limited melt depth was achieved. Because of this, and due to the Ti capping layer, the (l) phase contained 10 at.% more Ti than planned, as confirmed by APT. This effect was increased in the flank part of region (III) due to the clearly anisotropic thermal transport within the multilayer. Hence, Ti-rich phases like β-Ti or Ti_3Al should preferably form during solidification, as the TEM analyses confirmed. Since the initial cooling rate was found larger than those closer to the interference maximum, the transition to β-Ti could be bypassed and Ti_3Al was formed in the flank. Closing in to the centre, β-Ti was confirmed in line with the hypothesis. For the fused silica substrate, where a larger melt depth was achieved and the increased $\tau_{(l)}$ effected more efficient intermixing, $L1_0$-TiAl was achieved in the intended composition range. By this, the capability of the presented hypothesis is successfully demonstrated.

7.2. Consequences on designing LIMET processing

To approach the intended systematic application of LIMET to multilayer thin film processing, the role and mutual interdependence of the different processing parameters as determined in this study shall be lined up here. In addition, the applicability of the master curves (see figures 3.10 and 3.11, section 3.2.3) describing the microstructural and phase selection based on kinetic and thermodynamic approximations will be addressed. In a nutshell, three different aspects of the processing result can be influenced to some extent:

1. Type of transformation – (s)-state interreaction or (l)-(s) transition:
   Here, parameters addressing the *mixing behaviour* and the *duration* of this process are of primary interest. Thus, the material combination forming the multilayer exerts the most significant influence. For both observed transformations a large negative enthalpy of mixing ΔH_{mix} is beneficial since it promotes an efficient intermixing of the constituents both in (s) and (l) state. In order to trigger whether solidification or a (s) reaction takes place, the combination of melting temperatures T_m and seems to be paramount. Using one low-melting component supports the dissolution of the other into it at temperatures lower than $T_{m,high}$, thus facilitating the intermixing even at lower employed fluences. The same effect is evoked by using a substrate material with bad thermal transport properties, which also leads to increased mix durations. Moreover, solute diffusivity and its relation to self diffusion in solid-state amorphisation should also be considered.

2. Phase selection – Metastable or equilibrium phases or mixtures of both:
   Beside the implications imposed by the favoured type of transformation, the parameters governing the *cooling rate* and the *velocity* of the solidification front step into the foreground. Thus, LIMET parameters (d,F) and the substrate are in focus here. As can be inferred by the modified simulation results, both rising d and F effect a decrease in v_{iso}, which can be adjusted by appropriately selecting

these two parameters. This decrease is significantly altered by the substrate material, with a-SiO_2 effecting a more constant and low-speed $v_{iso}(d,F)$ field. With the velocity allowing for partitionless solidification, the local composition achieved in the molten volume narrows down the range of possible phases.

Finally, the interfacial cooling rate $\dot{T}_i$ and its evolution along the solidification path dictates the possibility to bypass crystallisation or ordering transitions and thus the locally resulting phase. Here, the multilayer material selection once again comes into play because phases with large compositional existence ranges and simple structures are preferred. The experiments of this study confirmed these implications of Turnbull´s rule (see section 3.2.3). Periodicity and fluence serve the same purpose in determining the energy deposited in an individual interference maximum. For periodicities above 8 μm, the cooling rate becomes independent of the selected substrate. Moreover, the interaction of adjacent maximum positions is avoided, which is inferred by $\dot{T}_i$ behaving more independent from F for large d. The minimum fluence to achieve a complete modification of the multilayer down to the substrate, 150 mJ/cm^2 is necessary on a-SiO_2 and sc-Si affords 250 mJ/cm^2 irrespective of d. Keeping in mind the need to sustain substrate adhesion, a maximum fluence threshold exists, here found on the order of only 50 to 100 mJ/cm^2 above these limits, thus narrowing down the processing window.

3. Microstructure – Transformed volume fraction and resulting grain morphology:
Here, the *capability to transport heat* away from the interference maximum zone is paramount due to its implications on the solidification front velocity v_i and the local temperature gradient ∇T_i. Initially, the composite heat transport behaviour of the multilayer material combination is important. In order to promote a through reaction, a more or less isotropic or preferably depth-oriented transfer proves useful. The example of Ti/Al showed that a more lateral transport leads to a more spread

out and surface-concentrated heat distribution effecting a less efficient intermixing within the heat-affected volume. Judging from simulated results for ∇T_i, the transport of heat into the substrate prevails for periodicities larger than $8\,\mu$m. It is intuitively clear that its magnitude is increased if a substrate with better thermal transport properties is employed. Nevertheless, the microstructure found here proved that planar solidification was favoured irrespective of substrate or multilayer material. As for the size of the heat-affected zone, substrate as well as (d,F)-selection exert a joint effect. Consistently, increasing F leads to an increasing modified volume, reaching a saturation value of 40 % of the half-period volume for sc-Si and 60 % for a-SiO_2. Applying periodicities smaller than $8\,\mu$m, and fluences larger than $250\,\mathrm{mJ/cm^2}$, the adjacent maxima influence each other leading to even larger heat-affected volumes up to a complete modification.

Transferring the results of this thesis to the aforementioned master curves draws an ambivalent picture of their usability. Looking at the microstructural findings confirming planar and segregation free solidification it is qualitatively clear, that either the limit of the thermal gradient or of the solidification front velocity associated with the absolute stability of the (s)-(l) interface (see figure 3.10 (a)) were effectively surpassed. With the available data it could not be conclusively distinguished, whether LIMET managed to overcome only one or even both of them. Figure 3.10 (b) depicts the corresponding limit associated with chemical composition. Since this schematic was elaborated for dilute alloys, the significant supersaturations achieved by LIMET make its use questionable. Hence it was concluded for the present case, that these schematics serve well as a means to theoretically describe the interdependence of these parameters and to explain the microstructural outcome after the treatment. Conversely, they cannot be applied for predictive purposes.

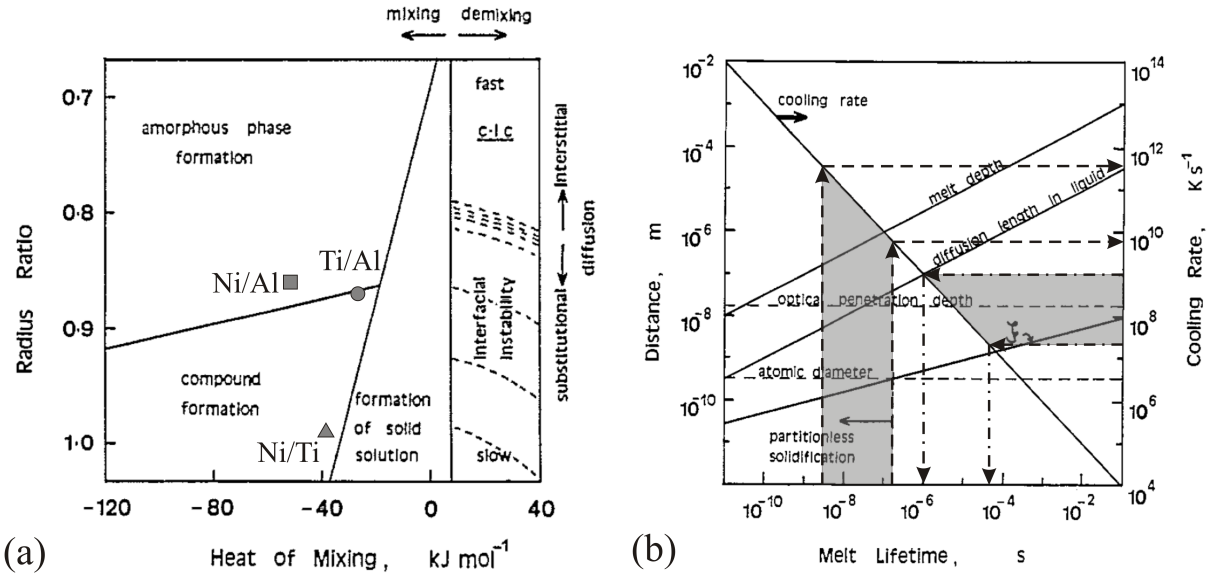


Figure 7.11.: Updated version of figure 3.11 (modified from [106]) containing information on the material systems investigated here and the simulation results (grey-coloured areas): Greer´s master curves on (a) thermodynamic interaction and diffusional mass transport of pure multilayer components and (b) pulsed laser treatment parameters with critical diffusional and microstructural dimensions.

In order to assess Greer's master curves (see figure 3.11) dealing with the thermodynamics of phase formation and diffusional mass transport in confined media (a) as well as critical dimensions of mass transport during pulsed-laser treatments (b), the data of the present study were inscribed there. Figure 7.11 shows the thus altered diagrams containing the properties of the material systems under investigation here (a) and the critical time scales obtained by FEM simulations (b).

Since the argument on phase formation (c.f. figure 7.11 (a)) was devised for transformations in (s) and (l) state, the outcome of both identified LIMET-triggered mechanisms might be evaluated. The ratio of atomic sizes and the enthalpy of mixing both of Ni/Al and Ti/Al are located closely to the boundary delineating the parameter fields indicating the formation of compound and amorphous phases. This fits reasonably to the

experimental findings described above. In contrast to this, Ni/Ti is located close to the boundary between compound and solid solution formation, which is not backed by the results of this thesis.
Introducing the typical range of simulated data on melt duration $\tau_{(l)}$ and cooling rate $\dot{T}_i$ (see grey-coloured fields in figure 7.11 (a)) into the diagram relating critical time scales, the limitation of the employed simplifications becomes evident. Just looking at the simulated $\tau_{(l)}$, the experimentally observed partitionless solidification is confirmed. Extending this range along the simplified relation between $\tau_{(l)}$ and $\dot{T}_i$, cooling rates on the order of 10^{10} to $10^{12}\,\mathrm{K/s}$ are predicted (see dashed straight lines). This stands in contrast to the simulated cooling rates at the solidification front, which according to Greer´s calculation are effected by melt durations three orders of magnitude larger than FEM estimations.

It is apparent that the simplifications employed to devise both of these diagrams are too coarse to allow for meaningful predictions even with some tolerance. Finally, both sets of master curves can be treated as being capable of indicating tendencies regarding the resulting phases and microstructure, but fail in respect to reliability making post-mortem experimental evaluation indispensable.

Part IV.

Conclusions and outlook

8. Conclusions and outlook

The main task of the present thesis was to elucidate whether LIMET heat treatment of multilayered metallic thin films might be turned into a reproducible processing method allowing for the manufacture of à priori designed architecture materials on the μm scale. To this end, four different branches of investigation were identified (see section 1.3) and successfully pursued, as the oncoming summary will show:

1. It was possible to determine appropriate selections of LIMET parameters (d,F) and material combinations which led to a heat-affected zone spanning the whole stack thickness. Both via actual experiments and FEM simulations a reasonable LIMET processing window was identified in dependence on the chosen substrate. This window allows for stable, saturated modification conditions whilst impeding mutual interaction of adjacent interference maximum sites and circumventing damage to the thin film-substrate system. Especially when comparing the TEM cross-sectional views on interference maximum locations obtained in the present thesis to those of preceding studies ([19][60]), the efficiency and reproducibility of the identified processing window becomes evident. To this end, the reader is invited to compare figure 1.1 representing the extent of modification achieved in Daniel´s thesis to figures 6.18 and 6.19 showing the present results.

2. The combined use of the complementary, high-resolution characterisation techniques TEM and APT in scrutinising the local modification of structure, microstructure and chemistry proved useful in the identification of the metal physical

processes triggered by the LIMET process. Through this correlative microscopy approach it was possible to show, that both induced transformations types are of polymorphous nature. Initially, the multilayers underwent a solid state amorphisation reaction. Only if a significant amount of liquefied material could be generated, resolidification became the dominant process. It was found, that the latter is treated best according to present theories on partitionless rapid solidification under super lateral growth conditions. It is worthwhile trying to apply these findings to the structural and microstrutural modification achieved during Daniel´s thesis [19]. As can be inferred from figure 1.1 (c) to (e), LIMET there effected only asymmetric diffusion and formation of small intermetallic nuclei in a near-surface portion of the thin film stack.

3. This systematic comparison of FEM estimations and experimental measurment provided the dimensions of the obtained LIMET heat-affected zones for the first time. It consistently showed that FEM thermal simulations yield underestimated values which could be attributed to the model not accounting for released amounts of free energy of mixing from compound formation. Due to the fact that the relative energetic difference between those to contributions only amounts to 10 %, it was deemed a negligible error if free energy of the liquid phase was taken to represent the intermixing process. Then, the simulated laser was treated as a carrier for both the laser-delivered energy and the energetic contribution of elemental mixing. Using the resulting actual fluence, a workaround to fix this underestimation was devised by replacing the values of nominal fluence measured during the LIMET processing. This approach yielded a close agreement between simulation and reality making it a powerful amendment which enables an accurate à priori estimation of the modified material volume.

4. Thanks to joining the localised data obtained by correlative microscopy with data extracted from the modified simulations, the aforementioned metal physical mech-

anisms could not only be unequivocally identified: together with approaches of non equilibrium thermodynamics and diffusional considerations they allowed to identify the main parameters governing microstructure and phase selection (solidification front velocity v_i, Péclet number β_{Pe}, interfacial thermal gradient ∇T_i and cooling rate $\dot{T}_i$) as well as their relation to the LIMET processing parameters. Clearly, phase selection here is governed by the locally present cooling rates and chemistry. Especially the latter can only be scrutinised by high-resolution methods on the nm-μm scale, once again reinforcing the utility of the correlative approach. Applying G-X^i characteristics in case of solid-state amorphisation and equilibrium phase diagrams in rapid solidification together with simulated effective temperatures and local chemical composition, a conclusive explanation of the present composition and distribution of phases was possible.

Clearly, the main results of this thesis made crucial contributions to a better understanding of the LIMET-induced modifications imposed on multilayered metallic thin films. Thanks to the correlative microscopy approach not only a reasonable processing window and the underlying mechanisms were elucidated; the simulation tool was improved to yield more accurate data useful to estimate LIMET-modified dimensions as well as to estimate critical processing parameters fitting the current theories on solid state amorphisation and rapid solidification. Moreover, for the first time within the framework of LIMET, the possibilities of non-equilibrium thermodynamics were addressed and successfully applied to explain phase selection. Additionally, resulting implications on the design of the multilayer-substrate combination were elaborated.

For more focused future studies in this field, this thesis provides the basis for a reasonable systematic approach encompassing material selection, processing parameters as well as experimental planning and theoretical considerations to assess the processing result. As a potential field for further development, material systems promoting solid state amorphisation might be of interest. The production of a composite material consisting

of long-range ordered adjacent crystalline and amorphous portions with good mutual cohesion opens up new possibilities to modify the mechanical behaviour of surfaces. Especially the combination of the different mechanisms in crystalline and amorphous metallic media with respect to elasticity, plasticity and crack propagation might yield interesting effects in fracture mechanics and tribological applications.

More generally, further improvements to LIMET processing of thin films are necessary to push this technique closer to application. First of all, the spatial inhomogeniety of the laser intensity distribution within the spot area needs to be removed or at least smoothed out. To this end, the optical setup needs alterations in order to remove the superposed near-field diffraction Fresnel pattern; a task actually being pursued in the course of another doctoral thesis. Second, the damage inflicted by delamination or decohesion from the substrate due to irradiation with higher fluences remains an issue. For this purpose, an approach devised by Kline and Leonard based on encapsulating the thin film might be pursued in oncoming studies [51][52]. There, the thin film of interest receives an additional capping layer of transparent a-SiO_2 which transmits the laser intensity and suppresses dewetting between film and substrate as well as increased topographic alterations. Incorporating and evolving these improvements to the amendments to LIMET achieved in this thesis might finally yield the potential to create a reliable, semi-empirically architectured composite for thin film applications.

Part V.

Appendices

Material data on selected phases

Phase	Ni/Al system: relevant phases				
	Al	NiAl	NiAl	Ni_3Al	Ni
Designation	/	β	/	γ'	γ
Strukturbericht	A1	B2	$L1_0$	$L1_2$	A1
Space group	$Fm\bar{3}m$	$Pm\bar{3}m$	P4/mmm	$Fm\bar{3}m$	$Fm\bar{3}m$
ICDD reference	04-0787	41-1188	[255]	[259]	04-0850

Table 1.: Structural data on the relevant phases of the Ni/Al system. Until otherwise stated, the structure data is taken from [190][163].

Phase	Ti/Al system: relevant phases				
	Al	TiAl	Ti_3Al	Ti	Ti
Designation	/	γ	α_2	β	α
Strukturbericht	A1	$L1_0$	$D0_{19}$	A2	A3
Space group	$Fm\bar{3}m$	P4/mmm	$P6_3/mmc$	$Im\bar{3}m$	$P6_3/mmc$
ICDD reference	04-0787	[260]	[260]	44-1288	44-1294

Table 2.: Structural data on the relevant phases of the Ti/Al system. Until otherwise stated, the structure data is taken from [190][141].

Phase	Ni/Ti system: relevant phases				
	Ni	NiTi	NiTi	Ti	Ti
Designation	/	/	/	/	/
Strukturbericht	A1	B2	B19'	A2	A3
Space group	$Fm\bar{3}m$	$Pm\bar{3}m$	$P2_1m$	$Im\bar{3}m$	$P6_3/mmc$
ICDD reference	04-0787	[261]	[261]	44-1288	44-1294

Table 3.: Structural data on the relevant phases of the Ti/Al system. Until otherwise stated, the structure data is taken from [190][163].

Multilayer	Composite thermal transport properties			
	$\lambda_{th,lat}$ (W/mK)	$\lambda_{th,dep}$ (W/mK)	$D_{th,lat}$ (10^{-6}m^2/s)	$D_{th,dep}$ (10^{-6}m^2/s)
Ni/Al	180	145	59	57
Ti/Al	131	40	55	18
Ni/Ti	49	31	16	22

Table 4.: Composite thermal properties of the investigated multilayer systems. Calculation based on equations 2.21 to 2.24 as well as the room temperature data given in table 4.2.

Multilayer thickness analysis

Layer i	Thickness		
	intended t_i (nm)	actual t_i (nm)	$\lvert\Delta t_i\rvert/t_i$ (%)
Ni capping	40.0	37.8±1.6	5.6
Al adhesive	50.0	41.9±6.0	16.3
Ni	20.0	22.7±1.5	13.7
Al	30.0	22.3±2.5	11.6
total	390.0	349.9±3.3	10.3

Table 5.: Comparison of intended and actual layer thickness as well as their relative deviation $|\Delta t_i|/t_i$ for as-deposited Ni/Al multilayers.

Layer i	Thickness		
	intended t_i (nm)	actual t_i (nm)	$\lvert\Delta t_i\rvert/t_i$ (%)
Ti capping	50.0	55.4±2.8	10.8
Ti adhesive	50.0	55.9±2.1	11.8
Ti	25.0	27.0±1.4	7.9
Al	25.0	25.4±1.4	1.6
total	425.0	451.6±2.5	6.3

Table 6.: Comparison of intended and actual layer thickness as well as their relative deviation $|\Delta t_i|/t_i$ for as-deposited Ti/Al multilayers.

Layer i	Thickness		
	intended t_i (nm)	actual t_i (nm)	$\lvert\Delta t_i\rvert/t_i$ (%)
Ti capping	40.0	49.1±5.2	1.8
Ti adhesive	50.0	45.8±2.9	8.5
Ni	20.0	19.9±1.4	0.2
Ti	30.0	25.4±0.4	15.4
total	410.0	386.9±7.4	5.6

Table 7.: Comparison of intended and actual layer thickness as well as their relative deviation $|\Delta t_i|/t_i$ for as-deposited Ni/Ti multilayers.

Bibliography

[1] Arzt, E.: *Size effects in materials due to microstructural and dimensional constraints: A comparative review.* Acta Materialia, 46(16):5611–5626, 1998.

[2] Gleiter, H.: *Nanocrystalline materials.* Progress in Materials Science, 33:223–315, 1989.

[3] Gleiter, H.: *Nanostructured materials: Basic concepts and microstructure.* Acta materialia, 48:1–29, 2000.

[4] Meyers, M.A., Mishra, A. and Benson, D.J.: *Mechanical properties of nanocrystalline materials.* Progress in Materials Science, 51(4):427–556, 2006.

[5] Nix, W.D.: *Mechanical properties of thin films.* Metallurgical and Materials Transactions A, 20(11):2217–2245, 1989.

[6] Misra, A. and Kung, H.: *Deformation behavior of nanostructured metallic multilayers.* Advanced Engineering Materials, 3(4):217–222, 2001.

[7] Friedman, L.H.: *Towards a full analytic treatment of the Hall–Petch behavior in multilayers: Putting the pieces together.* Scripta Materialia, 50(6):763–767, 2004.

[8] Spaepen, F.: *The art and science of microstructural control.* Science, 235:1010–1014, 1987.

[9] Brechet, Y. and Embury, J.D.: *Architectured materials: Expanding materials space.* Scripta Materialia, 68(1):1–3, 2013.

[10] Sarikaya, M.: *An introduction to biomimetics: A structural viewpoint.* Microscopy research and technique, 27(5):360–375, 1994.

[11] Barthelat, F.: *Biomimetics for next generation materials.* Philosophical transactions. Series A, Mathematical, physical, and engineering sciences, 365(1861):2907–2919, 2007.

[12] Fratzl, P.: *Biomimetic materials research: What can we really learn from nature's structural materials?* Journal of the Royal Society, Interface, 4(15):637–642, 2007.

[13] Bhushan, B.: *Biomimetics: Lessons from nature - An overview.* Philosophical transactions. Series A, Mathematical, physical, and engineering sciences, 367(1893):1445–1486, 2009.

[14] Peterlik, H., Roschger, P., Klaushofer, Klaus and Fratzl, P.: *From brittle to ductile fracture of bone.* Nature Materials, 5(1):52–55, 2006.

[15] Gao, H.: *Application of fracture mechanics concepts to hierarchical biomechanics of bone and bone-like materials.* International Journal of Fracture, 138(1-4):101–137, 2006.

[16] Fratzl, P. and Weinkamer, R.: *Nature's hierarchical materials.* Progress in Materials Science, 52(8):1263–1334, 2007.

[17] Mücklich, F., Lasagni, A. and Daniel, C.: *Laser interference metallurgy - Periodic surface patterning and formation of intermetallics.* Intermetallics, 13(3-4):437–442, 2006.

[18] Mücklich, F., Lasagni, A. and Daniel, C.: *Laser Interference Metallurgy-using interference as a tool for micro/nano structuringce Patterning and Formation of Intermetallics.* International Journal of Materials Research, 97(10):1–8, 2006.

[19] Daniel, C.: *Skalierung der Steifigkeit von dünnen Filmen mittels Laser-Interferenz-Metallurgie am Beispiel von Ni/Al-Multi-Filmen.* PhD thesis, Saarland University, Saarbrücken, Germany, 2005.

[20] Jäger, I.L. and Fratzl, P.: *Mineralized collagen fibrils: a mechanical model with a staggered arrangement of mineral particles.* Biophysical Journal, 79(4):1737–1746, 2000.

[21] Simha, N.K., Fischer, F.D., Kolednik, O. and Chen, C.R.: *Inhomogeneity effects on the crack driving force in elastic-plastic materials.* Journal of the Mechanics and Physics of Solids, 51:209–240, 2003.

[22] Simha, N.K., Fischer, F.D., Kolednik, O., Predan, J. and Shan, G.X.: *Crack Tip Shielding or Anti-shielding due to Smooth and Discontinuous Material Inhomogeneities.* International Journal of Fracture, 135(1-4):73–93, 2005.

[23] Fratzl, P., Gupta, H.S., Fischer, F.D. and Kolednik, O.: *Hindered crack propagation in materials with periodically varying Young's modulus—Lessons from biological materials.* Advanced Materials, 19(18):2657–2661, 2007.

[24] Meyers, M.A., Chen, P.-Y., Lin, A.Y.-M. and Seki, Y.: *Biological materials: Structure and mechanical properties.* Progress in Materials Science, 53:1–206, 2008.

[25] Mehrabian, R.: *Rapid solidification.* International Metals Review, 27(4):185–208, 1982.

[26] Poate, J.M.: *High speed crystal growth and solidification using laser heating.* Journal of Crystal Growth, 79:549–561, 1986.

[27] Baeri, P.: *Nanosecond laser-induced phase transitions and metastable phases quenching.* Philosophical Magazine B, 61(4):587–600, 1990.

[28] Hillert, M.: *Solute drag, solute trapping and diffusional dissipation of Gibbs energy.* Acta Materialia, 47(18):4481–4505, 1999.

[29] Aziz, M.J., Tsao, J.Y., Thompson, M.O., Peercy, P.S. and White, C.W.: *Solute trapping: Comparison of theory with experiment.* Physical Review Letters, 56(23):2489–2678, 1986.

[30] Aziz, M.J.: *Interface attachment kinetics in alloy solidification.* Metallurgical and Materials Transactions A, 27:671–686, 1996.

[31] Kittl, J.A., Aziz, M.J., Brunco, D.P. and Thompson, M.O.: *Test of kinetic models for interface velocity, temperature, and solute trapping in rapid solidification.* In *MRS Symposium Proceedings*, volume 398, pages 119–126. Materials Research Society, 1996.

[32] Kittl, J.A., Sanders, P.G., Aziz, M.J., Brunco, D.P. and Thompson, M.O.: *Complete experimental test of kinetic models for rapid alloy solidification.* Acta Materialia, 48:4797–4811, 2000.

[33] Aziz, M.J.: *Model for solute redistribution during rapid solidification.* Journal of Applied Physics, 53(2):1158–1168, 1982.

[34] Aziz, M.J. and Boettinger, W.J.: *On the transition from short-range diffusion-limited to collision-limited growth in alloy solidification.* Acta Materialia et Metallurgica, 42(2):527–537, 1994.

[35] Perepezko, J.H.: *Use of metastable phase diagrams in rapid solidification.* In *MRS Symposium Proceedings*, volume 19, pages 223–240. Materials Research Society, 1983.

[36] Johnson, W.L.: *Thermodynamic and kinetic aspects of the crystal to glass transformation in metallic materials.* Progress in Materials Science, 30(2):81–134, 1986.

[37] Cahn, R.W. and Haasen, P.: *Physical Metallurgy.* North Holland - Elsevier B.V., 4th edition, 1996.

[38] Spaepen, F. and Turnbull, D.: *Kinetics of motion of crystal-melt interfaces.* AIP Conference Proceedings, 50(1):73–83, 1979.

[39] von Allmen, M. and Affolter, K.: *Glass forming ability in transition metal films at $10^{10} K/s$.* In *MRS Symposium Proceedings*, volume 28, pages 81–85. Materials Research Society, 1984.

[40] Lin, C.-J., Spaepen, F. and Turnbull, D.: *Picosecond pulsed laser-induced melting and glass formation.* Journal of Non-Crystalline Solids, 61-62:767–772, 1984.

[41] Lin, C.-J. and Spaepen, F.: *Metallic glasses and metastable crystallline phases produced by picosecond laser quenching.* In *MRS Symposium Proceedings*, volume 28, pages 75–80. Materials Research Society, 1984.

[42] Lin, C.-J. and Spaepen, F.: *Nickel-Niobium alloys obtained by picosecond pulsed laser quenching.* Acta Metallurgica, 34(7):1367–1375, 1986.

[43] Wang, W.-K., Lobb, C.J. and Spaepen, F.: *Formation of metastable Nb-Si phases by picosecond and nanosecond laser quenching.* Materials Science and Engineering, 98:325–328, 1988.

[44] MacDonald, C.A., Malvezzi, A.M. and Spaepen, F.: *Picosecond time-resolved measurements of crystallization in noble metals.* Journal of Applied Physics, 65(1):129–136, 1989.

[45] Im, J.S. and Kim, H.J.: *On the super lateral growth phenomenon observed in excimer laser-induced crystallization of thin Si films.* Applied Physics Letters, 64(17):2303–2305, 1994.

[46] Im, J.S., Crowder, M.A., Sposili, R.S., Leonard, J.P., Kim, H.J., Yoon, J.H., Gupta, V.V., Song, H.J. and Cho, H.S.: *Controlled super-lateral growth of Si films for microstructural manipulation and optimization.* physica status solidi (a), 166:603–617, 1998.

[47] Aichmayr, G., Toet, D., Mulato, M., Santos, P.V., Spangenberg, A., Christiansen, S., Albrecht, M. and Strunk, H.P.: *Lateral grain growth during the laser interference crystallization of a-Si.* physica status solidi (a), 166:659–666, 1998.

[48] Grigoropoulos, C.P., Moon, S.-J., Lee, M., Hatano, M. and Suzuki, K.: *Thermal transport in melting and recrystallization of amorphous and polycrystalline Si thin films.* Applied Physics A: Materials Science & Processing, 69:S295–S298, 1999.

[49] Lee, M., Moon, S., Hatano, M., Suzuki, M. and Grigoropoulos, C.P.: *Relationship between fluence gradient and lateral grain growth in spatially controlled excimer laser crystallization of amorphous Silicon films.* Journal of Applied Physics, 88(9):4994–4999, 2000.

[50] Moon, S.-J., Lee, M. and Grigoropoulos, C.P.: *Heat transfer and phase transformations in laser annealing of thin Si films.* Journal of Heat Transfer, 124(2):253–264, 2002.

[51] Kline, J.E. and Leonard, J.P.: *Rapid lateral solidification of pure Cu and Au films encapsulated in SiO_2.* Applied Physics Letters, 86:201902–1–201902–3, 2005.

[52] Kline, J.E. and Leonard, J.P.: *Suppression of dewetting phenomena during excimer laser melting of thin metal films on SiO_2.* Thin Solid Films, 488(1-2):306–313, 2005.

[53] Zhong, R., Kulovits, A.K., Wiezorek, J.M.K. and Leonard, J.P.: *Four-zone solidification microstructure formed by laser melting of Copper thin films.* Applied Surface Science, 256(1):105–111, 2009.

[54] Kulovits, A.K., Zhong, R., Wiezorek, J.M.K. and Leonard, J.P.: *Electron microscopy of geometrically confined Copper thin films after rapid lateral solidification.* Thin Solid Films, 517(13):3629–3634, 2009.

[55] Kulovits, A.K., Wiezorek, J.M.K., LaGrange, T., Reed, B.W. and Campbell, G.H.: *Revealing the transient states of rapid solidification in Aluminum thin films using ultrafast in situ transmission electron microscopy.* Philosophical Magazine Letters, 91(4):287–296, 2011.

[56] Catrin, R., Lasagni, A.F., Gachot, C., Schmid, U. and Mücklich, F.: *Microstructural design of advanced architectures in Titanium/Platinum thin films by laser interference metallurgy.* Advanced Engineering Materials, 10(5):466–470, 2008.

[57] Gachot, C., Catrin, R., Lasagni, A., Schmid, U. and Mücklich, F.: *Comparative study of grain sizes and orientation in microstructured Au, Pt and W thin films designed by laser interference metallurgy.* Applied Surface Science, 255(10):5626–5632, 2009.

[58] Daniel, C., Lasagni, A. and Mücklich, F.: *Stress and Texture Evolution of Ni/Al Multi-Films by Laser Interference Irradiation.* Surface & Coatings Technology, 180-181:478–482, 2004.

[59] Lasagni, A., Holzapfel, C. and Mücklich, F.: *Periodic pattern formation of intermetallic phases with long range order by laser interferene metallurgy.* Advanced Engineering Materials, 7(6):487–492, 2005.

[60] Lasagni, A.F., Holzapfel, C., Weirich, T. and Mücklich, F.: *Laser interference metallurgy: A new method for periodic surface microstructure design on multilayered metallic thin films.* Applied Surface Science, 253(19):8070–8074, 2007.

[61] Kraft, O. and Volkert, C.A.: *Mechanical testing of thin films and small structures.* Advanced Engineering Materials, 3(3):99–110, 2001.

[62] Kraft, O.: *Encyclopedia of Materials: Science and Technology*, chapter Thin films: Mechanical testing, pages 9257–9262. Elsevier Science Ltd., 2001.

[63] Oliver, W.C. and Pharr, G.M.: *Measurements of hardness and elastic modulus by instrumented indentation: Advances in understanding and refinements to methodology.* Journal of Materials Research, 19(1):3–20, 2004.

[64] Spearing, S.M.: *Materials issues in microelectromechanical systems (MEMS).* Acta Materialia, 48:179–196, 2000.

[65] Detemple, E., Leibenguth, P., Gachot, C. and Mücklich, F.: *Large-area patterned formation of intermetallic phases on Ti/Al multilayer systems by laser interference metallurgy.* Thin Solid Films, 519(2):736–741, 2010.

[66] Schaaf, P.: *Laser nitriding of metals.* Progress in Materials Science, 47:1–161, 2002.

[67] Bäuerle, D.: *Laser processing and chemistry.* Springer, 4th edition, 2011.

[68] von Allmen, M. and Blatter, A.: *Laser-beam interactions with materials - Physical principles and application.* Springer, 2nd edition, 1995.

[69] Hügel, H. and Graf, T.: *Laser in der Fertigung.* Vieweg+Teubner, 2nd edition, 2009.

[70] Hecht, E.: *Optik.* Oldenbourg, 3rd edition, 2001.

[71] Born, M. and Wolf, E.: *Principles of optics - Electromagnetic theory of propagation, interference and diffraction of light.* Cambridge University Press, 7th edition, 1999.

[72] Dressel, M. and Grüener, G.: *Electrodynamics of Solids - Optical properties of electrons in matter.* Cambridge University Press, 1st edition, 2003.

[73] Meschede, D.: *Gerthsen Physik.* Springer, 21st edition, 2001.

[74] Feynman, R.P., Leighton, R.B. and Sands, M.: *Feynman Vorlesungen über Physik - Band II: Elektromagnetismus und Struktur der Materie.* Oldenbourg, 4th edition, 2001.

[75] Drude, P.: *Zur Elektronentheorie der Metalle.* Annalen der Physik, 306(3):566–613, 1900.

[76] Bloembergen, N.: *Pulsed laser interactions with condensed matter.* In *MRS Symposium Proceedings*, volume 51, pages 3–13. Materials Research Society, 1985.

[77] Marín, E., Delgado-Vasallo, O. and Valiente, H.: *A temperature relaxation method for the measurement of the specific heat of solids at room temperature in student laboratories.* American Journal of Physics, 71(10):1032–1036, 2003.

[78] Baehr, H.D. and Stephan, K.: *Wärme- und Stoffübertragung.* Springer, 5th edition, 2006.

[79] Lasagni, A.F.: *Advanced design of periodical structures by laser interference metallurgy in the micro/nano scale on macroscopic areas.* PhD thesis, Saarland University, Saarbrücken, Germany, 2006.

[80] Schommer, S.: *Untersuchung der tribologischen Eigenschaften von laserstrukturierten Ti/Al-Multischichtsystemen.* Diploma thesis, Saarland University, Saarbrücken, Germany, 2011.

[81] Salazar, A.: *On thermal diffusivity.* European Journal of Physics, 24:351–358, 2003.

[82] Marín, E.: *Characteristic dimensions for heat transfer.* Latin American Journal of Physics Education, 4(1):56–60, 2010.

[83] Marín, E.: *The role of thermal properties in periodic time-varying phenomena.* European Journal of Physics, 28(3):429–445, 2007.

[84] Jacobson, L.A. and McKittrick, J.: *Rapid solidification processing.* Materials Science and Engineering R, 11:355–408, 1994.

[85] Turnbull, D.: *Metastable structures in metallurgy.* Metallurgical Transactions A, 12:695–708, 1981.

[86] Bormann, R.: *Phase reactions under highly non-equilibrium conditions.* Materials Science and Engineering A, 226-228:268–273, 1997.

[87] Perepezko, J.H.: *Nucleation-controlled reactions and metastable structures.* Progress in Materials Science, 49(3-4):263–284, 2004.

[88] Shechtman, D., Blech, I., Gratias, D. and Cahn, J.W.: *Metallic phase with long-range orientational translational symmetry.* Physical Review Letters, 53(20):1951–1954, 1984.

[89] Shechtman, D. and Blech, I.: *The microstructure of rapidly solidified Al_6Mn.* Metallurgical and Materials Transactions A, 16(6):1005–1012, 1985.

[90] Boettinger, W.J.: *Growth kinetic limitations during rapid solidification.* In *MRS Symposium Proceedings*, volume 8, pages 15–31. Materials Research Society, 1982.

[91] Kurz, W. and Trivedi, R.: *Rapid solidification processing and microstructure formation.* Materials Science and Engineering A, 179-180:46–51, 1994.

[92] Haasen, P.: *Physical Metallurgy.* Cambridge University Press, 3rd edition, 1996.

[93] Porter, D.A., Easterling, K.E. and Sherif, M.E.: *Phase transformations in metals and alloys.* CRC Press, 3rd edition, 2009.

[94] Jackson, K.A.: *Liquid metals and solidification*, chapter Mechanisms of growth, pages 174–186. ASM, 1958.

[95] Schleip, E., Herlach, D.M. and Feuerbacher, B.: *External seeding of a metastable metallic phase.* Europhysics Letters, 11(8):751–755, 1990.

[96] Herlach, D.M.: *Non-equilibrium solidification of undercooled metallic melts.* Materials Science and Engineering R, 12:177–272, 1991.

[97] Uhlmann, D.R.: *A kinetic treatment of glass formation.* Journal of Non-Crystalline Solids, 7(4):337–348, 1972.

[98] Thompson, C.V. and Spaepen, F.: *Homogeneous crystal nucleation in binary metallic melts.* Acta Metallurgica, 31(12):2021–2027, 1983.

[99] Turnbull, D.: *On the relation between crystallization rate and liquid structure.* Journal of Physical Chemistry, 66(4):609–613, 1962.

[100] Kurz, W. and Gilgien, P.: *Selection of microstructures in rapid solidification processing.* Materials Science and Engineering A, 178:171–178, 1994.

[101] Coriell, S.R. and Turnbull, D.: *Relative roles of heat transport and interface rearrangement rates in the rapid growth of crystals in undercooled melts.* Acta Metallurgica, 30(12):2135–2139, 1982.

[102] Aziz, M.J. and Kaplan, T.: *Continuous growth model for interface motion during alloy solidification.* Acta Metallurgica, 36(8):2335–2347, 1988.

[103] Assadi, H. and Greer, A.L.: *The interfacial undercooling in solidification.* Journal of Crystal Growth, 172(1-2):249–258, 1997.

[104] Hillert, M. and Schalin, M.: *Modeling of solute drag in the massive phase transformation.* Acta Materialia, 48(2):461–468, 2000.

[105] Hillert, M., Odqvist, J. and Agren, J.: *Comparison between solute drag and dissipation of Gibbs energy by diffusion.* Scripta Materialia, 45:221–227, 2001.

[106] Greer, A.L.: *Diffusion and reactions in thin films.* Applied Surface Science, 86:329–337, 1995.

[107] Bormann, R., Gärtner, F. and Zöltzer, K.: *Application of the calphad method of amorphous phase formation.* Journal of the Less-Common Metals, 145:19–29, 1988.

[108] Bormann, R. and Zöltzer, K.: *Determination of the thermodynamic functions and calculations of phase diagrams for metastable phases.* physica status solidi (a), 131:691–705, 1992.

[109] Ishihara, K.N. and Shingu, P.H.: *Calculation of T_0 curves and metastable phase equilibria in connection with rapid solidification.* Materials Science and Engineering, 63(2):251–256, 1984.

[110] Kurz, W. and Trivedi, R.: *Solidification microstructures: Recent developments and future directions.* Acta Metallurgica et Materialia, 38(1):1–17, 1990.

[111] Trivedi, R. and Kurz, W.: *Solidification microstructures: A conceptual approach.* Acta Metallurgica et Materialia, 42(1):15–23, 1994.

[112] Perepezko, J.H.: *Nucleation controlled phase selection during solidification.* Materials Science and Engineering A, 413-414:389–397, 2005.

[113] Freund, L.B. and Suresh, S.: *Thin film materials - Stress, defect formation and surface evolution.* Cambridge University Press, 1st edition, 2003.

[114] Jadaan, O.M., Nemeth, N.N., Bagdahn, J. and Sharpe, W.N.: *Probabilistic Weibull behavior and mechanical properties of MEMS brittle materials*. Journal of Materials Science, 38(20):4087–4113, 2003.

[115] Gachot, C., Leibenguth, P. and Mücklich, F.: *´Tribological properties of laser interference induced microstructural architectures in metallic systems*, pages 59–66. Wiley-VCH, 2009.

[116] Salmang, H. and Scholze, H.: *Keramik - Teil 2 Keramische Werkstoffe*. Springer, 6. edition, 1993.

[117] GVB GmbH: *Eigenschaften unserer Quarzglasplatten aus EN08 Material*, 6 2011.

[118] Haynes, W.M.: *Handbook of chemistry and physics*. CRC Press, 91st edition, 2010.

[119] Baker, H. (Ed.): *ASM Handbook - Volume 3, Alloy Phase Diagrams*. ASM International, 1st edition, 1992.

[120] Sauthoff, G.: *Materials science and technology - Structure and properties of nonferrous alloys*, chapter 11 - Intermetallics, pages 645–803. Wiley-VCH, 1995.

[121] Westbrook, J.H. and Fleischer, R.L.: *Structural applications of intermetallic compounds*. John Wiley & Sons, Inc., 2nd edition, 2000.

[122] Westbrook, J.H. and Fleischer, R.L.: *Magnetic, electrical and optical properties and applications of intermetallic compounds*. John Wiley & Sons, Inc., 2nd edition, 2000.

[123] Desai, P.D.: *Thermodynamic properties of selected binary Aluminum alloy systems*. Journal of Physical and Chemical Reference Data, 16(1):109–124, 1987.

[124] Ansara, I., Sundman, B. and Willemin, P.: *Thermodynamic modeling of ordered phases in the Ni-Al system*. Acta Metallurgica, 36(4):977–982, 1988.

[125] Ansara, I., Dupin, N., Lukas, H.L. and Sundman, B.: *Thermodynamic assessment of the Al-Ni system.* Journal of Alloys and Compounds, 247:20–30, 1997.

[126] Pasturel, A., Colinet, C., Paxton, A.T. and van Schilfgaarde, M.: *First-principles determination of the Ni-Al phase diagram.* Journal of Physics: Condensed Matter, 4:945–959, 1992.

[127] Springer, Landolt-Börnstein, New Series IV/19B, SGTE: *2 Binary Systems: Al-Ni (Aluminium-Nickel)*, 10655491-46 2012.

[128] Springer, Landolt-Börnstein, New Series IV/5A, SGTE: *Phase Equilibria, Crystallographic and Thermodynamic Data of binary Alloys: Al-Ni (Aluminium-Nickel)*, 10000866-125 2012.

[129] Springer, Landolt-Börnstein, New Series IV/12A Supplement to IV/5A, SGTE: *Phase Equilibria, Crystallographic and Thermodynamic Data of Binary Alloys: Al-Ni (Aluminium-Nickel)*, 10793176-104 2012.

[130] Guard, R.W. and Tukalo, A.M.: *Mechanical properties of intermetallic compounds*, page 141. John Wiley & Sons, Inc., 1960.

[131] Ball, A.: *Observation of a martensitic transformation in the compound NiAl.* Metal Science, 1:47–48, 1967.

[132] Rosen, S. and Goebel, J.A.: *The crystal structure of Nickel-rich NiAl and martensitic NiAl.* Transactions of the Metallurgical Society AIME, 242(4):722–724, 1968.

[133] Enami, K. and Nenno, S.: *Memory effect in Ni-36.8 at. pct Al martensite.* Metallurgical and Materials Transactions B, 2:1487–1490, 1971.

[134] Tanner, L.E., Pelton, A.R., VanTendeloo, G., Schryvers, D. and Wall, M.E.: *Premartensitic microstructures in Ni-Al ordered $\beta 2$ phase: I - Effects induced by cooling.* Scripta Metallurgica et Materialia, 24:1731–1736, 1990.

[135] George, E.P., Liu, C.T., Horton, J.A., Sparks, C.J., Kao, M., Kunsmann, H. and King, T.: *Characterization, processing, and alloy design of NiAl-based shape memory alloys.* Materials Characterization, 32:139–160, 1994.

[136] Blobaum, K.J., Van Heerden, D., Gavens, A.J. and Weihs, T.P.: *Al/Ni formation reactions: characterization of the metastable Al_9Ni_2 phase and analysis of its formation.* Acta Materialia, 51(13):3871–3884, 2003.

[137] Munir, Z.A. and Anselmi-Tamburini, U.: *Self-propagating exothermic reactions: The synthesis of high-temperature materials by combustion.* Materials Science Reports, 3(7-8):277–365, 1989.

[138] Ma, E., Thompson, C.V., Clevenger, L.A. and Tu, K.N.: *Self-propagating explosive reactions in Al/Ni multilayer thin films.* Applied Physics Letters, 57(12):1262–1264, 1990.

[139] Dyer, T.S. and Munir, Z.A.: *Self-propagating exothermic reactions: The synthesis of high-temperature materials by combustion.* Metallurgical and Materials Transactions B, 26(6):603–610, 1995.

[140] Huang, W. and Chang, Y.A.: *A thermodynamic analysis of the Ni-Al system.* Intermetallics, 6(6):487–498, 1998.

[141] Springer, Landolt-Börnstein, New Series IV/19B, SGTE: *2 Binary Systems: Al-Ti (Aluminium-Titanium)*, 10655491-53 2012.

[142] Liang, W.W.: *A thermodynamic assessment of the Aluminum-Titanium system.* Calphad, 7(1):13–20, 1983.

[143] Gros, J.P., Sundman, B. and Ansara, I.: *Thermodynamic modeling of the Ti-rich phases in the Ti-Al system.* Scripta metallurgica, 22:1587–1591, 1988.

[144] Kainuma, R., Palm, M. and Inden, G.: *Solid-phase equilibria in the Ti-rich part of the Ti-Al system.* Intermetallics, 2:321–332, 1994.

[145] Zhang, F., Chen, S.L., Chang, Y.A. and Kattner, U.R.: *A thermodynamic description of the Ti-Al system.* Intermetallics, 5(6):471–482, 1997.

[146] Ohnuma, I., Fujita, Y., Mitsui, H., Ishikawa, K., Kainuma, R. and Ishida, K.: *Phase equilibria in the Ti–Al binary system.* Acta Materialia, 48(12):3113–3123, 2000.

[147] Kainuma, R., Sato, J., Ohnuma, I. and Ishida, K.: *Phase stability and interdiffusivity of the $L1_0$-based ordered phases in Al-rich portion of the Ti–Al binary system.* Intermetallics, 13(7):784–791, 2005.

[148] Schuster, J.C. and Palm, M.: *Reassessment of the binary Aluminum-Titanium phase diagram.* Journal of Phase Equilibria and Diffusion, 27(3):255–277, 2006.

[149] Colinet, C. and Pasturel, A.: *Ab initio calculation of the formation energies of $L1_2$, $D0_{22}$, $D0_{23}$ and one dimensional long period structures in $TiAl_3$ compound.* Intermetallics, 10:751–764, 2002.

[150] Wang, L., He, B. and Jiang, X.H.: *Modeling the velocity of self-propagating exothermic reactions in multilayer foils.* Combustion Science and Technology, 182(8):1000–1008, 2010.

[151] Colinet, C.: *The thermodynamic properties of rare earth metallic systems.* Journal of Alloys and Compounds, 225(1-2):409–422, 1995.

[152] Schuster, J.C. and Palm, M.: *Reassessment of the binary Aluminum-Titanium phase diagram.* Journal of Phase Equilibria and Diffusion, 27(3):255–277, 2006.

[153] Buehler, W.J. and Wiley, R.C.: *TiNi-ductile intermetallic compound.* Transactions of ASM, 55:269–276, 1962.

[154] Otsuka, K. and Ren, X.: *Recent developments in the research of shape memory alloys.* Intermetallics, 7(5):511–528, 1999.

[155] Bhattacharya, K.: *Microstructure of martensite.* Oxford University Press, 1st edition, 2004.

[156] Otsuka, K. and Ren, X.: *Physical metallurgy of Ti–Ni-based shape memory alloys.* Progress in Materials Science, 50(5):511–678, 2005.

[157] Bhattacharya, K.: *Thin films of active materials.* In *Nonlinear Homogenization and its Applications to Composites, Polycrystals and Smart Materials*, pages 15–44. NATO ARW, 2001.

[158] Le, D.H., Colinet, C., Hicter, P. and Pasturel, A.: *Theoretical description of phase equilibrium in the nickel-titanium system.* Journal of Physics: Condensed Matter, 3:9965–9974, 1991.

[159] Zöltzer, K. and Bormann, R.: *Thermodynamics of stable and metastable phases in the NiTi system and its application to amorphous phase formation.* Journal of the Less-Common Metals, 140:335–343, 1988.

[160] Colinet, C. and Pasturel, A.: *Thermodynamics of the Nickel-Titanium system.* Physica B, 192:238–246, 1993.

[161] Pasturel, A., Colinet, C., Nguyen Manh, D., Paxton, A.T. and van Schilfgaarde, M.: *Electronic structure and phase stability study in the Ni-Ti system.* Physical Review B, 52(21):15176–15190, 1995.

[162] Bellen, P., Hari Kumar, K.C. and Wollants, P.: *Thermodynamic assessment of the Ni-Ti phase diagram.* Zeitschrift für Metallkunde, 87(12):972–978, 1996.

[163] Springer, Landolt-Börnstein, New Series IV/19B, SGTE: *2 Binary Systems: Ni-Ti (Nickel-Titanium)*, 10757285-36 2012.

[164] Dong, C.: *Binary alloy phase diagrams, 2nd edition*, chapter Nickel-Titanium. ASM International, 1990.

[165] Adams, D.P., Rodriguez, M.A., McDonald, J.P, Bai M.M., Jones, E., Brewer, L.N. and Moore, J.J.: *Reactive Ni/Ti nanolaminates.* Journal of Applied Physics, 106(9):093505–1 – 093505–8, 2009.

[166] Gavens, A.J., Van Heerden, D. and Mann, A.B.: *Effect of intermixing on self-propagating exothermic reactions in Al/Ni nanolaminate foils.* Journal of Applied Physics, 87(3):1255–1263, 2000.

[167] Mattox, D.M.: *Handbook of Physical Vapor Deposition (PVD) Processing - Film Formation, Adhesion, Surface Preparation and Contamination Control.* Noyes Publications, 1st edition, 1998.

[168] Haefer, R.A.: *Oberflächen- und Dünnschichttechnologie Teil 1: Beschichtungen von Oberflächen.* Springer, 1st edition, 1987.

[169] Wobrock, M.C.: *Präparation von Ti/Ni Dünnschichten mittels Ionenstrahl PVD für die Herstellung des thermischen Formgedächtniseffektes durch nachgeschaltete thermische Behandlungsverfahren.* Student research project, Saarland University, Saarbrücken, Germany, 2010.

[170] Maldovan, M. and Thomas, E.L.: *Periodic Materials and Interference Lithography for Photonics, Phononics and Mechanics.* Wiley-VCH, 1st edition, 2009.

[171] Detemple, E.: *Untersuchung der Steifigkeitsskalierung am Beispiel von LIMET-strukturierten Ti/Al-Multilayern mittels Bulge-Test.* Diploma thesis, Saarland University, Saarbrücken, Germany, 2008.

[172] Schramm Benítez, I.C.: *Localized formation of intermetallic phases by LIMET in Ni/Al multilayer thin films.* Master´s thesis, Saarland University, Saarbrücken, Germany, 2010.

[173] Gachot, C., Rosenkranz, A., Reinert, L., Ramos-Moore, E., Souza, N., Müser, M.H. and Mücklich, F.: *Dry friction between laser-patterned surfaces: Role of alignment, structural wavelength and surface chemistry.* Tribology Letters, 49(1):193–202, 2013.

[174] Manzoni, A.: *Periodische LIMET-Strukturierung von metallischen Multilayer-Dünnschichten zur lokalen Erzeugung von intermetallischen Phasen.* Diploma thesis, Saarland University, Saarbrücken, Germany, 2008.

[175] Wobrock, M.C.: *Laserinterferenz-Metallurgie von Ti/Ni Multilayern zur lokalen Induzierung des Formgedächtniseffektes.* Diploma thesis, Saarland University, Saarbrücken, Germany, 2011.

[176] Giannuzzi, L.A. and Stevie, F.A.: *Introduction to Focus Ion Beams.* Springer, 1st edition, 2005.

[177] Volkert, C.A. and Minor, A.: *Focused ion beam micromachining.* MRS Bulletin, 32(5):389–399, 2007.

[178] Mayer, J., Giannuzzi, A., Kamino, T. and Michael, J.: *TEM sample preparation and FIB-induced damage.* MRS Bulletin, 32(5):400–407, 2007.

[179] Bals, S., Tirry, W., Geurts, R., Yang, Z. and Schryvers, D.: *High-quality sample preparation by low kV FIB thinning for analytical TEM measurements.* Microscopy and Microanalysis, 13(2):80–86, 2007.

[180] Kiener, D., Motz, C., Rester, M., Jenko, M. and Dehm, G.: *FIB damage of Cu and possible consequences for miniaturized mechanical tests.* Materials Science and Engineering A, 459(1-2):262–272, 2007.

[181] Thompson, K., Lawrence, D., Larson, D.J., Olson, J.D., Kelly, T.F. and Gorman, B.P.: *In situ site-specific specimen preparation for atom probe tomography.* Ultramicroscopy, 107(2-3):131–139, 2007.

[182] Kelly, T.F. and Miller, M.K.: *Invited review artivle: Atom probe tomography.* Review of Scientific Instruments, 78(3):031101–1–20, 2007.

[183] Miller, M.K. and Forbes, R.G.: *Atom probe tomography.* Materials Characterization, 60(6):7461–469, 2009.

[184] Miller, M.K., Russell, K.F., Thompson, K., Alvis, R. and Larson, D.J.: *Review of atom probe FIB-based specimen preparation methods.* Microscopy and Microanalysis, 13(6):428–436, 2007.

[185] Seidman, D.N. and Stiller, K.: *An atom-probe tomography primer.* MRS Bulletin, 34(10):717–724, 2009.

[186] de Graef, M.: *Introduction to conventional transmission electron microscopy.* Cambridge University Press, 1st edition, 2003.

[187] Reimer, L. and Kohl, H.: *Transmission electron microscopy.* Springer, 5th edition, 2008.

[188] Williams, D.B. and Carter, C.B.: *Transmission electron microscopy - I-IV.* Springer, 2nd edition, 2009.

[189] Zou, Z., Hovmöller, S. and Oleynikov, P.: *Electron crystallography - Electron microscopy and electron diffraction.* Oxford Science Publications, 1st edition, 2011.

[190] International Center for Diffraction Data: *PDF2-Release 2011 – PCPDFWin Database Version 2.1102.* International Center for Diffraction Data, 2011.

[191] Larson, D.J., Cerezo, A., Juraszek, J., Hono, K. and Schmitz, G.: *Atom-probe tomographic studies of thin films and multilayers.* MRS Bulletin, 34(10):732–737, 2009.

[192] Alvis, R. and Kelly, T.F.: *Atom-probe microscopy LEAPs the chasm to mainstream applications.* Microscopy Today, (September):46–11, 2008.

[193] Gerstl, S.S.A.: *Three-dimensional nanometer scale analyses of precipitate structures and local compositions in TiAl engineering alloys.* PhD thesis, Northwestern University, Evanston, U.S.A., 2006.

[194] Miller, M.K., Cerezo, A. and Hetherington, M.G.: *Atom probe field ion microscopy.* Oxford Science Publications, 1st edition, 1996.

[195] Gault, B., Moody, M.P., Cairney, J.M. and Ringer, S.P.: *Atom probe microscopy.* Springer, 1st edition, 2012.

[196] Kingham, D.R.: *The post-ionization of field evaporated ions: A theoretical explanation of multiple charge states.* Surface Science, 116(2):273–301, 1982.

[197] Modest, M.F.: *Handbook of laser materials processing*, chapter Reflectivity and absorbtivity of opaque surfaces, pages 175–181. Magnolia Publishing, Inc., 2001.

[198] Zavecz, T.E. and Saifi, M.A.: *Metal reflectivity under high-intensity optical radiation.* Applied Physics Letters, 26(4):165–168, 1975.

[199] Metev, S.M. and Veiko, V.P.: *Laser-assisted microtechnology.* Springer, 2nd edition, 1995.

[200] Ready, J.F.: *Change of reflectivity of metallic surfaces during irradiation by CO_2-TEA laser pulses.* IEEE Journal of Quantum Electronics, 12(2):137–142, 1976.

[201] Niedrig, H.: *Bergmann-Schäfer Lehrbuch der Experimentalphysik - Band 3 Optik*. Walter de Gruyter Verlag, 10th edition, 2004.

[202] Zhang, X. and Grigoropoulos, C.P.: *Thermal conductivity thin films and diffusivity of free-standing silicon nitride thin films*. Review of Scientific Instruments, 66(2):1115–1120, 1995.

[203] Revaz, B., Zink, B.L., O'Neil, D., Hull, L. and Hellman, F.: *Numerical simulation of the heat transfer in amorphous silicon nitride membrane-based microcalorimeters*. Review of Scientific Instruments, 74(10):4389–4403, 2003.

[204] Ye, T., Suo, Z. and Evans, A.G.: *Thin film cracking and the roles of substrate and interface*. International Journal of Solids and Structures, 29(21):2639–2648, 1992.

[205] Nakamura, T. and Kamath, S.M.: *Three-dimensional effects in thin film fracture mechanics*. Mechanics of Materials, 13(1):67–77, 1992.

[206] Ohring, M.: *Materials science of thin films – Deposition & structure*. Academic Press, 2nd edition, 2001.

[207] Thornton, J.A.: *The microstructure of sputter-deposited coatings*. Journal of Vacuum Sciance and Technology A, 4(6):3059–3065, 1986.

[208] Barna, P.B. and Adamik, M.: *Fundamental structure forming phenomena of polycrystalline films and the structure zone models*. Thin Solid Films, 317:27–33, 1998.

[209] Petrov, I., Barna, P.B., Hultman, L. and Greene, J.E.: *Microstructural evolution during film growth*. Journal of Vacuum Sciance and Technology A, 21(5):S117–S127, 2003.

[210] Anders, A.: *A structure zone diagram including plasma based deposition and ion etching.* Thin Solid Films, 518(15):4087–4090, 2010.

[211] Thompson, C.V.: *Grain growth in thin films.* Annual Review of Materials Science, 20(1):245–268, 1990.

[212] Springer, Landolt-Börnstein, New Series IV/12A Supplement to IV/5A, SGTE: *Phase Equilibria, Crystallographic and Thermodynamic Data of Binary Alloys: Al-Ti (Aluminium-Titanium)*, 10793176-128 2012.

[213] Bonetti, E., Valdré, G., Enzo, S. and Cocco, G.: *Lattice destabilization and amorphization by mechanical alloying in the Ti-Al system.* Journal of Alloys and Compounds, 194(2):331–338, 1993.

[214] Gerasimov, K.B. and Pavlov, S.V.: *Metastable Ti-Al phases obtained by mechanical alloying.* Journal of Alloys and Compounds, 242(1-2):136–142, 1996.

[215] Schwarz, R.B., Petrich, R.R. and Saw, C.K.: *The synthesis of amorphous Ni-Ti alloy powders by mechanical alloying.* Journal of Non-Crystalline Solids, 76:281–302, 1985.

[216] Hollanders, M.A. and Thijsse, B.J.: *Simultaneous amorphization at interfaces and grain boundaries in an Ni/Ti multilayer.* Journal of Non-Crystalline Solids, 117-118:696–699, 1990.

[217] Aliaga, L.C.R., De Oliveira, M.F., Bolfarini,C., Botta, W.J. and Kiminami, C.S.: *Selection of good glass former compositions in Ni–Ti system using a combination of topological instability and thermodynamic criteria.* Journal of Non-Crystalline Solids, 354(17):1932–1935, 2008.

[218] Houard, J., Vella, A., Vurpillot, F. and Deconihout, B.: *Optical near-field absorption at a metal tip far from plasmonic resonance.* Physical Review B, 81:125411–1 – 125411–5, 2010.

[219] Dmitrieva, O., Choi, P., Gerstl, S.S.A., Ponge, D. and Raabe, D.: *Pulsed-laser atom probe studies of a precipitation hardened maraging TRIP steel.* Ultramicroscopy, 111(6):623–627, 2011.

[220] Okamoto, H.: *Phase diagram updates: Al-Ti (Aluminum-Titanium).* Journal of Phase Equilibria, 14(1):120–121, 1993.

[221] Thompson, G.B., Fraser, H.L. and Miller, M.K.: *Atom probe tomography characterization of multilayer films.* Microscopy and Microanalysis, 9(Supplement 2):574–575, 2003.

[222] Gault, B., Loi, S.T., Araullo-Peters, V.J., Stephenson, L.T., Moody, M.P., Shrestha, S.L., Marceau, R.K.W., Yao, L., Cairney, J.M. and Ringer, S.P.: *Dynamic reconstruction for atom probe tomography.* Ultramicroscopy, 111(11):1619–1624, 2011.

[223] Vurpillot, F., Larson, D.J. and Cerezo, A.: *Improvement of multilayer analyses with a three-dimensional atom probe.* Surface and Interface Analysis, 36:552–558, 2004.

[224] Vurpillot, F., Gruber, M., Da Costa, G., Martin, I., Renaud, L. and Bostel, A.: *Pragmatic reconstruction methods in atom probe tomography.* Ultramicroscopy, 111(8):1286–1294, 2011.

[225] Bachhav, M., Danoix, R., Hannoyer, D., Ogale, S. and Vurpillot, F.: *Investigation of Wüstite ($Fe_{1-x}O$) femtosecond laser assisted atom probe tomography.* Ultramicroscopy, 111(6):584–588, 2011.

[226] Okamoto, H.: *Phase diagram updates: Al-Ni (Aluminum-Nickel).* Journal of Phase Equilibria, 14(2):257–259, 1993.

[227] Herlach, D.M., Feuerbacher, B. and Schleip, E.: *Phase seeding in the solidification of an undercooled melt.* Materials Science and Engineering A, 133:795–798, 1991.

[228] Schwarz, R.B. and Johnson, W.L.: *Formation of an amorphous alloy by soldi-state reaction of the pure polycrystalline metals.* Physical Review Letters, 51(5):415–418, 1983.

[229] Perepezko, J.H., Chang, Y.A., Fecht, H.J. and Zhang, M.X.: *Metastable phase equilibria and solid state amorphization.* Journal of the Less-Common Metals, 140:287–297, 1988.

[230] Saunders, N. and Miodownik, A.P.: *Thermodynamic aspects of amorphous phase formation.* Journal of Materials Research, 1(1):38–46, 1986.

[231] Kyllesbech Larsen, K., Karpe, N., Bøttiger, J. and Bormann, R.: *Ion irradiation induced phase formation in Al-Ni.* Journal of Materials Research, 7(4):861–867, 1992.

[232] Kyllesbech Larsen, K., Skovmand, S., Karpe, N., Bøttiger, J. and Bormann, R.: *On the phase formation during ion beam mixing of Al-Ti.* Nuclear Instruments and Methods B, 80-81:390–393, 1993.

[233] Thompson, C.V.: *On the role of diffusion in phase selection during reactions at interfaces.* Journal of Materials Research, 7(2):367–373, 1992.

[234] Desré, P.J. and Yavari, A.R.: *Suppression of crystal nucleation in amorphous layers with sharp concentration gradients.* Physical Review Letters, 64(13):1533–1536, 1990.

[235] Hodaj, F. and Desré, P.: *Effect of a sharp gradient of concentration on nucleation of intermetallics at interfaces between polycrystalline layers.* Acta Materialia, 44(11):4485–4490, 1996.

[236] Hodaj, F., Gusak, A.M. and Desré, P.: *Effect of sharp concentration gradients on the nucleation of intermetallics in disordered solids: Influence of the embryo shape.* Philosophical Magazine A, 77(6):1471–1479, 1998.

[237] Cahn, J.W. and Hilliard, J.E.: *Free energy of a nonuniform system - I. Interfacial free energy.* The Journal of Chemical Physics, 28(2):258–267, 1958.

[238] Ma, E., Thompson, C.V. and Clevenger, L.A.: *Nucleation and growth during reactions in multilayer Al/Ni films: The early stage of Al_3Ni formation.* Journal of Applied Physics, 69(4):2211–2218, 1991.

[239] Busch, R., Gärtner, F., Borchers, C., Haasen, P. and Bormann, R.: *Microstructure development during rapid solidification of highly supersaturated Cu-Co alloys.* Acta Metallurgica et Materialia, 43(9):3467–3475, 1995.

[240] Miedema, A.R., Boom, R. and De Boer, F.R.: *On the heat of formation of solid alloys.* Journal of the Less-Common Metals, 41:283–298, 1975.

[241] Van der Kolk, G.J., Miedema, A.R. and Niessen, A.K.: *On the composition range of amorphous binary transition metal alloys.* Journal of the Less-Common Metals, 145:1–17, 1988.

[242] Hollanders, M.A., Thijsse, B.J. and Mittemeijer, E.J.: *Amorphization along interfaces and grain boundaries in polycrystalline multilayers: An x-ray-diffraction study of Ni/Ti multilayers.* Physical Review B, 42(9):5481–5494, 1990.

[243] Hollanders, M.A., Thijsse, B.J. and Mittemeijer, E.J.: *A model for interdiffusion in polycrystalline multilayers and its application to solid state amorphization.* physica status solidi (a), 127:133–146, 1991.

[244] Masuhr, A., Waniuk, T.A., Busch, R. and Johnson, W.L.: *Time scales for viscous flow, atomic transport and crystallization in the liquid and supercooled*

liquid states of $Zr_{41.2}Ti_{13.8}Cu_{12.5}Ni_{10.0}Be_{22.5}$. Physical Review Letters, 82(11):2290–2293, 1999.

[245] Mehrer, H.: *Diffusion in solids.* Springer, 1st edition, 2007.

[246] Terada, Y., Ohkubo, K., Nakagawa, K., Mohri, T. and Suzuki, T.: *Thermal conductivity of B2 aluminide and titanides.* Intermetallics, 3(5):347–355, 1995.

[247] Bostanjoglo, O. and Penschke, V.: *Kinetics of laser-induced phase transitions in Ni-Al alloys.* Journal of Applied Physics, 73(12):8201–8205, 1993.

[248] Du, Y., Chang, Y.A., Huang, B., Gong, W., Jin, Z., Xu, H., Yuan, Z., Liu, Y., He, Y. and Xie, F.-Y.: *Diffusion coefficients of some solutes in fcc and liquid Al: critical evaluation and correlation.* Materials Science and Engineering A, 363(1-2):140–151, 2003.

[249] Robertson, I.M. and Wayman, C.M.: *Tweed microstructures I. Characterization in β-NiAl.* Philosophical Magazine A, 48(3):421–442, 1983.

[250] Robertson, I.M. and Wayman, C.M.: *Tweed microstructures II. In several phases of the Ni-Al system.* Philosophical Magazine A, 48(3):443–467, 1983.

[251] Boettinger, W.J. and Aziz, M.J.: *Theory for the trapping of disorder and solute in intermetallic phases by rapid solidification.* Acta Metallurgica, 37(12):3379–3391, 1989.

[252] Boettinger, W.J.: *Thermodynamic constraints on non-equilibrium solidification of ordered intermetallic compounds.* Materials Science and Engineering A, 133:438–442, 1991.

[253] Assadi, H. and Greer, A.L.: *Solidification of intermetallic compounds.* In *MRS Symposium Proceedings*, volume 400, pages 173–184. Materials Research Society, 1996.

[254] Assadi, H. and Greer, A.L.: *Site-ordering effects on element partitioning during rapid solidification of alloys.* Nature, 383(12):150–152, 1996.

[255] Khachaturyan, A.G., Shapiro, S.M. and Semenovskaya, S.: *Adaptive phase formation in martensitic transformation.* Physical Review B, 43(13):10832–10843, 1991.

[256] Khachaturyan, A.G., Shapiro, S.M. and Semenovskaya, S.: *Adaptive phase in martensitic transformation.* Materials Transactions JIM, 33(3):278–281, 1992.

[257] Kockar, B., Karaman, I., Kim, J.I., Chumlyakov, Y.I., Sharp, J. and Yu, C.-J.: *Thermomechanical cyclic response of an ultrafine-grained NiTi shape memory alloy.* Acta Materialia, 56(14):3630–3646, 2008.

[258] Assadi, H., Barth, M., Greer, A.L. and Herlach, D.M.: *Kinetics of solidification of intermetallic compounds in the Ni-Al system.* Acta Materialia, 46(2):491–500, 1998.

[259] Mohan Rao, P.V., Satyanarayana Murthy, K., Suryanarayana, S.V. and Nagender Naidu, S.V.: *Effect of ternary additions on the room temperature lattice parameter of Ni_3Al.* physica status solidi (a), 133(2):231–235, 1992.

[260] Novoselova, T., Celotto, S., Morgan, R., Fox, P. and O'Neill, W.: *Formation of TiAl intermetallics by heat treatment of cold-sprayed precursor deposits.* Journal of Alloys and Compounds, 436:67–77, 2007.

[261] Kaack, M.: *Elastische Eigenschaften von NiTi-Formgedächtnis-Legierungen.* PhD thesis, Ruhr-Universität Bochum, Germany, 2002.

List of Figures

1.1. Schematic representation of two adjacent interference maxima (*max*) embedded into a minimum region (*min*). The heat-affected zone (grey) is suitable for a *through reaction* (a). Corresponding TEM foil extracted perpendicular to the periodic line pattern (b) with close-up image of the modified surface layers (c). The structural situation within unaffected (d) and processed multilayer (e) is shown in according SADs (modified from [19]). 10

1.2. Local variation of indentation hardness and reduced elastic modulus between adjacent min and max positions (a). Wafer-bow results of the global elastic behaviour of large-area LIMET treated Ni/Al multilayers plotted as a function of $1/d^2$ with linear regression following Jäger´s bone model (taken from [19]). 12

3.1. Change in volume free energy (a) in dependence on temperature in (s) and (l) and change in free energy (b) during homogeneous nucleation of a sphere with radius r. (c) schematically shows the energetic difference between homogeneous and heterogeneous nucleation (all modified from [93]). 30

3.2. Schematic situation at a (s)-(l) interface when (a) heat is extracted into (s) and (b) heat is conducted into a supercooled liquid: temperature distribution (left) and associated isotherms (right) (modified from [93]). . 32

3.3. Hypothetical binary phase diagram with linearised phase boundaries (a) and assumed idealised situation (b) for unidirectional planar solidification of an alloy with composition X_0 (modified from [93]). 34
3.4. Constitutional undercooling at a planar solidification front: composition profile during steady-state growth (a) and temperature profile $T_{(l)}$ (b) for heat extraction into (s) along with equilibrium liquidus temperature characteristic T_e (modified from [93]). 36
3.5. Schematic atomic arrangement during growth of a solidification front from left to right (a) depicting the trapping a solute atom (no. 4) into (s) (taken from [33]). (b) general free energy characteristic for transformations involving an activated state of higher free energy (modified from [93]). . . . 40
3.6. Range of solidification front velocities typically encountered in rapid solidification (a) including distinct intervals of different dominating phenomena (according to [91]). Functional course of non-equilibrium patition coefficient k_v under rapid solidification conditions (b) in dependence of normalised interface velocity equal to the Péclet number (modified from [34]). 42
3.7. Fractional contributions of solute drag, solute trapping and kinetics to the resulting interfacial undercooling as a function of logarithmic normalised interface velocity (equal to logarithmic Péclet number). As shown, for each velocity regime the atomic attachment is dominated by one of these undercooling contributions (modified from [103]). 45
3.8. Molar free energy curve (a) for a solid solution, where the pure components A and B share the same crystal structure (modified from [93]). Concept of the rule of parallel tangents: (b) schematic free energy diagram of two phases at liquidus temperature T_L and (c) the situation for an arbitrary nucleation temperature $T_N < T_L$ (modified from [98][37]). . . 47

3.9. Effect of the different contributions to interfacial undercooling as introduced in figure 3.6 on the shape of a hypothetical phase diagram: true kinetic undercooling (a) shifts the phase boundaries to lower temperatures, solute drag (c) effects skewing and the boundaries fall on the T_0 line for solute trapping (c) in effect (modified from [103]). 49
3.10. Schematic representation of regions of different resulting solidifcation microstructures for different selections of solidification parameters: (a) temperature gradient vs. interfacial velocity (taken from [84]) and (b) alloy composition vs. interfacial velocity (taken from [110]). 52
3.11. Greer´s simplified master curves on (a) thermodynamic interaction and diffusional mass transport of pure multilayer components and (b) pulsed laser treatment parameters with critical diffusional and microstructural dimensions (both taken from [106]). 55

4.1. Equilibrium phase diagram of Ni/Al system (taken from [127]). 62
4.2. Equilibrium phase diagram of Ti/Al system (taken from [141]). 64
4.3. Equilibrium phase diagram of Ni/Ti system (taken from [163]). 65

5.1. Intended specimen stack design with respective capping and adhesive layers including the devised nominal values for individual layer t_i and total stack thicknesses t_{tot}. 68
5.2. General outline of (a) the I-PVD chamber used (ion beam direction and sputter plume indicated schematically) and (b) the custom-made rotation holder for the different substrates. 71
5.3. Calculated two-beam interference pattern (a) according to equation 5.3 (modified from [171]) and general two-beam LIMET setup (b) with general coordinate frame used in this thesis (modified from [172] and [173]). 74

5.4. Sequence of SEM micrographs depicting FIB machining of APT specimens: preliminary wedge-shaped specimen attached to micromanipulator directly after site-specific lift-out (a). LIMET maximum location at microtip array post prior to Pt-deposition (b) and final APT specimen tip of this region (c) after annular milling and low-kV polishing. 77

5.5. Schematic representation of the general setup of the APT system employed in this thesis. The trajectory of the ions through the reflectron lens is indicated by the curved lines (modified and rearranged after [182][192][183]). 80

5.6. Schematic depiction of a half-period of multilayer stack and substrate as used in the FEM simulations along with the spatial intensity distribution effective during LIMET: $I(x)$ representing the lateral and $I(z)$ the depth component (modified from [80]). 84

6.1. 2D representation of the $T(\vec{r},t)$ results (a) of the FEM thermal simulation obtained for Ni/Al on sc-Si irradiated using a nominal fluence F of $275\,\mathrm{mJ/cm^2}$. General coordinate frame used in the following for the description of the FEM results (b) introducing the propagation coordinates of the (s)-(l) interface (points A and B of the component with smaller T_m) as well as the effective thermal gradient ∇T there. 91

6.2. Direct comparison of the thermal simulation results obtained for Ni/Al on sc-Si (□) and fused silica (■) when varying d and F: (a) maximum temperature T_{max} at the multilayer surface of the interference maximum location. (b) fraction of molten Al and (c) duration of the Al melt. . . . 93

6.3. Direct comparison of the thermal simulation results obtained for Ni/Al on sc-Si (□) and fused silica (■) when varying d and F: normalised lateral propagation of point A l_{top} (a) and normalised propagation of point B in lateral l_{bot} (b) as well as in depth direction t_{dep} (c) (all quantities introduced in figure 6.1 (b)). 96

6.4. Direct comparison of the thermal simulation results obtained for Ni/Al on sc-Si (□) and fused silica (■) when varying d and F: Thermal gradient at A-B boundary in lateral (a) as well as in depth direction (b). Corresponding heat flow angle α (c) (all quantities introduced in figure 6.1 (b)). 99

6.5. Direct comparison of the thermal simulation results obtained for the three multilayer material systems (1-Ni/Al, 2-Ti/Al and 3-Ni/Ti) on sc-Si (open forms) and fused silica (filled forms) when varying F for a constant periodicity of 8 μm: (a) maximum temperature T_{max} at the multilayer surface of the interference maximum location. (b) fraction of molten $T_{m,low}$ component and (c) corresponding melt duration. 102

6.6. Direct comparison of the thermal simulation results obtained for the three multilayer material systems (1-Ni/Al, 2-Ti/Al and 3-Ni/Ti) on sc-Si (open forms) and fused silica (filled forms) when varying F for a constant periodicity of 8 μm: normalised lateral propagation of point A l_{top} (a) and normalised propagation of point B in lateral l_{bot} (b) as well as in depth direction t_{dep} (c) (all quantities introduced in figure 6.1 (b)). 104

6.7. Ni/Al as-deposited multilayer on sc-Si: TEM micrograph (a) and corresponding SADP (b) with qualitative phase analysis. 107

6.8. Ti/Al as-deposited multilayer on sc-Si: TEM micrograph (a) and corresponding SADP (b) with qualitative phase analysis. 109

6.9. Ni/Ti as-deposited multilayer on sc-Si: TEM micrograph (a) and corresponding SADP (b) with qualitative phase analysis. 110

6.10. Characterisation of the spatial intensity distribution of a LIMET spot obtained by beam profiling (a) (modified from [172]): 2D colour coded representation (top) and 1D profile measured along the dash dot line (bottom). SEM top-view micrograph of a typical LIMET spot (b): zone suitable for site-specific specimen preparation (*prep zone*) indicated. . . . 112

6.11. SEM top-view micrographs of the damage inflicted to Ni/Al multilayers on the different substrates (sc-Si (a), a-Si_xN_y (b) and fused silica (c)) when using fluences slightly above the identified ablation limit. The inserts show close-up images to the scale of the highlighting boxes. 114

6.12. SEM top-view micrographs of the damage inflicted to Ni/Al multilayers when using different periodicities (4 μm (a), 8 μm (b) and 16 μm (c)) at a constant fluence of 275 mJ/cm^2. 116

6.13. SEM top-view micrographs of the damage inflicted the three multilayer material systems deposited on sc-Si (Ni/Al (a), Ti/Al (b) and Ni/Ti (c)) when using the same (d,F) conditions. 117

6.14. SEM/FIB cross-section micrographs obtained for Ni/Al multilayers on the different substrates (sc-Si (a), a-Si_xN_y (b) and fused silica (c)) for LIMET processing at $d = 8\,\mu$m using the individual optimum fluences for LIMET given there. 120

6.15. SEM/FIB cross-section micrographs obtained for Ni/Al multilayers on sc-Si substrate for different LIMET periodicities (4 μm (a), 8 μm (b) and 16 μm (c)) using the optimum fluence 275 mJ/cm^2. 122

6.16. Direct comparison between FEM estimated normalised dimensions of the heat-affected zone (designated □) and the corresponding results obtained by cross-sectional imaging (■) for Ni/Al on sc-Si substrate: lateral expansion at the multilayer surface l_{top} (a), lateral expansion at the substrate interface l_{bot} (b) and depth expansion t_{dep} (c). 124

6.17. Direct comparison between FEM estimated normalised dimensions of the heat-affected zone (designated □) and the corresponding results obtained by cross-sectional imaging (■) for Ni/Al on a-SiO_2 substrate: lateral expansion at the multilayer surface l_{top} (a), lateral expansion at the substrate interface l_{bot} (b) and depth expansion t_{dep} (c). 125

6.18. TEM micrographs obtained for Ni/Al multilayers on the different substrates (sc-Si (a), a-Si_xN_y (b) and fused silica (c)) for LIMET processing at $d = 8\,\mu$m using the individual optimum fluences for LIMET given there. The schematic representation of the heat-affected zone and its surroundings (d) introduces the designation of three distinct regions with different processing result ((I) to (III)) along with the A-B boundary representing the $T_{m.low}$ isothermal. 128

6.19. TEM structural analysis of the vicinity of an interference maximum obtained for Ni/Al on sc-Si after LIMET treatment using $d = 8\,\mu$m and $F = 275\,\mathrm{mJ/cm^2}$: TEM micrograph (a) indicating the different processing regions and the location of the site-specific SAD analyses. SADP of the unmodified region (I) (b), the transition between regions (I) and (II) (c) as well as region (II) alone. 130

6.20. TEM structural analysis of an interference maximum obtained for Ni/Al on sc-Si after LIMET treatment using $d = 8\,\mu$m and $F = 275\,\mathrm{mJ/cm^2}$: TEM micrograph (a) indicating the location of the site-specific SAD analyses. SADP zone axis images of region (III) flank (b), and two individual grains within region (III) plateau (c) and (d). 133

6.21. TEM structural analysis of an interference maximum obtained for Ni/Al on a-SiO_2 after LIMET treatment using $d = 8\,\mu$m and $F = 150\,\mathrm{mJ/cm^2}$: TEM micrograph (a) indicating the location of the site-specific SAD analyses. SADP zone axis images of two individual grains within region (III) (b) and (c) as well as region (II) (d). 136

6.22. TEM micrographs obtained for Ti/Al and Ni/Ti multilayers on the different substrates (sc-Si (a) and (c) as well as fused silica (b) and (d)) for LIMET processing at $d = 8\,\mu$m using the individual optimum fluences for LIMET given there. The identified A-B boundaries are indicated. 138

6.23. Direct comparison between FEM estimated normalised dimensions of the heat-affected zone (open forms) obtained for the three multilayer material systems (1-Ni/Al, 2-Ti/Al and 3-Ni/Ti) and the corresponding results obtained by cross-sectional imaging (filled forms) on sc-Si substrate when varying F for a constant periodicity of $8\,\mu$m: lateral expansion at the multilayer surface l_{top} (a), lateral expansion at the substrate interface l_{bot} (b) and depth expansion t_{dep} (c). 141

6.24. Direct comparison between FEM estimated normalised dimensions of the heat-affected zone (open forms) obtained for the three multilayer material systems (1-Ni/Al, 2-Ti/Al and 3-Ni/Ti) and the corresponding results obtained by cross-sectional imaging (filled forms) on a-SiO_2 substrate when varying F for a constant periodicity of $8\,\mu$m: lateral expansion at the multilayer surface l_{top} (a), lateral expansion at the substrate interface l_{bot} (b) and depth expansion t_{dep} (c). 142

6.25. TEM structural analysis of an interference maximum obtained for Ti/Al on sc-Si after LIMET treatment using $d = 8\,\mu$m and $F = 275\,\mathrm{mJ/cm^2}$: TEM micrograph (a) indicating the location of the site-specific SAD analyses. SADP zone axis images of region (III) flank (b), and region (III) centre at the thin film surface (c) as well as close to the substrate interface (d). 144

6.26. TEM structural analysis of an interference maximum obtained for Ti/Al on a-SiO_2 after LIMET treatment using $d = 8\,\mu$m and $F = 200\,\mathrm{mJ/cm^2}$: TEM micrograph (a) indicating the location of the site-specific SAD analyses. SADP zone axis images of region (III) flank close to the substrate interface (b) and at the thin film surface (c) as well as region (III) centre (d). 146

6.27. TEM structural analysis of an interference maximum obtained for Ni/Ti on sc-Si after LIMET treatment using $d = 8\,\mu$m and $F = 275\,\mathrm{mJ/cm^2}$: TEM micrograph (a) indicating the location of the site-specific SAD analyses. SADP zone axis images of region (III) flank (b) and (c) as well as region (III) centre. 148

6.28. TEM structural analysis of an interference maximum obtained for Ni/Ti on a-SiO_2 after LIMET treatment using $d = 8\,\mu$m and $F = 200\,\mathrm{mJ/cm^2}$: TEM micrograph (a) indicating the location of the site-specific SAD analyses. SADP zone axis images of the transition between region (II) and region (III) flank (b), region (III) flank alone (c) as well as region (III) centre. 150

6.29. Background corrected mass-spectrum typical for the Ni/Al multilayer specimens (correction based on protocol contained in analysis software IVAS): 58.2 Mio ions recorded, 47.8 Mio analysed, background level 2.68 ppm/ns with peak characteristics FWHM 1201.7 and FWTM 575.5. 153

6.30. Site-specific APT analysis of distinct processing regions of LIMET treated Ni/Al on sc-Si substrates: The TEM micrograph (a) indicates the approximate extraction locations for the subsequently analysed APT specimen tips. The latter are shown along with their corresponding APT 3D reconstructions in (b) for region (II), (c) for region (III) flank and (d) region (III) plateau. For the sake of better visibility 0.3 % of the Ni and the Al atoms and 100 % of the O atoms are visualised there. 155

6.31. Site-specific APT analysis of distinct processing regions of LIMET treated Ni/Al on sc-Si substrates: The TEM micrograph (a) indicates the approximate extraction locations for the subsequently analysed APT specimen tips. The 1D-concentration profiles calculated from a 40 nm-diameter cylindric ROI of the latter are shown in (b) for region (II), (c) for region (III) flank and (d) region (III) plateau. 157
6.32. Dedicated analysis of Ni/Al region (II) APT specimen tip: 3D reconstruction (a) of the specimen showing 50.0 at.% Ni iso-surfaces. (b) and (c) show proxigrams of these iso-surfaces summarised over upper (b) and lower (c) layer interfaces. 160
6.33. Dedicated analysis of Ni/Al region (III) flank APT specimen tip: close-up TEM micrograph and corresponding 3D reconstruction (a) of the specimen showing only the O 4.0 at.% iso-surfaces. The latter are confirming the presence of differently shaped O aggregates. (b) to (d) show proxigrams of individual O aggregates found at different depth coordinates z of the specimen tip. 162
6.34. Dedicated analysis of Ni/Al region (III) plateau APT specimen tip: close-up TEM micrograph and corresponding 3D reconstruction (a) of the specimen showing only the O 4.0 at.% iso-surfaces. Both images confirm the presence of globular O aggregates. (b) shows a proxigram calculated of five individual O aggregates. 163
6.35. Background corrected mass-spectrum for the Ti/Al multilayer specimens (correction based on IVAS protocol, courtesy of Cameca Instruments Inc.).164

6.36. Site-specific APT analysis of distinct processing regions of LIMET treated Ti/Al on sc-Si substrates (modified and corrected from [65]): The TEM micrograph (a) indicates the approximate extraction locations for the subsequently analysed APT specimen tips. The latter are shown along with their corresponding APT 3D reconstructions in (b) for region (II), (c) for region (III) flank and (d) region (III) centre (SEM micrographs of the specimen tips courtesy of Cameca Instruments Inc.; modified from [65]). . 166

6.37. Site-specific APT analysis of distinct processing regions of LIMET treated Ti/Al on sc-Si substrates (modified and corrected from [65]): The TEM micrograph (a) indicates the approximate extraction locations for the subsequently analysed APT specimen tips. The 1D-concentration profiles calculated from a cylindric ROI of the latter are shown in (b) for region (II), (c) for region (III) flank and (d) region (III) centre (modified from [65]). 167

6.38. Background corrected mass-spectrum typical for the Ni/Ti multilayer specimens (correction based on IVAS protocol): 55.9 Mio ions recorded, 34.7 Mio analysed, background level 5.74 ppm/ns with peak characteristics FWHM 1259.1 and FWTM 653.5. 169

6.39. Site-specific APT analysis of distinct processing regions of LIMET treated Ni/Ti on sc-Si substrates: The TEM micrograph (a) indicates the approximate extraction locations for the subsequently analysed APT specimen tips. The latter are shown along with their corresponding APT 3D reconstructions in (b) for region (III) flank and (c) region (III) centre. For the sake of better visibility 1 % of the Ni and the Ti atoms and 100 % of the O atoms are visualised there. 171

6.40. Site-specific APT analysis of distinct processing regions of LIMET treated Ni/Al on sc-Si substrates: The TEM micrograph (a) indicates the approximate extraction locations for the subsequently analysed APT specimen tips. The 1D-concentration profiles calculated from a 40 nm-diameter cylindric ROI of the latter are shown in (b) for region (III) flank and (C) region (III) plateau. 172

6.41. Dedicated analysis of Ni/Ti region (III) centre APT specimen tip: close-up TEM micrograph (a) and corresponding 3D reconstruction (b) of the specimen showing only the O 5.0 at.% (left) and N 2.5 at.% iso-surfaces (right). Both images confirm the presence of globular aggregates taken as residues from the original Ti layer. 173

6.42. Comparative overview of TEM, APT and FEM results obtained on Ni/Al multilayers on sc-Si (a) and a-SiO_2 substrate (b). Isotherms of T_m^{Al} (left) and $0.3 \cdot T_m^{Ni}$ (right) are included in each case. 175

6.43. Comparative overview of TEM, APT and FEM results obtained on Ti/Al multilayers on sc-Si (a) and a-SiO_2 substrate (b). Isotherms of T_m^{Al} (left) and $0.3 \cdot T_m^{Ti}$ (right) are included in each case. 177

6.44. Comparative overview of TEM, APT and FEM results obtained on Ni/Ti multilayers on sc-Si (a) and a-SiO_2 substrates (b). Isotherms of T_m^{Ni} (left) and $0.3 \cdot T_m^{Ti}$ (right) are included in each case. 179

7.1. Schematic visualisation of the working hypothesis on mass transport and solidification: spatial distribution of laser intensity (a) over a half-period of a pristine multilayer (b). Setting in of enhanced (s) diffusion and thus solid state amorphisation in region (II) (c). Subsequent formation of region (III) by melting of the low-T_m component (d) with Marangoni convection active. Situation of maximum expansion of the heat-affected zone before onset of resolidification (e). 182

7.2. Schematic visualisation of Desré´s treatment on thermodynamic nucleation barriers: two assumed compositional gradients $\nabla X^i(z)$ over an amorphous layer (a) (please note the counterintuitive selection of coordinate axes) and the G-X^i curves associated to the amorphous and the intermetallic phase under consideration (modified from [234]) 187
7.3. General approach of using G-X^i curves to assess phase formation under metastable conditions (a) and corresponding G-X^{Ni} curve for Ni/Al system at T=700 K according to Thermocalc and [231] (b). Grey-coloured area corresponds to the APT-determined composition within the indicated region. 190
7.4. G-X^{Ti} curve for Ti/Al system at T=700 K according to Thermocalc and [232](a) and G-X^{Ni} curve for Ni/Ti system at T=1100 K according to Thermocalc (b). Grey-coloured areas correspond to the APT determined compositions within the indicated regions. 193
7.5. Relative increase of fluence $\Delta F/F$ through the released ΔG_{mix} for Ni/Al on sc-Si (a) and a-SiO_2 (b). In both cases, the characteristic calculated for 4 μm, 8 μm and 16 μm periodicity are depicted (dashed lines). 198
7.6. Reevaluated direct comparison between FEM estimated normalised dimensions of the heat-affected zone (designated □) and the modified results of cross-sectional imaging (■) for Ni/Al on sc-Si substrate: lateral expansion at the multilayer surface l_{top} (a), lateral expansion at the substrate interface l_{bot} (b) and depth expansion t_{dep} (c). 200
7.7. Reevaluated direct comparison between FEM estimated normalised dimensions of the heat-affected zone (designated □) and the modified results of cross-sectional imaging (■) for Ni/Al on a-SiO_2 substrate: lateral expansion at the multilayer surface l_{top} (a), lateral expansion at the substrate interface l_{bot} (b) and depth expansion t_{dep} (c). 201

7.8. FEM estimated isotherm velocities v_{iso} as a function of periodicity (continuous line for $d = 8\,\mu$m) and fluence (dash dot lines at $200\,\mathrm{mJ/cm^2}$ and $300\,\mathrm{mJ/cm^2}$, respectively) for sc-Si (a) and a-SiO_2 substrate (b). 203

7.9. FEM estimated cooling rates $\dot{T}_i$ at the T_m^{Al} isotherm at its maximum lateral propagation as a function of periodicity (continuous line for $4\,\mu$m, $8\,\mu$m and $16\,\mu$m) for sc-Si (a) and a-SiO_2 (b). 207

7.10. TEM micrograph of Ni/Al region (III) on sc-Si substrate (a). dark-field imaging of $L1_0$-NiAl herring-bone morphology (b) and corresponding SADP (c): habit plane m and two twin orientation variants s_1 and s_2 indicated. Close-up dark-field imaging of central region (III) exhibiting prospective anti phase boundary (APB) structures in B2-NiAl (d). 211

7.11. Updated version of figure 3.11 (modified from [106]) containing information on the material systems investigated here and the simulation results (grey-coloured areas): Greer´s master curves on (a) thermodynamic interaction and diffusional mass transport of pure multilayer components and (b) pulsed laser treatment parameters with critical diffusional and microstructural dimensions. 217

List of Tables

4.1. Relevant thermal and thermodynamic properties of the employed MEMS substrate materials at room temperature along with their literature sources. T_m is amended by boiling point T_b and softening temperature T_{soft} if applicable (Si_xN_y decomposes at 2173 K). Until otherwise stated, the data are valid for bulk material and stem from [118]. 60

4.2. Relevant thermal and thermodynamic properties at room temperature of the metallic materials employed for multilayer deposition (from [118]). . . 61

5.1. Optimum process parameters for I-PVD deposition of metallic multilayered thin films applicable to all employed target materials. 72

5.2. Optimum process parameters for laser pulsing APT analyses of metallic multilayered thin films. An effective charge-state-ratio (CSR) of 0.024 was obtained. 83

6.1. Decomposed atomic composition of the overall recorded ions for the Ni/Al APT specimens (rounded to two digits). 153

6.2. Decomposed atomic composition of the overall recorded ions for the Ni/Ti APT specimens (rounded to two digits) 170

1. Structural data on the relevant phases of the Ni/Al system. Until otherwise stated, the structure data is taken from [190][163]. . . . . B

2. Structural data on the relevant phases of the Ti/Al system. Until otherwise stated, the structure data is taken from [190][141]. C
3. Structural data on the relevant phases of the Ti/Al system. Until otherwise stated, the structure data is taken from [190][163]. C
4. Composite thermal properties of the investigated multilayer systems. Calculation based on equations 2.21 to 2.24 as well as the room temperature data given in table 4.2. . . . . D
5. Comparison of intended and actual layer thickness as well as their relative deviation $|\Delta t_i|/t_i$ for as-deposited Ni/Al multilayers. . . . . E
6. Comparison of intended and actual layer thickness as well as their relative deviation $|\Delta t_i|/t_i$ for as-deposited Ti/Al multilayers. . . . . F
7. Comparison of intended and actual layer thickness as well as their relative deviation $|\Delta t_i|/t_i$ for as-deposited Ni/Ti multilayers. . . . . F